

Spin-motion coupling in cold atomic gases

by

A. P. Koller

M.S., University of Massachusetts Boston, 2011

B.S., Massachusetts Institute of Technology, 2005

A thesis submitted to the
Faculty of the Graduate School of the
University of Colorado in partial fulfillment
of the requirements for the degree of
Doctor of Philosophy
Department of Physics

2017

This thesis entitled:
Spin-motion coupling in cold atomic gases
written by A. P. Koller
has been approved for the Department of Physics

Prof. Ana Maria Rey

Prof. John Bohn

Date _____

The final copy of this thesis has been examined by the signatories, and we find that both the content and the form meet acceptable presentation standards of scholarly work in the above mentioned discipline.

Koller, A. P. (Ph.D., Physics)

Spin-motion coupling in cold atomic gases

Thesis directed by Prof. Ana Maria Rey

The interplay between spin and motional degrees of freedom in interacting electron systems has been a long-standing research topic in condensed matter physics. Interactions can modify the behavior of individual electrons and give rise to emergent collective phenomena such as superconductivity and colossal magnetoresistance. Theoretical understanding of non-equilibrium dynamics in interacting fermionic matter is limited, however, and many open questions remain. Ultracold atomic Fermi gases, with precisely controllable parameters, offer an outstanding opportunity to investigate the emergence of collective behavior in out-of-equilibrium settings. In this thesis we will describe how an optical lattice clock operated with neutral Fermionic atoms can be turned into a quantum simulator of charged particles in a strong magnetic field. We will then discuss the counterintuitive notion that weak interactions in a Fermi gas can lead to large scale collective behavior and global correlations. These ideas are being tested experimentally at JILA and the University of Toronto. We also investigate in detail the so-called spin model approximation which is used extensively throughout this thesis.

Acknowledgements

I would like to thank my Advisor Ana Maria Rey for all her help and advice, as well as for the opportunity I have had to work with and learn from a true professional. This work would not be possible without my collaborators: Michael Wall, Alexey Gorshkov, Michael Beverland, Kaden Hazard, Andrew Sykes, John Corson, Jose D’Incao, Chris Greene, John Bohn, Gorjan Alagic, Michael Martin, Josh Mundinger, Shuming Li, Xibo Zhang, Nigel Cooper, Jun Ye, Shimon Kolkowitz, Sarah Bromley, Tim Bothwell, Arghavan Safavi-Naini, Peiru He, and Ed Marti. Additionally, I have had the pleasure of sharing offices, discussions, and meetings with my additional fellow group mates Salvatore Manmana, Johannes Schachenmayer, Michael Foss-Feig, Oscar Pabon, Martin Garttner, Leonid Isaev, Robert Lewis-Swan, and Bihui Zhu.

There are so many close friends I have met in Boulder that it is challenging to name them all. Here is my attempt, limited mostly to the 2011 CU incoming physics graduate student class, in no particular order: Jorge Nicholas Hernandez Charpak, Jack Houlton, Oscar Henriksson, Dani Meriman, Paige Warmker, Tyler Gorda, AJ Johnson, Catherine Klauss, Yomay Shyur, Ben Pollard, Sara Campbell, Brian O’Callahan, Bob Peterson, Victor Colussi, Andy Missert, Liz Shanblatt, Ben Chapman, Michelle Miller, Scott Johnson, Teesa Christian, Andrea Egan, Brad Dinardo, Judith and Trevor, Adam Reed, and Dan Maser.

Lastly, I would like to thank Helen McCreery and my mother Eileen Landy for all their love and support.

Contents

Chapter

1	Introduction	1
1.1	Many Body Physics in Optical Lattice Clocks	2
1.1.1	The spin model approximation and beyond	2
1.1.2	Synthetic spin orbit coupling in an optical lattice clock	3
1.2	Spin dynamics in a magnetic field gradient	4
1.3	Nonequilibrium dynamics in other quantum gases	4
1.3.1	SU(N) quantum magnets in a flat-bottomed potential	5
1.3.2	Quench dynamics of a strongly interacting Bose gas	5
1.4	Outline of this thesis	5
1.5	Summary	7
2	Background	8
2.1	Motivation: many body physics in cold atoms systems and quantum simulation . . .	8
2.2	Two level atoms probed by light	9
2.2.1	Rabi spectroscopy	10
2.2.2	Ramsey Spectroscopy	11
2.3	Ultracold fermi gases	12
2.4	Optical lattices	14

3	Synthetic Spin Orbit Coupling in an Optical Lattice Clock	16
3.1	Introduction	16
3.2	Implementation	18
3.3	Probing the Chiral Band Structure	20
3.3.1	Lineshape and extraction of $\theta_{\mathbf{n}q}$ from momentum-resolved Rabi spectroscopy	20
3.4	Interaction Hamiltonian with the spin model assumption	23
3.5	Probing s -wave Interactions via Ramsey Spectroscopy	24
3.5.1	First-order density shift in Ramsey spectroscopy	26
3.6	Probing Beyond Mean Field Interactions via a Sliding Superlattice	28
3.6.1	Interacting dressed states with a sliding clock superlattice	31
3.7	Relative strength of ee losses for Sr.	34
3.8	Experiment	34
3.8.1	Measurement protocol	44
3.8.2	Characterization of the trapping potential	46
3.8.3	Band preparation	46
3.8.4	Measurements of axial heating and loss rates	48
3.8.5	Perturbative model	49
3.9	Summary	53
4	Single Particle Spin Dynamics in a Magnetic Field Gradient	55
4.1	Introduction	55
4.2	Spectroscopic Protocol	57
4.3	Linear Magnetic Field	58
4.3.1	Derivation of generalized coherent-state formula	59
4.3.2	Spin dynamics	60
4.3.3	Dynamics for a spin-echo sequence	62
4.3.4	General Considerations	65

4.4	Quadratic Magnetic Field	68
4.4.1	Spin Dynamics	70
4.4.2	Spin-echo sequence for quadratic magnetic field	71
4.4.3	General Considerations	72
4.5	Dynamics in three dimensions	74
4.5.1	Comparison with experiment	75
4.6	Summary and Outlook	77
5	Interacting Spin Dynamics in a Two Component Fermi Gas	78
5.1	Setup	80
5.2	The generalized spin model approximation	82
5.3	Spin observables	83
5.4	Dynamics in a linear gradient	86
5.5	Correlations	86
5.6	The generalized spin model approximation: validity and discussion	89
5.7	Spin segregation	92
5.7.1	Zero temperature spin density profile	96
5.7.2	High temperature spin density profile	98
5.7.3	Comparison with experiment in Ref. [14]	101
5.8	Scaling of dynamical quantities	104
5.9	Spin collisions in a one dimensional harmonic trap	106
5.9.1	Protocol 1: coherent spin domain wall	107
5.9.2	Protocol 2: coherent displaced initial state	109
5.10	Outlook	111
6	Beyond the Spin Model Approximation	112
6.1	Introduction	112
6.2	The spin model approximation for two atoms in an atomic clock	112

6.2.1	Setup	114
6.2.2	The spin model.	115
6.2.3	Fermions with s-wave interactions in one dimension	115
6.2.4	Ramsey dynamics in the spin model approximation	116
6.2.5	Ramsey dynamics in the weakly interacting regime ($u_{\uparrow\downarrow}^{1,0} \ll \omega_z$)	117
6.2.6	Ramsey dynamics in the strongly-interacting regime ($u_{\uparrow\downarrow}^{1,0} \gtrsim \omega_z$)	121
6.2.7	Fermions with s-wave interactions in two dimensions	124
6.3	Validity of the spin model for $N > 2$	125
6.3.1	Many Body Spin Echo	126
6.4	Validation of the spin model for spin-dependent traps and importance of corrections	126
6.5	Summary and Outlook.	132
7	Appendix A: High-temperature thermal average of density shift	136
8	Appendix B: Behavior of the Dicke Gap G	139
9	Appendix C: Matrix product state simulations	142
	Bibliography	145

Figures

Figure

- 2.1 (a) A Rabi sequence illuminates a two level atom for time t corresponding to pulse area $\theta = \Omega t$. (b) In a Ramsey sequence, two short Rabi pulses are separated by a dark time t during which the laser is turned off. 10
- 2.2 (a) Dynamics of $\langle n_e \rangle$ for a Rabi sequence for three different detunings. (b) Rabi lineshape evaluated at $t = \pi/2\Omega$ and Lorentzian envelope. 11
- 2.3 Geometry of optical lattices in one, two, and three dimensions. Image courtesy of Michael Foss-Feig. 14
- 3.1 (a) A clock laser along the Z direction of wavelength λ and Rabi frequency Ω interrogates the $^1S_0(g)$ - $^3P_0(e)$ transition in fermionic alkaline-earth atoms trapped in an optical lattice with magic wavelength λ_m . The transverse confinement is provided by Gaussian curvature of the lattice beams with harmonic frequency $h\nu_\perp$. Many transverse modes \mathbf{n} are populated at current operating temperatures. (b) The phase difference ϕ between adjacent sites j and $(j+1)$ induces SOC when atoms can tunnel with mode-dependent tunnel-coupling $J_{\mathbf{n}}$, realizing a synthetic two-leg ladder with flux ϕ per plaquette. 17

- 3.2 (a) SOC band structure for $\delta = -2J_0$, $\Omega_0 = J_0$ (solid lines) and $\Omega_0^p = 0.05J_0$ (dashed lines). The axial depth is $V = 12$ recoils, $J_0/h = 42$ Hz and $\nu_\perp \approx 900$ Hz. Colors correspond to state character, with g (e) being more blue (red). (b) Chiral Bloch vector angle, θ_{0q} , in the xz plane extracted from Rabi spectroscopy using the protocol explained in the text. The figure shows three temperatures for the parameters of (a). 18
- 3.3 (a) Thermally averaged Rabi lineshape fully accounting for trap non-separability. SOC-induced peaks are visible even at $T = 3\mu\text{K}$. (b) Three pulse sequences used to extract θ_{0q} in Fig. (2) of the main text. 22
- 3.4 A clock laser pulse with pulse area θ_1 imprints a phase difference ϕ between atoms in neighboring sites. Atom tunneling, J_n , allows for s -wave interactions, $\propto U_{eg}^-$, which are signaled as a density shift in Ramsey spectroscopy after a second pulse of area θ_2 is applied. 25
- 3.5 (a) An additional counter-propagating probing beam with a differential phase Υ generates a sliding superlattice potential, shown for $\phi = 7\pi/6$, corresponding to an ^{87}Sr OLC. For weak tunneling $J \ll \Omega$ transport is energetically suppressed except at resonant defect points (circled). (b) Two-particle interaction sectors classified by the total polarization M_x and spatial symmetry of the dressed states. An oval (figure-eight) denotes a symmetric (antisymmetric) spatial wavefunction. (c) Dynamics of a single particle at the tunneling resonance for two temperatures (red solid and blue dashed) and an off-resonant site (black dotted) for $J_0/h = 8\text{Hz}$, $\Omega_0/h = 1\text{kHz}$, $\phi = 7\pi/6$. (d) Normalized differential excitation extracted as explained in the text with the interaction parameters of Ref. [50]. The $M_x = 0$ components (solid lines) involve the s -wave sector, and so display a strong dependence of contrast on temperature, while the $M_{\pm 1}$ sectors (dashed lines) experience only weaker single-particle thermal dephasing. 29

- 3.6 Spin-orbit coupling (SOC) in a 1D lattice with tunable tunneling. **a**, Atoms are trapped in a 1D optical lattice formed by interfering a strong trapping beam (power P_1 , wavelength $\lambda_L = 813$ nm) with a counter-propagating, tunably attenuated retro-reflection (variable power P_2 , represented by a cartoon knob). The atoms are probed on the narrow clock transition with an ultra-stable clock laser ($\lambda_c = 698$ nm, Rabi frequency Ω). The resulting SOC Hamiltonian is equivalent to that of charged fermions on a synthetic 2D ladder, with horizontal tunneling rate J , vertical tunneling rate Ω , and a synthetic magnetic field flux $\phi = \pi\lambda_L/\lambda_c$. **b**, The clock laser couples the dispersion curve for $|g\rangle_{n_z=0}$ (dashed red line) to the quasimomentum-shifted curve for $|e\rangle_0$ (dashed blue line), resulting in spin-orbit coupled bands (solid bichromatic lines). **c**, Clock spectroscopy ($\Omega \approx 2\pi \times 200$ Hz, 80 ms pulse duration) at four axial trapping potentials (data and fits are shifted upward for clarity). When $P_2 = 0$ mW, the sidebands and carrier merge into a Doppler broadened Gaussian (red diamonds). The solids lines are theoretical calculations using a model that perturbatively treats the axial and radial coupling. **d**, Spectroscopy of atoms in $|e\rangle_0$, prepared by driving the $|g\rangle_0 \rightarrow |e\rangle_0$ transition, then removing any remaining atoms in $|g\rangle$ 37

- 3.7 Van Hove singularities and band mapping. **a**, Excited state fraction following a π -pulse ($\Omega = 2\pi \times 100$ Hz) at four axial trapping potentials, with the atoms initially prepared in $|g\rangle_0$. The curves are offset in both x and y for clarity. The split peaks at $U_z/E_r \leq 13.7$ are a result of divergences in the atomic density of states known as Van Hove singularities (VHSs). **b**, Ground state fraction following a Rabi pulse for the same potentials shown in **a**, with the atoms initially prepared in $|e\rangle_1$. The duration of the Rabi pulse was varied to improve population contrast. **c**, The splitting between the VHS peaks in the $|g\rangle_0 \rightarrow |e\rangle_0$ (purple circles) and $|g\rangle_1 \rightarrow |e\rangle_1$ (orange squares) transition lineshapes as a function of trapping potential, extracted using fits as shown in **a** and **b**. Horizontal error bars are $1\text{-}\sigma$ standard error estimates from spectroscopy of the axial sidebands, vertical error bars are $1\text{-}\sigma$ standard error estimates for the extracted VHS splitting. The no-free parameter predicted VHS splittings for atoms in the ground and first excited bands of a 1D sinusoidal lattice (purple and orange dashed lines respectively,) and for a model including the transverse motional modes and finite atomic temperatures (purple and orange solid lines) are shown for comparison. 40
- 3.8 Bloch oscillations. (Lower right inset,) The split Rabi lines shown in Fig. 2a,b enable the spectral selection of atoms with a particular quasimomentum q^* . A π -pulse ($\Omega = 2\pi \times 100$ Hz) tuned to the left Van Hove peak is applied (red arrow) and the remaining ground state atoms are removed. (Upper left inset,) In a lattice tilted with respect to gravity, the atoms initially prepared with corresponding $q^* \approx \pi$ (red arrow) undergo Bloch oscillations. (Main figure,) Following a variable wait time t from the end of the first π -pulse, a second π -pulse is applied, revealing a highly asymmetric lineshape (first blue curve at 25 ms). The atoms undergo Bloch oscillations, resulting in periodic oscillations of the lineshape as the waiting time between the first and second pulse is varied. The curves are offset in both x and y for clarity. 43

- 3.9 Rabi measurements of the chiral Bloch vector. **a**, Atoms are selectively prepared in a quasimomenta window using a π -pulse ($\Omega = 2\pi \times 10$ Hz,) with five different pulse detunings (colored arrows). An axial potential of $U_z/E_r = 15.6$ is used, resulting in $\Delta/(2\pi) \approx 67$ Hz. A second stronger Rabi pulse ($\Omega = 2\pi \times 100$ Hz) tuned to the right Van Hove peak is used to generate SOC (red star). **b**, The chiral Bloch vectors corresponding to the detunings in **a** are shown, along with the clock state spin precession for each vector. **c**, The SOC band structure experienced by the atoms during the second pulse, with each quasimomenta window color coded to match the detunings in **a**. The selection windows overlap, with the width of each window only intended to illustrate their relative values. **d**, Excited state fraction as a function of duration of the second pulse for the five initial pulse detunings shown in **a** (data points), along with the no-free parameters dynamics predicted by a semi-classical model (colored solid lines). **(Inset,)** Corresponding extracted chiral Bloch vector angle for each quasimomenta window centered at q^* 45
- 3.10 Band preparation. (a) Spectroscopy of the carrier and inter-band transitions from the initial $|g\rangle_0$ state. In order to prepare atoms exclusively in the $n_z = 1$ band, a clock laser pulse is applied to the $|g\rangle_0 \rightarrow |e\rangle_1$ blue sideband transition, which is at a detuning $\delta/2\pi \approx \nu_z - E_r/2\pi\hbar = 35$ kHz for $U_z/E_r = 30.5$. A strong “clearing” pulse is then applied to remove any remaining atoms in $|g\rangle$, leaving atoms in $|e\rangle$ unperturbed. The remaining atoms are thus purified in the $n_z = 1$ Bloch band, and can be used for further experiments or measurements. (b) Spectroscopy of the sidebands following this protocol, with the anharmonicity of the band spacing resulting in an unequal frequency spacing between the $|e\rangle_1 \rightarrow |g\rangle_2$ and $|e\rangle_1 \rightarrow |g\rangle_0$ sideband transitions about the $|e\rangle_1 \rightarrow |g\rangle_1$ carrier transition. 47

- 4.1 Dynamics of spin observables in a linear magnetic field with $x_0 = a_H$. (a) $\langle \hat{S}^Z(x, t) \rangle = \frac{1}{2} (|\psi_\uparrow(x, t)|^2 - |\psi_\downarrow(x, t)|^2)$ shows the spin up/down densities oscillating in their traps centered at $x = \mp x_0$. (b) Magnitude of $\langle \hat{S}^+(x, t) \rangle$, which measures the magnetization at point x . The magnetization decays when the spin up/down densities are separated. 60
- 4.2 Phase space plots of $\langle x \rangle$ and $\langle p \rangle$ for the $|\uparrow\rangle$ state (blue, solid) and $|\downarrow\rangle$ state (red, dashed) for a spin-echo sequence in a linear magnetic field. Here $p_0 = 1/a_0$, and the total time is $2\pi/\omega$. The two spin states evolve along circular trajectories centered at $\mp x_0$. (a) At half the total dark time, π/ω , the spin-echo π pulse swaps the spin states. The spin wavefunctions are thus displaced by $2x_0$ from the centers of their respective harmonic traps. For the second half of the dark time they evolve in circular trajectories twice as large, centered at $\mp 2x_0$, resulting in a final configuration shown in (b). The spin-echo pulse leads to greater dephasing of the spin observables due to larger final phase-space displacement. 64
- 4.3 Contrast decay for the case of a linear magnetic field at times comparable to the trap period, for zero temperature and high temperature ($T \gg T_F$), with and without spin-echo (SE). The quantum degenerate case uses $N = 19$ and all cases use $x_0 = 0.24a_H$, consistent with Ref. [10]. $T = 10T_F$ in the high temperature case. Higher temperature leads to faster contrast decay since the particles have a larger average energy. The spin-echo removes the second-order contribution to the contrast decay, resulting in slower decay at short times. However, at long times the contrast decay is larger when a spin-echo pulse is applied. The period of the dynamics is also $4\pi/\omega$ with a spin-echo pulse instead of $2\pi/\omega$ 66
- 4.4 Linear magnetic field: (a) demagnetization time vs. magnetic field gradient. (b) Demagnetization time vs. temperature where the Fermi temperature $T_F = N\omega$. Using parameters from Ref. [10], these timescales are faster than those obtained in the experiment, suggesting that strong interactions suppress the role of single particle dynamics. 67

- 4.5 Dynamics of spin observables in a quadratic magnetic field with $B = 0.65\omega^2$. (a) $\langle \hat{S}^Z(x, t) \rangle$ shows the spin up/down densities breathing in their traps centered at $x = 0$. The rates of their breathing, $\omega^\pm = \sqrt{\omega^2 \pm B}$, are incommensurate. The standard deviations of the densities are $a^\pm = 1/\sqrt{\omega^\pm}$, hence spin up (down) becomes more concentrated at the center (edge) of the trap. (b) Magnitude of $\langle \hat{S}^+(x, t) \rangle$ (contrast), which measures the magnetization at position x . The magnetization decays when the spin up/down densities are separated. Note that decays/revivals of the magnetization are aperiodic. 69
- 4.6 Quadratic magnetic field: (a) demagnetization time with and without spin-echo vs. temperature, where the Fermi temperature $T_F = N\omega$, and (b) contrast decay vs. time, using parameters from Ref. [14]. The timescales are on the order of or faster than the timescale of spin segregation in the experiment ($\sim 100\text{ms}$). Additionally, application of a spin-echo pulse leads to faster demagnetization. 73
- 4.7 Comparison of the data with the formula for single particle spin dynamics (Eq. 4.37). The single particle formulas work better at short times before other effects, likely from interactions and magnetic field curvature, become important. 76
- 5.1 (a) Atoms spin-polarized along X occupy single-particle eigenstates, labeled by mode number n . The potential is quenched to a spin-dependent form, and dynamics result from a spin model with long ranged interactions (green wavy lines) in energy space. (b) The state $|\psi\rangle$ is a coherent superposition of spins in many mode configurations (unoccupied modes are represented by open circles). In each configuration particles are localized in mode space, with spin model Hamiltonian \hat{H}_i^{sm} . Coherences between the configurations capture motional effects. 81

- 5.2 Magnetization dynamics for a constant gradient. Collective $\langle \hat{\mathcal{S}}^X \rangle$ for a $x_0 = 0.1a_H$ (a) (and $x_0 = 0.3a_H$ (e)) displays global interaction-induced demagnetization, which damps single-particle oscillations. Collective (generic) Ising solutions, black lines, give the demagnetization envelopes. Local magnetizations $\langle \hat{\mathcal{S}}^{X,Y,Z}(x) \rangle$ with $x_0 = 0.1a_H$ (b-d) (and $x_0 = 0.3a_H$ f-h) reflect similar behavior, both shown with $u_{\uparrow\downarrow} = 0.35\omega$. 84
- 5.3 Dynamics for a linear gradient. (a) Spin self-rephasing for $\omega_B = 0.1\omega$: as interactions increase, demagnetization is suppressed and $\langle \hat{\mathcal{S}} \rangle$ precesses collectively in the XY plane (inset). (b) Dynamics in a strong linear gradient show damping of large single particle oscillations, where the damping envelopes are given by the generic Ising solutions. (c, d) Dynamics of the spin population difference $\langle \hat{S}^Z(x) \rangle$ in real space, showing oscillations where spin up is concentrated towards the center of the cloud and spin down is concentrated towards the edge of the cloud. The rate of these oscillations is proportional to the interaction strength. The results in (c, d) are what is known as “spin segregation” and will be discussed in greater detail in Section 5.7. 85
- 5.4 (Color online) (a) Real part of the connected correlation function $\text{Re}[G^{++}(x, 0; t)]$ for a weak gradient ($x_0 = 0.1a_H, u_{\uparrow\downarrow} = 0.35\omega$). Correlations grow collectively due to the long-ranged nature of the interactions in energy space, and peak when the gas is demagnetized. (b) For a linear gradient in the self-rephasing regime ($\omega_B = 0.1\omega, u_{\uparrow\downarrow} = 0.45\omega$), the connected correlator $\text{Re}[G^{++}(x, 0; t)]$ rotates collectively in the XY plane. For weak interactions or strong gradients (c, d), interactions collectively damp the correlations arising from quantum statistics (upper panels are non-interacting). 88

- 5.5 Spin model approximation vs. full Hamiltonian for 5 particles with $x_0 = 0.1a$ and $u_{\uparrow\downarrow} = 0.35\omega$. (a) $\langle \hat{\mathcal{S}}^X \rangle$ quench dynamics for initial modes $\{0,1,2,3,4\}$, representing a zero temperature gas, along with (b) the connected correlator $G^{++}(x=0, x' = 0.5a_H)$. Single-particle oscillations are damped by interactions, and the long time dynamics is well-reproduced by the spin model approximation with decay envelope given by the collective Ising solutions. (c) Dynamics for initial modes $\{0,3,4,5,6\}$ representing a more dilute gas. (d) Dynamics of a pure XXZ spin Hamiltonian with the same parameters, for each of the lowest “one-hole” mode configurations. The dynamics of each configuration is very similar, explaining why the dynamics of a quench – involving many configurations – can be approximated by a single configuration. The interaction parameters vary slowly with parameter index, as shown in (e,f) for $x_0 = 0.1a_H$ and (g,h) for $x_0 = 0.3a_H$ 91
- 5.6 (a) Magnitude of of the total field $B_n \hat{\sigma}_n^Z$, which contains both single particle ($B^{sp} \hat{\sigma}_n^Z$) and interaction ($B_n^{u\uparrow\downarrow} \hat{\sigma}_n^Z$) terms, for a linear gradient with $\Delta\omega = 0.08\omega$. Even for strong interactions ($u_{\uparrow\downarrow} = 0.5\omega$), the Hamiltonian is not significantly modified by the interaction-induced terms $B_n^{u\uparrow\downarrow}$ which appear when $J_{nm}^Z \neq J_{mn}^Z$. (b) For $u_{\uparrow\downarrow} = 0.5\omega$ the $B_n^{u\uparrow\downarrow}$ terms do not grow with particle number. 92
- 5.7 Spin segregation dynamics at zero temperature with parameters taken from [Du 2008]. (a) DMRG simulation of the time evolution of the spin densities $n_\alpha(x)$, $\alpha = \uparrow\downarrow$, at the center of the trap ($x = 0$) normalized by $n_0 = (n_\uparrow(0) + n_\downarrow(0))/2$. (b) Simulated time evolution of $(n_\uparrow(0) - n_\downarrow(0))/n_0$ compared with the analytic formula in Eq. 5.20. The formula accurately predicts the timescale of the oscillation over many periods, and accurately captures the amplitude for about one oscillation period, whose timescale is set by the gap G . The damping seen in the numerics comes from leakage of population outside of the Dicke/spin-wave manifolds. (b) Difference in cloud profiles $(n_\uparrow(x) - n_\downarrow(x))/n_0$ at $t = 50/\omega$ and $t = 100/\omega$: Eq. 5.20 predicts the cloud shape to within about 10%. 96

5.8	Comparison of the cloud profiles $(n_{\uparrow}(x) - n_{\downarrow}(x))/n_0$ at $t = 50/\omega$ between the DMRG simulation, Eq. 5.20 which sums over every oscillator mode, and the approximate analytic expression in Eq. 5.27 which is valid for $N \gg 1$. The three cloud shapes have almost perfect agreement at this time.	98
5.9	(a) Analytic results for the spin segregated cloud shape at both zero temperature and $T = 4T_F$ taken at 200ms. The thermal cloud is shown at a late time, past its time of validity, but nevertheless qualitatively reproduces many of the features seen in the cloud image from [14] shown in (b).	100
5.10	(a) Spin wave energies vs. particle number for a 3D system with parameters taken from [14], based on Monte Carlo sampling of harmonic oscillator mode configurations. Extrapolated to $N = 2 \times 10^5$ particles, at $T = 4T_F$ the average energy is $\approx 2.12 \times 2\pi$ Hz and the Dicke gap (minimum energy) is $\approx 0.34 \times 2\pi$ Hz, both much smaller than the single particle inhomogeneity of $4.85 \times 2\pi$ Hz. For $N = 2 \times 10^5$ particles at $T = 0$ the Dicke gap is $\approx 39.53 \times 2\pi$ Hz. (b) Spin wave energies vs. particle number for a 1D system at $T = 0$ with parameters taken from [14]. At $N = 560$ the Dicke gap is $3.92 \times 2\pi$ Hz, much larger than the inhomogeneity of $0.70 \times 2\pi$ Hz.	101
5.11	Dynamics of the cloud center taken from [14]. The dynamics can be reproduced using a high temperature average.	102
5.12	Scaling. (a) Dynamics vs. N for a constant gradient $x_0 = 0.1a_H$, from which τ_M is extracted and found to scale like $\tau_M \sim N^{-.823}$, close to the N^{-1} prediction. (b) Dynamics and scaling of τ_M vs. x_0 which agrees well with the prediction x_0^{-2} , for $N = 10$. (c) $\langle \hat{S}^X \rangle / N$ vs. N , when $\omega_B = 0.1\omega$, from which ω_{rot} is extracted and agrees well with the prediction $\omega_{rot} = N\Delta\omega$. (d) $\langle \hat{S}^X \rangle$ vs. ω_B for $N = 10$. Predictions fail when $\omega_B \sim u_{\uparrow\downarrow}$. (All cases are $u_{\uparrow\downarrow} = 0.35\omega$.) (e) μ_{2z} , vs. $u_{\uparrow\downarrow}$; oscillations become more pronounced for stronger interactions. ω_{seg} scales linearly with $u_{\uparrow\downarrow}$. $\langle \mu_{2z} \rangle \sim u_{\uparrow\downarrow}^{-.887}$, close to the prediction of $u_{\uparrow\downarrow}^{-1}$	105

- 5.13 Testing the spin model approximation with simulations of four particles for an initial state with a domain wall. Plotted are the center of mass position of the spin- \uparrow cloud as a function of time for two different domain wall sizes ($x_0 = \{1.0a_H, 0.5a_H\}$) and three different interaction strengths ($u_{\uparrow,\downarrow} = \{0.1\omega, 0.2\omega, 0.4\omega\}$). We see that the spin model captures the timescales of the decay and growth of those oscillations, but does not accurately capture the amplitude after the initial collapse. 108
- 5.14 Testing the spin model approximation with simulations of four particles for a coherent displaced initial state. Plotted are the center of mass position of the spin- \uparrow cloud as a function of time for two different initial displacements ($x_0 = \{0.1a_H, 0.5a_H\}$) and three different interaction strengths ($u_{\uparrow,\downarrow} = \{0.1\omega, 0.2\omega, 0.4\omega\}$). We see that the spin model captures the timescales of the growth and decay of those oscillations, but does not accurately capture the amplitude of those oscillations. 110
- 6.1 (a) Ramsey spectroscopy of two interacting spin-1/2 particles. (b) In a harmonic trap the spectrum degeneracy allows near-resonant mode-changing collisions coupled to the spin dynamics. 113
- 6.2 Ramsey dynamics [see Eq. (6.4)] with $\delta = 0$: (a) 1D spin model, exact solution, and projection of population onto initial mode (here $n_1 = 10$ and $n_2 = 0$), with $u_{\uparrow\downarrow}^{1,0} \approx 0.2\omega_z$. Dephasing of the exact dynamics results from mode changes. (b) Thermal averages in 2D: spin model vs. effective spin model, at different temperatures, with $u_{\uparrow\downarrow}^{1,0} \approx 0.04\omega_{\perp}$. For both figures: $\theta_1 = \theta_2 = \pi/3$, with thermally-averaged inhomogeneity $\langle\Delta\Omega\rangle/\langle\Omega\rangle = 0.3$. $\theta_i = \Omega t_i$ are bare pulse areas. 118

- 6.3 Thermally averaged frequency shifts: (a) 1D spin model and exact solution vs. population excitation fraction (number of atoms in \uparrow divided by the total number of atoms) after the first pulse, at intermediate and long times. Here $u_{\uparrow\downarrow} \equiv u_{\uparrow\downarrow}^{1,0} \approx 0.2\omega_z$. (b) Frequency shifts for 2D spin model vs. effective spin model, with $u_{\uparrow\downarrow} \equiv u_{\uparrow\downarrow}^{1,0} \approx 0.04\omega_{\perp}$. For both figures: $T = 208\hbar\omega_{\perp}/k_B$, $\theta = \theta_1 = \theta_2$, $\omega_z = \omega_{\perp} = 700 \times 2\pi\text{Hz}$, and thermally-averaged inhomogeneity $\langle\Delta\Omega\rangle/\langle\Omega\rangle = 0.3$. $\theta_i = \Omega t_i$ are bare pulse areas. . 119
- 6.4 (a) Ramsey dynamics [see Eq. (6.4)] with $\delta = 0$ predicted by the 1D spin model (solid) and the exact solution (dashed) for an initial $(n_1 = 6, n_2 = 3)$ mode configuration. Strong interactions ($u_{\uparrow\downarrow}^{1,0} = 100\omega_z$) are assumed during the dark time. In the limit of strong interactions the two particles develop a node in their relative coordinate and the period of the Ramsey dynamics becomes the trap period since it is the only energy scale left in the problem. (b) Numerical results for the $(n_1 = 0, n_2 = 1)$ mode configuration with initial conditions and parameters described in Section 6.3 and $u = 10\omega$, confirming the result that Ramsey dynamics takes place at the trap period for strong interactions. (c) Numerical results for the $(n_1 = 2, n_2 = 1, n_3 = 0)$ mode configuration with initial conditions and parameters described in Section 6.3 and $u = 10\omega$, again showing oscillations at the trap frequency rather than the interaction frequency. 123
- 6.5 Dynamics of a Ramsey sequence in a one dimensional harmonic trap with inhomogeneous Rabi frequencies. For two particles in a Fermi-degenerate initial condition (a, b), the predictions of the spin model closely match those of the full Hamiltonian up to a phase shift that depends on the interaction strength u . For two particles in this initial configuration, no resonant mode changes are possible, so this phase shift results from either changes in the wavefunctions or from non-resonant mode changes. For three particles in a Fermi degenerate initial condition (c, d), the spin model does not work as well at long times since after two of the spins are flipped, Pauli blocking no longer prevents resonant mode changes. 127

6.6	Effect of a spin echo and many body spin echo sequence. (a) Ramsey dynamics with inhomogeneous Rabi frequencies, comparing the spin model and Full Hamiltonian. (b) A spin echo sequence does not change the Ramsey dynamics under the spin model approximation but does modify the dynamics under the full Hamiltonian, due to the coupling of spin and motion via mode changes. (c) Similarly, the many body spin echo completely removes the dynamics under the spin model approximation but does not remove all the effects of the full Hamiltonian. Parts (d - f) show similar results for three particles.	128
6.7	Demagnetization following a spin-dependent displacement. The exact (red solid) and spin-model (blue dashed) dynamics of the collective spin for an initially polarized state subject to a spin-dependent displacement of harmonic traps by $x_0 = 0.1a_H$ (top panel) or $x_0 = 0.3a_H$ (bottom panel). The overall demagnetization and revival timescales are well-captured by the spin model approach, while smaller-scale features due to interaction-modified motion in trap are not captured. Note that non-interacting motion in the trap is exactly captured within the spin model framework.	133
6.8	Infidelity of spin model in a harmonic trap with and without corrections. Allowing all resonant mode changes $(0, \infty)$ enhances the fidelity approximately 100-fold. Non-resonant terms, $(1, \infty)$, for instance, enhance the fidelity but by a smaller margin. Thus resonant terms are the most important corrections to the spin model.	134
6.9	Convergence of spin model $(0, d)$ with range d . Most of the convergence of the fidelity of the state is accomplished by the inclusion of the first non-resonant term $(0, 1)$	134
6.10	Infidelity of spin model in a gaussian trap (dark), compared to a harmonic trap (light), with and without corrections to the spin model, for $U = 0.1\hbar\omega$. The anharmonicity of the gaussian trap enhances suppresses mode changes and enhances the fidelity of the state.	135

8.1	Scaling of the Dicke gap G with magnetic field gradient and particle number. (Left panel) Scaling of the Dicke gap with particle number for constant gradients of strength $x_0 = 0.05$ and 0.1 and linear gradients of strength $\omega_B = 0.1$ and 0.4 (all quantities are measured in oscillator units). All gaps increase with N to a certain gradient-dependent critical value and then decrease, with larger gaps for smaller gradients. (Right panels) Scaling of the Dicke gap at fixed particle number $N = 10$ and 20 with the constant (center panel) or linear (right panel) gradient strength. The gap closes for weaker gradient as the particle number increases, demonstrating that larger particle numbers require smaller gradients to be in the near-Heisenberg regime. For even smaller gradients, the gap increases with particle number, more effectively enforcing collective behavior.	140
-----	---	-----

Chapter 1

Introduction

A spin-1/2 particle, also known as a qubit or a two-state system, is the simplest nontrivial quantum mechanical object. It is also the *most* quantum mechanical object, since measurement of a spin component leads to complete uncertainty in the values of the other spin components. Interacting spin systems are thus of fundamental importance to the study of quantum many body physics. Typically, the spins are fixed to a lattice and interact either with their nearest neighbor spins or via long ranged interactions. Rich physics, both in and out equilibrium, can result from studying interacting spins on a lattice.

Cold atom experiments have emerged as one of the most fruitful platforms with which to study quantum many body physics, due to the low temperatures achieved, and the exquisite control available over various experimental parameters. However, it is often difficult to engineer pure lattice spin models where the spins do not move, and more convenient or more interesting to prepare cold atoms in a trapped gas or an optical lattice where the atoms can tunnel between lattice sites. The question then becomes, what happens when the interacting spins are allowed to move? What new physics can emerge and how do we study it? These questions are the focus of this thesis.

Most of the topics discussed in this thesis involve gases of fermions with a spin-1/2 degree of freedom. Due to the Pauli exclusion principle, spin polarized fermions do not experience s-wave interactions at low temperatures. Interactions arise when the spins are rotated inhomogeneously. Each of the problems we studied represents a different type of inhomogeneity that can arise in a gas of spin-1/2 particles, inducing interactions and different types of interesting physics. For instance, in

an optical lattice clock, the clock laser can rotate spins on different lattice sites by differing amounts. Within a single well of the optical lattice, the laser can rotate spins in an energy-dependent way, leading to s-wave interactions which degrade the clock signal. We investigated this problem [1], and a similar problem in a flat bottom potential [2].

Our methods involve the so-called spin model approximation, which assumes motional modes are frozen during the dynamics, and has been used to predict density shifts in the clocks [3–5]. For each of the problems outlined below, we are either using the spin model approximation [2, 6, 7], investigating its range of validity [1], or both [8]. Through these studies we have come to a much deeper understanding of why the spin model approximation works so well, and when and how it breaks down.

1.1 Many Body Physics in Optical Lattice Clocks

In an optical lattice, atoms are trapped in the periodic potential created by a standing wave of light. This potential mimics the physics of electrons in the periodic potential of their parent ions in a metal. An optical lattice clock, such as the JILA Sr clock, takes advantage of a deep lattice potential to freeze the motion of the atoms along the direction of the probing laser which interrogates their long lived electronic transition. In fact, the sensitivity is so great that even weak interactions between the atoms at the Hz level can degrade the clock signal. A better understanding of the theory of atomic collisions can thus help experimenters engineer more precise clocks. An alternative perspective is that the clock can be used to study fundamental quantum many body effects in a controlled setting, and spectroscopically resolve them even when interactions are at the \sim Hz level. Thus theory and experiment of optical lattice clocks are evolving hand in hand.

1.1.1 The spin model approximation and beyond

The main approximation used to model interactions in the clock is to assume the occupied single particle harmonic oscillator modes are frozen during interaction events. Interactions either leave the spins and modes unchanged (the direct interaction) or exchange spin states between

modes (the exchange interaction). This model correctly predicted the density shifts seen in the clocks [3–5].

The justification for this so-called spin model approximation is two-fold. First of all, when interactions are weak, they cannot overcome the energy barrier required to change the modes of the atoms after a collision event, with energy splitting determined by the harmonic ($\hbar\omega$). Secondly, the trapping potential is not exactly harmonic, and the anharmonicity and non-separability of the true gaussian trapping potential can suppress what would otherwise be resonant exchange processes that might contribute to the dynamics even for weak interactions. However, there are regimes when these resonant processes might be important, which motivated us to try to understand these processes. In Ref. [1] we tested the validity of the spin model approximation by comparing its predictions to exact analytic expressions for two fermions. We found that at long times compared to the trapping period the spin model approximation breaks down. Many other frequencies appear in the dynamics associated with resonant mode changes that can occur in a harmonic potential. Interestingly, the spin model is much better at predicting the behavior of spin observables than it is at reproducing the correct state of the system. This is because even when processes occur that are beyond the scope of the spin model, the system typically ends up in a configuration with very similar dynamics. This is a common theme that we found throughout our studies and is one of the reasons why the spin model approximation works so well.

1.1.2 Synthetic spin orbit coupling in an optical lattice clock

The phase of the clock laser naturally varies over the length of the optical lattice. In a deep lattice, this phase is unimportant for the measurement of any observables since atoms in different lattice sites never see each other. If the atoms are allowed to tunnel between lattice sites, however, this phase difference becomes important – it is effectively a spin inhomogeneity that varies in space. We analyzed this system in a proposal for generating synthetic spin orbit coupling in the clock [6]. We showed that at the single particle level this spin orbit coupling could be implemented and measured in current optical lattice clocks even at their operating micro-Kelvin temperatures. The

predicted behavior was observed in a recent experiment[7]. We also made predictions for how the spin orbit coupling will lead to and be modified by interactions. We are currently working with the JILA Sr team to verify these predictions.

1.2 Spin dynamics in a magnetic field gradient

The application of a magnetic field gradient is a simple experimental protocol that induces dynamics in a gas of spin-1/2 atoms. The gradient rotates spins at different rates depending on their position in the cloud, and the resulting spin inhomogeneities induce interactions. A number of recent cold atom experiments have utilized this idea to study spin transport and other dynamical phenomena [9–15].

First, we studied the problem of non-interacting spin dynamics in these systems [16] in detail. We found the interesting result that a spin-echo sequence cannot remove the effect of the magnetic field gradient. Next, to model interactions we applied the same spin model formalism previously used to model atomic clocks. The model worked very well and allowed us to keep the problem “fully quantum,” rather than resorting to mean field or semi-classical methods. We achieved the best to date agreement with the spin segregation experiment of Ref. [15]. We predicted long-time demagnetization that was not captured by the time dependent Hartree-Fock approximation [17], but was seen in experiment [9]. We are currently collaborating with the Ultracold Atoms Group at the University of Toronto, with the goal of observing the predicted demagnetization in the weakly interacting regime.

1.3 Nonequilibrium dynamics in other quantum gases

Two projects, which led to references [18] and [19], also involved the study of nonequilibrium dynamics in quantum gases but were thematically different enough that they have been omitted from the body of this thesis. We briefly describe these projects here.

1.3.1 $SU(N)$ quantum magnets in a flat-bottomed potential

Unlike a harmonic oscillator with equally spaced energy levels, a flat-bottomed potential (also known as a square well) is anharmonic and there are no degeneracies associated with mode exchanges between two interacting particles. Thus, the use of the spin model approximation to model such a system is appropriate. Additionally, all interaction parameters are equal, leading to a fully collective model for interactions. We showed that n thermal fermionic alkaline-earth atoms in a flat-bottom trap allow one to robustly implement a spin model displaying two symmetries: the S_n symmetry that permutes atoms occupying different vibrational levels of the trap and the $SU(N)$ symmetry associated with N nuclear spin states. The symmetries make the model exactly solvable, which, in turn, enables the analytic study of dynamical processes such as spin diffusion in this $SU(N)$ system. We also showed how to use this system to generate entangled states that allow for Heisenberg-limited metrology. This highly symmetric spin model should be experimentally realizable even when the vibrational levels are occupied according to a high-temperature thermal or an arbitrary non-thermal distribution. [19].

1.3.2 Quench dynamics of a strongly interacting Bose gas

Motivated by a recent experiment [20], we studied the dynamics of a Bose gas following a sudden change (quench) of the interaction strength from weakly interacting to strongly interacting [18]. We studied the problem at the two-body, three-body, and many-body level. We made quantitative predictions for the behavior of the momentum distribution and Tan's contact out of equilibrium that have motivated a great deal of subsequent research [21–25].

1.4 Outline of this thesis

In Chapter 2 we provide background information on several topics that are central to this thesis: many body physics in cold atom systems, two level atoms and their interaction with light, Rabi and Ramsey spectroscopy, ultracold Fermi gases, and optical lattices.

In Chapter 3 we propose the use of optical lattice clocks operated with fermionic alkaline-earth-atoms to study spin-orbit coupling (SOC) in interacting many-body systems. The SOC emerges naturally during the clock interrogation when atoms are allowed to tunnel and accumulate a phase set by the ratio of the “magic” lattice wavelength to the clock transition wavelength. We demonstrate how standard protocols such as Rabi and Ramsey spectroscopy, that take advantage of the sub-Hertz resolution of state-of-the-art clock lasers, can perform momentum-resolved band tomography and determine SOC-induced s -wave collisions in nuclear spin polarized fermions. With the use of a second counter-propagating clock beam, we propose a method to engineer controlled atomic transport and study how it is modified by p - and s -wave interactions. The proposed spectroscopic probes provide clean and well-resolved signatures at current clock operating temperatures. We then describe the results of a recent experiment at JILA using fermionic ^{87}Sr to produce SOC. APK contributed to the theory model used to describe the experiment, but the experiment was conducted by the Sr team in the June Ye group.

In Chapter 4, motivated by several experimental efforts to understand spin diffusion and transport in ultracold fermionic gases, we study the spin dynamics of initially spin-polarized ensembles of harmonically trapped non-interacting spin-1/2 fermionic atoms, subjected to a magnetic field gradient. We obtain simple analytic expressions for spin observables in the presence of both constant and linear magnetic field gradients, with and without a spin-echo pulse, and at zero and finite temperatures. The analysis shows the relevance of spin-motional coupling in the non-interacting regime where the demagnetization decay rate at short times can be faster than the experimentally measured rates in the strongly interacting regime under similar trapping conditions. Our calculations also show that particle motion limits the ability of a spin-echo pulse to remove the effect of magnetic field inhomogeneity, and that a spin-echo pulse can instead lead to an increased decay of magnetization at times comparable to the trapping period.

In Chapter 5 we develop a framework for studying the dynamics of weakly interacting fermionic gases following a spin-dependent change of the trapping potential which illuminates the interplay between spin, motion, Fermi statistics, and interactions. The key idea is the projection

of the state of the system onto a set of lattice spin models defined on the single-particle mode space. Collective phenomena, including the global spreading of quantum correlations in real space, arise as a consequence of the long-ranged character of the spin model couplings. This approach achieves good agreement with prior measurements and suggests a number of directions for future experiments.

In Chapter 6 we examine the validity of the spin model approximation which is used extensively throughout this thesis. We calculate the Ramsey dynamics exactly for two interacting spin-1/2 particles in a harmonic trap. We focus on *s*-wave-interacting fermions in quasi-one and two-dimensional geometries. We find that in 1D the spin model assumption works well over a wide range of experimentally-relevant conditions, but can fail at time scales longer than those set by the mean interaction energy. Surprisingly, in 2D a modified version of the spin model is exact to first order in the interaction strength. This analysis is important for a correct interpretation of Ramsey spectroscopy and has broad applications ranging from precision measurements to quantum information and to fundamental probes of many-body systems. We also examine the validity of the spin model approximation for the case of more than two particles, and for the problem of spin-dependent trapping potentials (Chapter 5).

1.5 Summary

In this thesis we study a variety of problems in cold atomic gases in which spin and motional dynamics are coupled. These systems display rich physics and dynamics which are being investigated by various experimental groups around the world. There remain many open questions, such as how the spin model approximation can be improved, and how quantum correlations spread in a gas. These investigations may be important for quantum technologies that utilize cold gases, as well as for improving our understanding of fundamental quantum many body physics.

Chapter 2

Background

2.1 Motivation: many body physics in cold atoms systems and quantum simulation

Quantum mechanics is arguably the most successful theory in the history of science. A famous example is the calculation of the anomalous magnetic moment of the electron, which has now been calculated to 13 decimal places of accuracy [26]. Another recent triumph of quantum mechanics, relevant for this thesis, is the engineering of atomic clocks with accuracy and stability at the 10^{-18} level, meaning they would not lose a second in the lifetime of the universe [27, 28].

As successful as quantum mechanics has been, its predictive power is severely limited in many body interacting systems. The Hilbert space for such systems grows exponentially with particle number making exact diagonalization impossible for systems with more than a few particles. So, the study of many body physics relies on approximations and on experimental results. Interacting electrons in solid state systems have a few disadvantages: they are extremely complicated, usually contain defects and disorder, and are not often tunable. Due to the electron mass and densities in typical systems, dynamics takes place on timescales that are usually too fast to measure. Ultracold atomic gases, on the other hand, with precisely controllable parameters, offer an outstanding opportunity to investigate the interesting behavior that can emerge in interacting quantum systems both in and out of equilibrium. The ability to load atoms into optical lattices has allowed for the simulation of systems that obey the same Hamiltonians that describe electrons moving in the periodic potential of a lattice [29]. The field of quantum simulation has emerged as one of the most

promising directions for the future of atomic physics. Experimenters have the ability to engineer “analog” quantum computers, that simulate a known but intractable Hamiltonian. For instance, a synthetic gauge field in an optical lattice clock – the subject of Chapter 3 in this thesis – is an example of a cold atom system whose Hamiltonian mimics that which describes charged particles in a strong magnetic field (although in this case the Hamiltonian is non interacting).

2.2 Two level atoms probed by light

The electronic structure of atoms is very complicated, but often a laser probe can essentially isolate two of those levels, allowing us to model the atoms as a simple two level system with a ground, $|g\rangle$, and an excited level, $|e\rangle$. While we should keep in mind that the idea of a two level atom is never exact¹, a great deal of atomic physics can be understood within this approximation. If the energy separation between the two states is $\hbar\omega_0$ we can write the Hamiltonian for this system simply as

$$\hat{H}_0 = \hbar\omega_0|e\rangle\langle e|. \quad (2.1)$$

From this point on we will set $\hbar = 1$ unless otherwise stated. Since a typical light field such as a laser contains many coherent photons, we can treat the light classically. Additionally, the electric field of the light will interact much more strongly with the atom than its magnetic field, so we need only consider the classical electric field. The classical electric field associated with a plane wave can be written as

$$\vec{E}(t) = \vec{E}_0 e^{-i\omega_L t} + \vec{E}_0^* e^{i\omega_L t}, \quad (2.2)$$

where ω_L is the angular frequency of the light. Under the dipole approximation, the light-matter interaction can be written as $\hat{H}_{LM} = -\vec{d} \cdot \vec{E}$ where \vec{d} is the dipole moment operator of the atom. The Rabi frequency, which is the coupling between $|e\rangle$ and $|g\rangle$ due to the laser light is defined as $\Omega = \langle g|\vec{d}|e\rangle \cdot \vec{E} \equiv \vec{d}_{eg} \cdot \vec{E}$. The Hamiltonian is thus

$$\hat{H} = \hat{H}_0 + H_{LM} = \omega_0|e\rangle\langle e| - \frac{1}{2} \left[(\Omega e^{-i\omega_L t} + \Omega^* e^{i\omega_L t}) |e\rangle\langle g| + \text{H.c.} \right], \quad (2.3)$$

¹ Famously, “There are no two level atoms.” - Bill Phillips [30].

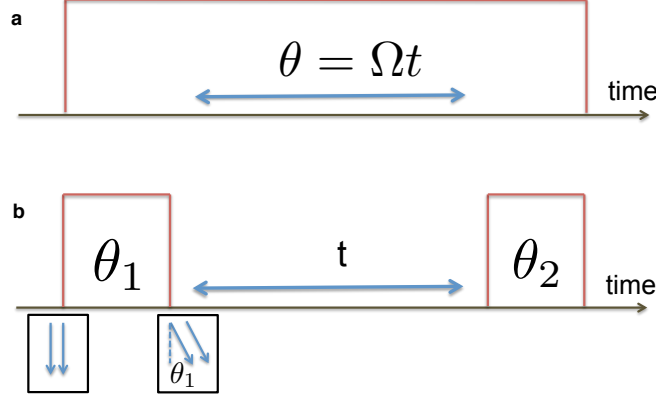


Figure 2.1: (a) A Rabi sequence illuminates a two level atom for time t corresponding to pulse area $\theta = \Omega t$. (b) In a Ramsey sequence, two short Rabi pulses are separated by a dark time t during which the laser is turned off.

where H.c. denotes the Hermitian conjugate. In the rotating frame of the laser, the $g - e$ coupling contains two terms, one $\propto e^{i(\omega_L + \omega_0)}$ and the other $\propto e^{i(\omega_L - \omega_0)}$. The first term is usually ignored, since $\omega_L + \omega_0$ is typically much larger than any other frequency scale in the problem. Retaining only the second term is called the Rotating Wave Approximation, which allows us to write the Hamiltonian for the two level atom in a much simpler form in the rotating frame of the laser:

$$\hat{H} = \frac{\delta}{2} (|e\rangle\langle e| - |g\rangle\langle g|) - \frac{\Omega}{2} (|e\rangle\langle g| - \Omega^* |g\rangle\langle e|), \quad (2.4)$$

where $\delta = \omega_L - \omega_0$ is known as the detuning of the laser from the atomic transition [30].

2.2.1 Rabi spectroscopy

A typical goal of spectroscopy is to determine the frequency of the atomic transition ω_0 . Comparing this frequency to the laser frequency is equivalent to locating the laser frequency such that $\delta = 0$.

In Rabi spectroscopy, illustrated in Fig. 2.1(a), atoms are prepared in a well defined spin state and illuminated with coherent light, usually from a laser, after which the spin state is measured. If the atoms start in the $|g\rangle$ state and are illuminated for a time t , the expectation value for the

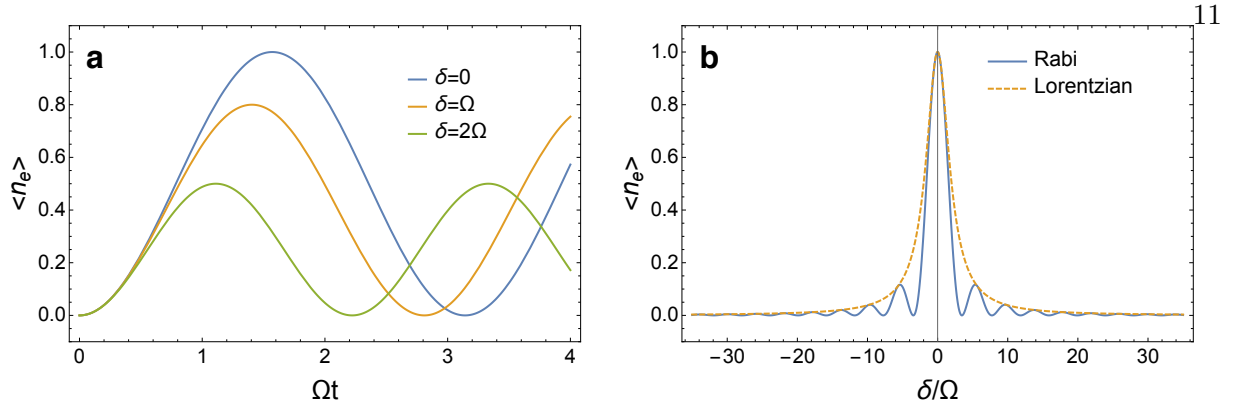


Figure 2.2: (a) Dynamics of $\langle n_e \rangle$ for a Rabi sequence for three different detunings. (b) Rabi lineshape evaluated at $t = \pi/2\Omega$ and Lorentzian envelope.

number of e atoms, n_e , is

$$\langle n_e \rangle = \frac{\Omega^2}{\Omega^2 + \delta^2/4} \sin^2 \left(t \sqrt{\Omega^2 + \delta^2/4} \right). \quad (2.5)$$

The quantity $\sqrt{\Omega^2 + \delta^2/4}$ is often called the effective Rabi frequency. In frequency space, this lineshape is peaked at $\delta = 0$ with a Lorentzian envelope (See Fig. 2.2). Longer probing times and smaller Rabi frequencies allow for enhanced resolution of the peak and thus more precise spectroscopy.

2.2.2 Ramsey Spectroscopy

Rabi spectroscopy has the benefit of being a very simple procedure, but for many reasons Ramsey spectroscopy, illustrated in Fig. 2.1(b), is often the preferred spectroscopic procedure. In Ramsey spectroscopy, two short Rabi pulses with pulse areas θ_1 and θ_2 are separated by a “dark time” t during which the laser is turned off. For a sample initially polarized in the $|g\rangle$ state the resulting dynamics are

$$\langle n_e - n_g \rangle / 2 = \sin \theta_1 \sin \theta_2 \cos \delta t - \cos \theta_1 \cos \theta_2. \quad (2.6)$$

Unlike Rabi spectroscopy, the laser is turned off during the dark time so amplitude fluctuations of the laser are not an issue during the dark time, and longer probe times can be utilized to obtain more precise measurements. Additionally, as long as the duration of each of the Rabi pulses θ_1

and θ_2 is much shorter than the typical time between atomic collisions, the spins can be rotated independently of interactions. And of course, the fact that the laser is off during the dark time means the behavior of the atoms during the dark time can be probed directly, independent of their interaction with the laser light. In optical lattice clocks, which are the subject of Chapter 3, Ramsey spectroscopy is used to look for an interaction-induced frequency shift which manifests as a modification to the bare atomic transition frequency.

2.3 Ultracold fermi gases

Here we will give a brief discussion of an ideal Fermi gas in a harmonic potential given by

$$V = \frac{1}{2}m\omega_x^2x^2 + \frac{1}{2}m\omega_y^2y^2 + \frac{1}{2}m\omega_z^2z^2, \quad (2.7)$$

where m is the atomic mass and ω_i is the trapping frequency in the i th direction. The ideal Fermi gas is a model system with a number of applications, such as electrons in a metal. Interactions and other complications will of course modify these results, but often the non-interacting ideal gas can reveal a surprising amount of information about a system. Here we will consider a two species fermi gas, where the spin degree of freedom $\sigma = \uparrow, \downarrow$ or g, e as in the previous section. Due to the Pauli exclusion principle, a spin polarized sample at zero temperature will fill all the harmonic oscillator modes up to the Fermi energy

$$E_F^{ho} = (6N_\sigma)^{1/3}\omega_{ho}, \quad (2.8)$$

where $\omega_{ho} \equiv (\omega_x\omega_y\omega_z)^{1/3}$. This is the harmonic trap analog of the well-known Fermi energy in a box potential. The difference, of course, has to do with the equally-spaced energy levels in a harmonic trap compared to the anharmonic energies in a box potential $\hbar^2k^2/2m$ at momentum k . The Fermi temperature is defined as $T_F = E_F^{ho}/k_B$, where k_B is Boltzmann's constant. At a finite temperature, the Fermi distribution function for each species is

$$f(r, p) = \frac{1}{\exp[\beta(p^2/2m + V(r) - \mu) + 1]}, \quad (2.9)$$

where $\beta = 1/k_B$ and μ is the chemical potential which obeys

$$N_\sigma = \left(\frac{1}{2\pi}\right)^3 \int dr dp f(r, p) = \int \frac{g(\epsilon) d\epsilon}{\exp[\beta(\epsilon - \mu) + 1]}, \quad (2.10)$$

and $g(\epsilon)$ is the density of states at energy ϵ , given by $g(\epsilon) = \epsilon^2/2\omega_{ho}^3$ [31].

In the limit of high particle number, at zero temperature the gas profile in real space becomes the so-called Thomas Fermi distribution

$$n_\sigma(r) = \frac{8N_\sigma}{\pi^2 R_x^0 R_y^0 R_z^0} \left[1 - \left(\frac{x}{R_x^0}\right)^2 - \left(\frac{y}{R_y^0}\right)^2 - \left(\frac{z}{R_z^0}\right)^2 \right], \quad (2.11)$$

where $R_i^0 = a_{ho}(48N_\sigma)^{1/6}\omega_{ho}/\omega_i$ is the Thomas Fermi radius, and $a_{ho} = \sqrt{1/m\omega_{ho}}$ is the harmonic oscillator length. Finite size effects manifest as small “ripples” on top of this ellipsoidal cloud.

For ultracold two-component fermions, the only allowed interactions are through the $\uparrow\downarrow$ channel. For the ground state of an interacting Fermi gas, pairing between \uparrow and \downarrow fermions is important. There is probably no more famous example than the BCS theory of superconductivity [31], which involves pairing between spins of opposite momentum. However, cold atom systems are often probed far from equilibrium, and, for the cases considered in this thesis, pairing is somewhat unimportant. Consider a typical procedure used in an experiment: the fermions are prepared in a harmonic trap with their spins initially polarized in the \downarrow state. A Rabi pulse rotates the spins with a pulse area of $\pi/2$ such that each spin is in a superposition of \uparrow and \downarrow , and then an inhomogeneity, such as a magnetic field gradient (the problem considered in Chapters 4 and 5), rotates the spins at different rates, inducing interactions. Because cold atom systems typically start in a spin polarized state, each fermion occupies a different harmonic oscillator mode. This state is quite “far” from the expected ground state, where each mode contains both an \uparrow and \downarrow . Thus, the theoretical tools needed to analyze the nonequilibrium dynamics of such systems are quite different from those needed to compute the ground state properties of interacting Fermi gases. The main theoretical tool that we use, known as the spin model approximation and described in more detail in Chapter 3, is such a tool that is useful for high temperature or far from equilibrium spin-1/2 systems where pairing is relatively unimportant.

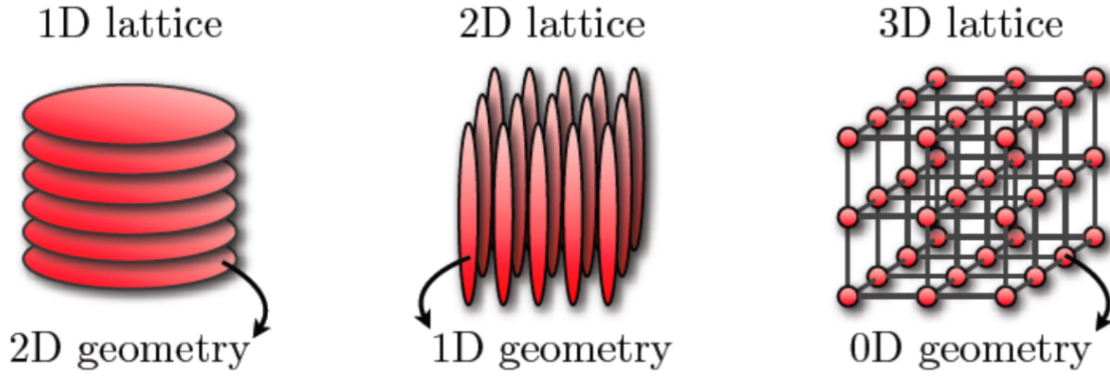


Figure 2.3: Geometry of optical lattices in one, two, and three dimensions. Image courtesy of Michael Foss-Feig.

2.4 Optical lattices

Counter propagating laser beams can be interfered to yield a sinusoidal light intensity pattern known as an optical lattice. Depending on the number of lasers used, the geometry can be controlled from a one dimensional optical lattice to a three dimensional optical lattice (See Fig. 2.3). Due to the interaction with the light field, atoms can become trapped in such a periodic potential, and in recent years optical lattices have become one of the most important tools for studying atomic many body physics. Although the energy scales are quite different, atoms hopping in an optical lattice are analogous to electrons moving in the periodic potential of the ionic crystalline background of a metal. Optical lattices can also be made “deep” enough to suppress tunneling between lattice sites. The control over the tunneling rate, which will be explored more in Chapter 3, is one of the advantages of studying atoms in optical lattices.

When the detuning of the laser light is much larger than the Rabi frequency, $|\delta| \gg \Omega$, the second order energy shift to the atomic transition is given by

$$\Delta E^{(2)} = \pm \frac{|\Omega|^2}{4\delta}, \quad (2.12)$$

where $+$ is for the $|g\rangle$ state and $-$ is for the $|e\rangle$ state. This is known as the AC-Stark shift [30]. The sign of the energy shift depends on the sign of the detuning. Since the Rabi frequency is

proportional to the electric field, it varies sinusoidally in space in an optical lattice: $\Omega = \Omega(\vec{r})$. For $\delta < 0$ (red detuned laser) the atoms will be attracted to stronger regions of the light field, and for $\delta > 0$ (blue detuned laser) the atoms will be repelled by stronger regions of the light field. For each detuning, the atoms experience a periodic potential due to the light-matter interaction which traps them in the optical lattice. For a red detuned laser, the potential minima correspond to the locations of maximum laser intensity, and for a blue detuned laser the potential minima are at the locations of minimum laser intensity.

Chapter 3

Synthetic Spin Orbit Coupling in an Optical Lattice Clock

3.1 Introduction

The recent implementation of synthetic gauge fields and spin-orbit coupling (SOC) in neutral atomic gases [32–34, 34] is a groundbreaking step towards using these fully-controllable systems to synthesize and probe novel topological states of matter. So far optical Raman transitions have been used to couple different internal (e.g. hyperfine) states while transferring net momentum to the atoms. However, in alkali atoms Raman-induced spin-flips inevitably suffer from heating mechanisms associated with spontaneous emission. While this issue has not yet been an impediment for the investigation of non-interacting processes or mean field effects [32, 33], it could limit the ability to observe interacting many-body phenomena that manifest at longer timescales. Finding alternative, more resilient methods for generating synthetic SOC, and probing its interplay with interactions, is thus highly desirable.

To reduce heating, the use of atoms with richer internal structure such as alkaline-earth-atoms (AEAs) [35, 36] or lanthanide atoms such as Dy and Er [37] have been suggested. In addition to long-lived electronic states AEAs also offer accessible electronic state-dependent trapping potentials with applications that range from the generation of synthetic gauge fields [35] and particle number fractionalization [38, 39] to quantum information processing [40, 41]. So far most of the existing proposals require complicated experimental set-ups including laser-assisted tunneling and rectification protocols or have been targeted to study the non-interacting regime [36]. Here, we demonstrate that SOC emerges naturally in cold AEA optical lattice clocks [42] that use a “magic”

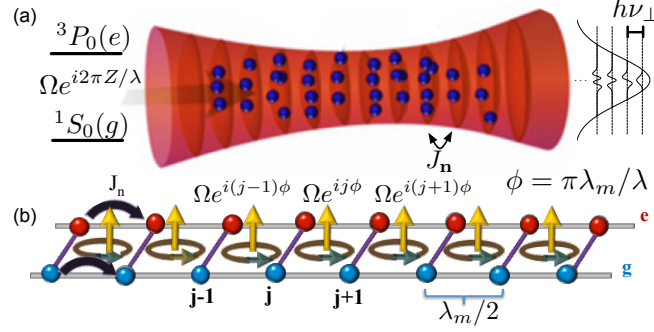


Figure 3.1: (a) A clock laser along the Z direction of wavelength λ and Rabi frequency Ω interrogates the $^1S_0(g)$ - $^3P_0(e)$ transition in fermionic alkaline-earth atoms trapped in an optical lattice with magic wavelength λ_m . The transverse confinement is provided by Gaussian curvature of the lattice beams with harmonic frequency $h\nu_{\perp}$. Many transverse modes \mathbf{n} are populated at current operating temperatures. (b) The phase difference ϕ between adjacent sites j and $(j + 1)$ induces SOC when atoms can tunnel with mode-dependent tunnel-coupling $J_{\mathbf{n}}$, realizing a synthetic two-leg ladder with flux ϕ per plaquette.

(state independent) lattice. This is because the clock laser imprints a phase that varies significantly from one lattice site to the next as it drives an ultra-narrow optical transition. Our implementation (1) uses a direct transition to a long-lived electronic clock state with natural lifetime $\gtrsim 10^2$ s [43], and thus heating from spontaneous emission is negligible; (2) takes advantage of the sub-Hz resolution of clock lasers [44–47]; and (3) accesses the regime where the interaction energy per particle, U , is weak compared to the characteristic trapping energies [48–53] but comparable to SOC scales determined by J , the tunneling, and Ω , the clock Rabi frequency. This regime allows us to investigate the interplay of interactions and SOC, to carry out controllable analytic calculations and make concrete predictions and to devise feasible interaction sensitive probing protocols accessible and testable in current experiments.

In the first protocol, we demonstrate that momentum-resolved tomography of chiral band structures can be performed using Rabi spectroscopy in the parameter regime $J \sim \Omega \gg U$. In the second protocol we show that the modification of collisional properties by SOC [33, 54] is manifest in standard Ramsey spectroscopy, focusing on the parameter regime $J \gtrsim U$. In the final protocol, controlled and spatially resolved atomic transport [55–62] is induced by an additional counter-propagating clock beam that exhibits a controllable phase difference with respect to the

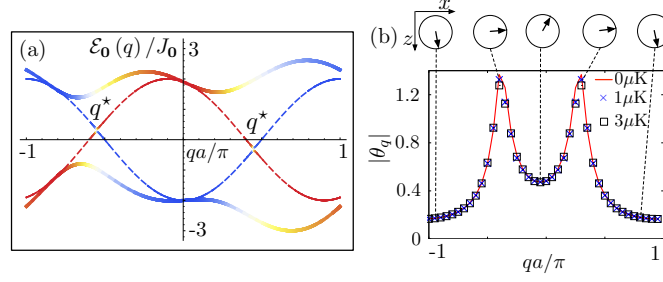


Figure 3.2: (a) SOC band structure for $\delta = -2J_0$, $\Omega_0 = J_0$ (solid lines) and $\Omega_0^p = 0.05J_0$ (dashed lines). The axial depth is $V = 12$ recoils, $J_0/h = 42$ Hz and $\nu_\perp \approx 900$ Hz. Colors correspond to state character, with g (e) being more blue (red). (b) Chiral Bloch vector angle, $\theta_{\mathbf{q}}$, in the xz plane extracted from Rabi spectroscopy using the protocol explained in the text. The figure shows three temperatures for the parameters of (a).

original probe beam. Interaction effects beyond mean field are shown to modify the dynamics in the parameter regime $\Omega \gg J \sim U$. Inelastic collisions in the excited state impose limitations in the probing time [52, 53, 63, 64], however, they can be dynamically accounted for during clock interrogation as demonstrated in Refs. [48, 52]. We also show that losses can be used as a resource for state preparation and readout.

3.2 Implementation

Current OLCs interrogate the $^1S_0(g)$ - $^3P_0(e)$ transition of ensembles of thousands of nuclear spin polarized fermionic AEAs trapped in a deep 1D optical lattice that splits the gas in arrays of 2D pancakes [42](see Fig.3.1). The lattice potential uses the magic-wavelength, λ_m to generate identical trapping conditions for the two states. At current operating temperatures, $T \sim \mu\text{K}$ [48] the population of higher axial bands is negligible ($\lesssim 5\%$). On the other hand, along the transverse directions, where the confinement is provided wholly by the Gaussian curvature of the optical lattice beams, modes are thermally populated with an average number of mode quanta $\langle n \rangle \sim 50$. To generate SOC coherent tunneling between lattice sites is required. Our proposal is to superimpose a running-wave beam on the lattice potential:

$$V_{\text{ext}}(\mathbf{R}) = -\exp\left(-\frac{2R^2}{w_0^2}\right) \left[V_{\text{const}} + V \cos^2\left(\frac{2\pi Z}{\lambda_m}\right) \right]; \quad (3.1)$$

this increases the transverse confinement without significantly affecting the axial motion [65]. Here, w_0 is the beam waist, R the transverse radial coordinate, Z the axial coordinate, V the axial lattice corrugation, and V_{const} the running-wave induced potential. By increasing V_{const} as V is lowered, the transverse confinement frequency $\nu_{\perp} \sim \sqrt{\frac{1}{m\pi^2 w_0^2}(V_{\text{const}} + V)}$, with m the atom mass, is kept constant while the tunneling rate along the axial direction increases.

Since $V_{\text{ext}}(\mathbf{R})$ is discretely translationally invariant along the axial direction, atoms trapped in the lowest axial lattice band are governed by the Hamiltonian $\hat{H}^0 = \sum_{\mathbf{n}} \hat{H}_{\mathbf{n}}^0$

$$\hat{H}_{\mathbf{n}}^0 = \sum_{q,\alpha} E_{\alpha,\mathbf{n},q} \hat{n}_{\alpha,\mathbf{n},q} - \sum_q \left[\frac{\Omega_{\mathbf{n}}}{2} \hat{a}_{+, \mathbf{n}, q+\phi}^{\dagger} \hat{a}_{-, \mathbf{n}, q} + \text{H.c.} \right]. \quad (3.2)$$

Throughout, $q = \tilde{q}a$ is the dimensionless product of axial quasimomentum \tilde{q} and lattice spacing $a = \lambda_m/2$, $\hat{a}_{\alpha,\mathbf{n},q}$ annihilates a fermion in the two-dimensional transverse mode \mathbf{n} , quasimomentum q , state $\alpha = \pm$ (for e and g), and $\hat{n}_{\alpha,\mathbf{n},q} = \hat{a}_{\alpha,\mathbf{n},q}^{\dagger} \hat{a}_{\alpha,\mathbf{n},q}$. The energy $E_{\alpha,\mathbf{n},q}(q) = \alpha \frac{\delta}{2} + \bar{E}_{\mathbf{n}} - 2J_{\mathbf{n}} \cos(q)$ has contributions from the mode dependent tunneling $J_{\mathbf{n}}$, the average energy of the transverse mode \mathbf{n} , $\bar{E}_{\mathbf{n}}$, and the laser detuning δ . $\Omega_{\mathbf{n}}$ is the Rabi frequency for mode \mathbf{n} . The clock laser with wavelength λ imprints a phase that varies between adjacent lattice sites by $\phi = \pi \lambda_m / \lambda$.

If one views the two internal states as a discrete synthetic dimension [66, 67], as shown in Fig. 3.1, $\hat{H}_{\mathbf{n}}^0$ describes the motion of a charged particle on a two-leg ladder in a magnetic field with flux ϕ per lattice plaquette. \hat{H}^0 hence has the interpretation of many copies of those ladders – one for each transverse mode. By performing a gauge transformation $\hat{a}_{+,q+\phi,\mathbf{n}} \rightarrow \hat{a}_{+,q,\mathbf{n}}$, $\hat{H}_{\mathbf{n}}^0$ becomes diagonal in momentum space with the excited state dispersion shifted by ϕ , $q \rightarrow q + \phi$. The latter can be then conveniently written in terms of spin-1/2 operators acting on the populated modes

$$\hat{H}^0 = - \sum_{\mathbf{n},q} \mathbf{B}_{\mathbf{n}q} \cdot \hat{\vec{S}}_{\mathbf{n}q} \quad (3.3)$$

where $\mathbf{B}_{\mathbf{n}q} = (\Omega_{\mathbf{n}}, 0, \Delta E_{\mathbf{n}}(q, \phi) + \delta)$, $\Delta E_{\mathbf{n}}(q, \phi) \equiv 2J_{\mathbf{n}} [\cos(q) - \cos(q + \phi)]$, and $\hat{S}_{\mathbf{n}q}^{x,y,z}$ are spin-1/2 angular momentum operators. The eigenstates are described by Bloch vectors pointing in the xz plane, with a direction specified by a single angle $\theta_{\mathbf{n}q} = \arctan\left(\frac{\Omega_{\mathbf{n}}}{\Delta E_{\mathbf{n}}(q, \phi) + \delta}\right)$ (Fig. 3.2(a)). The q dependence of this angle is a manifestation of chiral spin-momentum locking, which is directly

connected to the topological chiral edge modes of the two-dimensional Harper-Hofstadter model [67, 68].

3.3 Probing the Chiral Band Structure

We first discuss the use of Rabi spectroscopy to probe the non-interacting chiral band structure of Eq. (3.3). In the regime $\Omega_0 \ll J_0$, there exists a finite window of δ s where the two dispersions cross at two special quasimomentum points $q_{\mathbf{n}}^*$ (Fig. 3.2(a)). The window, whose width is $8J_{\mathbf{n}}|\sin \frac{\phi}{2}|$, is signaled in the carrier linewidth, and thus when resolved it can be used to determine ϕ . At finite temperature, many transverse modes are populated and hence the dependence of $\Omega_{\mathbf{n}}$ and $J_{\mathbf{n}}$ on \mathbf{n} could broaden the line and in general prevent an accurate determination of ϕ . However, a direct simulation of the Rabi lineshape using the potential Eq. (3.1) demonstrates that the features of the ideal, zero-temperature lineshape are captured even for a temperature of $3\mu\text{K}$.

The ability to resolve the $q_{\mathbf{n}}^*$ resonances that appear across the entire Brillouin zone (BZ) as the detuning is varied can be used to perform momentum resolved spectroscopy and to precisely determine the chiral Bloch vector angle θ_{0q} for given values of Ω_0 and δ from Rabi oscillations. We propose the use of a three spectroscopic sequences. One sequence selectively excites atoms at $q_{\mathbf{n}}^*$ from g to e and induces Rabi oscillations. Another filters the dynamics of the excited atoms from the remaining g atoms and the third is used to “correct” imperfections arising from finite temperature. As shown in Fig. 3.2(b), this protocol allows us to extract θ_{0q} over the BZ. This method is not restricted to OLCs, requiring only a stable probe, and complements other techniques for measuring band structures [69–71] used in degenerate Fermi gases.

3.3.1 Lineshape and extraction of θ_{nq} from momentum-resolved Rabi spectroscopy

As described in the previous section, SOC introduces substructure in the Rabi lineshape within a window of width $8J_{\mathbf{n}}\left|\sin \frac{\phi}{2}\right|$ of the carrier frequency. At finite temperature, many transverse modes are populated and hence the dependence of $\Omega_{\mathbf{n}}$ and $J_{\mathbf{n}}$ on \mathbf{n} could broaden the line and destroy this substructure. However, a direct simulation of the Rabi lineshape using the potential

Eq. (1) demonstrates that the features of the ideal, zero-temperature lineshape are captured up to a temperature of $3\mu\text{K}$ as shown in Fig. 3.3(a). Thanks to the clock's sub-Hz resolution it will be possible to resolve the lineshape for a wide range of lattice parameters.

We now turn to the extraction of the chiral Bloch vector angle $\theta_{\mathbf{n}q}$ with Rabi spectroscopy. The eigenstates of Eq. (3) may be written as

$$\begin{aligned} |\psi_{n,q,-}\rangle &= \cos \frac{\theta_{nq}}{2} |gqn\rangle + \sin \frac{\theta_{nq}}{2} |eqn\rangle \\ |\psi_{n,q,+}\rangle &= -\sin \frac{\theta_{nq}}{2} |gqn\rangle + \cos \frac{\theta_{nq}}{2} |eqn\rangle, \end{aligned} \quad (3.4)$$

with energies

$$E_{n,q,\pm} = \frac{E_n(q) + E_n(q + \phi) + \delta}{2} \pm |\mathbf{B}_{nq}|, \quad (3.5)$$

and magnetization

$$\langle \psi_{n,q,\pm} | \hat{S}_{n,q}^z | \psi_{n,q,\pm} \rangle = \frac{\pm \cos \theta_{nq}}{2}. \quad (3.6)$$

Using the above, the expected Rabi dynamics in the ideal case for an arbitrary initial state $\alpha|g\mathbf{n}q\rangle + \beta|e\mathbf{n}q\rangle$ is found to be

$$\begin{aligned} S^z(\alpha, \beta, t) &= \frac{1}{2} \left(|\beta|^2 - |\alpha|^2 \right) \left[\cos^2 \theta_{nq} + \cos(2B_{nq}t) \sin^2 \theta_{nq} \right] + \mathcal{R}(\alpha^* \beta) \cos \theta_{nq} \sin \theta_{nq} (\cos(2B_{nq}t) - 1) \\ &\quad + \mathcal{I}(\alpha^* \beta) \sin \theta_{nq} \sin(2B_{nq}t). \end{aligned} \quad (3.7)$$

The protocol extracting the chiral Bloch vector angle $\theta_{\mathbf{n}q}$ involves three sequences (Fig. 3.3(b)). All sequences start by preparing the atoms in g . In sequence I, a narrow π -pulse about the x axis is applied at the detuning δ^* associated with the q_0^* resonance. The Rabi frequency of the pulse, Ω_0^p , should be weak enough to guarantee that only atoms within a narrow window centered around q_0^* are transferred to e . Atoms with $q \neq q_0^*$ are off-resonant and remain in g . Next the detuning and Rabi frequency are quenched to the desired values Ω_0 and δ , and Rabi oscillations are recorded. Sequence II is identical, except that the initial pulse is about $-x$. Sequence III uses no initial pulse, but is otherwise the same as sequence I. The dynamics in I contains information about $\theta_{q_0^*}$,

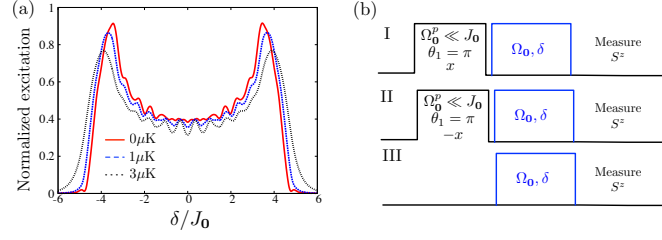


Figure 3.3: (a) Thermally averaged Rabi lineshape fully accounting for trap non-separability. SOC-induced peaks are visible even at $T = 3\mu\text{K}$. (b) Three pulse sequences used to extract θ_{0q} in Fig. (2) of the main text.

but this information will be buried in the signal of the $q \neq q_0^*$ atoms. Subtracting the dynamics of I and III isolates the dynamics of q_0^* atoms. Sequence II is required because due to the mode dependence of $\Omega_{\mathbf{n}}$, a π -pulse is not experienced by all atoms populated at the transverse modes at high temperature. The dynamics of the atoms with q_0^* that remain in g is cancelled by taking the average between sequences I and II, which effectively deals with only the atoms transferred to e . The dynamics for the sequences I, II, and III given in the main text are $S^z(\sqrt{1-f_{\mathbf{n}}^2}, -if_{\mathbf{n}}, t)$, $S^z(\sqrt{1-f_{\mathbf{n}}^2}, if_{\mathbf{n}}, t)$, and $S^z(1, 0, t)$, respectively, where $f_{\mathbf{n}} \approx 1$ is the excitation fraction resulting from the initialization π -pulse. This gives the subtracted signal

$$\frac{S^z(\sqrt{1-f_{\mathbf{n}}^2}, -if_{\mathbf{n}}, t) + S^z(\sqrt{1-f_{\mathbf{n}}^2}, if_{\mathbf{n}}, t)}{2} - S^z(1, 0, t) = f_{\mathbf{n}}^2 (\cos^2 \theta_{\mathbf{n}q} + \cos(2|B_{\mathbf{n}q}|t) \sin^2 \theta_{\mathbf{n}q}) . \quad (3.8)$$

For a single frequency $|B_{\mathbf{n}q}|$, and $\theta_{\mathbf{n}q}$ can be inferred from these oscillations as $2 \tan^2 \theta_{\mathbf{n}q} = (\max - \min)/\text{mean}$. In the multiple-frequency case this is no longer a strict equality, but Fig. 2(b) shows that determining $\theta_{\mathbf{n}q}$ in this fashion from the thermal average of Eq. (3.8) is nevertheless robust. In addition, the validity of this approach can be quantitatively estimated by the equality $(\max + \min)/\text{mean} = 2$, which employs the same assumptions.

3.4 Interaction Hamiltonian with the spin model assumption

The Hamiltonian governing fermionic AEAs in an optical lattice clock may be written:

$$\begin{aligned}
\hat{H} &= \hat{H}_0 + \hat{H}_I + \hat{H}_L, \\
\hat{H}_0 &= \sum_{\alpha} \int d\mathbf{r} \hat{\psi}_{\alpha}(\mathbf{r}) \left[-\frac{\hbar^2}{2m} \nabla^2 + V_{\text{ext}}(\mathbf{r}) \right] \hat{\psi}_{\alpha}(\mathbf{r}) - \hbar\delta \int d\mathbf{r} \hat{\psi}_e^{\dagger}(\mathbf{r}) \hat{\psi}_e(\mathbf{r}), \\
\hat{H}_I &= \frac{4\pi\hbar^2 a_{eg}^-}{m} \int d\mathbf{r} \hat{\psi}_e^{\dagger}(\mathbf{r}) \hat{\psi}_e(\mathbf{r}) \hat{\psi}_g^{\dagger}(\mathbf{r}) \hat{\psi}_g(\mathbf{r}) \\
&\quad + \sum_{\alpha\beta} \frac{3\pi\hbar^2 b_{\alpha\beta}^3}{m} \int d\mathbf{r} W \left[\hat{\psi}_{\alpha}^{\dagger}(\mathbf{r}), \hat{\psi}_{\beta}^{\dagger}(\mathbf{r}) \right] \left(W \left[\hat{\psi}_{\alpha}^{\dagger}(\mathbf{r}), \hat{\psi}_{\beta}^{\dagger}(\mathbf{r}) \right] \right)^{\dagger}, \\
\hat{H}_L &= -\frac{\hbar\Omega}{2} \int d\mathbf{r} \left[\hat{\psi}_e^{\dagger}(\mathbf{r}) e^{i2\pi Z/\lambda} \hat{\psi}_g(\mathbf{r}) + \text{H.c.} \right], \tag{3.9}
\end{aligned}$$

where m is the atomic mass, $\hat{\psi}_{\alpha}(\mathbf{r})$ is a fermionic field operator for state $\alpha \in \{g, e\}$, $W \left[\hat{A}(\mathbf{r}), \hat{B}(\mathbf{r}) \right] = (\nabla \hat{A}(\mathbf{r})) \hat{B}(\mathbf{r}) - \hat{A}(\mathbf{r}) (\nabla \hat{B}(\mathbf{r}))$ is the Wronskian, and $\delta = \omega_l - \omega_0$ is the difference between the clock laser frequency ω_l and atomic frequency ω_0 in the rotating frame of the laser. The Hamiltonian \hat{H}_0 contains the kinetic energy and trapping potential $V_{\text{ext}}(\mathbf{r})$, \hat{H}_I contains the effects of s -wave interactions with scattering length a_{eg}^- and p -wave interactions with interaction volumes $b_{\alpha\beta}^3$ between nuclear spin-polarized AEAs, and \hat{H}_L describes the coupling of internal levels to the clock laser. We assume that the optical lattice is deep enough that we can neglect interactions occurring between different lattice sites, and so consider only interactions between particles occupying the same lattice site. Further, we enact the spin model approximation [51], which neglects all interactions which do not preserve the single-particle transverse mode occupations during a two-body collision. The spin model Hamiltonian hence keeps only direct terms, in which the two colliding particles remain in their same transverse motional quantum states, and exchange processes where the transverse quantum numbers of the two colliding particles are exchanged. The spin model Hamiltonian is valid when interactions are smaller than the spacing between transverse modes, and also when anharmonicity of the potential prevents collisional exchange of mode energy between transverse dimensions.

To derive a Hubbard model amenable for direct calculation, we expand the field operators in

a basis of single-particle eigenfunctions. In order to facilitate thermal averages, we take this set of functions to be the eigenfunctions of \hat{H}_0 , $\psi_{q,n}(\mathbf{r})$, which are indexed in terms of a quasimomentum q and a transverse mode index \mathbf{n} . Enacting this expansion with the approximations of the last paragraph, we find

$$\begin{aligned} \hat{H}_I = & \frac{1}{4L} \sum_{\alpha\beta} \sum_{\{\mathbf{n}_1, \mathbf{n}_2\}} \sum_{qq'\Delta q} \left[(2 - \delta_{\mathbf{n}_1 \mathbf{n}_2}) \left(U_{\{\mathbf{n}_1, \mathbf{n}_2\}}^{\alpha\beta} + V_{\{\mathbf{n}_1, \mathbf{n}_2\}}^{\alpha\beta} \right) \hat{a}_{\alpha, q+\Delta q, \mathbf{n}_1}^\dagger \hat{a}_{\beta, q'-\Delta q, \mathbf{n}_2}^\dagger \hat{a}_{\beta, q', \mathbf{n}_2} \hat{a}_{\alpha, q, \mathbf{n}_1} \right. \\ & \left. + 2(1 - \delta_{\mathbf{n}_1 \mathbf{n}_2}) \left(V_{\{\mathbf{n}_1, \mathbf{n}_2\}}^{\alpha\beta} - U_{\{\mathbf{n}_1, \mathbf{n}_2\}}^{\alpha\beta} \right) \hat{a}_{\beta, q'-\Delta q, \mathbf{n}_1}^\dagger \hat{a}_{\alpha, q+\Delta q, \mathbf{n}_2}^\dagger \hat{a}_{\beta, q', \mathbf{n}_2} \hat{a}_{\alpha, q, \mathbf{n}_1} \right]. \end{aligned} \quad (3.10)$$

Here, L is the number of lattice sites, the sum over $\{\mathbf{n}_1, \mathbf{n}_2\}$ means the sum over distinct, ordered pairs of transverse modes, q, q' , and Δq are quasimomenta in the first Brillouin zone (BZ), greek letters denote internal electronic states $\alpha, \beta \in \{g, e\}$, and the interaction matrix elements may be written as

$$U_{\{\mathbf{n}_1, \mathbf{n}_2\}}^{\alpha\beta} = (1 - \delta_{\alpha\beta}) \frac{8\pi\hbar^2}{m} a_s S_{\mathbf{n}_1 \mathbf{n}_2 \mathbf{n}_2 \mathbf{n}_1}, \quad V_{\{\mathbf{n}_1, \mathbf{n}_2\}}^{\alpha\beta} = \frac{12\pi\hbar^2}{m} b_{\alpha\beta}^3 P_{\mathbf{n}_1 \mathbf{n}_2 \mathbf{n}_2 \mathbf{n}_1} \quad (3.11)$$

by defining the integrals

$$\begin{aligned} S_{\mathbf{n}'_1 \mathbf{n}'_2 \mathbf{n}_2 \mathbf{n}_1} &= \int d\mathbf{r} \psi_{i, \mathbf{n}'_1}^*(\mathbf{r}) \psi_{i, \mathbf{n}'_2}^*(\mathbf{r}) \psi_{i, \mathbf{n}_2}(\mathbf{r}) \psi_{i, \mathbf{n}_1}(\mathbf{r}), \\ P_{\mathbf{n}'_1 \mathbf{n}'_2 \mathbf{n}_2 \mathbf{n}_1} &= \int d\mathbf{r} W \left[\psi_{i, \mathbf{n}'_1}^*(\mathbf{r}), \psi_{i, \mathbf{n}'_2}^*(\mathbf{r}) \right] W \left[\psi_{i, \mathbf{n}_1}(\mathbf{r}), \psi_{i, \mathbf{n}_2}(\mathbf{r}) \right]. \end{aligned} \quad (3.12)$$

In the latter two expressions, the wavefunctions are localized Wannier-type functions obtained from the quasimomentum-indexed eigensolutions (Bloch functions) of the full 3D potential as $\psi_{j, \mathbf{n}}(\mathbf{r}) = \frac{1}{\sqrt{L}} \sum_{q \in \text{BZ}} e^{-iqr_j} \psi_{q, \mathbf{n}}(\mathbf{r})$ [65]. We can also define the mode-dependent tunneling and Rabi frequency in terms of these functions as

$$\begin{aligned} J_{\mathbf{n}} &= - \int d\mathbf{r} \psi_{j, \mathbf{n}}(\mathbf{r}) \left[-\frac{\hbar^2}{2m} \nabla^2 + V_{\text{ext}}(\mathbf{r}) \right] \psi_{j+1, \mathbf{n}}(\mathbf{r}), \\ \Omega_{\mathbf{n}} &= \Omega \int d\mathbf{r} \psi_{j, \mathbf{n}}(\mathbf{r}) e^{i2\pi Z/\lambda} \psi_{j, \mathbf{n}}(\mathbf{r}). \end{aligned} \quad (3.13)$$

3.5 Probing s -wave Interactions via Ramsey Spectroscopy

To access the interplay between SOC and interactions we propose to use Ramsey spectroscopy (Fig. 3.4). The first pulse rotates the Bloch vector, initially pointing down, by an angle θ_1 , set

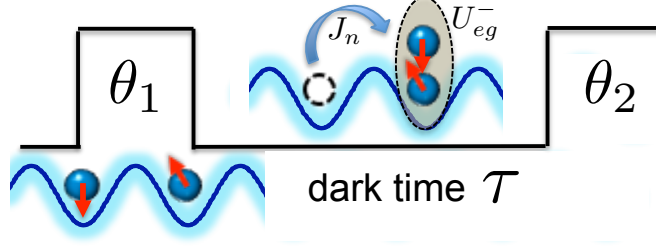


Figure 3.4: A clock laser pulse with pulse area θ_1 imprints a phase difference ϕ between atoms in neighboring sites. Atom tunneling, J_n , allows for s -wave interactions, $\propto U_{eg}^-$, which are signaled as a density shift in Ramsey spectroscopy after a second pulse of area θ_2 is applied.

by the pulse area, and the second converts the accumulated phase during the dark time τ into a $g - e$ population difference measured as Ramsey fringes. Interactions induce a density-dependent frequency shift in the fringes.

Interactions between two nuclear spin polarized atoms depend on the motional and electronic degrees of freedom [51]. When the atoms collide they experience s -wave interactions, characterized by the elastic scattering length a_{eg} , when their electronic state is antisymmetric $(|eg\rangle - |ge\rangle)/\sqrt{2}$. They can also collide via p -wave interactions, described by the corresponding p -wave elastic scattering volumes b_{gg}^3 , b_{ee}^3 , and b_{eg}^3 , in the three possible symmetric electronic configurations $|gg\rangle$, $|ee\rangle$, $(|eg\rangle + |ge\rangle)/\sqrt{2}$, respectively. In addition to elastic interactions, atoms can also exhibit inelastic collisions. In ^{87}Sr only the ee type has been observed to give rise to measurable losses [50] while in $^{173,171}\text{Yb}$, both ee and eg losses have been reported [52, 53, 63].

When tunneling is suppressed the differential phase imparted by the laser is irrelevant, and as long as Ω_n is the same for all modes – a condition well-satisfied in current OLCs [48] – the collective spin of the atoms within each lattice site remains fully symmetric after the pulse and only p -wave collisions occur during the dark time. Measurements under this condition [48, 49] indeed observed a frequency shift linearly dependent on the excitation fraction of atoms, $(1 - \cos\theta_1)/2$ and fully consistent with a p -wave interacting model [51]. If instead tunneling is allowed during the dark time, atoms become sensitive to the spatially inhomogeneous spin rotation from the site-dependent laser phase, which in turn allows for s -wave collisions after a tunneling event (see Fig. 3.4). The s -wave

collisions in SOC-coupled spin polarized fermions can lead to exotic phases of matter including topological quantum liquids [72, 73].

In the regime of weak interactions compared to tunneling, we compute the dynamics perturbatively, and find that SOC manifests itself in the density shift at short times as

$$\Delta\nu = \Delta\nu_0 \left[1 + \frac{4\langle J^2 \rangle_{T_R} \tau^2 \zeta \cos \theta_1 \sin^2 \frac{\phi}{2}}{3\hbar^2 (C - \chi \cos \theta_1)} \right], \quad (3.14)$$

where $\Delta\nu_0 = N(C - \chi \cos \theta_1)$ is the density shift in the absence of tunneling [48, 51], N the mean atom number per pancake, $\langle J^2 \rangle_{T_R}$ the thermally averaged squared tunneling rate, $\zeta = (V^{eg} - U^{eg})/2$, $\chi = (V^{ee} + V^{gg} - 2V^{ge})/2$, and $C = (V^{ee} - V^{gg})/2$, with $V^{\alpha\alpha'} = b_{\alpha\alpha'}^3 \langle P \rangle_{T_R}$ and $U^{eg} = a_{eg} \langle S \rangle_{T_R}$. Here, $\langle P \rangle_{T_R} \propto (T_R)^0$ and $\langle S \rangle_{T_R} \propto T_R^{-1}$ correspond to the thermal averages of the p -wave and s -wave mode overlap coefficients respectively [51], and T_R is the radial temperature. For the JILA ^{87}Sr clock operated at $T_R \sim (1 - 5)\mu\text{K}$ and $\theta_1 \ll \pi$ for $\tau \sim 80$ ms, $\Delta\nu_0 \sim -5\text{Hz}$. Since SOC introduces contributions from s -wave interactions, which can be one order of magnitude larger than p -wave at $T_R \sim 1\mu\text{K}$, then from Eq. 3.14 we expect significant modifications of the density shift. In the JILA ^{87}Sr clock the ratio of elastic to inelastic p -wave collision rates has been measured to be ~ 2 under typical conditions [48, 50], and losses have been compensated during clock operation by dynamically tracking the population decay during the dark time [48, 49]. In Ramsey interrogated SOC systems with dominant s -wave elastic collisions, inelastic processes are expected to become even less relevant.

3.5.1 First-order density shift in Ramsey spectroscopy

Here we compute the density shift (Eq. 3.14) to first order in interactions using an interaction picture perturbation series. In particular, we write the propagator during the dark time evolution in terms of a truncated Dyson series $e^{-i\hat{H}t} = e^{-i\hat{H}_0 t} - i \int_0^t dt' e^{-i\hat{H}_0(t-t')} \hat{H}_1 e^{-i\hat{H}_0 t'}$. At the end of the dark time, a spin-rotation pulse of area θ_2 is applied, and then the total \hat{S}^z is measured. These two operations can be combined as the measurement of the operator $\hat{S}_\theta^z = \sum_{nq} [\cos \theta \hat{S}_{qn}^z - \sin \theta \hat{S}_{qn}^y]$.

Hence, the first-order result of the Ramsey sequence is

$$\langle \hat{S}^z(\tau) \rangle = \langle \psi(\theta_1) | e^{i\hat{H}_0\tau} \hat{S}_{\theta_2}^z e^{-i\hat{H}_0\tau} | \psi(\theta_1) \rangle + 2\mathcal{I} \left[\langle \psi(\theta_1) | e^{i\hat{H}_0\tau} \hat{S}_{\theta_2}^z \int_0^\tau dt e^{-i\hat{H}_0(\tau-t)} \hat{H}_I e^{-i\hat{H}_0 t} | \psi(\theta_1) \rangle \right], \quad (3.15)$$

where $|\psi(\theta_1)\rangle$ is the state resulting from applying the first Ramsey pulse to an initial state $|\tilde{i}\rangle$.

We will parameterize the initial state in terms of products of single-particle eigenstates $|i\rangle = \prod_{i=1}^N \hat{a}_{gq_i n_i}^\dagger |\text{vac.}\rangle$, where $|\text{vac.}\rangle$ is the vacuum, N the number of particles, and $\{q_i, \mathbf{n}_i\}$ the initial distinct set of populated quasimomenta and transverse modes, so that

$$|\psi(\theta_1)\rangle = \prod_{j=1}^N \left(\cos \frac{\theta_1}{2} \hat{a}_{g, q_j, \mathbf{n}_j}^\dagger + i \sin \frac{\theta_1}{2} \hat{a}_{e, q_j, \mathbf{n}_j}^\dagger \right). \quad (3.16)$$

From this, we find that the non-interacting dynamics are given as

$$\langle \psi(\theta_1) | e^{i\hat{H}_0\tau} \hat{S}_{\theta_2}^z e^{-i\hat{H}_0\tau} | \psi(\theta_1) \rangle = \sum_{i=1}^N \left[-\frac{\cos \theta_1 \cos \theta_2}{2} + \frac{\sin \theta_1 \sin \theta_2}{2} \cos(\delta\tau - \Delta E_{\mathbf{n}_i}(q_i, \phi)\tau) \right], \quad (3.17)$$

where $E_{\mathbf{n}}(q)$ is the single-particle dispersion and

$$\Delta E_{\mathbf{n}}(q, \phi) \equiv E_{\mathbf{n}}(q + \phi) - E_{\mathbf{n}}(q), \quad (3.18)$$

is the difference in single-particle dispersion of the e and g states.

Writing the non-interacting result as $\langle \hat{S}^z(\tau) \rangle = A(\tau) \cos(\delta\tau) + B(\tau) \sin(\delta\tau) + \text{const.}$ we can extract the density shift as $\Delta\nu = \frac{1}{2\pi\tau} \arctan\left(\frac{B(\tau)}{A(\tau)}\right)$ and the normalized contrast decay as $\mathcal{C}(\tau) = \frac{\sqrt{A^2(\tau) + B^2(\tau)}}{\sqrt{A^2(0) + B^2(0)}}$. For a single particle with momentum q and transverse mode n , the density shift is $\Delta E_{\mathbf{n}}(q, \phi)/2\pi$. Assuming short times compared to the tunneling bandwidth, the density shifts for all particles add as $\Delta\nu = \sum_{i=1}^N \Delta E_{\mathbf{n}_i}(q_i, \phi)/2\pi N + \mathcal{O}(\tau^2)$. The contrast decay at short times is given as $\mathcal{C}(\tau) = 1 - \frac{1}{2N^2} \left(\sum_{i=1}^N \Delta E_{\mathbf{n}_i}(q_i, \phi) \right)^2 \tau^2 + \frac{1}{2N} \sum_{i=1}^N \Delta E_{\mathbf{n}_i}^2(q_i, \phi) \tau^2 + \mathcal{O}(\tau^4)$. This single-particle contribution will dominate over the $\sim U^2 \tau^2$ decay of the contrast due to interactions at short times and in the regime of weak interactions compared to the tunneling.

The contribution to the dynamics at the lowest order in interactions is given as

$$\begin{aligned}
& 2\mathcal{I} \left[\langle \psi(\theta_1) | e^{i\hat{H}_0\tau} \hat{S}_{\theta_2}^z \int_0^\tau dt e^{-i\hat{H}_0(\tau-t)} \hat{H}_I e^{-i\hat{H}_0 t} | \psi(\theta_1) \rangle \right] \\
&= \frac{\tau}{L} \sum_{\{p_1, p_2\}} \left\{ \sin \theta_1 \sin \theta_2 \sin \left[\left(\delta - \frac{\Delta E_{\mathbf{n}_{p_1}} + \Delta E_{\mathbf{n}_{p_2}}}{2} \right) \tau \right] \right. \\
&\times \left[\left(C_{\{\mathbf{n}_{p_1} \mathbf{n}_{p_2}\}} - \chi_{\{\mathbf{n}_{p_1} \mathbf{n}_{p_2}\}} \cos \theta_1 \right) \cos \left(\frac{\Delta E_{\mathbf{n}_{p_1}} - \Delta E_{\mathbf{n}_{p_2}}}{2} \tau \right) \right. \\
&\left. \left. - \frac{\cos \theta_1}{2} (2 - \delta_{\mathbf{n}_{p_1} \mathbf{n}_{p_2}}) \zeta_{\{\mathbf{n}_{p_1} \mathbf{n}_{p_2}\}} \left[\cos \left(\frac{\Delta E_{\mathbf{n}_{p_1}} - \Delta E_{\mathbf{n}_{p_2}}}{2} \tau \right) - \text{sinc} \left(\frac{\Delta E_{\mathbf{n}_{p_1}} - \Delta E_{\mathbf{n}_{p_2}}}{2} \tau \right) \right] \right] \right\}
\end{aligned} \tag{3.19}$$

where the mode-dependent spin model parameters are

$$\begin{aligned}
C_{\{\mathbf{n}_1 \mathbf{n}_2\}} &= \frac{V_{ee12} - V_{gg12}}{2} \\
\chi_{\{\mathbf{n}_1 \mathbf{n}_2\}} &= \frac{V_{ee12} + V_{gg12} - 2V_{eg12}}{2} \\
\zeta_{\{\mathbf{n}_1 \mathbf{n}_2\}} &= \frac{V_{eg12} - U_{eg12}}{2}.
\end{aligned} \tag{3.20}$$

Taking a series in the tunneling bandwidth, the zeroth order term for a given pair of particles is $(C - \chi \cos \theta_1) \sin \theta_1 \sin \theta_2 \sin \delta \tau$, which has been obtained in previous works [48]. The thermally averaged density shift in the high-temperature limit will be given in the next section.

3.6 Probing Beyond Mean Field Interactions via a Sliding Superlattice

The third interrogation protocol we discuss is accomplished by generating a sliding superlattice via a pair of counter-propagating beams close to resonance with the clock transition and with a global phase difference $\Upsilon(t)$ which can be controlled in time (see Fig. 3.5(a)). The non-interacting Hamiltonian, written using a Wannier orbital basis along the lattice direction, is

$$\begin{aligned}
\hat{H}_L^0 &= - \sum_{\mathbf{n}, j, \alpha} \left(J_{\mathbf{n}} \left[\hat{a}_{\alpha, \mathbf{n}, j}^\dagger \hat{a}_{\alpha, \mathbf{n}, j+1} + \text{H.c.} \right] - \frac{\delta}{2} \alpha \hat{n}_{\alpha, j} \right) \\
&- \sum_{\mathbf{n}, j} \left(\Omega_{\mathbf{n}} \cos(\Upsilon(t) - j\phi) \left[\hat{a}_{+, \mathbf{n}, j}^\dagger \hat{a}_{-, \mathbf{n}, j} + \text{H.c.} \right] \right).
\end{aligned} \tag{3.21}$$

As $\Upsilon(t)$ is changed, the clock laser standing wave “slides” with respect to the optical lattice. This allows for the minimum realization of a topological pump when $\Upsilon(t)$ is adiabatically varied from

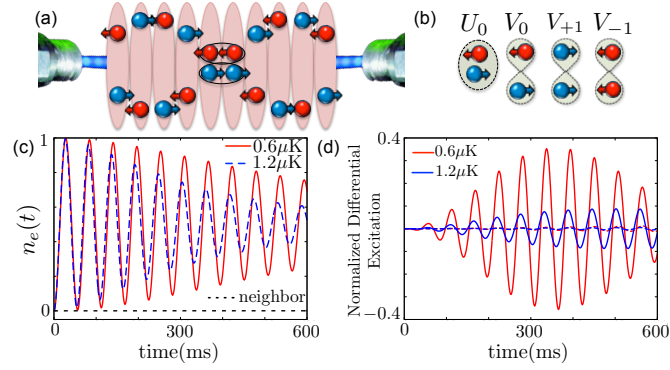


Figure 3.5: (a) An additional counter-propagating probing beam with a differential phase Υ generates a sliding superlattice potential, shown for $\phi = 7\pi/6$, corresponding to an ^{87}Sr OLC. For weak tunneling $J \ll \Omega$ transport is energetically suppressed except at resonant defect points (circled). (b) Two-particle interaction sectors classified by the total polarization M_x and spatial symmetry of the dressed states. An oval (figure-eight) denotes a symmetric (antisymmetric) spatial wavefunction. (c) Dynamics of a single particle at the tunneling resonance for two temperatures (red solid and blue dashed) and an off-resonant site (black dotted) for $J_0/h = 8\text{Hz}$, $\Omega_0/h = 1\text{kHz}$, $\phi = 7\pi/6$. (d) Normalized differential excitation extracted as explained in the text with the interaction parameters of Ref. [50]. The $M_x = 0$ components (solid lines) involve the s -wave sector, and so display a strong dependence of contrast on temperature, while the $M_{\pm 1}$ sectors (dashed lines) experience only weaker single-particle thermal dephasing.

$0 \rightarrow 2\pi$ [55–59]. In the weak tunneling limit the quantized nature of particle transport can be directly linked to spatially isolated tunneling resonances [59]. We now show how those resonances can be spectroscopically measured.

Let us first consider the case $J_{\mathbf{n}} = \delta = 0$ and set $\phi = 7\pi/6$, relevant for the ^{87}Sr system. We write $\Upsilon = (2\pi s + \Delta\Upsilon)/12$, with $0 \leq \Delta\Upsilon < 2\pi$ and s an integer. Under these conditions, the localized dressed eigenstates are spin-polarized along $\pm x$ alternating between neighboring sites except for “defects” at $j_d(r) = 6r + 3 + s$ (r an integer) when $\cos(\Upsilon - \Delta\Upsilon/12 - j_d\phi) = 0$ and the ground states at $j_d(r)$ and $j_d(r) + 1$ point along the same direction. Since tunneling preserves polarization, it is suppressed when $J_{\mathbf{n}} \ll \Omega_{\mathbf{n}}$ due to the energy offset $\sim \Omega$ between neighboring sites. The one exception is the case $\Delta\Upsilon = \pi$ where the defect pair $j_d(r)$ and $j_d(r) + 1$ is resonantly tunnel-coupled. Quantized transport occurs when $\Delta\Upsilon$ is slowly varied across the resonance. Instead of adiabatic transport we propose to spectroscopically resolve the resonance using a Ramsey-type protocol. Here, atoms initially prepared in g at $|\delta| \gg \Omega_0$ are adiabatically transferred to the ground dressed state by slowly turning off δ at $\Upsilon = (2\pi s + \Delta\Upsilon_p)/12$ with $\Delta\Upsilon_p \neq \pi$. Then Υ is quenched so resonant tunneling is allowed, $s \rightarrow s + 1$ and $\Delta\Upsilon = \pi$, and the system evolves for a time τ . Following this evolution tunneling is turned off and the phase switched back, $s + 1 \rightarrow s$ and $\Delta\Upsilon \rightarrow \Delta\Upsilon_p$. Those atoms which have tunneled at the resonant sites are now in an excited state of the local dressed basis. These excitations can be measured by adiabatically converting the dressed excitations to “bare” e excitations by adiabatically ramping on $\delta \gg \Omega_0$; this leads to a measurable excited state population $n_e(t)$. In Fig. 3.5(c) we show these tunneling resonances are clearly observable even at finite temperature. Moreover, since resonances are spatially well-separated (every six sites), they can be resolved with low-resolution imaging.

Interactions modify the transport dynamics in this pumping protocol. The sliding superlattice simplifies the treatment of interactions by isolating resonant site pairs $\{j_d, j_d + 1\}$. We consider the case where at most two atoms occupy the resonant sites, a condition which can be achieved by decreasing the atomic density with a large-volume dipole trap [44]. The two particle states can be classified in terms of the atoms’ spin polarization along x in four sectors: three symmetric

ones (triplets) with total x polarization $M_x = +1, -1, 0$ and a $M_x = 0$ singlet. Within each sector, the dressed states' interaction parameters are given by $V_{+1} = V_{-1} = (V^{gg} + V^{ee} + 2V^{eg})/4$, $V_0 = (V^{gg} + V^{ee})/2$ and $U_0 = U^{eg}$ (see Fig. 3.5(b)). Since the p -wave parameters are not SU(2) symmetric, i.e. $b_{ee} \neq b_{gg} \neq b_{eg}$, the triplet sectors are coupled. However, in the weakly interacting limit $V^{\alpha\beta} \ll \Omega$, the triplets are separated by energy gaps $\sim \Omega$ and coupling between the sectors can be neglected. The singlet sector is always decoupled from the triplets.

Within each sector interactions modify the dynamics, making it sensitive to temperature and density. The modifications can be extracted by performing measurements of the atom number-normalized excitation fraction for different densities and then differentiating the high-density and low-density results. This procedure removes the single-particle contribution and is particularly suitable for characterizing the role of interactions in clock experiments [48, 50]. The normalized differential excitation is shown in Fig. 3.5(d). For the adiabatic dressed state preparation, all four manifolds, and hence all interaction parameters $V_{\pm,0}, U_0$, contribute to the dynamics. A filtering protocol that uses the ee losses can be used to separate the dynamics of the various sectors. For example, by transferring all atoms to the e state and holding before the adiabatic ground state preparation, the doubly occupied $M_x = \pm 1$ triplet sectors will be removed and only the $M_x = 0$ singlet and triplet remain and contribute (here the ground dressed states have one atom at j_d and $j_d + 1$). As shown in Fig. 3.5 the dynamics of the $V_{\pm,0}$ and U_0 sectors can be distinguished by the different scaling of the p - and s -wave interaction parameters with temperature T_R , $V_{\pm,0}(T_R) \sim \text{const.}$ and $U_0(T_R) \sim T_R^{-1}$ [51] (See Fig.3.5(d)). By comparing these dynamics to that without the holding time, information about the $M_x = \pm 1$ dynamics can be extracted. In general s -wave interactions, purely elastic for nuclear-spin-polarized Sr, dominate the normalized differential contrast, with p -wave contributions (including losses) relevant only at hotter temperatures.

3.6.1 Interacting dressed states with a sliding clock superlattice

The results of the previous section were derived by considering the dynamics of two atoms in neighboring sites $j_d(r)$ and $j_d(r) + 1$ which are tunnel-coupled for a sliding lattice clock phase $\Delta\Upsilon =$

π . We will take these two atoms to have different transverse mode indices \mathbf{n} and \mathbf{m} . Interactions in the s -wave channel occur between these atoms when they are in an antisymmetric electronic state $|\Lambda_{\text{eg}}^-\rangle \equiv (|ge\rangle - |eg\rangle)/\sqrt{2}$ with a symmetric spatial wave function $|\Psi_{\mathbf{nm}}^+\rangle \equiv (|\mathbf{nm}\rangle_j + |\mathbf{mn}\rangle_j)$, with the subscript j denoting the lattice site index. Instead, p -wave interactions occur when the atoms are in a symmetric electronic state $|\Lambda_{\text{eg}}^+\rangle \equiv (|ge\rangle + |eg\rangle)/\sqrt{2}$ and an antisymmetric spatial wave function $|\Psi_{\mathbf{nm}}^-\rangle \equiv (|\mathbf{nm}\rangle_j - |\mathbf{mn}\rangle_j)$. For the purposes of describing the system dynamics at Δ *Upsilon* = π , where $|\rightarrow\rangle = (|g\rangle + |e\rangle)/\sqrt{2}$ is the single-well electronic ground state and $|\leftarrow\rangle = (|g\rangle - |e\rangle)/\sqrt{2}$ the excited state, it is useful to employ the states

$$\begin{aligned}
t, 1 : & |2^{++}, 0\rangle, |0, 2^{++}\rangle, |\rightarrow_{\mathbf{n}}, \rightarrow_{\mathbf{m}}\rangle, |\rightarrow_{\mathbf{m}}, \rightarrow_{\mathbf{n}}\rangle, \\
t, -1 : & |2^{--}, 0\rangle, |0, 2^{--}\rangle, |\leftarrow_{\mathbf{n}}, \leftarrow_{\mathbf{m}}\rangle, |\leftarrow_{\mathbf{m}}, \leftarrow_{\mathbf{n}}\rangle \\
t, 0 : & |2^{\pm}, 0\rangle, |0, 2^{\pm}\rangle, \frac{|\rightarrow_{\mathbf{n}}, \leftarrow_{\mathbf{m}}\rangle - |\rightarrow_{\mathbf{m}}, \leftarrow_{\mathbf{n}}\rangle}{\sqrt{2}}, \frac{|\leftarrow_{\mathbf{n}}, \rightarrow_{\mathbf{m}}\rangle - |\leftarrow_{\mathbf{m}}, \rightarrow_{\mathbf{n}}\rangle}{\sqrt{2}} \\
s, 0 : & |2^{\mp}, 0\rangle, |0, 2^{\mp}\rangle, \frac{|\rightarrow_{\mathbf{n}}, \leftarrow_{\mathbf{m}}\rangle + |\rightarrow_{\mathbf{m}}, \leftarrow_{\mathbf{n}}\rangle}{\sqrt{2}}, \frac{|\leftarrow_{\mathbf{n}}, \rightarrow_{\mathbf{m}}\rangle + |\leftarrow_{\mathbf{m}}, \rightarrow_{\mathbf{n}}\rangle}{\sqrt{2}},
\end{aligned} \tag{3.22}$$

where

$$\begin{aligned}
|2^{++}\rangle &= |\rightarrow\rightarrow\rangle |\Psi_{\mathbf{nm}}^-\rangle, \\
|2^{--}\rangle &= |\leftarrow\leftarrow\rangle |\Psi_{\mathbf{nm}}^-\rangle, \\
|2^{\pm}\rangle &= \frac{|\rightarrow\leftarrow\rangle + |\leftarrow\rightarrow\rangle}{\sqrt{2}} |\Psi_{\mathbf{nm}}^-\rangle, \\
|2^{\mp}\rangle &= \frac{|\rightarrow\leftarrow\rangle - |\leftarrow\rightarrow\rangle}{\sqrt{2}} |\Psi_{\mathbf{nm}}^+\rangle.
\end{aligned} \tag{3.23}$$

In each four-state sector the Hamiltonian may be written as

$$\hat{H}_{\mu, M_x} = 2M_x \Omega \mathbb{I} + \begin{pmatrix} U_{\mu, M_x} & 0 & J & J \\ 0 & U_{\mu, M_x} & -J & -J \\ J & -J & 0 & 0 \\ J & -J & 0 & 0 \end{pmatrix}, \tag{3.24}$$

where $\mu = t, s$, $U_{t, M_x} = V_{M_x}$, $U_{s, 0} = U_0$, \mathbb{I} is the identity operator, and we have set $\Omega_{\mathbf{n}} = \Omega_{\mathbf{m}} = \Omega$ and $J_{\mathbf{n}} = J_{\mathbf{m}} = J$ for simplicity. The $s, 0$ singlet sector is rigorously decoupled from the others,

but there is mixing between the triplet sectors proportional to the spin model parameters χ and C . These couplings are neglected due to the large single-particle energy difference $\sim \Omega$ between coupled manifolds with the assumed separation of energy scales $\Omega \gg J, V, U$.

The Hamiltonians Eq. (3.24) may be readily diagonalized, leading to the eigenvalues $2M_x\Omega, 2M_x\Omega + U, 2M_x\Omega + \frac{U}{2} \pm \sqrt{4J^2 + \frac{U^2}{4}}$. At high temperatures compared to the tunneling, and for the adiabatic preparation procedure described in the main text, the observed dynamics will be an equal weight superposition of the dynamics from the initial states $|2^{++}, 0\rangle, |0, 2^{--}\rangle, |\rightarrow_{\mathbf{n}}, \leftarrow_{\mathbf{m}}\rangle$, and $|\rightarrow_{\mathbf{m}}, \leftarrow_{\mathbf{n}}\rangle$. The dynamics of the number of excitations following adiabatic conversion back to the “bare” g/e basis for these states are

$$\begin{aligned} |2^{++}, 0\rangle, |0, 2^{--}\rangle \rightarrow n_e(t) &= 1 - \cos \frac{V_1 t}{2} \cos \left(t \sqrt{4J^2 + \frac{V_1^2}{4}} \right) - \frac{V_1 \sin \frac{V_1 t}{2} \sin \left(t \sqrt{4J^2 + \frac{V_1^2}{4}} \right)}{\sqrt{16J^2 + V_1^2}}, \\ |\rightarrow_{\mathbf{n}}, \leftarrow_{\mathbf{m}}\rangle, |\rightarrow_{\mathbf{m}}, \leftarrow_{\mathbf{n}}\rangle \rightarrow n_e(t) &= \\ 1 - \frac{1}{2} \left(\cos \frac{V_0 t}{2} \cos \left(t \sqrt{4J^2 + \frac{V_0^2}{4}} \right) + \cos \frac{U_0 t}{2} \cos \left(t \sqrt{4J^2 + \frac{U_0^2}{4}} \right) \right) \\ - \frac{1}{2} \left(\frac{V_0 \sin \frac{V_0 t}{2} \sin \left(t \sqrt{4J^2 + \frac{V_0^2}{4}} \right)}{\sqrt{16J^2 + V_0^2}} + \frac{U_0 \sin \frac{U_0 t}{2} \sin \left(t \sqrt{4J^2 + \frac{U_0^2}{4}} \right)}{\sqrt{16J^2 + U_0^2}} \right). \end{aligned} \quad (3.25)$$

For small interactions compared to tunneling, we can expand the result to lowest order in interactions, and find the thermally averaged dynamics

$$n_e(t) = 2 \sin^2(Jt) - \frac{(U_0^2 + V_0^2 + 2V_1^2) t (\sin(2Jt) - 2Jt \cos(2Jt))}{64J}. \quad (3.26)$$

In addition to the above two-particle dynamics, there will be contributions from experimental realizations in which the resonant double well has only a single particle. Here, the dynamics is $n_e(t) = \sin^2(Jt)$. Writing p_1 as the probability of a single particle in a given double well and p_2 as the probability of having two particles, the small-interaction dynamics averaged over all realizations is hence

$$n_e(t) = (p_1 + 2p_2) \sin^2(Jt) - p_2 \frac{(U_0^2 + V_0^2 + 2V_1^2) t (\sin(2Jt) - 2Jt \cos(2Jt))}{64J}. \quad (3.27)$$

Noting that $p_1 + 2p_2 = N$ is the average number, we can subtract the measurements of $n_e(t)/N$ for two different densities with single- and double-occupancy probabilities (p_1, p_2) and (p'_1, p'_2) and

numbers N and N' , respectively, to find

$$\Delta[n_e(t)/N] = - \left(\frac{p_2}{N} - \frac{p'_2}{N'} \right) \frac{(U_0^2 + V_0^2 + 2V_1^2) t (\sin(2Jt) - 2Jt \cos(2Jt))}{64J}. \quad (3.28)$$

In this way we separate the single-particle contrast decay due to a thermal spread in $J_{\mathbf{n}}$ from the contrast decay due to interactions.

3.7 Relative strength of ee losses for Sr.

As shown in Ref. [51], at the mean-field level the time dependence of the coherence between the e and g states is affected by both elastic and inelastic processes. Here, we have in mind the Sr system, for which no eg losses have been measured [50]. While s -wave ee losses with associated scattering length $46a_0$ (a_0 the Bohr radius) have been measured for colliding particles with an antisymmetric nuclear spin state [50], these play no role for the nuclear-spin-polarized system we consider in this work. In the nuclear-spin-polarized case, only ee p -wave losses have a measurable effect, while elastic p -wave interactions occur in all (ee , eg , and gg) channels. The elastic processes are characterized by the quantity

$$B_{\text{eff}} = N (C - \chi \cos \theta), \quad (3.29)$$

where C and χ were defined in Eq. 3.20. Meanwhile, the inelastic processes are associated with the decay rate $\Gamma_{ee}N_e/2$. To estimate the relative effect of losses, we use that $\Gamma_{ee}/V^{ee} = \beta_{ee}^3/b_{ee}^3$, with b and β elastic and inelastic p -wave scattering parameters, measured to be $b_{eg}^3 = -169^3a_0^3$, $b_{ee}^3 = -119^3a_0^3$, $\beta_{ee}^3 = 125^3a_0^3$, and $b_{gg}^3 = 74^3a_0^3$ for Sr [50]. Using typical interrogation conditions of $\pi/2$ pulses in which $N_e = N/2$, we then find $|B_{\text{eff}}/(\Gamma_{ee}N_e/2)| = 2.14$, approximated as 2 in the main text.

3.8 Experiment

Here we describe the results of a recent experiment at JILA using fermionic ^{87}Sr to produce SOC. APK contributed to the theory model used to describe the experiment, but the experiment

was conducted by the Sr team in the June Ye group, and the remainder of this chapter is adapted from Ref. [7]. The experiment uses clock spectroscopy to prepare lattice band populations, internal electronic states, and quasimomenta, as well as to produce SOC dynamics. The exceptionally long lifetime of the excited clock state (160 s) eliminates decoherence and atom loss from spontaneous emission at all relevant experimental timescales, allowing subsequent momentum- and spin-resolved *in situ* probing of the SOC band structure and eigenstates. The experimenters utilized these capabilities to study Bloch oscillations, spin-momentum locking, and Van Hove singularities in the transition density of states. The results lay the groundwork for the use of OLCs to probe novel SOC phases of matter.

When tunneling is allowed, spin-orbit coupling emerges naturally in a nuclear spin polarized ^{87}Sr OLC during laser interrogation of the narrow linewidth $^1S_0(|g\rangle) - ^3P_0(|e\rangle)$ clock transition at wavelength $\lambda_c = 698$ nm (Fig. 3.6a). The lattice used to confine the atoms has a wavelength $\lambda_L = 813$ nm. At this “magic” wavelength, the band structures of the two clock states are identical with band energies $E_{n_z}(q)$, determined by the discrete band index n_z and quasimomentum q in units of \hbar/a , where the lattice constant $a = \lambda_L/2$ and \hbar is the Planck constant divided by 2π . When an atom is excited from $|g\rangle$ to $|e\rangle$ using a clock laser with Rabi frequency Ω and frequency detuning δ from the clock transition, energy and momentum conservation require a change in atomic momentum by $2\pi\hbar/\lambda_c$.

The resulting Hamiltonian can be diagonalized in quasimomentum space by performing a gauge transformation $|e, q\rangle_{n_z} \rightarrow |e, q + \phi\rangle_{n_z}$, where $\phi = \pi\lambda_L/\lambda_c \approx 7\pi/6$. Fig. 3.6b shows the transformed $|g\rangle$ and $|e\rangle$ bands for $n_z = 0$, the ground state band, under the rotating-wave approximation when $\delta = 0$. The transformed SOC Hamiltonian is given by [74]

$$H_{SOC} = -\hbar \sum_q \vec{B}_{n_z}(q, \Omega, \delta) \cdot \vec{S}, \quad (3.30)$$

where the components of \vec{S} are $\hat{S}^{X,Y,Z}$, the spin-1/2 angular momentum operators for the two clock states. $\vec{B}_{n_z}(q, \Omega, \delta)$ is an effective, quasimomentum-dependent magnetic field given by

$$\vec{B}_{n_z}(q, \Omega, \delta) = [B_{n_z}^X(\Omega), 0, B_{n_z}^Z(q, \delta)] = [\Omega, 0, (E_{n_z}(q) - E_{n_z}(q + \phi))/\hbar + \delta], \quad (3.31)$$

where in the tight binding limit $E_0(q) = -2\hbar J \cos(q)$, and J is the tunneling rate between nearest neighbor lattice sites. The eigenstates of H_{SOC} are described by Bloch vectors in the \hat{X} - \hat{Z} plane, pointing along the magnetic field $\vec{B}_{n_z}(q, \Omega, \delta)$, with their orientation specified by the chiral Bloch vector angle θ_B with respect to the \hat{Z} axis[74], where

$$\theta_B = \arctan\left(\frac{\Omega}{(E_{n_z}(q) - E_{n_z}(q + \phi))/\hbar + \delta}\right). \quad (3.32)$$

The q dependence of θ_B is a manifestation of chiral spin-momentum locking[67, 74]. To connect this system to related works on synthetic gauge fields[34, 36, 75–79], we can treat the internal clock transition ($|g\rangle \rightarrow |e\rangle$) as a synthetic dimension[66], as shown in Fig. 3.6a. In this case, an atom following a closed trajectory about a single plaquette ($|m, g\rangle \rightarrow |m + 1, g\rangle \rightarrow |m + 1, e\rangle \rightarrow |m, e\rangle \rightarrow |m, g\rangle$) accumulates a phase, given by the same ϕ defined previously, which resembles the flux experienced by a charged particle in the presence of an external magnetic field. In this picture, the chiral Bloch vector angle θ_B is directly connected to the topological nature of chiral edge modes of the two-dimensional Hofstadter model[67, 76]. Coupling multiple nuclear spin states with our synthetic gauge fields should enable the realization of topological bands[37, 75] and exotic phases in higher dimensions[80].

In the experiment, several thousand nuclear-spin polarized fermionic ^{87}Sr atoms are cooled and loaded into a horizontal one-dimensional optical lattice aligned along the \hat{z} -axis with $\sim 2 \mu\text{K}$ temperatures. The lattice is formed using a high power ($P_1 \approx 3 \text{ W}$) incoming beam focused down to a beam waist $w_0 \approx 45 \mu\text{m}$ and a strongly attenuated retro-reflection with tunable power ($0 \leq P_2 \leq 50 \text{ mW}$, Fig. 3.6a). This enables the radial trap frequency to effectively remain constant at $\nu_r \approx 450 \text{ Hz}$, while U_z can be tuned via P_2 over a wide range from $U_z/E_r = 0$ to $U_z/E_r > 200$, where $E_r = \frac{\hbar^2 k_L^2}{2m}$ is the lattice recoil energy, and m is the atomic mass. This corresponds to axial

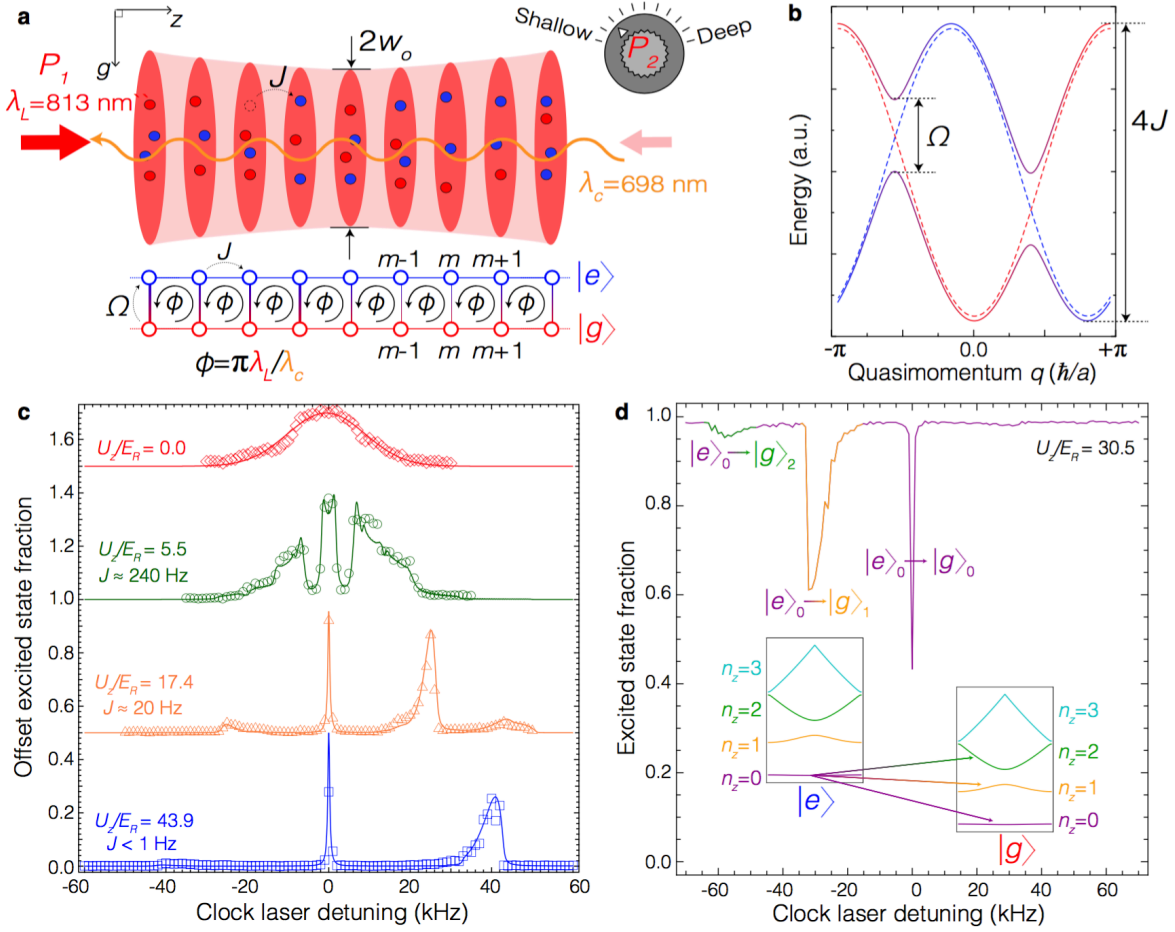


Figure 3.6: Spin-orbit coupling (SOC) in a 1D lattice with tunable tunneling. **a**, Atoms are trapped in a 1D optical lattice formed by interfering a strong trapping beam (power P_1 , wavelength $\lambda_L = 813$ nm) with a counter-propagating, tunably attenuated retro-reflection (variable power P_2 , represented by a cartoon knob). The atoms are probed on the narrow clock transition with an ultra-stable clock laser ($\lambda_c = 698$ nm, Rabi frequency Ω). The resulting SOC Hamiltonian is equivalent to that of charged fermions on a synthetic 2D ladder, with horizontal tunneling rate J , vertical tunneling rate Ω , and a synthetic magnetic field flux $\phi = \pi\lambda_L/\lambda_c$. **b**, The clock laser couples the dispersion curve for $|g\rangle_{n_z=0}$ (dashed red line) to the quasimomentum-shifted curve for $|e\rangle_0$ (dashed blue line), resulting in spin-orbit coupled bands (solid bichromatic lines). **c**, Clock spectroscopy ($\Omega \approx 2\pi \times 200$ Hz, 80 ms pulse duration) at four axial trapping potentials (data and fits are shifted upward for clarity). When $P_2 = 0$ mW, the sidebands and carrier merge into a Doppler broadened Gaussian (red diamonds). The solid lines are theoretical calculations using a model that perturbatively treats the axial and radial coupling. **d**, Spectroscopy of atoms in $|e\rangle_0$, prepared by driving the $|g\rangle_0 \rightarrow |e\rangle_0$ transition, then removing any remaining atoms in $|g\rangle$.

trap frequencies $\nu_z \approx 2E_r\sqrt{U_z/E_r}/2\pi\hbar$ up to ~ 100 kHz. When $\nu_z \gtrsim 40$ kHz, site to site tunneling takes longer than experimentally relevant timescales and the atoms are effectively localized to single lattice sites, as is standard in OLC operation[44]. However, for smaller ν_z tunneling between nearest neighbor lattice sites is important and occurs at a rate $J_{\mathbf{n}_r}$ that depends on the radial mode index \mathbf{n}_r . In this regime, atomic motion in the axial direction is described by delocalized Bloch states characterized by n_z and q . For a ~ 2 μ K thermal distribution, the atoms are predominantly in the $n_z = 0$ axial ground band and completely fill the band. The average radial mode occupation is $\langle n_r \rangle \sim 100$.

The clock laser is locked to an ultra-stable optical cavity[44] with a linewidth of ~ 26 mHz. Because the clock laser is co-linear with the lattice axis, coupling to the radial motional modes is suppressed, and for the entirety of this work the system will be treated as quasi-one-dimensional, with relatively minor corrections arising from the thermal average of the Rabi frequency $\Omega_{\mathbf{n}_r}$ and the tunneling rate $J_{\mathbf{n}_r}$ over the radial mode occupation. For the sake of clarity we therefore drop the radial mode index from Ω and J . Throughout this work the clock laser Rabi frequency Ω is measured on resonance with the carrier at $\delta = 0$ with a high axial trapping frequency $\nu_z > 50$ kHz. The mean particle number per lattice site was kept in the range $N \sim 1 - 10$, which for the operating conditions results in a density-dependent many-body interaction rate of $N\chi/(2\pi) \lesssim 1$ Hz, where χ is the two-body interaction rate[48]. For the experiments presented here $\Omega \gg N\chi$, and thus the results are all well described by a single particle model.

Unlike previous studies of SOC in ultra-cold atoms in which time of flight (TOF) measurements are used to determine the momentum distribution[29, 34, 36, 37, 75, 76, 79, 81, 82], all of the data presented here is measured *in situ* using clock spectroscopy[44]. Clock spectroscopy provides precise measurement and control of the atomic spin and motional degrees of freedom, access to the atomic density of states, and offers the prospect for real-time, non-destructive measurement of atom dynamics in the lattice. At the end of each experiment the number of atoms in the $|e\rangle$ and $|g\rangle$ states are counted using a cycling transition, and the normalized population fraction in each state is extracted. For example, Fig. 3.6c presents spectroscopy of the carrier and motional

sideband transitions at four different axial trapping potentials, with the atoms initially prepared in $|g\rangle_0$. Here each data point was taken with a new sample of ^{87}Sr at a different clock laser detuning. At $U_z/E_r = 43.9$ (blue squares) the atoms are strongly confined and the data is well described by a simple model that neglects tunneling between lattice sites[83]. However, as P_2 is turned down and the trapping potential is reduced to $U_z/E_r = 5.5$ (green circles) the carrier transition exhibits a broad, sharp splitting, which is no longer consistent with atoms localized to single sites. A model that perturbatively treats the axial and radial coupling[83] fully reproduces the measured lineshapes (solid lines).

The narrow $|g\rangle_0 \rightarrow |e\rangle_0$ carrier transition centered at $\delta/(2\pi) = 0$ kHz enables the preparation of atoms in the $|e\rangle_0$ state, from which spectroscopy can also be performed, as shown in Fig. 3.6d. Due to the long lifetime of $|e\rangle$ we do not observe spin state relaxation to $|g\rangle$ for the time scales explored in this experiment (< 150 ms). In addition to the carrier transition, motional sidebands corresponding to axial inter-band transitions are also apparent in Fig. 3.6d. The measured lineshape in this case is also fully captured by the perturbative model (solid lines). At high trapping potential (blue squares) the prominent blue-detuned sideband at $\delta/(2\pi) \approx 40$ kHz corresponds to the $|g\rangle_0 \rightarrow |e\rangle_1$ transition. The corresponding red-detuned sideband at $\delta/(2\pi) \approx -40$ kHz is suppressed because the atoms have been prepared predominantly in the $n_z = 0$ ground band. The inter-band transitions can also be used to selectively prepare the atoms in specific Bloch bands. For example, in order to prepare atoms exclusively in the $n_z = 1$ band, a clock laser pulse is applied to the $|g\rangle_0 \rightarrow |e\rangle_1$ blue sideband transition. A strong “clearing” pulse is then applied to remove any remaining atoms in $|g\rangle$, leaving atoms in $|e\rangle$ unperturbed. The remaining atoms are thus purified in the $n_z = 1$ Bloch band, and can be used for further experiments or measurements.

Fig. 3.7 demonstrates the use of selective band preparation to probe the impact of SOC on the $|g\rangle_0 \rightarrow |e\rangle_0$ and $|e\rangle_1 \rightarrow |g\rangle_1$ carrier transitions. In Fig. 3.7a, the atoms are initially prepared in $|g\rangle_0$, and a π -pulse of the clock laser is applied. At $U_z/E_r = 63.2$ (narrow blue diamonds) the result is a typical Fourier-limited Rabi lineshape of the $|g\rangle_0 \rightarrow |e\rangle_0$ transition. However, as U_z is reduced (in the regime $U_z > E_r$), the transition begins to broaden and split into two peaks, with the

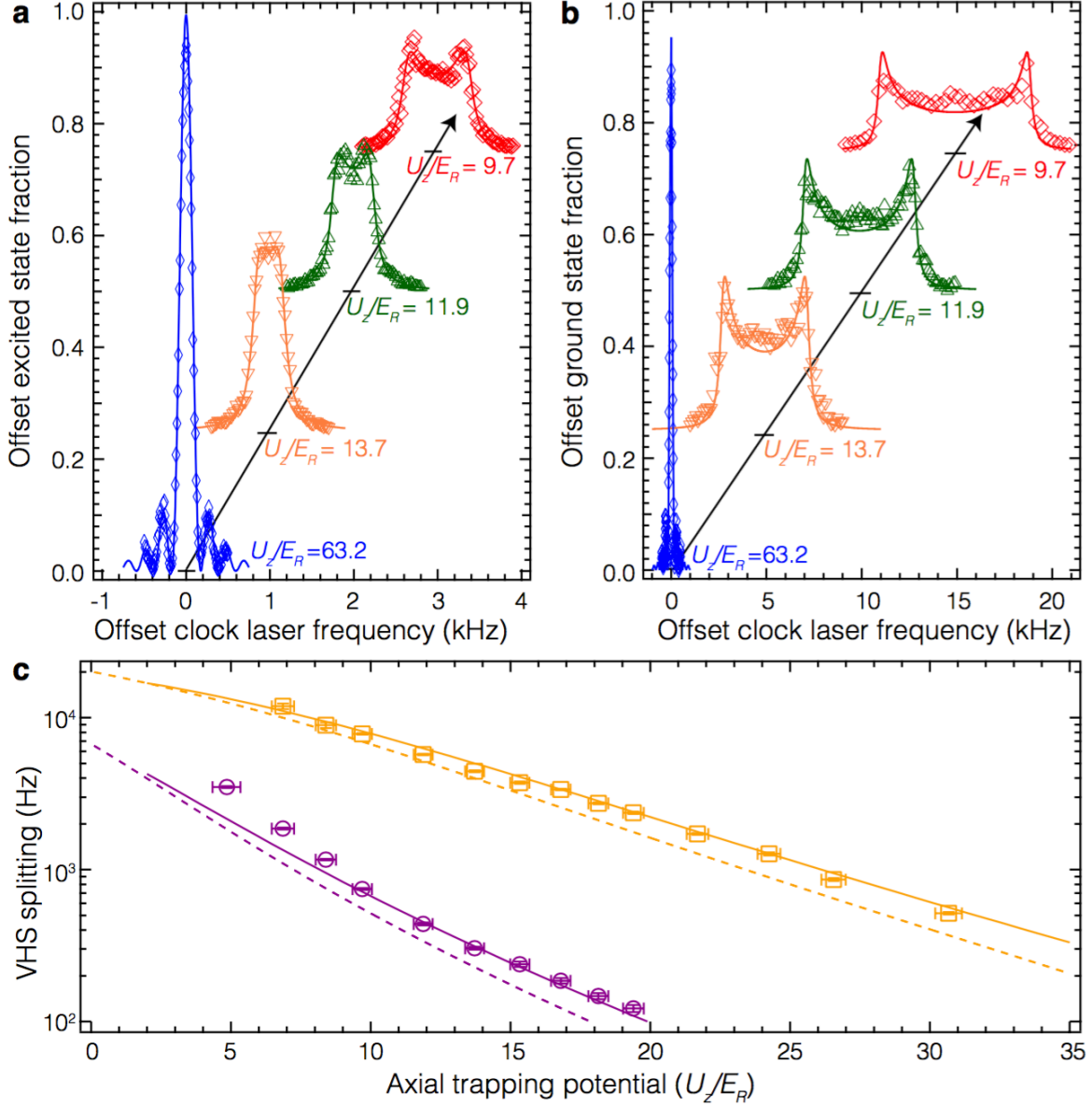


Figure 3.7: Van Hove singularities and band mapping. **a**, Excited state fraction following a π -pulse ($\Omega = 2\pi \times 100$ Hz) at four axial trapping potentials, with the atoms initially prepared in $|g\rangle_0$. The curves are offset in both x and y for clarity. The split peaks at $U_z/E_R \leq 13.7$ are a result of divergences in the atomic density of states known as Van Hove singularities (VHSs). **b**, Ground state fraction following a Rabi pulse for the same potentials shown in **a**, with the atoms initially prepared in $|e\rangle_1$. The duration of the Rabi pulse was varied to improve population contrast. **c**, The splitting between the VHS peaks in the $|g\rangle_0 \rightarrow |e\rangle_0$ (purple circles) and $|g\rangle_1 \rightarrow |e\rangle_1$ (orange squares) transition lineshapes as a function of trapping potential, extracted using fits as shown in **a** and **b**. Horizontal error bars are $1\text{-}\sigma$ standard error estimates from spectroscopy of the axial sidebands, vertical error bars are $1\text{-}\sigma$ standard error estimates for the extracted VHS splitting. The no-free parameter predicted VHS splittings for atoms in the ground and first excited bands of a 1D sinusoidal lattice (purple and orange dashed lines respectively,) and for a model including the transverse motional modes and finite atomic temperatures (purple and orange solid lines) are shown for comparison.

splitting scaling proportionally to the tunneling rate in the lowest Bloch band, which scales[29] as $J \approx (4/\hbar\sqrt{\pi})E_r(U_z/E_r)^{3/4} \exp[-2\sqrt{U_z/E_r}]$. As shown in Fig. 3.7b, the same behavior is observed when the atoms are initially prepared in the $|e\rangle_1$ state, with the $|e\rangle_1 \rightarrow |g\rangle_1$ transition exhibiting much larger splittings compared to the $|g\rangle_0 \rightarrow |e\rangle_0$ transition for the same axial potential.

The split lineshapes of the clock carrier transition at low U_z , which have been theoretically predicted[74, 84], can be understood by considering the band dispersion curves presented in Fig. 3.6b. Because the $|g\rangle_0$ and $|e\rangle_0$ bands are shifted with respect to each other in quasimomentum by ϕ , the transition frequency is q dependent. In the tight-binding approximation, the largest momentum-induced detuning from the bare clock transition frequency is given by $\Delta = 4J|\sin(\phi/2)|$, where $4J$ is the bandwidth of the $n_z = 0$ ground band, and $\sin(\phi/2) = 0.97 \approx 1$, resulting in an overall broadening of the transition by $2\Delta \approx 8J$. The probability of a transition between the two bands at a specific q is then determined by the joint transition density of states, which diverges at saddle points in the energy difference between the band dispersion curves. These divergence points in the density of states of a crystalline lattice are called Van Hove singularities (VHSs), and are well known from optical absorption spectra in solids and scanning tunneling microscopy[85, 86]. The measured lineshapes are a convolution of the atomic transition density of states with the Rabi lineshape for a single atom. In Fig. 3.7a and b, two VHS peaks are visible at $\delta = \pm\Delta$ when $\Delta > \Omega$, while at higher trapping potentials $\Delta \ll \Omega$ and the two VHS peaks merge into the standard Rabi lineshape.

Optical clock spectroscopy also provides a direct, *in situ* probe of the Bloch bandwidths, and thus of the tunneling rate J , through the VHS splitting. We demonstrate the power of this technique by measuring Rabi lineshapes at a range of axial potentials from $U_z/E_r = 5.5$ to $U_z/E_r = 63.2$, and fitting a convolution of the joint transition density of states for the SOC bands with the measured Rabi lineshape at high U_z/E_r to extract the VHS splitting (with example fits shown in Fig. 3.7a and b). The extracted splittings for the $|g\rangle_0 \rightarrow |e\rangle_0$ (purple circles) and $|e\rangle_1 \rightarrow |g\rangle_1$ (orange squares) transitions are plotted as a function of trapping potential in Fig. 3.7c. Only splittings for which the two peaks were resolvable are shown. At $U_z/E_r = 5.5$ the VHS splitting of the $|e\rangle_1 \rightarrow |g\rangle_1$

transition overlapped with the inter-band transitions and the splitting could not be unambiguously extracted. The no-free parameter VHS splitting anticipated for atoms in a 1D lattice (purple and orange dashed lines respectively for $n_z = 0$ and $n_z = 1$), as well as the splitting predicted by the perturbative model (solid lines), are shown for comparison. The origin of the slight difference between the experimental data and the model prediction in the ground band at lower trapping potentials may be related to inhomogeneities in the axial trapping potential across the populated lattice sites, or an incomplete theory description of the transverse/longitudinal coupling.

Just as the spectroscopically resolved sidebands enabled band preparation, the quasimomentum dependence of the clock transition frequency enables the selective preparation and subsequent manipulation of atoms with particular quasimomenta (Fig. 3.8). Following initialization in the $|g\rangle_0$ state, a clock pulse with Rabi frequency $\Omega < 2\Delta$ is applied to the carrier transition with a detuning $|\delta^*| \leq \Delta$. Only atoms with quasimomenta in a window centered around $q^* \approx \arccos(\delta^*/\Delta)$ with a width bounded by $2\pi\Omega/\Delta$ will be excited to $|e\rangle_0$, while atoms with quasimomenta outside this window will be left in $|g\rangle$. A strong “clearing” pulse is applied to remove atoms in $|g\rangle$, leaving only the atoms in $|e\rangle_0$ with quasimomenta in the window centered around q^* . Following a variable wait time t , a second π -pulse is used to measure the lineshape. If the lattice is tilted with respect to gravity, during the wait time the atoms will undergo Bloch oscillations[87], with their quasimomenta evolving as $q(t) = q_o + \nu_B t$, where q_o is the initial quasimomentum of the atom, and the value of $q(t)$ is restricted to the first Brillouin zone. The Bloch oscillation frequency ν_B is given by $\nu_B = (mg\lambda_L \sin(\theta_L))/(4\pi\hbar)$, where g is the acceleration due to gravity, and θ_L is the angle of tilt of the lattice. In this *in situ* observation of Bloch oscillations in a tilted lattice[88], the highly asymmetric lineshapes oscillate back and forth as the quasimomenta cycles through the Brillouin zone at a frequency of $\nu_B = 14$ Hz, corresponding to a lattice tilt of $\theta_L = 16$ milliradians.

We characterize the q dependence of the chiral Bloch vector angle θ_B (Eq. 3.32) using the same quasimomentum selection technique used to observe Bloch oscillations. For these measurements the lattice tilt was adjusted to minimize $\nu_B \leq 3$ Hz, with $\theta_L \leq 3.5$ milliradians. As shown in Fig. 3.9a, atoms are prepared in $|e\rangle_0$ with quasimomenta q^* . In five separate experiments q^*

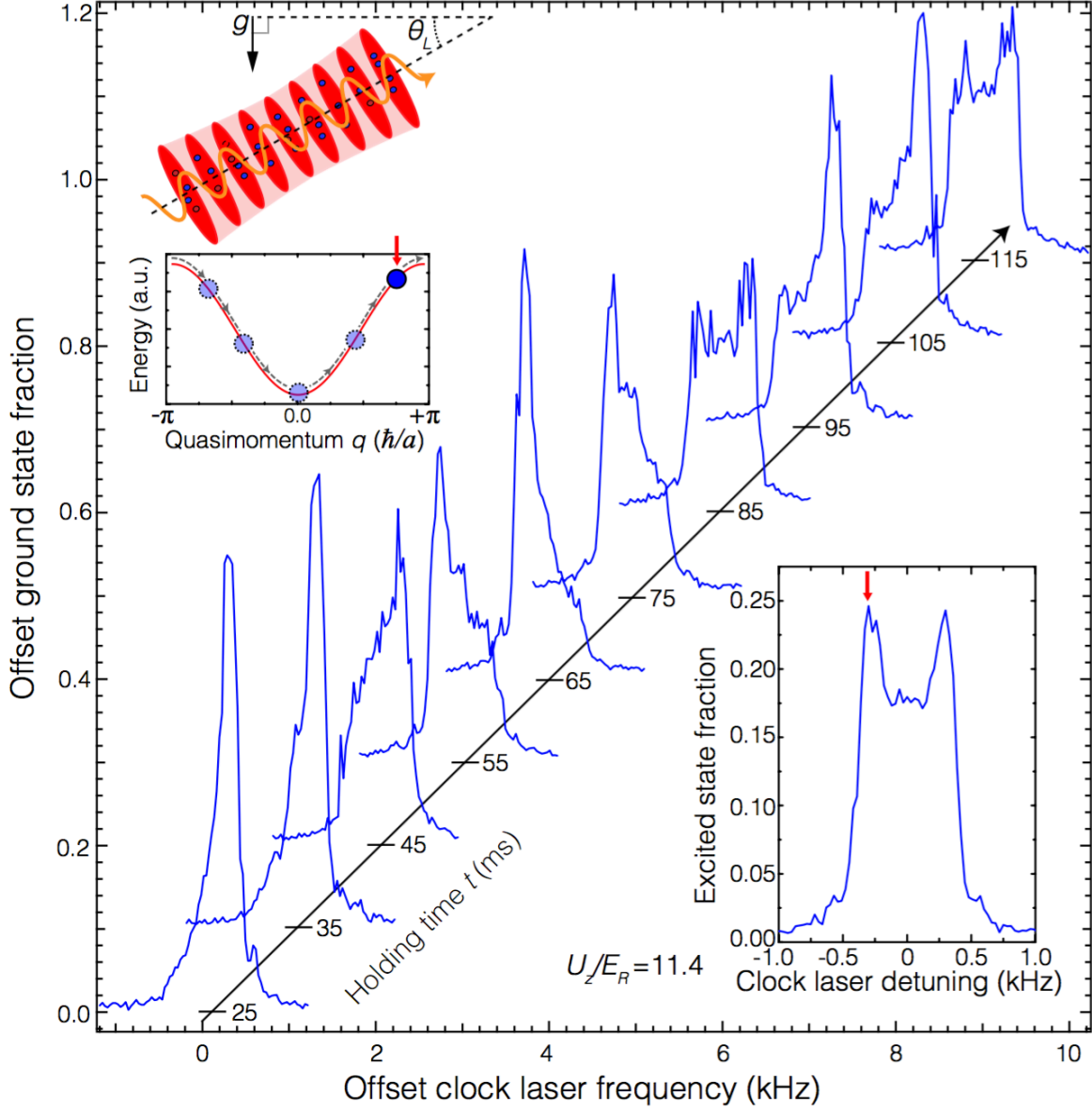


Figure 3.8: Bloch oscillations. (Lower right inset,) The split Rabi lines shown in Fig. 2a,b enable the spectral selection of atoms with a particular quasimomentum q^* . A π -pulse ($\Omega = 2\pi \times 100$ Hz) tuned to the left Van Hove peak is applied (red arrow) and the remaining ground state atoms are removed. (Upper left inset,) In a lattice tilted with respect to gravity, the atoms initially prepared with corresponding $q^* \approx \pi$ (red arrow) undergo Bloch oscillations. (Main figure,) Following a variable wait time t from the end of the first π -pulse, a second π -pulse is applied, revealing a highly asymmetric lineshape (first blue curve at 25 ms). The atoms undergo Bloch oscillations, resulting in periodic oscillations of the lineshape as the waiting time between the first and second pulse is varied. The curves are offset in both x and y for clarity.

is varied using a range of detunings δ^* spanning the two VHS peaks (colored arrows). A strong Rabi pulse of duration τ is applied with detuning δ corresponding to the right VHS peak (red star), generating SOC with the corresponding q^* -dependent chiral Bloch vector (pointing along the direction of the effective magnetic field $\vec{B}_{n_z}(\Omega, q, \delta)$) shown in Fig. 3.9b, and with the SOC band structure shown in Fig. 3.9c. In Fig. 3.9d, the resulting population fraction in $|e\rangle$ for each prepared q^* (with corresponding color coding) is plotted as a function of the evolution time τ . The dynamics are entirely captured by the q^* -dependent spin precessions about the chiral Bloch vectors depicted in Fig. 3.9b. The theoretical calculations involve no free parameters and use only the experimental values of δ^* , δ , ν_B , and Ω (colored solid lines in Fig. 3.9c). The dephasing of the spin precession at longer τ is well described by the known initial distribution of quasimomenta q^* , and could be mitigated by reducing the Rabi frequency used for the q^* selection with respect to the VHS splitting 2Δ , at the cost of reduced signal to noise ratio due to the smaller number of atoms selected. In the inset of Fig. 3.9d we plot the corresponding extracted chiral Bloch vector angle $|\theta_B|$ for each initial pulse detuning as a function of prepared quasimomenta q^* . Because there exists a one-to-one correspondence between the topological chiral edge modes of the two-dimensional Hofstadter model[77, 78] and the energy bands and eigenstates of the synthetic ladder[67, 76] shown in Fig. 3.6a, the q^* dependence of $|\theta_B|$ that we measure spectroscopically is a direct manifestation of the well-defined chirality of the edge states of the Hofstadter Hamiltonian. The presence of spin-momentum locking in the ladder eigenmodes has been previously observed using TOF[34, 36, 37, 66, 75, 76, 80].

3.8.1 Measurement protocol

To load the optical lattice, ^{87}Sr atoms are cooled with two sequential 3D magneto-optical-traps (MOTs), the first using the strong $^1\text{S}_0 \rightarrow ^1\text{P}_1$ transition (461 nm), and the second using the narrower $^1\text{S}_0 \rightarrow ^3\text{P}_1$ transition (689 nm). Following the second MOT, the atoms are sufficiently cold and dense to be trapped in the optical lattice. Once in the lattice, the atoms are first nuclear spin-polarized, and then further cooled using axial sideband and radial doppler cooling on the 689

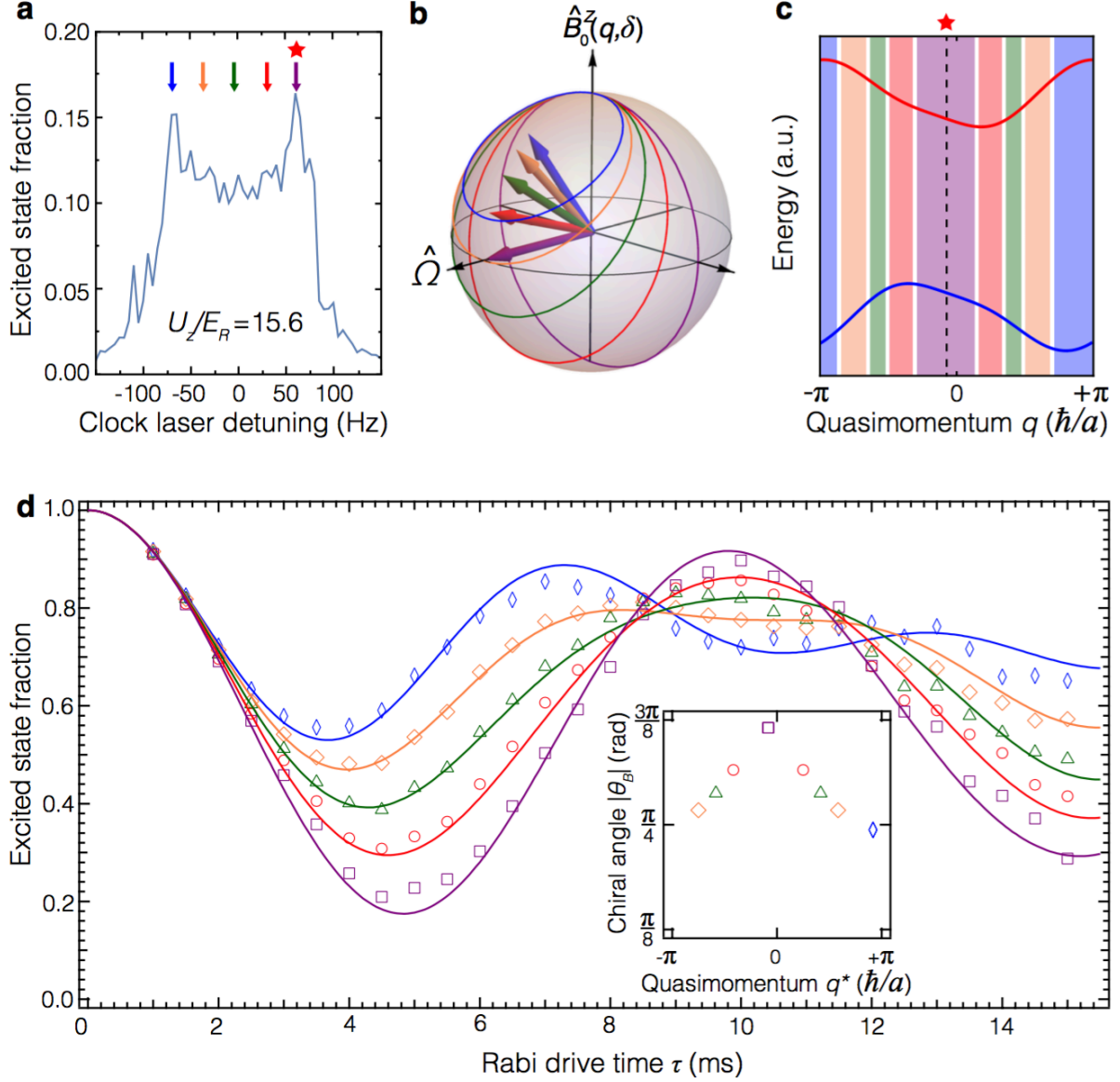


Figure 3.9: Rabi measurements of the chiral Bloch vector. **a**, Atoms are selectively prepared in a quasimomenta window using a π -pulse ($\Omega = 2\pi \times 10$ Hz,) with five different pulse detunings (colored arrows). An axial potential of $U_z/E_R = 15.6$ is used, resulting in $\Delta/(2\pi) \approx 67$ Hz. A second stronger Rabi pulse ($\Omega = 2\pi \times 100$ Hz) tuned to the right Van Hove peak is used to generate SOC (red star). **b**, The chiral Bloch vectors corresponding to the detunings in **a** are shown, along with the clock state spin precession for each vector. **c**, The SOC band structure experienced by the atoms during the second pulse, with each quasimomenta window color coded to match the detunings in **a**. The selection windows overlap, with the width of each window only intended to illustrate their relative values. **d**, Excited state fraction as a function of duration of the second pulse for the five initial pulse detunings shown in **a** (data points), along with the no-free parameters dynamics predicted by a semi-classical model (colored solid lines). (**Inset,**) Corresponding extracted chiral Bloch vector angle for each quasimomenta window centered at q^* .

nm transition.

At the end of each experiment the population of the $|g\rangle$ state is measured by driving the atoms on the 461 nm cycling transition and counting the emitted photons. After 5 ms all $|g\rangle$ atoms have been heated out of the lattice, at which point the atoms in $|e\rangle$ are optically pumped into the $|g\rangle$ state and are counted in the same manner. A 5 ms long 461 nm pulse is also used as the “clearing” pulse to remove ground state atoms in the protocols used for preparing atoms in specific bands and with select quasimomenta.

3.8.2 Characterization of the trapping potential

The cylindrically symmetric trapping potential experienced by an atom at position z along the axis of propagation of the lattice beams and a distance r from the center of the beams is given by

$$V(r, z) = - (V_{\text{const}} + U_z \cos^2(k_L z)) e^{-2r^2/w_0^2}, \quad (3.33)$$

where $V_{\text{const}} = \alpha(\lambda_L) (P_1 + P_2 - 2\sqrt{P_1 P_2}) / (\pi \epsilon_0 c w_0^2)$, $U_z = 4\alpha(\lambda_L) \sqrt{P_1 P_2} / (\pi \epsilon_0 c w_0^2)$, $k_L = 2\pi/\lambda_L$, ϵ_0 is the permittivity of free space, c the speed of light, and $\alpha(\lambda_L)$ is the AC polarizability evaluated at λ_L . Because $P_1 \gg P_2$, to first order the trapping potential in the radial direction is proportional to $V_{\text{const}} \propto P_1$, while the periodic axial trapping potential $U_z \propto \sqrt{P_1 P_2}$. In contrast to prior experiments that generate synthetic gauge fields by periodically shaking the optical lattice potential[89–91], here the lattice potential is kept constant, and it is the probing laser itself that induces the SOC.

3.8.3 Band preparation

In Fig. 3.10, we demonstrate how the inter-band transitions can be used for band preparation. Fig. 3.10a shows spectroscopy of the carrier and inter-band transitions from the initial $|g\rangle_0$ state. In order to prepare atoms exclusively in the $n_z = 1$ band, a clock laser pulse is applied to the $|g\rangle_0 \rightarrow |e\rangle_1$ blue sideband transition, which is at a detuning $\delta/2\pi \approx \nu_z - E_r/2\pi\hbar = 35$ kHz for

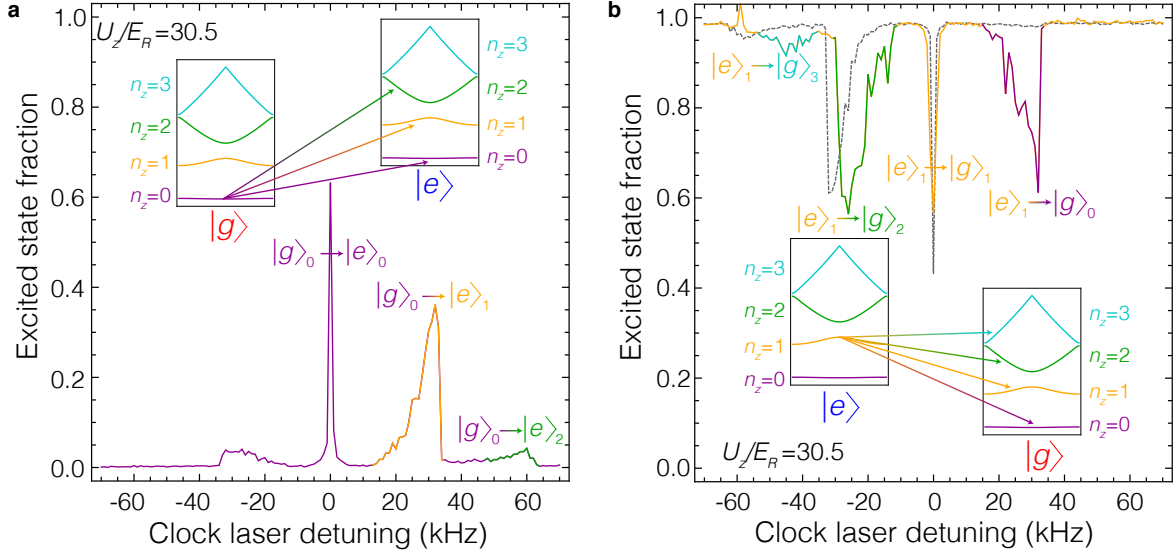


Figure 3.10: Band preparation. (a) Spectroscopy of the carrier and inter-band transitions from the initial $|g\rangle_0$ state. In order to prepare atoms exclusively in the $n_z = 1$ band, a clock laser pulse is applied to the $|g\rangle_0 \rightarrow |e\rangle_1$ blue sideband transition, which is at a detuning $\delta/2\pi \approx \nu_z - E_r/2\pi\hbar = 35$ kHz for $U_z/E_R = 30.5$. A strong “clearing” pulse is then applied to remove any remaining atoms in $|g\rangle$, leaving atoms in $|e\rangle$ unperturbed. The remaining atoms are thus purified in the $n_z = 1$ Bloch band, and can be used for further experiments or measurements. (b) Spectroscopy of the sidebands following this protocol, with the anharmonicity of the band spacing resulting in an unequal frequency spacing between the $|e\rangle_1 \rightarrow |g\rangle_2$ and $|e\rangle_1 \rightarrow |g\rangle_0$ sideband transitions about the $|e\rangle_1 \rightarrow |g\rangle_1$ carrier transition.

$U_z/E_r = 30.5$. A strong “clearing” pulse is then applied to remove any remaining atoms in $|g\rangle$, leaving atoms in $|e\rangle$ unperturbed. The remaining atoms are thus purified in the $n_z = 1$ Bloch band, and can be used for further experiments or measurements. Fig. 3.10b shows spectroscopy of the sidebands following this protocol, with the anharmonicity of the band spacing resulting in an unequal frequency spacing between the $|e\rangle_1 \rightarrow |g\rangle_2$ and $|e\rangle_1 \rightarrow |g\rangle_0$ sideband transitions about the $|e\rangle_1 \rightarrow |g\rangle_1$ carrier transition. The transitions out of $|e\rangle_0$ from Fig. 1d in the main text are shown for comparison. In contrast to prior experiments[92, 93] no band relaxation has been observed out of the $|e\rangle_1$ state over a waiting time greater than 500 ms, due to the dilute atomic conditions achieved in the current experiment.

3.8.4 Measurements of axial heating and loss rates

The axial heating rate in our lattice was measured using spectroscopy of the axial motional sidebands. The atoms were prepared in $|e\rangle_0$, and the clock laser was applied on resonance with the carrier transition for a variable wait time of up to 155 ms. The atoms in $|g\rangle$ were removed with a clearing pulse, and spectroscopy of the remaining atoms in $|e\rangle$ was performed. The axial sideband asymmetry was then used to determine the temperature and heating rate. The measurement was performed in both the strong confinement ($U_z/E_r \approx 200$) and tunneling allowed ($U_z/E_r \approx 10$) regimes. In both cases, the results were consistent with no axial heating over the 155 ms wait time. This is consistent with previous measurements of the temperature dependence of the clock transition coherence²⁰.

The loss rates out of $|e\rangle$ were measured by preparing the atoms in $|e\rangle_0$, leaving the atoms in the dark for a variable wait time of up to 1.5 s, and then counting the number of atoms in the $|e\rangle$ and $|g\rangle$ states. Loss of atoms due to inelastic p-wave $e - e$ scattering was observed with a density dependent loss rate consistent with previous measurements[52]. For the atomic densities used in this work, the measured loss rate corresponded to $\sim 1.5 \text{ s}^{-1}$, and thus did not have an impact on the measurements presented here due to their shorter timescales. For future many-body experiments with higher desired densities, the temperature can be lowered by loading the lattice from a Fermi-

degenerate gas²⁶, and the inelastic p-wave $e - e$ collisions will be significantly suppressed. An additional one body loss rate of $\sim 0.2 \text{ s}^{-1}$ was observed, consistent with the vacuum limited lifetime in the chamber. Finally, a $|e\rangle \rightarrow |g\rangle$ spin flip rate of $\sim 0.1 \text{ s}^{-1}$ was observed, consistent with previously measured two-photon Raman scattering from the lattice light via the 3P_1 state[94]. While this spin-flip rate is entirely negligible for the measurements presented here, it may set a limit on future SOC experiments, potentially requiring a different lattice geometry.

3.8.5 Perturbative model

For the current experimental temperatures and loading conditions, to an excellent approximation, we can treat the coupling between the axial and radial degrees of freedom perturbatively and expand Eq. (3.33) up to second order in r :

$$V(r, z) = V_z(z) + V_r(r) + \eta V_{\text{coupl}}(r, z) + \mathcal{O}(r^4) \quad (3.34)$$

with $V_z(z) = -U_z \cos^2(k_L z)$, $V_r(r) = m\omega_r^2 r^2/2$, and $V_{\text{coupl}}(r, z) = -V_r(r) \sin^2(k_L z)$. Here, $\omega_r = 2\sqrt{\frac{U_z + V_{\text{const}}}{mw_0^2}}$, m is the atom mass, and $\eta = \frac{U_z}{U_z + V_{\text{const}}}$ is an expansion parameter. To zeroth order in η the Hamiltonian is separable in the r and z coordinates. In this limit the radial eigenfunctions are harmonic oscillator functions, $\langle \mathbf{r} | n_r, v \rangle = \phi_{n_r, v}(\mathbf{r})$ with eigenenergies $E_{n_r, v} = \hbar\omega_r(|v| + 2n_r + 1)$ parameterized by the radial quantum number $n_r = 0, 1, \dots$, and the azimuthal quantum number $-n_r \leq v \leq n_r$. The axial eigenfunctions are Bloch functions, $\langle z | n_z, q \rangle = \psi_{n_z, q}(z)$ with a band structure $E_{n_z}(q)$. For the cosinusoidal potential in consideration the latter can be obtained analytically in terms of the even and odd Mathieu functions, $\psi_{n_z, q} = \text{MathieuC}[a(q, U_z/(4E_r)), U_z/(4E_r), z] + i\text{MathieuS}[a(q, U_z/(4E_r)), U_z/(4E_r), z]$ and $E_{n_z}(q)/E_r = a(q, U_z/(4E_r))$, where the parameter a is the characteristic Mathieu value and for suitably chosen n_z -dependent ranges of q .

Treating $V_{\text{coupl}}(r, z)$ using first order perturbation theory in η yields the energies:

$$E_{n_z, n_r, v}(q) = E_{n_r, v} + E_{n_z}(q) - \frac{1}{2}\eta E_{n_r, v} \langle n_z, q | \sin^2(k_L z) | n_z, q \rangle. \quad (3.35)$$

This expression generalizes the one obtained by Blatt **et al.**²⁰ in the deep lattice limit to include quasimomentum dependence of the energies and beyond-lowest-order anharmonic effects in the axial dimension. We note that one can also analytically compute the first order corrections in terms of the unperturbed band energies using the Feynman-Hellman theorem, $\langle n_z, q | \sin^2(k_L z) | n_z, q \rangle = \left(\frac{1}{2} + \frac{\partial E_{n_z}(q)}{\partial U_z} \right)$. This term has both q -independent and q -dependent components. The former lead to thermally-dependent shifts of the mean band energies, and the latter gives a renormalization of the tunneling rate which depends on the radial temperature. We have explicitly checked the validity of the perturbative energy expression by numerically finding the exact eigenstates of Eq. (3.33) [65].

3.8.5.1 Lineshape evaluation

To evaluate the lineshapes we perform a thermal average using Boltzmann distributions with radial and axial temperatures T_r and T_z , respectively. The contribution to the lineshape from the ℓ^{th} axial sideband, assuming atoms are initially populating the ℓ_0 band and internal state $\alpha = \pm$ (here $+$ is for g and $-$ is for e), is:

$$P_\ell^\pm = \sum_{n_z, n_r, v, q} \frac{q_z(\ell_0, n_z, q) q_r(\ell_0, n_r, v)}{Z_r(\ell_0) Z_z(\ell_0)} \left| \frac{\Omega_{n_z, \ell, q}}{\Omega_{n_z, \ell, q, n_r, v}^{\pm \text{eff}}} \right|^2 \sin^2 \left[\frac{t}{2} \Omega_{n_z, \ell, q, n_r, v}^{\pm \text{eff}} \right] \quad (3.36)$$

where $\Omega_{n_z, \ell, q, n_r, v}^{\pm \text{eff}} \equiv \sqrt{|\Omega_{n_z, \ell, q}|^2 + (\pm \delta - (E_{n_z + \ell, n_r, v}(q + \phi) - E_{n_z, n_r, v}(q))/\hbar)^2}$ is the effective Rabi frequency, $\Omega_{n_z, \ell, q} \approx \Omega \langle n_z + \ell, q + \phi | e^{i2\pi z/\lambda_c} | n_z, q \rangle$ the Rabi frequencies and Ω the “bare” Rabi frequency. Note that in the regime where the tight binding approximation is valid (i.e. not very shallow lattices) $\Omega_{n_z, \ell, q}$ is a slowly varying function of q . On the other hand, it has a strong dependence on ℓ and for $|\ell| > 0$ it is suppressed by the Lamb-Dicke parameter $\eta_{LD} = k_L \sqrt{\frac{\hbar}{2\omega_z m}}$, resulting in an effective Rabi frequency for the first sidebands, $\ell = \pm 1$, that is approximately an order of magnitude below that of the carrier.

We have also introduced the Boltzmann factors $q_z(\ell_0, n_z, q) \equiv \exp[-\beta_z (E_{n_z + \ell_0, 0, 0}(q) - E_{\ell_0, 0, 0}(0))]$ and $q_r(\ell_0, n_r, v) \equiv \exp[-\beta_r \sum_{q'} (E_{n_z + \ell_0, n_r, v}(q') - E_{n_z + \ell_0, 0, 0}(q'))/L]$ with $\beta_{z,r} = 1/k_B T_{z,r}$ and L the total number of lattice sites. $Z_r(\ell_0) = \sum_{n_z, q} q_z(\ell_0, n_z, q)$ and $Z_r(\ell_0) = \sum_{n_r, v} q_r(\ell_0, n_r, v)$ are the radial and axial partition functions.

There are three leading mechanisms that lead to broadening of the lineshape. One arises from the thermal population of different quasimomentum states combined with the finite momentum transfer by the probe laser when interrogating the clock states. This type of motion-induced broadening, which is a direct signature of the spin-orbit coupling mechanism, is the lattice analogue of Doppler broadening²¹, generally discussed in the spectra of free particles. For the lattice case, instead of plane waves carrying specific momentum, one needs to think about Bloch waves described by two quantum numbers, the quasi-momentum and band index. The second broadening mechanism is power broadening arising for strong Rabi pulses. For our spectroscopic parameters only the carrier transition is affected by it. The last source of broadening is the coupling between the radial and axial degrees of freedom, and thus is strongly determined by the trapping frequencies and radial temperature. At short probing times (less than π pulses), this type of broadening in the carrier transition can be characterized by using a temperature dependent tunneling rate as we will explain below. For the sidebands, axial-radial coupling is the leading broadening mechanism²⁰ and it has been shown that it is well captured by the perturbative approach.

However, the first-order perturbative approach neglects the radial dependence of the Rabi frequencies and radial sideband transitions induced by the laser. As discussed in detail in Ref. [20], the omitted higher order terms can lead to a dephasing of the coherent oscillations in P_ℓ^\pm at times long compared to a π -pulse and induce additional broadening of the sideband spectra. Nevertheless, those effects can be accounted for by using an effective radial temperature, which we used as an effective fitting parameter, and by performing for the case of long probe times a time-average of Eq. (3.36), which yields

$$\bar{P}_\ell^\pm = \frac{1}{2} \sum_{n_z, n_r, v, q} \frac{q_z(\ell_0, n_z, q) q_r(\ell_0, n_r, v)}{Z_r(\ell_0) Z_z(\ell_0)} \left| \frac{\Omega_{n_z, \ell, q}}{\Omega_{n_z, \ell, q, n_r, v}^{\pm \text{eff}}} \right|^2. \quad (3.37)$$

The clock spectroscopy shown in Fig. 1c was taken by applying the clock laser at high power ($\Omega = 2\pi \times 200$ Hz) and for many Rabi periods (during 80 ms) and thus we used Eq. 3.37 to model the experiment and treated the radial temperature as a fitting parameter. The radial temperatures that provided the best fit varied between $7 - 9$ μK and thus were higher than the experimentally

measured radial temperatures through motional spectroscopy of the sidebands, consistent with previous detailed studies of the sideband lineshapes²⁰.

For the carrier transition the dominant decoherence mechanism arising from radial sideband transitions manifests at long probing times as dephasing. The perturbative model, Eq. 3.36 with $l = 0$, does an excellent job for pulses shorter than a π pulse. However, for the longer pulse employed (panel e), the perturbative theory captures only the width of the lineshape and not its amplitude.

3.8.5.2 Theoretical fit function to extract the VHS splittings

The coupling between the radial and axial degrees of freedom can be accounted for in the carrier lineshape by defining an effective thermally averaged tunneling rate. In the regime where the tight binding approximation is valid, $\langle \Delta E_{n_z, n_r, v}(q) \rangle \equiv \langle E_{n_z, n_r, v}(q + \phi) - E_{n_z, n_r, v}(q) \rangle \approx -2\hbar J_{n_z}^{T_r} (\cos(q + \phi) - \cos(q))$, where $\langle \bullet \rangle$ denotes radial thermal averaging, and n_r and v the radial and azimuthal harmonic oscillator mode numbers. Thus one can replace the effective Rabi coupling $\Omega_{n_z, \ell, q, v}^{\pm \text{eff}}$ for the carrier ($\ell = 0$),

$$\Omega_{n_z, 0, q, n_r, v}^{\pm \text{eff}} \rightarrow \Omega_{n_z}^{\pm \text{eff}}(q) = \sqrt{\Omega_{n_z, 0, q}^2 + \left(\pm \delta + 4J_{n_z}^{T_r} \sin(\phi/2) \sin(\phi/2 + q) \right)^2}, \quad (3.38)$$

where $J_{n_z}^{T_r}$ is the thermally averaged tunneling rate, and $\Omega_{n_z, \ell, q}$ is the Rabi coupling for the ℓ^{th} axial sideband. Even when the tight-binding approximation no longer holds, we can reproduce the VHS splittings by matching the thermally averaged bandwidth, computed from the analytic expression for the perturbative energies given above, to the tight-binding expression, $\max_q \langle \Delta E_{n_z, n_r, v}(q) \rangle - \min_q \langle \Delta E_{n_z, n_r, v}(q) \rangle = 8\hbar J_{n_z}^{T_r} \sin(\phi/2)$. This expression, together with the approximation that all atoms are initially in the $\ell_0 = 0, 1$ band and that $\hbar J_{\ell_0}^{T_r} \ll k_B T_z$, is used to fit the carrier lineshapes shown in Fig. 2 by convolving the resulting Rabi lineshape with the joint transition density of states $\mathcal{D}_{\ell_0, T_r}$:

$$\bar{P}_0^{\pm} \approx \frac{1}{4\pi} \int_{-\pi}^{\pi} dq \left| \frac{\Omega_{\ell_0, 0, 0}}{\Omega_{\ell_0}^{\pm \text{eff}}(q)} \right|^2 = \frac{1}{2} \int_{-|4J_{\ell_0}^{T_r} \sin(\phi/2)|}^{|4J_{\ell_0}^{T_r} \sin(\phi/2)|} d\epsilon \mathcal{D}_{\ell_0, T_r}(\epsilon) \frac{\Omega_{\ell_0, 0, 0}^2}{\Omega_{\ell_0, 0, 0}^2 + (\pm \delta - \epsilon)^2} \quad (3.39)$$

where

$$\mathcal{D}_{\ell_0, T_r}(\epsilon) = \begin{cases} \frac{1}{\sqrt{(4J_{\ell_0}^{T_r} \sin(\phi/2))^2 - \epsilon^2}} & -|4J_{\ell_0}^{T_r} \sin(\phi/2)| \leq \epsilon \leq |4J_{\ell_0}^{T_r} \sin(\phi/2)| \\ 0 & \text{otherwise} \end{cases}. \quad (3.40)$$

When fitting this function to the split line data of the type shown in Fig. 2a,b to extract the VHS splitting plotted in Fig. 2c, the only free parameters used are a single parameter for the thermally averaged tunnel coupling J , and an additional parameter for the amplitude of the split line. The amplitude is only required as a free parameter when a pulse longer than a single π -pulse is used to increase the excitation fraction. The no free-parameters theory predictions plotted in Fig. 2c were generated by applying the perturbative model to measured spectra of the motional sidebands at each axial trapping potential. As mentioned above, the radial temperatures used for the perturbative model varied between $7 - 9 \mu\text{K}$.

3.8.5.3 Chiral Bloch vector dynamics

To model the chiral Bloch vector dynamics, the Rabi oscillations measured after preparing the atoms within a window of quasimomenta centered around q^* and width Δq are expressed as,

$$\bar{P}_0^+(q^*) = \frac{1}{\Delta q} \sum_{q \in \Delta q} \left| \frac{\Omega_{0,0,0}}{\Omega_0^{\text{eff}}(q^* + \Delta q)} \right|^2 \sin^2 \left[\frac{t}{2} \Omega_0^{\text{eff}}(q^* + \Delta q) \right]. \quad (3.41)$$

To model the window, we simulate the atom preparation using a π -pulse ($\Omega = 2\pi \times 10 \text{ Hz}$) with five different initial pulse detunings δ^* . Because the Rabi frequency and tunneling rates are comparable, the window is relatively broad, and this results in dephasing of the quasimomenta-dependent Rabi oscillations shown in Fig. 4d when a second, stronger Rabi pulse is applied. For the theory lines presented in Fig. 4, we set $\Delta = (4J_{\ell_0}^{T_r} \sin(\phi/2)) = 2\pi \times 67 \text{ s}^{-1}$ and $\Delta q \sim L/2$.

3.9 Summary

We have described approaches to implement and probe SOC and its interplay with s - and p - wave interactions in OLCs. These open the unique opportunity of exploring, for the first time,

a controllable interplay of interactions, spin-orbit coupling, and non-trivial topology in regimes where a complete theoretical treatment can also be performed. While the described protocols work at the temperatures achievable in current OLCs, their sensitivity and applicability are expected to significantly improve when operating the clock in the quantum degenerate regime. Moreover, if nuclear spins are included, they can open a window for the investigation of SOC with $SU(N)$ -symmetric collisions [95].

We described the recent experimental implementation and characterized SOC and a synthetic momentum-dependent magnetic field with fermions in an OLC. The experiment observed clean experimental signatures of SOC physics at μK temperatures without cooling to Fermi degeneracy, and observed no decoherence or heating at timescales of hundreds of milliseconds. The recent realization of a Fermi-degenerate 3D OLC[96] opens a window to the implementation of two and three-dimensional SOC, tuning of the SOC phase ϕ , and the lower temperatures required for the preparation of novel many-body states[37, 75, 97]. While this experiment focused entirely on single particle physics, many-body correlations and $SU(N)$ symmetry have been previously observed in Refs. [48, 50], offering exciting prospects for studying the interplay between SOC and interactions in higher synthetic dimensions

Chapter 4

Single Particle Spin Dynamics in a Magnetic Field Gradient

4.1 Introduction

Understanding spin transport in quantum systems is central to many fields of physics and can have important applications for the development of quantum technologies. Recently there has been much experimental progress studying spin diffusion [9–11, 17, 98–102] and spin segregation dynamics (time-dependent separation of the spatial distributions of the spin components) [13–15, 103–106] in trapped atomic gases. A typical experimental protocol consists of preparing a transversely spin-polarized gas and then observing the spin relaxation dynamics under the influence of a magnetic field gradient. For instance, Ref. [10] measured the demagnetization timescale in a constant magnetic field gradient and determined the spin diffusion constant. Similarly, Ref. [14] measured the segregation of the spin populations in a magnetic field gradient with linear spatial dependence. Although the goal of the experiments is to understand the many-body interacting spin dynamics, it is important to have a clear understanding of the non-interacting physics and how the spin-motion coupling alone affects the spin demagnetization. A thorough analysis of the non-interacting system will help provide the foundation necessary for understanding the complex spin dynamics induced by the interplay between interactions and motional effects.

In this chapter we provide analytic expressions for the demagnetization exhibited by a harmonically trapped and non-interacting spin-1/2 Fermi gas at both zero and finite temperatures. We study the spin dynamics with and without a spin-echo pulse and in the presence of magnetic field gradients with constant or linear spatial dependence. The spin dynamics is oscillatory, and

depends on details of the differential motion of the spin components. In the case of a constant gradient (magnetic field that varies linearly with position), the atoms oscillate at the trap frequency but in opposite directions along the gradient depending on their spin projection. We show that this periodic motion gives rise to a fast demagnetization but not to a net spin rotation. In the case of a linear gradient (magnetic field that varies quadratically with position), the spin components breathe at different rates and with different magnitudes, the dynamics is not periodic with the trap frequency, and the spin dynamics involves both a demagnetization and a net rotation of the collective spin. Since the harmonic oscillator Hamiltonian is symmetrical with respect to exchange of \hat{x} and \hat{p} in oscillator units, these magnetic field gradients can also be interpreted as a one-dimensional spin-orbit coupling $\propto \hat{\sigma}^Z \hat{p}$ [107, 108]; the results presented in this chapter also hold for quenches of such a spin-orbit coupling term.

In the non-interacting limit our analysis reveals that the transverse magnetization decays with a rate that grows with increasing particle number and temperature. The observed fast demagnetization rate at short times reflects the fact that samples with a large number of fermions occupy high harmonic oscillator modes that are widely spread across the trap and experience strong gradients. We also find that the spin-motion coupling cannot be removed by a spin-echo pulse, and such a pulse can instead lead to an enhanced decay rate of the magnetization of the gas. In unitary Fermi gas experiments this fast motion-induced demagnetization is suppressed at short times by interactions which instead lead to a diffusive decay of the magnetization.

This chapter is organized as follows: In Sec. 4.2 we present and discuss the spectroscopic protocol under consideration. In Sec. 4.3 and Sec. 4.4 we present the constant and linear gradient cases, respectively. In each of these sections we derive analytic expressions for the single particle dynamics and then formulate the spin dynamics of the many-particle system at finite temperature in terms of these expressions. We derive expressions for the dynamics both in the presence and absence of a spin-echo pulse and discuss experimental considerations. In Sec.4.5 we discuss how to implement these results in three dimensions and use them to model experimental data from the University of Toronto Ultracold Atoms group. Finally, in Sec.4.6, we finish with an outlook and

conclusions.

4.2 Spectroscopic Protocol

We begin by considering a single spin-1/2 particle of mass m confined in a one-dimensional harmonic trap with trapping frequency ω – results for ensembles of atoms are later calculated from sums over single particle dynamics. The spin dynamics is probed using Ramsey spectroscopy: at $t = 0$ the particle is prepared in an eigenstate of the harmonic trap and with spin $|\downarrow\rangle$. The spin of the particle is then rotated toward the X -axis by applying a resonant pulse with area θ_1 . Next, a position-dependent magnetic field $B_Z(x)$ pointing along Z is suddenly turned on, and the particle then evolves freely in the presence of the magnetic field for a dark time t , after which spin observables are measured.

Here, we focus on the case of Ramsey spectroscopy with an initial pulse area $\theta_1 = \pi/2$ that rotates the initial state to point along X (transverse direction). We also assume that the pulse has zero detuning from the atomic transition ($\delta = 0$). However, the results that follow are easily generalized to arbitrary θ_1 and finite detuning.

During the dark time the particle feels a potential

$$\begin{aligned}\hat{V}(\mathbf{x}) &= \hat{V}(x) + \hat{V}(y, z) \\ \hat{V}(x) &= \frac{1}{2}m\omega^2 x^2 + \Delta\mu B_Z(x)\hat{\sigma}^Z,\end{aligned}\tag{4.1}$$

where $\Delta\mu$ is the differential magnetic moment between the two spin states and $\hat{\sigma}^Z$ is the usual Pauli operator. Along the y and z directions the potential is assumed to be spin-independent. The dark time evolution of the state of the particle can be written as

$$|\Psi(\mathbf{x}, t)\rangle = \psi_\uparrow(\mathbf{x}, t)|\uparrow\rangle + \psi_\downarrow(\mathbf{x}, t)|\downarrow\rangle.\tag{4.2}$$

Due to the separability and the spin independence of the $\hat{V}(y, z)$ potential, if the system is prepared in an eigenstate of y and z , it will remain in that eigenstate and thus the dynamics is effectively one-dimensional. Because of this, we will restrict our analysis to the x dimension.

We focus on the collective observable $\hat{S}^+ = \hat{S}^X + i\hat{S}^Y$, where \hat{S}^α are the spin angular momentum operators. The expectation value of \hat{S}^+ takes the form of an integrated density

$$\begin{aligned}\langle \hat{S}^+ \rangle &= \frac{1}{2} \int dx \psi_\uparrow^*(x, t) \psi_\downarrow(x, t) \\ &\equiv \frac{1}{2} |A(t)| e^{i\Delta\nu(t)t}.\end{aligned}\tag{4.3}$$

Here the Ramsey fringe contrast $\mathcal{C}(t) \equiv |A(t)|/|A(0)|$, is related to the overlap of the $\psi_\uparrow(x, t)$ and $\psi_\downarrow(x, t)$ wavefunctions. The decay of the contrast is a measure of demagnetization. The frequency shift $\Delta\nu(t)$ measures the dynamical phase difference between the spins and gives rise in this case to a net motionally-induced precession of the total magnetization. Throughout we set $\hbar = 1$.

4.3 Linear Magnetic Field

First we consider the case of a magnetic field with linear spatial dependence $B_Z(x) = Bx/\Delta\mu$ where B is a constant with units of energy/length. Adding a linear potential to a harmonic potential results in a new harmonic potential with the same frequency but shifted in opposite directions for each of the two spin states. The potential is

$$\hat{V}(x) = \frac{1}{2} m\omega^2 (x + \hat{\sigma}^Z x_0)^2 - \frac{1}{2} m\omega^2 x_0^2.\tag{4.4}$$

Here, $a_H = \sqrt{1/m\omega}$ is the oscillator length and $x_0 = \frac{Ba_H^2}{\omega}$ is the displacement of the oscillator resulting from the magnetic field.

It is well known that the displaced ground state of a harmonic oscillator evolves with a probability distribution of constant shape but oscillating centroid, $|\psi_0(x, t)|^2 \propto e^{-(x-x_0(1-\cos(\omega t)))^2}$ [109]. A similar result can be derived for any eigenstate n . Namely, given a solution $\phi(x, t)$ to the time-dependent Schrödinger equation,

$$\psi(x, t) := \hat{D}(z_0 e^{-i\omega t}) \phi(x, t),\tag{4.5}$$

is also a solution to the time-dependent Schrödinger equation. The displacement operator is given by $\hat{D}(w) \equiv \exp(w\hat{a}^\dagger - w^*\hat{a})$ and z_0 is any complex number, corresponding to an initial displacement in

the position-momentum phase space [109]¹. This result allows us to calculate dynamics analytically and write the time evolution of an initial eigenstate as (See Appendix A):

$$\begin{aligned} \psi_n(x, t) = & e^{-i(n+\frac{1}{2})\omega t + i\frac{x_0^2}{a_H^2}(\frac{1}{2}\cos(\omega t)\sin(\omega t) - \sin(\omega t))} \\ & \times e^{-i\sigma x_0 \sin(\omega t)x/a_H^2} \phi_n\left(\frac{x + \sigma x_0(1 - \cos(\omega t))}{a_H}\right), \end{aligned} \quad (4.6)$$

where σ is the eigenvalue of $\hat{\sigma}^Z$. In Fig. 4.1(a), we plot the time evolution of the spin density in the Z -direction, $\langle \hat{S}^Z(x, t) \rangle = \frac{1}{2} (|\psi_\uparrow(x, t)|^2 - |\psi_\downarrow(x, t)|^2)$, for a single particle initially in the ground state of the harmonic oscillator, calculated using Eq. 4.6. The $|\uparrow\rangle$ and $|\downarrow\rangle$ densities maintain their same shape but oscillate about their respective equilibrium positions at the trap frequency.

4.3.1 Derivation of generalized coherent-state formula

Consider $\hat{H} = \frac{\hat{p}^2}{2m} + \frac{m\omega^2 \hat{x}^2}{2} = \omega(\hat{a}^\dagger \hat{a} + \frac{1}{2})$ and suppose that $|\phi\rangle$ is a solution to the (time-dependent) Schrödinger equation. We now show that $|\psi\rangle := \hat{D}(z := z_0 e^{-i\omega t})|\phi\rangle$ is also a solution, where \hat{D} is the phase-space displacement operator $\hat{D}(w) = \exp(w\hat{a}^\dagger - w^*\hat{a})$ and z_0 is any complex number, corresponding to the initial displacement in phase space.

Observing that $[\hat{a}, \hat{D}(z)] = z\hat{D}(z)$ and $[\hat{a}^\dagger, \hat{D}(z)] = z^*\hat{D}(z)$, we have

$$\begin{aligned} [\hat{H}, \hat{D}(z)] &= \omega \left(z\hat{a}^\dagger \hat{D}(z) + z^* \hat{D}(z) \hat{a} \right) \\ &= \omega \left(z\hat{a}^\dagger + z^* \hat{a} - z^* z \right) \hat{D}(z). \end{aligned} \quad (4.7)$$

Noting also that $\dot{z} = -i\omega z$, $\dot{z}^* = i\omega z^*$, we have from the Baker-Campbell-Hausdorff formula,

$$\begin{aligned} \frac{\partial}{\partial t} \hat{D}(z) &= \frac{\partial}{\partial t} \left(e^{z\hat{a}^\dagger} e^{-z^*\hat{a}} e^{-z_0^* z_0/2} \right) \\ &= -i\omega z \hat{a}^\dagger \hat{D}(z) + e^{z\hat{a}^\dagger} (-i\omega z^* \hat{a}) e^{-z^*\hat{a}} e^{-z_0^* z_0/2} \\ &= \left(-i\omega z \hat{a}^\dagger - i\omega z^* \hat{a} + i\omega z^* z \right) \hat{D}(z), \end{aligned} \quad (4.8)$$

¹ Note that the displacement operator $\hat{D}(w)$ depends on the boson operators \hat{a} which diagonalize the Hamiltonian at times $t > 0$

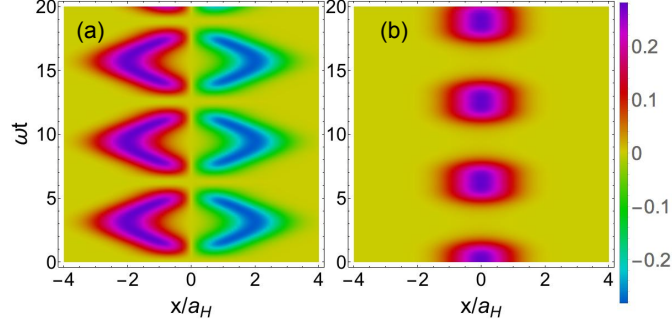


Figure 4.1: Dynamics of spin observables in a linear magnetic field with $x_0 = a_H$. (a) $\langle \hat{S}^Z(x, t) \rangle = \frac{1}{2} (|\psi_\uparrow(x, t)|^2 - |\psi_\downarrow(x, t)|^2)$ shows the spin up/down densities oscillating in their traps centered at $x = \mp x_0$. (b) Magnitude of $\langle \hat{S}^+(x, t) \rangle$, which measures the magnetization at point x . The magnetization decays when the spin up/down densities are separated.

since $[e^{z\hat{a}^\dagger}, \hat{a}] = -ze^{z\hat{a}^\dagger}$. Thus

$$\begin{aligned}
 i\frac{\partial|\psi\rangle}{\partial t} &= \omega \left(z\hat{a}^\dagger + z^*\hat{a} - z^*z \right) \hat{D}(z)|\phi\rangle + \hat{D}(z) \left(i\frac{\partial|\phi\rangle}{\partial t} \right) \\
 &= [\hat{H}, \hat{D}(z)]|\phi\rangle + \hat{D}(z)\hat{H}|\phi\rangle \\
 &= \hat{H}\hat{D}(z)|\phi\rangle = \hat{H}|\psi\rangle.
 \end{aligned} \tag{4.9}$$

4.3.2 Spin dynamics

We now use the above results to determine the spin dynamics for a single particle. Assuming that the particle begins in the n^{th} harmonic oscillator mode at time $t = 0$, we find

$$\begin{aligned}
 \langle \hat{S}^+ \rangle &= \frac{1}{2} \exp \left(-2 \frac{x_0^2}{a_H^2} (1 - \cos(\omega t)) \right) \\
 &\times L_n \left(4 \frac{x_0^2}{a_H^2} (1 - \cos(\omega t)) \right),
 \end{aligned} \tag{4.10}$$

where L_n is the n^{th} Laguerre polynomial.

We see that the contrast is suppressed exponentially with increasing x_0 . This is caused by the exponential suppression of the overlap integral between the spatial wavefunctions of the \uparrow and \downarrow spin states. As they move apart under the influence of their different potentials, the overlap decreases as a consequence of the wavepackets' Gaussian spatial localization, see Fig. 4.1(b). The contrast is periodic in time with period $2\pi/\omega$, due to the periodic motion of the two spin wavefunctions in

the trap. We also see that there is no frequency shift for the case of a linear magnetic field and the direction of the magnetization remains along Y . The two spin states, while displaced in position, experience harmonic potentials of the same frequency, so they have the same dynamical phase.

We now consider the dynamics of an ensemble of non-interacting fermions with this same protocol. An ensemble at zero temperature, initially spin-polarized, forms a Fermi-degenerate gas with all oscillator modes filled from $n = 0$ to $n = N - 1$, with N the number of particles. Here, we find

$$\begin{aligned}
\langle \hat{S}^+ \rangle^{\text{f.d.}} &= \sum_{n=0}^{N-1} \langle \hat{S}^+ \rangle_n \\
&= \frac{1}{2} e^{-2 \frac{x_0^2}{a_H^2} (1 - \cos(\omega t))} \sum_{n=0}^{N-1} L_n \left(4 \frac{x_0^2}{a_H^2} (1 - \cos(\omega t)) \right) \\
&= \frac{1}{2} e^{-2 \frac{x_0^2}{a_H^2} (1 - \cos(\omega t))} L_{N-1}^1 \left(4 \frac{x_0^2}{a_H^2} (1 - \cos(\omega t)) \right), \tag{4.11}
\end{aligned}$$

where $L_b^a(x)$ is the associated Laguerre polynomial and we have used the addition formula for Laguerre polynomials $\sum_{m=0}^n L_m^{(a)}(x) L_{n-m}^{(b)}(y) = L_n^{(a+b+1)}(x+y)$. The contrast decay per particle at short times is given by

$$\mathcal{C}(t)/N = 1 - E_F \frac{x_0^2}{a_H^2} \omega t^2 + \mathcal{O}(t^4), \tag{4.12}$$

with $E_F = k_B T_F = N\omega$ the Fermi energy of the gas, k_B is the Boltzmann constant, and T_F the Fermi temperature. Hence, the decay of the contrast per particle increases extensively as the number of particles increases.

For an ensemble at non-zero temperature, the associated Fermi-Dirac sums cannot be evaluated exactly, but can be approximated by energy integrals with a constant density of states to yield a formula for the short-time contrast decay per particle:

$$\begin{aligned}
\mathcal{C}(t)/N &= 1 - 2\bar{E} \frac{x_0^2}{a_H^2} \omega t^2 + \mathcal{O}(t^4) \\
\bar{E} &\approx \frac{1}{6N\omega\beta^2} \left[\pi^2 + 3 \ln(e^{\beta N\omega} - 1) + 6\text{Li}_2 \left(\frac{1}{1 - e^{\beta N\omega}} \right) \right], \tag{4.13}
\end{aligned}$$

where $\beta = 1/k_B T$, T the temperature and $\text{Li}_s(x)$ is the polylogarithm of order s .

In the limit of high temperature, $T/T_F \gg 1$, we can approximate the distribution function of the fermions with a Maxwell-Boltzmann distribution. For this ensemble the spin dynamics is given by

$$\begin{aligned} \langle \hat{S}^+ \rangle^{\text{M.B.}} &= \sum_{n=0}^{\infty} e^{-\beta\omega(n+1/2)} \langle \hat{S}^+ \rangle_n / \mathcal{Z} \\ &= \frac{1}{2} \exp \left[-2 \frac{x_0^2 (1 - \cos(\omega t))}{a_H^2 \tanh(\beta\omega/2)} \right], \end{aligned} \quad (4.14)$$

where $\mathcal{Z} = \sum_n e^{-\beta\omega(n+1/2)}$ is the partition function. At short times, we find the contrast per particle decays as $\mathcal{C}(t)/N = 1 - \frac{x_0^2}{a_H^2} \frac{1}{\tanh(\beta\omega/2)} \omega^2 t^2 + \mathcal{O}(t^4)$, which agrees with Eq. (4.13) when we identify the mean energy $\frac{1}{2} \tanh^{-1}(\beta\omega/2) = \bar{E}/\omega$. At $T/T_F \gg 1$, where this analysis is valid, $\bar{E} \approx k_B T$, and so the contrast decay rate increases linearly with temperature.

4.3.3 Dynamics for a spin-echo sequence

The spin-echo consists of an additional collective π rotation about X added at time $t/2$. This pulse swaps the states of the spin up and spin down components, with the goal of removing spin-dependent single-particle inhomogeneities. It is natural to wonder whether a spin-echo pulse will remove the effects of a magnetic field gradient, which is effectively a spatially-inhomogeneous detuning, when the particles themselves move in the trap. In the presence of a spin-echo pulse the evolution is given by:

$$\begin{aligned} \langle S^+ \rangle_{\text{SE}} &= \frac{1}{2} \exp \left(-16 \frac{x_0^2}{a_H^2} \sin^4 \left(\frac{\omega t}{4} \right) \right) \\ &\times L_n \left(32 \frac{x_0^2}{a_H^2} \sin^4 \left(\frac{\omega t}{4} \right) \right). \end{aligned} \quad (4.15)$$

The spin dynamics with a spin-echo pulse is periodic with period $4\pi/\omega$, twice the period of a Ramsey sequence without a spin-echo pulse. The short-time expansion of the contrast decay is

$$\mathcal{C}_{\text{SE}}(t) = 1 - \frac{1}{8} \left(n + \frac{1}{2} \right) \frac{x_0^2}{a_H^2} (\omega t)^4 + \mathcal{O}(t^6). \quad (4.16)$$

Note that the spin-echo removes the dominant $\mathcal{O}(t^2)$ contribution to the contrast decay at times much shorter than the motional period. This is consistent with the expectation that spin-echo removes the effect of inhomogeneities when motional effects can be neglected [110]. Beyond the short time limit the spin-echo pulse is not beneficial.

The behavior of the spin-echo signal at times comparable to the trap period can be visualized in phase space. To illustrate the dynamics, we rescale the phase space coordinates to x/x_0 and p/p_0 , where $p_0 = 1/a_0$, see Fig. (4.2). In this coordinate system, the expectation values $\langle x \rangle$ and $\langle p \rangle$ for the $|\uparrow\rangle$ state and $|\downarrow\rangle$ states initially move along circular trajectories centered at $\mp x_0$, reflecting their initial displacement from the center of their respective harmonic traps due to the magnetic field. The spin-echo π pulse switches the $|\uparrow\rangle$ and $|\downarrow\rangle$ states and while doing so it generally enhances the net displacement of the spin states from their motional centers. After the pulse the dynamics corresponds to circular trajectories with a new phase-space radius. For example, as shown in Fig. 4.2, if the echo is applied at π/ω (dark time $t = 2\pi/\omega$), the displacements following the spin-echo pulse are twice the displacements before the pulse.

For dark times less than half the motional period, the spin-echo improves the contrast, consistent with the short-time analysis. In the phase space picture this means that the displacement between $|\uparrow\rangle$ and $|\downarrow\rangle$ with spin-echo is smaller than without spin-echo. At a dark time of exactly half the motional period, the contrast decay with and without spin-echo is identical – this is illustrated in Fig. 4.3. In this case the phase space displacement without spin-echo is purely along x and the displacement with spin-echo is purely along p . For longer dark times, spin-echo increases dephasing, since it produces larger phase space displacements. The dephasing is maximal at dark times which are odd-integer multiples of the motional period. When the spin-echo pulse is applied at an integer multiple of the motional period, i.e. dark times of integer multiples of twice the motional period $t = 4\pi k/\omega$ (k an integer), both spin states have returned to the phase-space origin and the motional dynamics is unaffected by the spin-echo pulse. This explains the periodicity of the spin-echo signal with twice the motional period. We stress that the ability to decouple the spin-echo effect from motion is due to the two spin states sharing a common motional frequency.

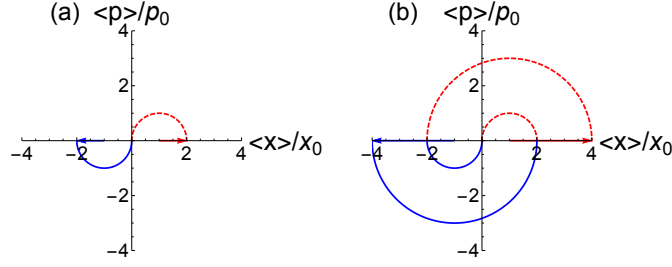


Figure 4.2: Phase space plots of $\langle x \rangle$ and $\langle p \rangle$ for the $|\uparrow\rangle$ state (blue, solid) and $|\downarrow\rangle$ state (red, dashed) for a spin-echo sequence in a linear magnetic field. Here $p_0 = 1/a_0$, and the total time is $2\pi/\omega$. The two spin states evolve along circular trajectories centered at $\mp x_0$. (a) At half the total dark time, π/ω , the spin-echo π pulse swaps the spin states. The spin wavefunctions are thus displaced by $2x_0$ from the centers of their respective harmonic traps. For the second half of the dark time they evolve in circular trajectories twice as large, centered at $\mp 2x_0$, resulting in a final configuration shown in (b). The spin-echo pulse leads to greater dephasing of the spin observables due to larger final phase-space displacement.

Although spin-echo is typically used to eliminate dephasing due to single particle inhomogeneities, in the presence of spin-motional coupling the particle motion during the dark time can worsen the resulting dephasing when a spin-echo pulse is applied.

We can calculate the dynamics of thermal ensembles with a spin-echo pulse. At zero temperature, the exact result is

$$\begin{aligned} \langle \hat{S}^+ \rangle_{\text{SE}}^{\text{f.d.}} &= \frac{1}{2} \exp \left(-16 \frac{x_0^2}{a_H^2} \sin^4 \left(\frac{\omega t}{4} \right) \right) \\ &\times L_{N-1}^1 \left(32 \frac{x_0^2}{a_H^2} \sin^4 \left(\frac{\omega t}{4} \right) \right). \end{aligned} \quad (4.17)$$

For an ensemble at arbitrary temperature the short time contrast decay is given by

$$\begin{aligned} \mathcal{C}_{SE}(t)/N &= 1 - 32 \bar{E} \frac{x_0^2}{a_H^2} \omega^3 t^4 + \mathcal{O}(t^6) \\ \bar{E} &\approx \frac{1}{6N\omega\beta^2} \left[\pi^2 + 3 \ln(e^{\beta N\omega} - 1) + 6 \text{Li}_2 \left(\frac{1}{1 - e^{\beta N\omega}} \right) \right], \end{aligned} \quad (4.18)$$

and at high temperature we can approximate the ensemble by a Maxwell-Boltzmann distribution to obtain

$$\langle \hat{S}^+ \rangle_{\text{SE}}^{\text{M.B.}} = \frac{1}{2} \exp \left[-16 \frac{x_0^2 \sin^4 \left(\frac{\omega t}{4} \right)}{a_H^2 \tanh(\beta\omega/2)} \right]. \quad (4.19)$$

The contrast at zero temperature and high temperature ($T \gg T_F$) are shown with and without spin-echo as a function of dark time in Fig. 4.3.

4.3.4 General Considerations

In general terms the contrast dynamics in the non-interacting regime is characterized by oscillatory behavior at the trap period arising from spin-motion coupling. At short times the contrast decays as $C(t) \approx 1 - \left(\frac{t}{\tau}\right)^2$ and in the presence of an echo-pulse as $C^{\text{SE}}(t) \approx 1 - \left(\frac{t}{\tau^{\text{SE}}}\right)^4$, where we identify τ and τ^{SE} as the demagnetization timescales without and with spin echo. Using Eqs. 4.13 and 4.18, the demagnetization timescales are given by:

$$\begin{aligned}\tau_{\text{lin}} &= \frac{a}{x_0} (2\omega \bar{E})^{-1/2} \\ \tau_{\text{lin}}^{\text{SE}} &= \left(32\omega^3 \frac{x_0^2}{a_H^2} \bar{E} \right)^{-1/4} \\ \bar{E} &\approx \frac{1}{6N\omega\beta^2} \left[\pi^2 + 3\ln(e^{\beta N\omega} - 1) + 6\text{Li}_2\left(\frac{1}{1 - e^{\beta N\omega}}\right) \right]\end{aligned}\quad (4.20)$$

The short time demagnetization rate can be significantly faster than demagnetization rates measured in recent experiments performed at unitarity [9–11], where the magnetization decay is mainly diffusive with a short time scaling given by $C^{\text{U}}(t) \approx 1 - \left(\frac{t}{\tau^{\text{U}}}\right)^3$. The different time dependence translates into a different dependence on the magnetic field gradient: while in the non-interacting regime the demagnetization rate scales as $1/\tau \sim B$ and $1/\tau^{\text{SE}} \sim \sqrt{B}$, in the interaction dominated regime it scales as $1/\tau \sim B^{2/3}$ [9–11].

The demagnetization rate in the non-interacting system increases with temperature at fixed particle number with and without echo. The increasing decay rate in the non-interacting limit simply reflects the increase in the mean energy per particle as the gas gets hotter. This behavior persists in the presence of interactions as observed in current experiments given that both the typical velocity and the mean free path (parameters that determine the spin diffusivity) increase with temperature. Fig. (4.4) (a-b) shows the demagnetization timescales. We use an effective one-dimensional number of particles, which scales like $N^{1/3}$, where N is the total number of particles in a three dimensional trap. The fact that the demagnetization rate due to the motion of the atoms

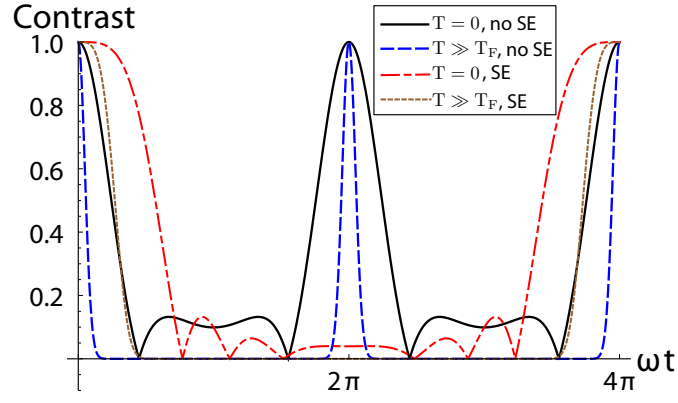


Figure 4.3: Contrast decay for the case of a linear magnetic field at times comparable to the trap period, for zero temperature and high temperature ($T \gg T_F$), with and without spin-echo (SE). The quantum degenerate case uses $N = 19$ and all cases use $x_0 = 0.24a_H$, consistent with Ref. [10]. $T = 10T_F$ in the high temperature case. Higher temperature leads to faster contrast decay since the particles have a larger average energy. The spin-echo removes the second-order contribution to the contrast decay, resulting in slower decay at short times. However, at long times the contrast decay is larger when a spin-echo pulse is applied. The period of the dynamics is also $4\pi/\omega$ with a spin-echo pulse instead of $2\pi/\omega$.

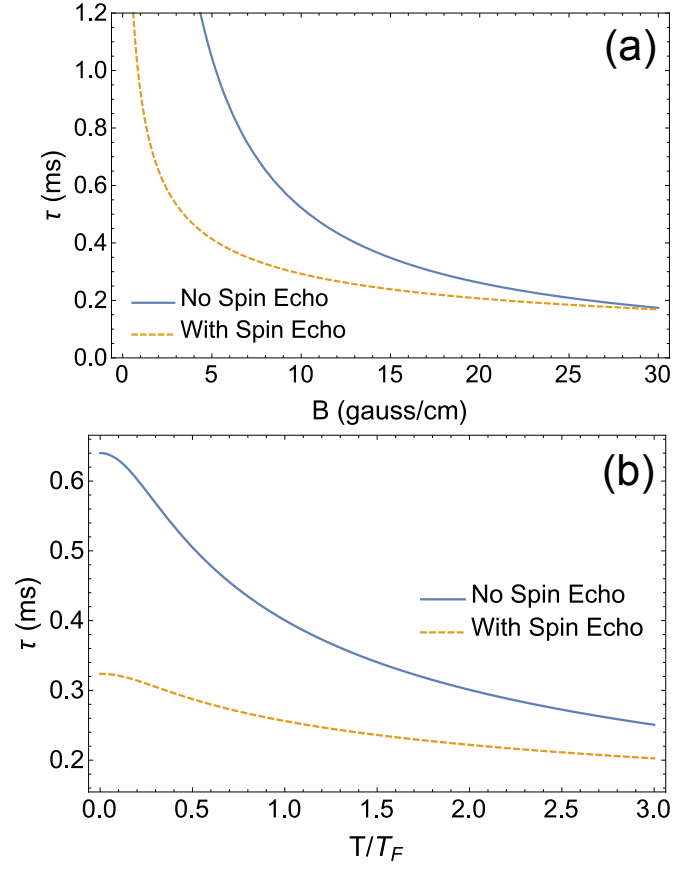


Figure 4.4: Linear magnetic field: (a) demagnetization time vs. magnetic field gradient. (b) Demagnetization time vs. temperature where the Fermi temperature $T_F = N\omega$. Using parameters from Ref. [10], these timescales are faster than those obtained in the experiment, suggesting that strong interactions suppress the role of single particle dynamics.

in the trap can be comparable or to faster than the spin diffusion decay rate makes it clear that one relevant role of strong interactions is to suppress the effects of single-particle motion.

4.4 Quadratic Magnetic Field

We now consider the case when the applied inhomogeneous magnetic field varies quadratically with position: $B_z(x) = mBx^2/\Delta\mu$. Here B is a constant with units of frequency². The total potential experienced by the atoms is

$$\hat{V}(x) = \frac{1}{2}m(\omega^2 + \hat{\sigma}^Z B)x^2. \quad (4.21)$$

Thus, each spin state sees a new trap frequency $\omega_\sigma = \sqrt{\omega^2 + \sigma B}$, with σ the eigenvalue of $\hat{\sigma}^Z$.

We can find the time dynamics of a harmonic oscillator eigenstate subjected to a sudden quench in the oscillator frequency by making the following ansatz, analogous to Eq. (4.6) for the linear case:

$$\psi_n(x, t) = \frac{e^{-i(n+\frac{1}{2})\phi_\sigma(t)}}{\sqrt{a_H\alpha_\sigma(t)}} \psi_n\left(\frac{x}{a_H\alpha_\sigma(t)}\right) e^{i\beta_\sigma(t)\frac{x^2}{2a_H^2}}, \quad (4.22)$$

where $\alpha_\sigma(t)$, $\beta_\sigma(t)$, and $\phi_\sigma(t)$ real functions which are independent of n . It can be shown that this ansatz represents a solution to the time-dependent Schrödinger equation if the functions $\alpha_\sigma(t)$, $\beta_\sigma(t)$, and $\phi_\sigma(t)$ satisfy

$$\begin{aligned} \alpha_\sigma''(t) + (\omega^2 + \sigma B)\alpha_\sigma(t) &= \frac{\omega^2}{\alpha_\sigma^3(t)}, \\ \beta_\sigma(t) &= \frac{\alpha_\sigma'(t)}{\alpha_\sigma(t)}, \\ \phi_\sigma'(t) &= \frac{1}{\alpha_\sigma^2(t)}. \end{aligned} \quad (4.23)$$

Equation (4.23) is a special case of the Ermakov equation, a well-studied nonlinear ordinary differential equation [111]. Defining $\tilde{B} = B/\omega^2$ as a dimensionless parameter, the solutions for our

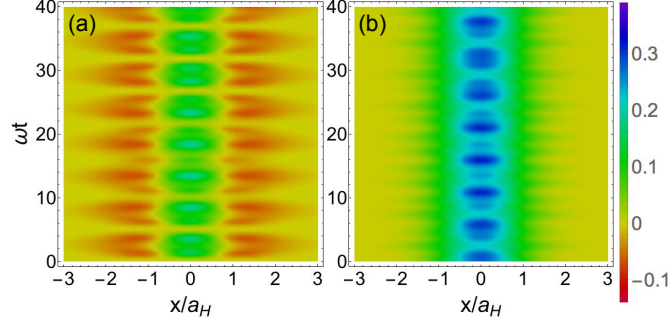


Figure 4.5: Dynamics of spin observables in a quadratic magnetic field with $B = 0.65\omega^2$. (a) $\langle \hat{S}^Z(x, t) \rangle$ shows the spin up/down densities breathing in their traps centered at $x = 0$. The rates of their breathing, $\omega^\pm = \sqrt{\omega^2 \pm B}$, are incommensurate. The standard deviations of the densities are $a^\pm = 1/\sqrt{\omega^\pm}$, hence spin up (down) becomes more concentrated at the center (edge) of the trap. (b) Magnitude of $\langle \hat{S}^+(x, t) \rangle$ (contrast), which measures the magnetization at position x . The magnetization decays when the spin up/down densities are separated. Note that decays/revivals of the magnetization are aperiodic.

particular case are

$$\begin{aligned}
 \alpha_\sigma(t) &= \sqrt{\frac{2 + \tilde{B}\sigma \left(1 + \cos\left(2\omega t\sqrt{1 + \tilde{B}\sigma}\right)\right)}{2\left(1 + \tilde{B}\sigma\right)}}, \\
 \beta_\sigma(t) &= -\frac{\tilde{B}\sqrt{1 + \tilde{B}\sigma} \sin\left(2\omega t\sqrt{1 + \tilde{B}\sigma}\right)}{2 + \tilde{B}\sigma \left(1 + \cos\left(2\omega t\sqrt{1 + \tilde{B}\sigma}\right)\right)}, \\
 \phi_\sigma(t) &= \left\lfloor \frac{\omega t\sqrt{1 + \tilde{B}\sigma}}{\pi} \right\rfloor \pi + \\
 &\quad + \frac{\pi}{2} - \arctan \left[\sqrt{1 + \tilde{B}\sigma} \cot \left(\omega t\sqrt{1 + \tilde{B}\sigma} \right) \right], \tag{4.24}
 \end{aligned}$$

where $\lfloor \cdot \rfloor$ is the floor function. The solutions $\psi_n(x, t)$ are wavefunctions whose probability densities maintain their original shape, up to periodic rescaling by $\alpha(t)$. The frequency associated with the “breathing” of the probability density is $2\omega\sqrt{1 + \tilde{B}\sigma}$, and hence the periods of oscillation are generally incommensurate for the spin up and spin down particles, see Fig. (4.5). These modes are the breathing analogs of the well-known coherent states of a harmonic oscillator.

Figure (4.5) also shows

$$\langle \hat{S}^Z(x, t) \rangle = \frac{1}{2} \left(|\psi_\uparrow(x, t)|^2 - |\psi_\downarrow(x, t)|^2 \right), \tag{4.25}$$

that reflects the breathing of the spin up/down densities around the trap centers at $x = 0$. The different standard deviations of the densities, $a^\pm = 1/\sqrt{\omega^\pm}$, also lead to a spin segregation, or spatial separation of the spin up/down densities: while the former becomes more localized towards the center, the latter becomes more concentrated at the edge of the trap.

4.4.1 Spin Dynamics

To calculate $\langle \hat{S}^+ \rangle = \frac{1}{2} \int dx \psi_\uparrow^*(x, t) \psi_\downarrow(x, t)$ we use Eq. (4.22) and write

$$\langle \hat{S}^+ \rangle = \frac{1}{2} \frac{\exp[i(\phi_\uparrow(t) - \phi_\downarrow(t))]}{\sqrt{\alpha_\uparrow(t)\alpha_\downarrow(t)}} I_n, \quad (4.26)$$

where

$$\begin{aligned} I_n &\equiv \frac{1}{2^n n! \sqrt{\pi}} \int dx e^{-ax^2} H_n(bx) H_n(cx) \\ a &= \frac{\alpha_\uparrow(t)^2 + \alpha_\downarrow(t)^2}{2\alpha_\uparrow(t)^2\alpha_\downarrow(t)^2} + \frac{1}{2}(\beta_\uparrow(t) - \beta_\downarrow(t)) \\ b &= \frac{1}{\alpha_\uparrow(t)}, \quad c = \frac{1}{\alpha_\downarrow(t)}, \end{aligned} \quad (4.27)$$

and $H_n(x)$ is a Hermite polynomial. Due to the difference in breathing frequencies, the spin up and spin down particles accumulate a different dynamical phase, unlike the case of a linear magnetic field. Because of this dynamical phase difference, there is a net frequency shift.

Using the generating function for the Hermite polynomials [112], we can find a generating function for the integrals I_n as

$$g_I(z) \equiv \frac{1}{\sqrt{a - 2bcz + (b^2 + c^2 - a)z^2}} = \sum_{n=0}^{\infty} I_n z^n, \quad (4.28)$$

which leads to the following closed form for $\langle \hat{S}^+ \rangle$:

$$\begin{aligned} \langle \hat{S}^+ \rangle &= \frac{1}{2} \frac{e^{i(\phi_\uparrow(t) - \phi_\downarrow(t))}}{\sqrt{a\alpha_\uparrow(t)\alpha_\downarrow(t)}} (g_1 g_2)^n \times \\ &\times {}_2F_1 \left[\frac{1-n}{2}, \frac{-n}{2}, 1, \frac{(g_1^2 - 1)(g_2^2 - 1)}{g_1^2 g_2^2} \right]. \end{aligned} \quad (4.29)$$

Here, $g_1 = b/\sqrt{a}$, $g_2 = c/\sqrt{a}$, and ${}_2F_1[\cdot]$ is the hypergeometric function. To illuminate this result

we can expand $\langle \hat{S}^+ \rangle$ to second order in ωt :

$$\begin{aligned} \langle \hat{S}^+ \rangle \approx & \frac{1}{2} \left[1 + \frac{iB}{\omega^2} (\omega t) \left(n + \frac{1}{2} \right) + \right. \\ & \left. - \frac{3}{4} \left(\frac{B}{\omega^2} \right)^2 (\omega t)^2 \left(n^2 + n + \frac{1}{2} \right) + O((\omega t)^3) \right]. \end{aligned} \quad (4.30)$$

We see that at short times the signal acquires a frequency shift $\Delta\nu = (B/\omega)(n + \frac{1}{2})$ and thus the collective spin exhibits a net precession in the X - Y plane. The frequency shift is a consequence of the additional frequency scale in the problem, namely, $\omega_{\uparrow} - \omega_{\downarrow} = \sqrt{\omega^2 + B} - \sqrt{\omega^2 - B} \approx B/\omega$ for $B \ll \omega^2$. Additionally, the contrast decays quadratically in Bt/ω , and depends on the mean of the squared energy. From the generating function, we can also find the Maxwell-Boltzmann thermal average exactly as $g_I(e^{-\beta\omega})/\mathcal{Z}$, which gives

$$\langle \hat{S}^+ \rangle^{\text{M.B.}} = \frac{1 \exp[i(\phi_{\uparrow}(t) - \phi_{\downarrow}(t))] \sinh(\beta\omega/2)}{\sqrt{(\alpha_{\downarrow}^2(t) + \alpha_{\uparrow}^2(t)) \cosh(\beta\omega) + \alpha_{\downarrow}(t)\alpha_{\uparrow}(t)(i\alpha_{\downarrow}(t)\alpha_{\uparrow}(t)(\beta_{\uparrow}(t) - \beta_{\downarrow}(t)) \sinh(\beta\omega) - 2)}}. \quad (4.31)$$

4.4.2 Spin-echo sequence for quadratic magnetic field

To find the spin dynamics we solve Ermakov equation with the conditions of a spin-echo sequence. The result, expanded at short times, is

$$\begin{aligned} \langle \hat{S}^+ \rangle \approx & \frac{1}{2} \left[1 - \frac{i}{8} \left(\frac{B}{\omega^2} \right) (\omega t)^3 \left(n + \frac{1}{2} \right) + \right. \\ & \left. - \frac{1}{16} \left(\frac{B}{\omega^2} \right)^2 (\omega t)^4 (n^2 + n + 1) + O((\omega t)^5) \right]. \end{aligned} \quad (4.32)$$

As was the case for the linear magnetic field, the spin-echo removes the leading order contrast decay, and also removes the leading order frequency shift. We again interpret this result as due to the fact that the particles do not move to first order in time, and so the spin-echo can remove the effectively-static dephasing at lowest order. For longer times, there is an essential difference in the present case compared to the magnetic field with linear position dependence: here, $\langle \hat{S}^+ \rangle$ is not a periodic function of time, as the two frequencies $\sqrt{\omega^2 + B}$ and $\sqrt{\omega^2 - B}$ are incommensurate

for general B . In the case of a linear magnetic field, the residual effects of the spin-echo pulse on motion can be removed by applying the spin-echo pulse after a single motional period, as both spin states oscillate at the trap frequency. In the quadratic case, the two spin states have different motional periods, and so a spin-echo pulse cannot remove motional effects from both spin states at long times.

4.4.3 General Considerations

For the quadratic magnetic field the contrast decay due to motional effects, expressed as a demagnetization rate, also exhibits a quadratic and quartic scaling with time with and without a spin-echo pulse, respectively. However, unlike the linear magnetic field case, there are generally no full revivals of the magnetization, due to the incommensurate breathing frequencies of the spin up and spin down densities. Using the approximation of a continuum of energies and a constant density of states, the corresponding demagnetization timescales are given by:

$$\begin{aligned}\tau_{\text{quad}} &= \frac{2}{\sqrt{3}} \left(\frac{\omega^2}{B} \right) (\bar{E}^2 - \omega^2/2)^{-1/2} \\ \tau_{\text{quad}}^{\text{SE}} &= 2\sqrt{\frac{\omega^2}{B}} [\omega^2 (\bar{E}^2 - 3\omega^2/4)]^{-1/4} \\ \bar{E}^2 &\approx \frac{\pi^2 \ln(e^{\beta N \omega} - 1) + \ln(e^{\beta N \omega} - 1)^3 - 6\text{Li}_3\left(\frac{1}{1-e^{\beta N \omega}}\right)}{3\beta^3 \omega (N+1)}\end{aligned}\tag{4.33}$$

where the last line gives the mean squared energy. In comparison to the case of a constant gradient, the rate is proportional to the mean squared energy rather than the mean energy, so the demagnetization rates increase more quickly with particle number and temperature than the linear case. In Fig. 4.6 we plot the demagnetization time and contrast decay for the quadratic magnetic field case with and without spin-echo, using experimental parameters from Ref. [14], but with the proper rescaling of particle number to account for the different dimensionality, as was done for the linear magnetic field case. Under these conditions a spin-echo pulse again leads to faster demagnetization. We find that the demagnetization timescales are on the order of or faster than the spin segregation timescales observed in an experiment in which interactions were non-negligible

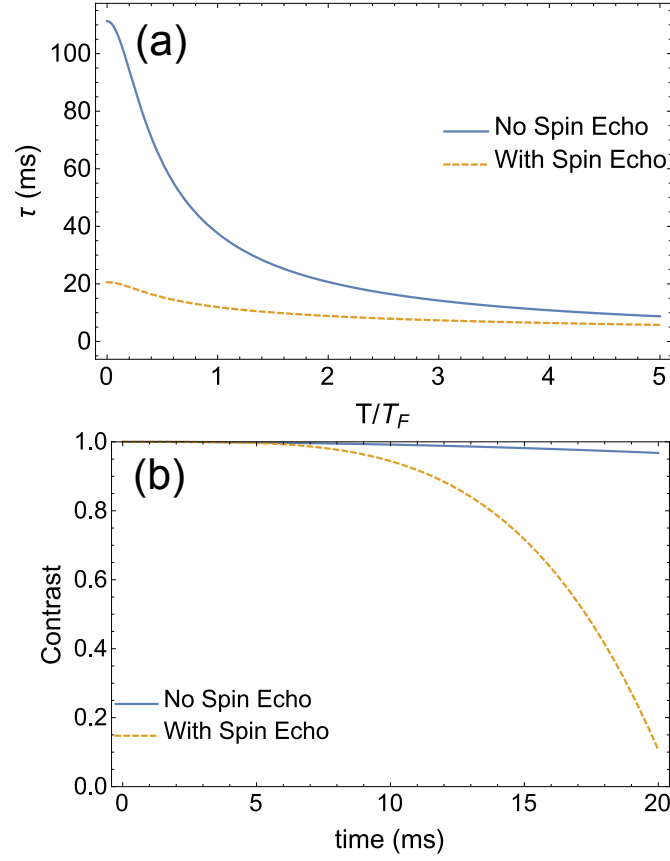


Figure 4.6: Quadratic magnetic field: (a) demagnetization time with and without spin-echo vs. temperature, where the Fermi temperature $T_F = N\omega$, and (b) contrast decay vs. time, using parameters from Ref. [14]. The timescales are on the order of or faster than the timescale of spin segregation in the experiment (~ 100 ms). Additionally, application of a spin-echo pulse leads to faster demagnetization.

($\sim 100\text{ms}$). There, the segregation timescales were dictated by the mean interaction energy of the gas. The faster short-time decay exhibited by the non-interacting system reveals once more the suppression of motional effects from interactions.

4.5 Dynamics in three dimensions

In the same way that we computed results in one dimension, we now consider a single spin-1/2 particle of mass m_a confined in a three-dimensional harmonic trap with trapping frequencies $\{\omega_x, \omega_y, \omega_z\}$ with a gradient applied along the x and z directions – results for ensembles of atoms are later calculated from sums over single particle dynamics. At $t = 0$ the particle is prepared in spin state $|\downarrow\rangle$, in an eigenstate of the gradient-free potential, after which the gradient is quenched on yielding a potential

$$\begin{aligned} V(x, y, z) &= \frac{1}{2}m_a (\omega_x x^2 + \omega_y y^2 + \omega_z z^2) + \sigma (B_x x + B_y y + B_z z) \\ &= \frac{1}{2}m_a (\omega_x (x + \sigma x_0)^2 + \omega_y (y + y_0)^2 + \omega_z (z + \sigma z_0)^2) + \text{const.} \end{aligned} \quad (4.34)$$

where $\sigma = 1(-1)$ for the $\uparrow (\downarrow)$ spin states, $x_0 = B_x/(m\omega_x^2)$, and $z_0 = B_z/(m\omega_z^2)$. The single particle eigenstates are shifted by x_0, y_0 , and z_0 . We can label the eigenstates as

$$\begin{aligned} \Phi_{\vec{n}=\{n_x, n_y, n_z\}}^\downarrow &= \phi_{n_x}(x - x_0) \phi_{n_y}(y - y_0) \phi_{n_z}(z - z_0), \\ \Phi_{\vec{n}=\{n_x, n_y, n_z\}}^\uparrow &= \phi_{n_x}(x + x_0) \phi_{n_y}(y + y_0) \phi_{n_z}(z + z_0), \end{aligned} \quad (4.35)$$

where $\phi_{n_i}(x)$ are the one dimensional wavefunctions for harmonic oscillators with frequencies ω_i .

Since the potential is separable in our problem, the overlap integral in three dimensions is just the product of the corresponding one dimensional overlap integrals. This implies:

$$\begin{aligned} \langle \hat{S}^+ \rangle_{3D} &= \frac{1}{2} \exp \left(-2 \frac{x_0^2}{a_x^2} (1 - e^{i\omega_x t}) - 2 \frac{y_0^2}{a_y^2} (1 - e^{i\omega_y t}) - 2 \frac{z_0^2}{a_z^2} (1 - e^{i\omega_z t}) \right) \\ &\times L_{n_x} \left(4 \frac{x_0^2}{a_x^2} (1 - \cos(\omega_x t)) \right) L_{n_y} \left(4 \frac{y_0^2}{a_y^2} (1 - \cos(\omega_y t)) \right) L_{n_z} \left(4 \frac{z_0^2}{a_z^2} (1 - \cos(\omega_z t)) \right), \end{aligned} \quad (4.36)$$

where $a_i = 1/\sqrt{m_a \omega_i}$ is the harmonic oscillator length in the i direction.

An ensemble at zero temperature, initially spin-polarized, forms a Fermi-degenerate (F.d.) gas with all oscillator modes filled from $\vec{n} = \{0, 0, 0\}$ to

$\vec{n} = \{N_x - 1, N_y - 1, N_z - 1\}$, where the total number of particles is $N_T = N_x N_y N_z$. Here, we find

$$\begin{aligned}
\langle \hat{S}^+ \rangle^{\text{F.d.}} &= \sum_{n_x=0}^{N_x-1} \sum_{n_y=0}^{N_y-1} \sum_{n_z=0}^{N_z-1} \langle \hat{S}^+ \rangle_{3D} \\
&= \frac{1}{2} \exp \left(-2 \frac{x_0^2}{a_x^2} (1 - e^{i\omega_x t}) - 2 \frac{y_0^2}{a_y^2} (1 - e^{i\omega_y t}) - 2 \frac{z_0^2}{a_z^2} (1 - e^{i\omega_z t}) \right) \\
&\times \sum_{n_x=0}^{N_x-1} \sum_{n_y=0}^{N_y-1} \sum_{n_z=0}^{N_z-1} L_{n_x} \left(4 \frac{x_0^2}{a_x^2} (1 - \cos(\omega_x t)) \right) L_{n_y} \left(4 \frac{y_0^2}{a_y^2} (1 - \cos(\omega_y t)) \right) L_{n_z} \left(4 \frac{z_0^2}{a_z^2} (1 - \cos(\omega_z t)) \right), \\
&= \frac{1}{2} \exp \left(-2 \frac{x_0^2}{a_x^2} (1 - e^{i\omega_x t}) - 2 \frac{y_0^2}{a_y^2} (1 - e^{i\omega_y t}) - 2 \frac{z_0^2}{a_z^2} (1 - e^{i\omega_z t}) \right) \\
&\times L_{N_x-1}^1 \left(4 \frac{x_0^2}{a_x^2} (1 - \cos(\omega_x t)) \right) L_{N_y-1}^1 \left(4 \frac{y_0^2}{a_y^2} (1 - \cos(\omega_y t)) \right) L_{N_z-1}^1 \left(4 \frac{z_0^2}{a_z^2} (1 - \cos(\omega_z t)) \right), \quad (4.37)
\end{aligned}$$

The contrast decay and frequency shift per particle at short times are given by

$$\begin{aligned}
\mathcal{C}(t)/N_T &= 1 - N_x \frac{x_0^2}{a_x^2} \omega_x^2 t^2 - N_y \frac{y_0^2}{a_y^2} \omega_y^2 t^2 - N_z \frac{z_0^2}{a_z^2} \omega_z^2 t^2 + \mathcal{O}(t^4) + \mathcal{O}\left(\frac{x_0^4}{a_x^4}\right), \\
\Delta\nu/N_T &= 2 \left(\frac{x_0^2}{a_x^2} \omega_x + \frac{y_0^2}{a_y^2} \omega_y + \frac{z_0^2}{a_z^2} \omega_z \right). \quad (4.38)
\end{aligned}$$

The decay of the contrast per particle increases extensively as the number of particles increases, but the frequency shift per particle is independent of N_T . From this expression we can define the single particle demagnetization time τ_M^{sp} , where the short time contrast decay per particle is given by $\mathcal{C}(t)/N_T = 1 - (t/\tau_M^{sp})^2$:

$$\tau_M^{sp} = \left(\frac{a_x^2}{x_0^2 N_x} + \frac{a_y^2}{y_0^2 N_y} + \frac{a_z^2}{z_0^2 N_z} \right)^{-\frac{1}{2}}. \quad (4.39)$$

This express gives the timescale of the initial short-time collapse of the magnetization due to single particle motion.

4.5.1 Comparison with experiment

We will compare our expressions for single particle dynamics with measurements taken by the University of Toronto ultracold atoms group on October 17, 2016 and November 4, 2016. The

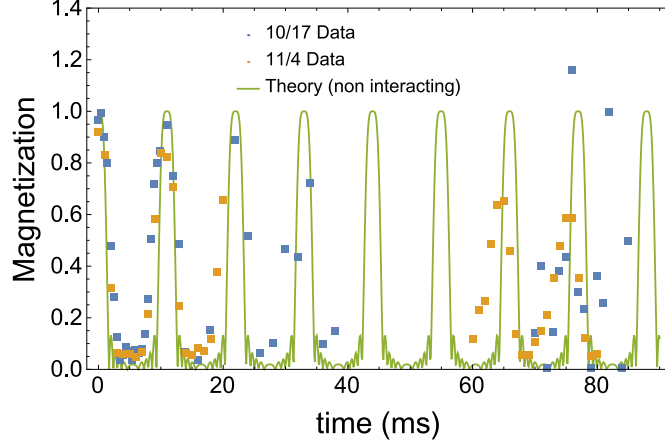


Figure 4.7: Comparison of the data with the formula for single particle spin dynamics (Eq. 4.37). The single particle formulas work better at short times before other effects, likely from interactions and magnetic field curvature, become important.

10/17 data is for 30800 ± 408 ^{40}K atoms close to quantum degeneracy ($T = 0.19 \pm 0.04T_F$, where T_F is the Fermi temperature) in a three dimensional harmonic trap with frequencies

$\{\omega_x, \omega_y, \omega_z\} = \{181.9 \pm 0.4, 665 \pm 30, 665 \pm 30\} \times 2\pi$ Hz. The 11/4 data has similar parameters of $N = 29162 \pm 541$ and $T/T_F = 0.24$.² The sample is close enough to quantum degeneracy that we will assume $T = 0$. Using these numbers, a Monte Carlo sampling determines that the lowest energy configuration is $\{N_x, N_y, N_z\} = \{73, 20, 20\}$. These parameters are very close to those used in the experiment of Ref. [10].

A magnetic field gradient is applied which has components $\{B_x, B_y, B_z\} = \{1.85, 0, 0\}$ G/cm with overall uncertainty of 20 %. A static magnetic field of 209 G is applied which is close to the zero crossing of the scattering length resonance. In Ref. [9] the differential magnetic moment of ^{40}K at 209.15 G was measured as $\Delta\mu = 152 \times 2\pi$ kHz/G and we assume an uncertainty of 10% based on a comparison with the numerical values given in Ref. [10]. Using these numbers, the applied gradients correspond to the lengths (and uncertainties)

$$x_0 = \frac{\hbar\Delta\mu B_x}{m_a\omega_x^2} = 1.17 \times 10^{-6} \text{ m} = 0.182a_x. \quad (4.40)$$

Using the given parameters, we get a good fit to the data with Eq. 4.37. The data and fit are shown

² On 11/4 an atom loss of about 15% was observed along with an increase in temperature of about 50% after the experimental runs. These measurements were not taken on 10/17.

in Fig. 4.7.

4.6 Summary and Outlook

We have demonstrated that the motion of non-interacting fermions in a trap can lead to demagnetization on timescales faster than those caused by interactions in recent experiments. Additionally, a spin-echo sequence can have the counterintuitive effect of enhancing the rate of demagnetization at times comparable to or longer than the motional period. The analysis present here, which exactly characterizes all the relevant timescales and parameters that determine the non-interacting spin dynamics of a finite temperature fermionic gas, can serve as a platform for a better understanding of the interplay between motional-induced and interaction-induced spin dynamics.

A logical direction for future work is to characterize the crossover from non-interacting to interacting dynamics. A promising avenue along these lines is to treat the occupation of single-particle energy states as fixed and consider the effect of interactions on these occupied single-particle states. This will be explored in detail in the next chapter.

Chapter 5

Interacting Spin Dynamics in a Two Component Fermi Gas

The interplay between spin and motional degrees of freedom in interacting electron systems has been a long-standing research topic in condensed matter physics. Interactions can modify the behavior of individual electrons and give rise to emergent collective phenomena such as superconductivity and colossal magnetoresistance [113]. Theoretical understanding of non-equilibrium dynamics in interacting fermionic matter is limited, however, and many open questions remain. Ultracold atomic Fermi gases, with precisely controllable parameters, offer an outstanding opportunity to investigate the emergence of collective behavior in out-of-equilibrium settings.

Progress in this direction has been made in recent experiments with ultracold spin-1/2 fermionic vapors, where initially spin-polarized gases were subjected to a spin-dependent trapping potential (Fig. 5.1) implemented by a magnetic field gradient [9–11], or a spin-dependent harmonic trapping frequency [12–15] – equivalent to a spatially-varying gradient. Even in the weakly interacting regime, drastic modifications of the single-particle dynamics were reported. Moreover, despite the local character of the interactions, collective phenomena were observed, including demagnetization and transverse spin-waves in the former, and a time-dependent separation (segregation) of the spin densities and spin self-rephasing in the latter. Although mean-field and kinetic theory formulations have explained some of these phenomena [15, 17, 98–102, 104–106, 114], a theory capable of describing all the time scales and the interplay between spin, motion, and interactions has not been developed.

In this chapter, we present a framework that accounts for the coupling of spin and motion

in weakly interacting Fermi gases. We qualitatively reproduce and explain all phenomena of the aforementioned experiments and obtain quantitative agreement with the results of Ref. [14]. In this formulation the state of the system is represented as a superposition of spin configurations which live on lattices whose sites correspond to modes of the underlying single-particle system. Within each configuration, the dynamics is described by a spin model with long-ranged couplings which generates collective quantum correlations and entanglement. Each sector evolves independently and the accumulated phase differences between sectors capture the interplay of spin and motion (Fig. 5.1 b). Using this formulation, we gain a great deal of insight about the dynamics, and can extract analytic solutions for spin observables and correlations in several limits. Although spin models in energy space [1, 3, 4, 19, 103, 115, 116] have been used before and agreed well with experiments [12, 116–121], their use was limited to pure spin dynamics (no motion). Our formulation allows us to track motional degrees of freedom, compute local observables, and determine how correlations spread in real space. This opens a route for investigations of generic interacting spin-motion coupled systems beyond current capabilities. Our predictions also suggest directions for future experiments in the weakly interacting regime, which might, for instance, investigate the collective rise of quantum correlations. In contrast to strongly coupled ultracold gases, where motion is quickly suppressed and features of the dynamics tend to be universal [9, 20, 122], in the weakly-interacting regime spin, motion, and interactions are all important and must be treated on the same level. At the end of this chapter we also present some preliminary results for another class of experiments involving the collision of a spin-up and spin-down spin cloud in a one dimensional harmonic trap using a similar formalism. We focus on the weakly-interacting regime in one dimension where fully-quantum treatments of the interactions are tractable. This work is meant to model the experiments in Refs. [122, 123] in the weakly-interacting, quantum degenerate regime.

Numerical simulations of non-equilibrium fermionic matter are notoriously difficult, and for many situations no efficient algorithms presently exist. In contrast, a wide variety of powerful analytical and numerical tools have been developed for lattice quantum spin models [124–131], making a spin model description of fermionic systems potentially very useful. To demonstrate

the capabilities of this approach, we use time-dependent matrix product state methods which are efficient in one-dimension, which were performed using extensions of the open source MPS library [132, 133]. We simulate systems of $N = 10 - 20$ particles; due to the coupling of spin and motion, the complexity of these simulations is similar to that of long-ranged and inhomogenous pure spin systems with $N \sim 100$ spins. We emphasize, however, that the mapping to a spin model, the corresponding analytic solutions, and the physical interpretations are valid in arbitrary dimensions. Thus the method described here will be useful for more generic cases as numerical techniques able to handle larger spin systems continue to improve.

5.1 Setup

This chapter is a continuation of the results of the previous chapter to the interacting case. For ease of exposition some of the quantities will be redefined, and we will re-describe the setup. We consider N identical fermionic atoms of mass m_a with a spin-1/2 degree of freedom $\alpha \in \{\uparrow, \downarrow\}$ trapped in a one dimensional harmonic oscillator of frequency ω , $V^0(x) = \frac{1}{2}m_a\omega^2x^2$. The gas begins spin-polarized in the \downarrow state and atoms populate distinct trap modes. The initial Hamiltonian is $\hat{H} = \hat{H}_0^{sp} + \hat{H}^{int}$ where

$$\begin{aligned}\hat{H}_0^{sp} &= \sum_{\alpha} \int dx \hat{\psi}_{\alpha}^{\dagger}(x) \left(-\frac{1}{2m_a} \frac{\partial^2}{\partial x^2} + V^0(x) \right) \hat{\psi}_{\alpha}(x), \\ \hat{H}^{int} &= \frac{2a_s}{m_a a_{\perp}^2} \int dx \hat{\rho}_{\uparrow}(x) \hat{\rho}_{\downarrow}(x).\end{aligned}\tag{5.1}$$

$\hat{\psi}_{\alpha}(x)$ is the fermionic field operator for spin α at point x , a_s is the s -wave scattering length, $\hat{\rho}_{\alpha}(x) = \hat{\psi}_{\alpha}^{\dagger}(x) \hat{\psi}_{\alpha}(x)$, $\hbar = 1$, and we have integrated over two transverse directions with small confinement length $a_{\perp} \ll a_H$, with $a_H = (m_a \omega)^{-\frac{1}{2}}$. Note that the initial spin-polarized sample will not experience interactions. A resonant $\pi/2$ pulse collectively rotates the spin to the X -axis, and a magnetic field gradient is suddenly turned on. This introduces a sudden change (quench) in the single-particle Hamiltonian \hat{H}_0^{sp} , which becomes spin-dependent, \hat{H}^{sp} , where

$$\hat{H}^{sp} = \sum_{\alpha} \int dx \hat{\psi}_{\alpha}^{\dagger}(x) \left(-\frac{1}{2m_a} \frac{\partial^2}{\partial x^2} + V^{\alpha}(x) \right) \hat{\psi}_{\alpha}(x).\tag{5.2}$$

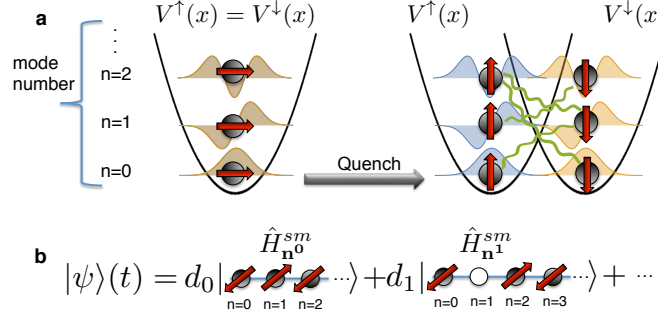


Figure 5.1: (a) Atoms spin-polarized along X occupy single-particle eigenstates, labeled by mode number n . The potential is quenched to a spin-dependent form, and dynamics result from a spin model with long ranged interactions (green wavy lines) in energy space. (b) The state $|\psi\rangle$ is a coherent superposition of spins in many mode configurations (unoccupied modes are represented by open circles). In each configuration particles are localized in mode space, with spin model Hamiltonian \hat{H}_i^{sm} . Coherences between the configurations capture motional effects.

This quench protocol is illustrated in Fig. 5.1(a). The spin-dependence of the trapping potential $V^{\alpha=\uparrow,\downarrow}(x)$ creates an inhomogeneity between the spin species, allowing contact s -wave collisions to occur. Expanding the field operators in the basis of single-particle eigenstates $\phi_n^\alpha(x)$ with associated creation operator $\hat{c}_{n\alpha}^\dagger$ and defining the interaction parameter $u_{\uparrow\downarrow} = 2a_s/(m_a a_H a_\perp^2)$, \hat{H}^{int} becomes $u_{\uparrow\downarrow} \sum_{nmpq} A_{nmpq} \hat{c}_{n\uparrow}^\dagger \hat{c}_{m\uparrow} \hat{c}_{p\downarrow}^\dagger \hat{c}_{q\downarrow}$, where $A_{nmpq} = a_H \int dx \phi_n^\uparrow(x) \phi_m^\uparrow(x) \phi_p^\downarrow(x) \phi_q^\downarrow(x)$.

To model two classes of experiments [9–11] and [12–15], we consider spin-dependent potentials of the form $V^{\alpha=\uparrow,\downarrow}(x) = V^0(x) + \Delta V^\alpha(x)$, with $\Delta V^\alpha(x)$ generated by a magnetic field with a constant gradient, $\Delta V^\alpha(x) = \pm Bx$, or a linear gradient, $\Delta V^\alpha(x) = \pm m_a \omega_B^2 x^2/2$. In both cases \hat{H}^{sp} can be written as:

$$\hat{H}^{sp} = \sum_n \left[\bar{\omega}(n+1/2) \hat{N}_n + \Delta\omega(n+1/2) \hat{\sigma}_n^Z \right], \quad (5.3)$$

with $\hat{N}_n = \hat{c}_{n\uparrow}^\dagger \hat{c}_{n\uparrow} + \hat{c}_{n\downarrow}^\dagger \hat{c}_{n\downarrow}$, and $\{\hat{\sigma}_n^X, \hat{\sigma}_n^Y, \hat{\sigma}_n^Z\} \equiv \sum_{\alpha,\beta} \hat{c}_{n\alpha}^\dagger \vec{\sigma}_{\alpha\beta} \hat{c}_{n\beta}$ where $\vec{\sigma}$ is a vector of Pauli matrices. The constant gradient shifts the trap for spin up (down) by x_0 ($-x_0$), with $x_0 = \frac{B}{m_a \omega^2}$, but does not change the frequency; $\bar{\omega} = \omega$ and $\Delta\omega = 0$. In a noninteracting gas the \downarrow and \uparrow densities and the magnetization oscillate at frequency ω due to this motion [16, 17]. A linear gradient adds an additional harmonic potential term resulting in different trap frequencies for the two spins: $\bar{\omega} = (\omega^\uparrow + \omega^\downarrow)/2$ and $\Delta\omega = (\omega^\uparrow - \omega^\downarrow)/2$. The non-interacting spin densities undergo a breathing

motion in their respective traps, leading to oscillations in the total magnetization [16]. A finite $\Delta\omega$ causes dephasing through rotations of the magnetization in the XY plane with mode-dependent rates.

5.2 The generalized spin model approximation

The quench of the trapping potential to a spin-dependent form projects the initially polarized state, which we take to be the ground state in this work, onto the eigenmode basis of \hat{H}^{sp1} . The resulting state $|\psi\rangle_{t=0}$ is a coherent superposition of many product states, each characterized by a set of populated modes $\mathbf{n}^i = \{\mathbf{n}_1^i, \mathbf{n}_2^i, \dots, \mathbf{n}_N^i\}$: $|\psi\rangle_{t=0} = \sum_i d_i \prod_{j=1}^N \hat{c}_{\mathbf{n}_j^i \sigma_j}^\dagger |0\rangle$. The coefficients d_i are determined by the change of basis associated with the eigenstates of $V^0(x)$ and $V^{\alpha=\uparrow,\downarrow}(x)$.

Our key approximation is that single particle modes either remain the same or are exchanged between two colliding atoms. Exact numerical calculations confirm the validity of this approximation in the weakly interacting regime. For each set \mathbf{n}^i the resulting total Hamiltonian takes the form of an XXZ spin model,

$$\hat{H}_{\mathbf{n}^i}^{sm} = \hat{H}_{\mathbf{n}^i}^{sp} - \frac{u_{\uparrow\downarrow}}{4} \sum_{n \neq m \in \mathbf{n}^i} \sum_{\nu=X,Y,Z} J_{nm}^\nu \hat{\sigma}_n^\nu \hat{\sigma}_m^\nu, \quad (5.4)$$

plus additional small density- $\hat{\sigma}^Z$ couplings which will be discussed in Section 5.6. Here, the Ising, $J_{nm}^Z \equiv A_{nnmm}$, and exchange, $J_{nm}^X = J_{nm}^Y = J_{nm}^\perp \equiv A_{nnmmn}$, couplings result from the overlap between the \uparrow and \downarrow single-particle eigenstates and are long-ranged ($\sim 1/\sqrt{|n-m|}$) in each direction (x, y, z) . In this approximation, each sector \mathbf{n}^i evolves independently, but with \mathbf{n}^i -dependent parameters, under Eq. 5.40. When computing observables, we account for both the interaction-driven spin dynamics within each \mathbf{n}^i sector, as well as the single particle dynamics determined from the coherences between sectors.

¹ The initial $2N$ spin-independent populated modes $(0, \dots, N-1$ for both spin-up and spin-down) are projected onto $2\tilde{N}$ modes, where the \tilde{N} modes for spin up are different than the \tilde{N} for spin down, and \tilde{N} is chosen such that the initial state is reproduced to an error of 10^{-16} in the norm

5.3 Spin observables

The local and collective magnetizations are given by $\hat{\mathcal{S}}(x) = \frac{1}{2} \sum_{nm, \alpha, \beta} \phi_n^\alpha(x) \phi_m^\beta(x) (\hat{c}_n^{\dagger\alpha} \vec{\sigma}_{\alpha\beta} \hat{c}_m^\beta)$ and $\hat{\mathcal{S}} = \int dx \hat{\mathcal{S}}(x)$. Fig. 5.2 summarizes the results for a constant gradient with $N = 10$.² At short times the collective magnetization $\langle \hat{\mathcal{S}}^X \rangle$ ((a) and (e)) exhibits characteristic single-particle oscillations at frequency ω ; these quickly dephase and are modulated by a global envelope with a longer time scale. Similar behavior is observed for the local magnetizations $\langle \hat{\mathcal{S}}^{X,Y,Z}(x) \rangle$ (b-d, f-h). Although the total $\langle \hat{\mathcal{S}}^{Y,Z} \rangle$ magnetizations are zero at all times, the local quantities $\langle \hat{\mathcal{S}}^{Y,Z}(x) \rangle$ evolve due to coherences between mode configurations. Their dynamics, however, are damped by interactions.

The dynamics can be understood as follows. For spin independent potentials, $J_{nm}^Z = J_{nm}^\perp$ and $\Delta\omega = 0$. The Hamiltonian $\hat{H}_{\mathbf{n}^i}^{sm}$ is SU(2) symmetric and commutes with $\hat{\mathcal{S}}^2$, where $\hat{\mathcal{S}} \equiv \frac{1}{2} \sum_n \hat{\sigma}_n$, and so its eigenstates can be labelled by the total spin S . When a gradient is applied, the SU(2) symmetry is broken by terms $\Delta_{nm} = J_{nm}^Z - J_{nm}^\perp$ ($\Delta\omega = 0$ for a constant gradient), and the Hamiltonian can be rewritten as $\hat{H}_{\mathbf{n}^i}^S + \hat{H}_{\mathbf{n}^i}^\delta$, where

$$\begin{aligned} \hat{H}_{\mathbf{n}^i}^S &= E_{\mathbf{n}^i} - \frac{u_{\uparrow\downarrow}}{4} \sum_{n \neq m \in \mathbf{n}^i} \left[J_{nm}^\perp \vec{\sigma}_n \cdot \vec{\sigma}_m + \bar{\Delta} \hat{\sigma}_n^Z \hat{\sigma}_m^Z \right], \\ \hat{H}_{\mathbf{n}^i}^\delta &= -\frac{u_{\uparrow\downarrow}}{4} \sum_{n \neq m \in \mathbf{n}^i} \delta_{nm} \hat{\sigma}_n^Z \hat{\sigma}_m^Z, \end{aligned} \quad (5.5)$$

$E_{\mathbf{n}^i} = \bar{\omega} \sum_{n \in \mathbf{n}^i} (n + 1/2)$ is a constant, $\bar{\Delta}$ is the average value of Δ_{nm} , and $\delta_{nm} = \Delta_{nm} - \bar{\Delta}$. $\hat{H}_{\mathbf{n}^i}^S$ commutes with $\hat{\mathcal{S}}^2$ so only $\hat{H}_{\mathbf{n}^i}^\delta$ induces transitions between manifolds of different S . For a sufficiently weak gradient, and $\delta_{nm} \ll J_{nm}^\perp$, a large energy gap G , which we call the **Dicke gap**, opens between the $S = N/2$ ‘‘Dicke’’ manifold and the $S = (N/2 - 1)$ ‘‘spin-wave’’ manifold. The state of the system begins in the Dicke manifold, and it remains there when terms in $\hat{H}_{\mathbf{n}^i}^\delta$ are small compared to this gap [134]. Dynamics resulting from the collective Ising term in $\hat{H}_{\mathbf{n}^i}^S$ is given by $\langle \hat{\mathcal{S}}^X \rangle_{\mathbf{n}^i} = \frac{N}{2} \cos^{N-1}(u_{\uparrow\downarrow} \bar{\Delta} t)$, and $\langle \hat{\mathcal{S}}^{Y,Z} \rangle_{\mathbf{n}^i} = 0$. Since the interaction parameters J_{nm}^Z and J_{nm}^\perp vary slowly with parameter index, the dynamics of $\langle \hat{\mathcal{S}}^X \rangle_{\mathbf{n}^i}$ is approximately the same for all i ,

² All simulations are for $N = 10$ unless stated otherwise.

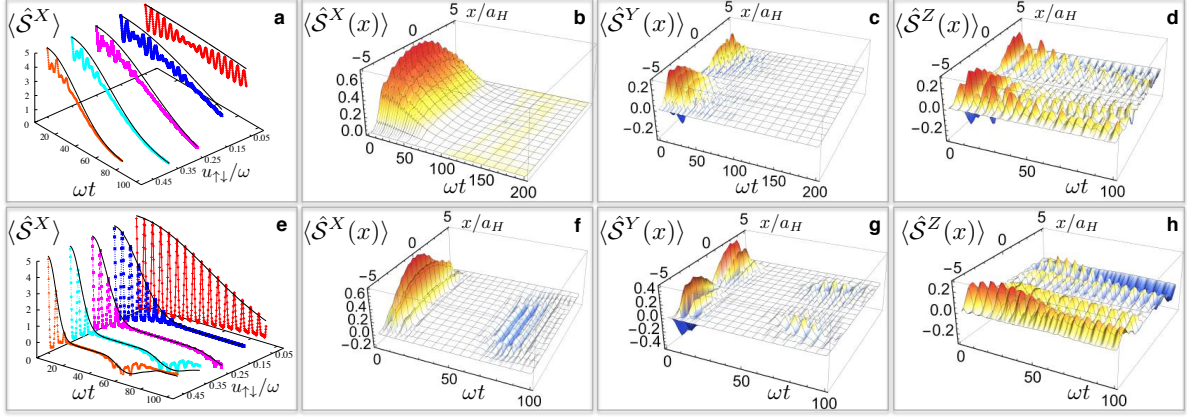


Figure 5.2: Magnetization dynamics for a constant gradient. Collective $\langle \hat{S}^X \rangle$ for a $x_0 = 0.1a_H$ (a) (and $x_0 = 0.3a_H$ (e)) displays global interaction-induced demagnetization, which damps single-particle oscillations. Collective (generic) Ising solutions, black lines, give the demagnetization envelopes. Local magnetizations $\langle \hat{S}^{X,Y,Z}(x) \rangle$ with $x_0 = 0.1a_H$ (b-d) (and $x_0 = 0.3a_H$ f-h) reflect similar behavior, both shown with $u_{\uparrow\downarrow} = 0.35\omega$.

and a single configuration $\mathbf{n}^0 \equiv \{0, 1, \dots, N-1\}$ well reproduces the demagnetization envelope (Fig. 5.2(a)).

For strong gradients, exchange processes are suppressed and the effective interaction Hamiltonian becomes a generic Ising model $\hat{H}_{\mathbf{n}^i}^{\text{Ising}} = -\frac{u_{\uparrow\downarrow}}{4} \sum_{n \neq m \in \mathbf{n}^i} J_{nm}^Z \hat{\sigma}_n^Z \hat{\sigma}_m^Z$, which also admits a simple expression for the spin magnetization dynamics [128–131] $\langle \hat{S}^X \rangle_{\mathbf{n}^i} = \sum_{n \in \mathbf{n}^i} \prod_{m \neq n \in \mathbf{n}^i} \cos(u_{\uparrow\downarrow} J_{nm}^Z t)$. In this limit the demagnetization envelope can be captured by the \mathbf{n}^0 realization of the generic Ising solution (Fig. 5.2(e)).

Short time dynamics of an XXZ Hamiltonian [135] is given by $\langle \hat{S}^X \rangle = \langle \hat{S}^X \rangle_{t=0} (1 - (t/\tau_M)^2) + O(t^3)$, where we define τ_M as the demagnetization time. By analyzing the scaling of the interaction parameters we find that $\tau_M \sim (Nu_{\uparrow\downarrow}x_0^2)^{-1}$, which agrees well the numerical scaling $\sim u_{\uparrow\downarrow}^{-1}x_0^{-2}N^{-0.823}$. Similar behavior was reported in Ref. [9] in the weakly-interacting regime³.

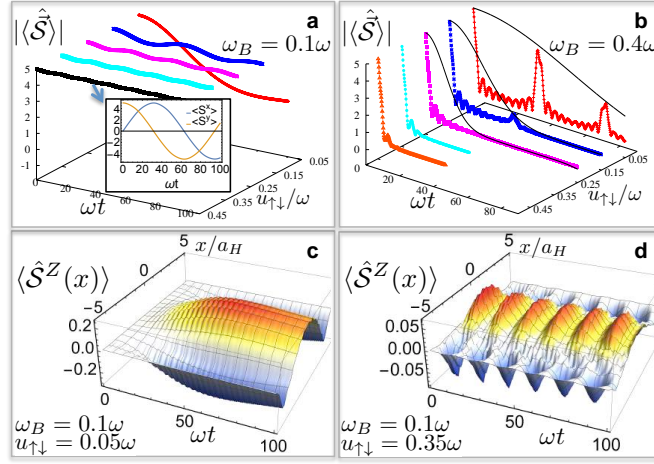


Figure 5.3: Dynamics for a linear gradient. (a) Spin self-rephasing for $\omega_B = 0.1\omega$: as interactions increase, demagnetization is suppressed and $\langle \hat{\mathcal{S}} \rangle$ precesses collectively in the XY plane (inset). (b) Dynamics in a strong linear gradient show damping of large single particle oscillations, where the damping envelopes are given by the generic Ising solutions. (c, d) Dynamics of the spin population difference $\langle \hat{S}^Z(x) \rangle$ in real space, showing oscillations where spin up is concentrated towards the center of the cloud and spin down is concentrated towards the edge of the cloud. The rate of these oscillations is proportional to the interaction strength. The results in (c, d) are what is known as “spin segregation” and will be discussed in greater detail in Section 5.7.

5.4 Dynamics in a linear gradient

Fig. 5.3 (a) shows the numerically-obtained total magnetization vs. interactions for a weak linear gradient. The magnetization remains nearly constant for sufficiently strong interactions, and the collective spin dynamics is a global precession in the XY plane (inset). This self-rephasing effect was experimentally reported in Ref. [12], and the spin model provides a simple interpretation. For a system in a weak gradient, the single-particle term $\propto \Delta\omega$ is the largest inhomogeneity. In this limit the Hamiltonian simplifies to $-\frac{u_{\uparrow\downarrow}}{4} \sum_{n \neq m} J_{nm}^{\perp} \vec{\sigma}_n \cdot \vec{\sigma}_m + \sum_n \Delta\omega(n + \frac{1}{2}) \hat{\sigma}_n^Z$. When $\Delta\omega N_{\mathbf{n}i}^{\text{ave}} \ll G$, where G is the Dicke gap and $N_{\mathbf{n}i}^{\text{ave}}$ is the average mode occupation, most of the population remains in the Dicke manifold. After projecting \hat{H}^{sp} onto the Dicke states, the dynamics is a collective precession in the XY plane of the generalized Bloch vector, i.e $\langle \hat{S}^{\pm}(t) \rangle = \langle \hat{S}^{\pm}(0) \rangle e^{\pm 2it(N_{\mathbf{n}i}^{\text{ave}} + \frac{1}{2})\Delta\omega}$, with $\hat{S}^{\pm} = \hat{S}^X \pm i\hat{S}^Y$. Demagnetization is suppressed when interactions ($\propto G$) dominate over the dephasing introduced by $\Delta\omega$. Under this condition, a large fraction of the population stays in the Dicke manifold.

For strong linear gradients exchange is suppressed and the demagnetization envelope is given by the generic Ising solutions. These simulations and predictions are shown in Fig. 5.3(b). Real space dynamics, some of which are shown in Fig. 5.3(c,d) in a linear gradient will be discussed in Section 5.7.

5.5 Correlations

Our approach can be used to compute higher-order correlations, such as the $G^{++}(x, x') = \langle \hat{S}^+(x) \hat{S}^+(x') \rangle - \langle \hat{S}^+(x) \rangle \langle \hat{S}^+(x') \rangle$ correlator shown in Fig. 5.4. Although the system is initially non-interacting, $G^{++}(t=0)$ shows finite anti-bunching correlations near $x \sim x'$ arising from Fermi statistics (mode entanglement) [136, 137]. At later times, correlations behave collectively, a distinct consequence of the long-range character of the spin coupling parameters [138–142].

For a weak constant gradient, the collective Ising model provides a good characterization of

³ We note that the spin echo pulse applied in Refs. [9, 10] modifies the single-particle physics [16], but does not affect the interaction-induced collective demagnetization

the correlation dynamics. For each spin configuration $G_{\mathbf{n}^i}^{++}(x, x'; t) = f_1^i(x, x') \cos^{N-2}(2u_{\uparrow\downarrow}\bar{\Delta}t) - f_2^i(x, x') \cos^{2N-2}(u_{\uparrow\downarrow}\bar{\Delta}t)$, where the functions $f_{1,2}^i(x, x')$ depend on the set of populated modes. G^{++} peaks at the time when the system has completely demagnetized (Fig. 5.4(a)). For a pure spin system with a collective Ising Hamiltonian, the state at this time is a Schrödinger-cat state [143, 144]. For the linear gradient in the self-rephasing regime, we observe collective precession of G^{++} (Fig. 5.4(b)). As interactions decrease or the inhomogeneity increases, correlations are strongly affected by the interplay between single-particle dynamics and interactions. Mode entanglement tends to cause an almost linear spreading of the correlations with time [145–147], while interactions tend to globally distribute and damp those correlations (Fig. 5.4(c,d)). Current experiments are in position to confirm these predictions.

The collective Ising solution gives the connected correlation function

$$G_{\mathbf{n}^i}^{++}(x, x'; t) = f_1^i(x, x') \cos^{N-2}(2u_{\uparrow\downarrow}\bar{\Delta}t) - f_2^i(x, x') \cos^{2N-2}(u_{\uparrow\downarrow}\bar{\Delta}t), \quad (5.6)$$

where the functions $f_{1,2}^i(x, x')$ are given by

$$\begin{aligned} f_1^i(x, x') &= \frac{1}{4} \sum_{nm \in \mathbf{n}^i} \left(\phi_n^\uparrow(x) \phi_n^\downarrow(x) \phi_m^\uparrow(x') \phi_m^\downarrow(x') - \phi_n^\uparrow(x) \phi_n^\downarrow(x') \phi_m^\uparrow(x') \phi_m^\downarrow(x) \right), \\ f_2^i(x, x') &= \frac{1}{4} \sum_{nm \in \mathbf{n}^i} \phi_n^\uparrow(x) \phi_n^\downarrow(x) \phi_m^\uparrow(x') \phi_m^\downarrow(x'). \end{aligned} \quad (5.7)$$

In Fig. 5.5(b) we show the connected correlator $G^{++}(x, x')$ evaluated at $x = 0, x' = 0.5a_H$, along with the analytic solution for the \mathbf{n}^0 mode configuration. The spin model approximation and analytic solution do an excellent job of reproducing the dynamics of the correlation function. For stronger gradients where the generic Ising model is a better description of the dynamics,

$$\begin{aligned} G_{\mathbf{n}^i}^{++}(x, x'; t) &= \\ & \frac{1}{4} \sum_{n,m \in \mathbf{n}^i} \left(\phi_n^\uparrow(x) \phi_n^\downarrow(x) \phi_m^\uparrow(x') \phi_m^\downarrow(x') - \phi_n^\uparrow(x) \phi_n^\downarrow(x') \phi_m^\uparrow(x') \phi_m^\downarrow(x) \right) \prod_{p \neq n, m \in \mathbf{n}^i} \cos(J_{np}^Z t + J_{mp}^Z t) \\ & - \frac{1}{4} \left[\sum_{n \in \mathbf{n}^i} \left(\phi_n^\uparrow(x) \phi_n^\downarrow(x) \right) \prod_{p \neq n \in \mathbf{n}^i} \cos(J_{np}^Z t) \right] \left[\sum_{n \in \mathbf{n}^i} \left(\phi_n^\uparrow(x') \phi_n^\downarrow(x') \right) \prod_{p \neq n \in \mathbf{n}^i} \cos(J_{np}^Z t) \right]. \end{aligned} \quad (5.8)$$

For the linear gradient in the self-rephasing regime, we observe collective precession of the correlation function G^{++} , seen in Fig. 5.4(b). As interactions decrease or the inhomogeneity in-

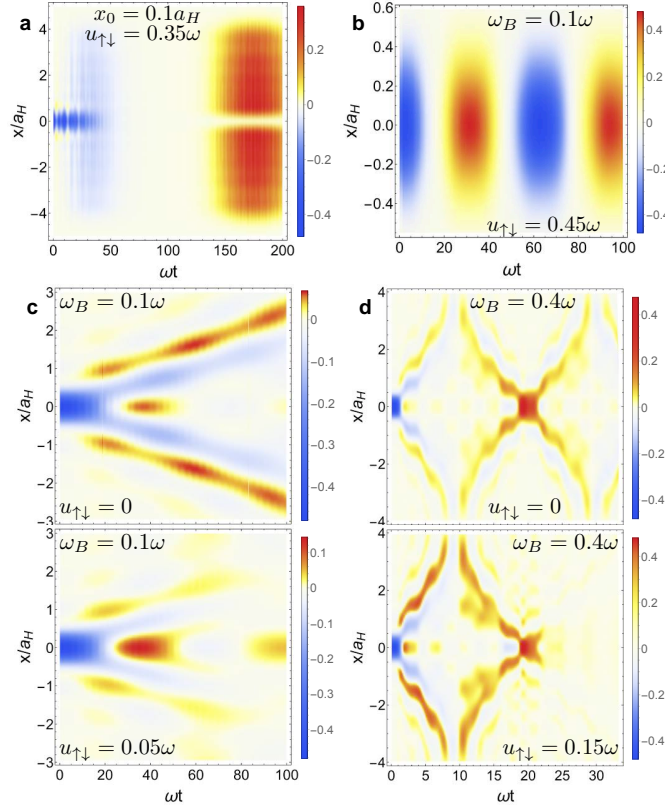


Figure 5.4: (Color online) (a) Real part of the connected correlation function $\text{Re}[G^{++}(x, 0; t)]$ for a weak gradient ($x_0 = 0.1a_H, u_{\uparrow, \downarrow} = 0.35\omega$). Correlations grow collectively due to the long-ranged nature of the interactions in energy space, and peak when the gas is demagnetized. (b) For a linear gradient in the self-rephasing regime ($\omega_B = 0.1\omega, u_{\uparrow, \downarrow} = 0.45\omega$), the connected correlator $\text{Re}[G^{++}(x, 0; t)]$ rotates collectively in the XY plane. For weak interactions or strong gradients (c, d), interactions collectively damp the correlations arising from quantum statistics (upper panels are non-interacting).

creases, mode entanglement tends to cause an almost linear spreading of the correlations with time [145–147]. Interactions tend to globally distribute and damp those correlations, as seen in Fig. 5.4(c, d).

5.6 The generalized spin model approximation: validity and discussion

The spin model approximation ignores interaction-induced changes of the single-particle motional quantum states and is thus only valid when interactions are weak compared to the harmonic oscillator energy spacing, $u_{\uparrow\downarrow} \ll \omega$. The range of validity of this approximation is essentially when the system is “collisionless,” although the exact crossover to the collisional regime depends not only on the interaction energy but also on the strength of the gradient for the quenches discussed in this work [17]. When interactions are weak compared to the oscillator spacing, collisional processes that do not conserve single particle energy can safely be ignored. However, processes that *do* conserve single particle energy, but at the same time change the populated single particle modes, i.e. “resonant” mode changes, can be important for a harmonic trap [1]. While there are a large number of such terms in a harmonic trap due to the equal spacing of energy levels, realistic optical traps in cold atom experiments include anharmonicity which breaks these degeneracies. In higher dimensions, the non-separability of the trapping potential suppresses the redistribution of energy modes in the transverse directions. When the energy differences due to anharmonicity and non-separability of the trapping potential are larger than the interaction strength, these terms will be suppressed. This was shown to be the case for example in Refs. [116, 119, 120] where a pure spin model accurately described the experimental observations. Additionally, at very low temperatures, Pauli blocking can partially prevent mode changing collisions for a spin-polarized sample, as recently observed in Ref. [148]. However, even in a spin-polarized gas, spin- and mode-changing processes may occur, resulting in a doubly occupied mode.

We compare exact diagonalization of the full Hamiltonian, including all interaction-induced mode changes, to the spin model prediction for a small number of particles to test its validity. The results are shown in Fig. 5.5. Panel (a) shows the dynamics of $\langle \hat{S}^X \rangle$ for five particles following

a quench of a constant gradient with $x_0 = 0.1a$ and $u_{\uparrow\downarrow} = 0.35\omega$. The quench induces single-particle dynamics which we observe as fast oscillations at the trapping period. In the spin model approximation, these oscillations are modified due to interactions and become damped at long times. The long time demagnetization and damping of single particle oscillations are well captured by the spin model approximation. Also plotted is the analytic solution for the collective Ising model which captures the demagnetization envelope. Fig. 5.5(c) shows the dynamics for a different initial mode configuration – $\{0, 3, 4, 5, 6\}$ – where Pauli blocking would not prevent several resonant mode changing processes. For instance, the process $(n = 0, m = 3) \rightarrow (n = 1, m = 2)$ is resonant. The spin model approximation works well even in this case.

The initial state after a quench is a superposition of many different product states of spins, in different mode configurations labeled \mathbf{n}^i . Because the interaction parameters vary slowly with parameter index, each \mathbf{n}^i has similar interaction parameters and similar dynamics. Fig. 5.5(d) shows the dynamics for 5 spins evolved under a pure XXZ Hamiltonian, with the same conditions as the dynamics in Fig. 5.5(a). Each curve represents a different “one-hole” mode configuration of five spins that differs from $\mathbf{n}^0 \equiv \{0, 1, 2, 3, 4\}$ by exactly one mode (\mathbf{n}^0 dynamics is also shown). For instance, the initially occupied modes are $\{0, 1, 2, 3, 5\}$ or $\{0, 1, 2, 4, 5\}$, etc. All these configurations contribute to the dynamics after a quench. Since they all have similar dynamics, however, we only need to consider the \mathbf{n}^0 configuration to reproduce the demagnetization envelope. The slow variation of the interaction parameters is illustrated in Fig. 5.5(e,f) where we plot the value of all the parameters J_{nm}^Z and J_{nm}^\perp for modes $n, m = 0$ through $n, m = 15$, sorted by value and labeled by a parameter index. In Fig. 5.5(g,h) we show that the interaction parameters also vary slowly for a stronger gradient, $x_0 = 0.3a_H$. The slow variation of interaction parameters also helps explain why mode changes are relatively unimportant: a mode change simply evolves the system to another mode configuration where the dynamics are nearly the same.

For a linear gradient, the direct interaction integrals are not symmetrical under mode ex-

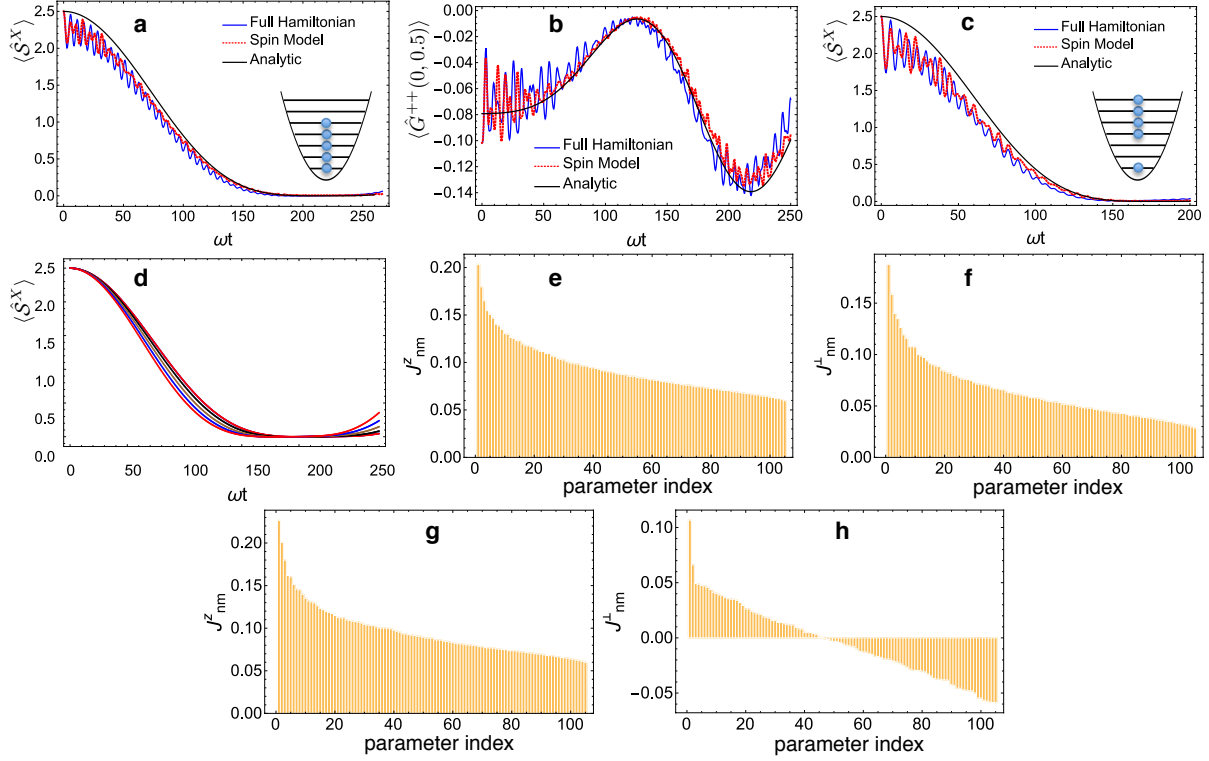


Figure 5.5: Spin model approximation vs. full Hamiltonian for 5 particles with $x_0 = 0.1a$ and $u_{\uparrow\downarrow} = 0.35\omega$. (a) $\langle \hat{S}^X \rangle$ quench dynamics for initial modes $\{0,1,2,3,4\}$, representing a zero temperature gas, along with (b) the connected correlator $G^{++}(x = 0, x' = 0.5a_H)$. Single-particle oscillations are damped by interactions, and the long time dynamics is well-reproduced by the spin model approximation with decay envelope given by the collective Ising solutions. (c) Dynamics for initial modes $\{0,3,4,5,6\}$ representing a more dilute gas. (d) Dynamics of a pure XXZ spin Hamiltonian with the same parameters, for each of the lowest “one-hole” mode configurations. The dynamics of each configuration is very similar, explaining why the dynamics of a quench – involving many configurations – can be approximated by a single configuration. The interaction parameters vary slowly with parameter index, as shown in (e,f) for $x_0 = 0.1a_H$ and (g,h) for $x_0 = 0.3a_H$.

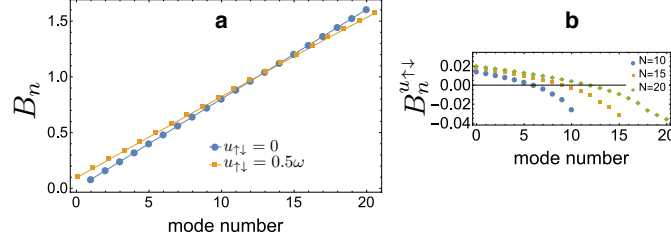


Figure 5.6: (a) Magnitude of the total field $B_n \hat{\sigma}_n^Z$, which contains both single particle ($B_n^{sp} \hat{\sigma}_n^Z$) and interaction ($B_n^{u_{\uparrow\downarrow}} \hat{\sigma}_n^Z$) terms, for a linear gradient with $\Delta\omega = 0.08\omega$. Even for strong interactions ($u_{\uparrow\downarrow} = 0.5\omega$), the Hamiltonian is not significantly modified by the interaction-induced terms $B_n^{u_{\uparrow\downarrow}}$ which appear when $J_{nm}^Z \neq J_{mn}^Z$. (b) For $u_{\uparrow\downarrow} = 0.5\omega$ the $B_n^{u_{\uparrow\downarrow}}$ terms do not grow with particle number.

change: $J_{nm}^Z \neq J_{mn}^Z$. The spin model Hamiltonian includes terms

$$\hat{H}^{as} = \frac{u_{\uparrow\downarrow}}{8} \sum_{n \neq m} (J_{nm}^Z - J_{mn}^Z) \left(\hat{\sigma}_n^Z \hat{N}_m - \hat{\sigma}_m^Z \hat{N}_n \right), \quad (5.9)$$

where $\hat{N}_n = \hat{N}_n^\uparrow + \hat{N}_n^\downarrow$ and $\hat{N}_n^\alpha = \hat{c}_{n\alpha}^\dagger \hat{c}_{n\alpha}$. These terms, when summed over the index m , represent an inhomogeneous magnetic field: $\sum_m \hat{H}^{as} = \sum_n B_n^{u_{\uparrow\downarrow}} \hat{\sigma}_n^Z$. This combines with the single particle field $B_n^{sp} = \Delta\omega(n+1/2)$ to yield a total $\hat{\sigma}_n^Z$ field $B_n \hat{\sigma}_n^Z$, where $B_n = B_n^{sp} + B_n^{u_{\uparrow\downarrow}}$. We find that even for relatively strong interactions ($u_{\uparrow\downarrow} = 0.5\omega$) $B_n^{u_{\uparrow\downarrow}} \ll B_n^{sp}$ for all n , as illustrated in Fig. 5.6, so these additional terms can be neglected. Additionally, $B_n^{u_{\uparrow\downarrow}}$ does not grow with particle number. Although these terms are not essential for the large-scale features of the dynamics, for completeness we include them in numerical simulations.

5.7 Spin segregation

Spin segregation in fermionic gases – a clear, spatial separation of the spin densities, first reported in Ref. [14] – occurs at timescales set by the mean interaction energy, and reverses sign when interactions are switched from attractive to repulsive. When $\Delta\omega N \ll G$, this effect can be understood as the result of off-resonant Rabi oscillations between the $S = N/2$ Dicke states and the $S = (N/2 - 1)$ spin-wave states, which are coupled by the gradient and whose energies are separated by the Dicke gap G . If the gradient is weak, one can ignore coherences developed between mode sectors, and approximate $\phi_n^\uparrow(x) \approx \phi_n^\downarrow(x) = \phi_n(x)$. In this limit the dynamics of the population

difference $\Delta n = n^\uparrow(x) - n^\downarrow(x)$ is approximately

$$\langle \Delta n \rangle = \frac{2\Delta\omega}{G} \sum_{n \in \mathbf{n}^i} \phi_n(x)^2 (n - N_{\mathbf{n}^i}^{\text{ave}}) (\cos(Gt) - 1). \quad (5.10)$$

The spin density changes sign when $n > N_{\mathbf{n}^i}^{\text{ave}}$. Spin segregation occurs as a result since high energy modes on average occupy positions further from the origin than low energy modes.

To understand this result in a many body system we have to consider the coupling of the Dicke states $|N/2, m_z\rangle$ to sectors with different total S . To first order, local spin operators $\hat{\sigma}_n^\alpha$ couple the Dicke states to the spin wave states $|N/2 - 1, m_z, k\rangle$ [117]. We will examine the dynamics within this subspace, assuming the population in the spin wave sector is much smaller than that of the Dicke sector, suppressed by the small parameter $\Delta\omega/u_{\uparrow\downarrow}$. We also assume that the interactions are fully collective for simplicity. The state of the system can be written as

$$|\psi\rangle = \sum_m c_m |m\rangle + \sum_{m,k} d_{mk} |mk\rangle, \quad (5.11)$$

where $|m\rangle$ are the Dicke states, labeled by their magnetization $m = -N/2, \dots, N/2 - 1, N/2$, N is the total number of particles, and $|mk\rangle$ are the spin wave states $|N/2 - 1, m_z, k\rangle$ where $k = 1, \dots, N - 1$. It is useful to define the matrix elements [117]

$$\begin{aligned} \langle m | \hat{\sigma}_n^Z | m' \rangle &= \frac{2m}{N} \delta_{mm'} \\ M_{mm'k}^n &= \langle m | \hat{\sigma}_n^Z | m'k \rangle = 2e^{2\pi i k n / N} \sqrt{\frac{(N/2)^2 - m^2}{N^2(N-1)}} \delta_{m,m'} \sim \frac{1}{\sqrt{N}}, \\ M_{mk}^n &\equiv M_{mmk}^n, \\ P_{mkm'k'}^n &= \langle mk | \hat{\sigma}_n^Z | m'k' \rangle = \left(-2e^{2\pi i (k' - k)n / N} + N\delta_{k,k'} \right) \frac{2m}{N(N-2)} \delta_{mm'} \sim \frac{1}{N}. \end{aligned} \quad (5.12)$$

(Note that “ n ” on the matrix elements is a superscript and not a power.) The M and P matrix elements scale differently with N such that the M elements will dominate in the thermodynamic limit.

We take the Heisenberg (weak gradient) limit of the interaction Hamiltonian combined with the single particle Hamiltonian which contains inhomogeneous terms $n\Delta\omega\hat{\sigma}_n^Z$ which induce transi-

tions outside of the Dicke Manifold:

$$\hat{H} = -\frac{u_{\uparrow\downarrow}}{4} \sum_{n \neq m} J_{nm}^{\perp} \vec{\sigma}_n \cdot \vec{\sigma}_m + \sum_n \left[\bar{\omega}(n+1/2) \hat{N}_n + \Delta\omega(n+1/2) \hat{\sigma}_n^Z \right], \quad (5.13)$$

We assume all the spin wave states have zero energy and the Dicke manifold is offset by the Dicke gap G . In the basis of Dicke and spin wave states the Hamiltonian is

$$\begin{aligned} \hat{H} = \\ E_{\bar{n}}^0 - G \sum_m |m\rangle \langle m| + \sum_n \Delta\omega(n+1/2) \sum_{m,m',k,k'} (M_{mk}^n |m\rangle \langle mk| + P_{mkm'k'}^n |mk\rangle \langle m'k'| + \text{H.c.}) . \end{aligned} \quad (5.14)$$

Where $E_{\bar{n}}^0 = N\bar{\omega}(\bar{n}+1/2)$, which depends on the set of occupied modes and will contribute an additional dynamical phase to $|\psi\rangle$ which will not contribute to the dynamics. We can use the fact that $M_{mk}^n \gg P_{mkm'k'}^n$ for $N \gg 1$ and drop the $P_{mkm'k'}^n$ terms. The Schrodinger equation implies

$$\begin{aligned} i\dot{c}_m &= -Gc_m + \sum_n \Delta\omega(n+1/2) M_{mk}^n d_{mk} \\ i\dot{d}_{mk} &= \sum_n \Delta\omega(n+1/2) M_{mk}^{n*} c_m. \end{aligned} \quad (5.15)$$

Assuming the population stays mostly in the Dicke manifold implies $c_m \gg d_{mk}$. Using this and $\Delta\omega \ll 1$ the equation of motion for c_m can thus be approximated as $i\dot{c}_m = -Gc_m$. With this additional approximation,

$$\begin{aligned} c_m(t) &= c_m(0) e^{iGt} \\ d_{mk}(t) &= \sum_n \Delta\omega(n+1/2) \frac{c_m(0) M_{mk}^{n*}}{G} (1 - e^{iGt}), \end{aligned} \quad (5.16)$$

where for a spin polarized sample initially pointing in the X -direction, the Dicke state coefficients are

$$c_m(0) = \sqrt{\frac{1}{2^N} \binom{N}{\frac{N}{2} + m}}. \quad (5.17)$$

The expectation of a generic spin operator is

$$\begin{aligned} \langle \hat{S}^\alpha \rangle &= \sum_{m,m'} c_m^* c_{m'} \langle m | \hat{S}^\alpha | m' \rangle + \sum_{m,k,m'} d_{mk}^* c_{m'} \langle mk | \hat{S}^\alpha | m' \rangle + \\ &+ \sum_{m,m',k'} c_m^* d_{m'k'} \langle m | \hat{S}^\alpha | m'k' \rangle + \sum_{m,k,m',k'} d_{mk}^* d_{m'k'} \langle mk | \hat{S}^\alpha | m'k' \rangle. \end{aligned} \quad (5.18)$$

Note that $d_{mk}^* d_{m'k'} \ll c_m^* d_{m'k'}$ so we ignore those terms. In our case we have

$$\begin{aligned} \langle \hat{\sigma}_{n'}^Z \rangle &= \frac{4\Delta\omega}{2^N N^2 (N-1)G} \sum_{n,m,k} (n+1/2) \binom{N}{\frac{N}{2}+m} ((N/2)^2 - m^2) e^{2\pi i k(n-n')/N} (e^{iGt} - 1) + \text{H.c.} \\ &= \frac{2\Delta\omega}{G} (n' - N_{\mathbf{n}^i}^{\text{ave}}) (\cos(Gt) - 1). \end{aligned} \quad (5.19)$$

where $N_{\mathbf{n}^i}^{\text{ave}}$ is the average mode number of the set of occupied modes \mathbf{n}^i . (In the above derivation the spin label n was arbitrary and the results hold for any configuration \mathbf{n}^i of N total spins.) Notice that the dynamics of $\sigma_{n'}^Z$ depends linearly on n' and changes sign when $n' > N_{\mathbf{n}^i}^{\text{ave}}$: high energy modes evolve differently from low energy modes, which is the origin of spin segregation.

We now proceed to use the spin model framework to model the segregation observed in Ref. [14]. Although the measurements were done in the high temperature regime, we first determine the role of single particle motion by modeling a simpler 1D case at zero temperature with the same effective parameters. This case can be exactly solved with t-DMRG and Figs. 5.3(b,c) show the dynamics of $(n^\uparrow(x) - n^\downarrow(x))/n_0$, where $n_0 = (n^\uparrow(0) + n^\downarrow(0))/2$. Single particle motion is negligible, and the dynamics is closely approximated by Eq. 5.10. This information allows us to model the actual experiment with a pure spin model. At the high temperature of the experiment, the Dicke gap significantly decreases, however, Eqn. 5.10 remains valid at short times when the majority of the population is in the Dicke manifold. The segregation obtained from a thermal average of Eqn. 5.10 well reproduces the experiment as shown in Fig. 3d. For this calculation the only free parameter is the asymptotic value of the density imbalance⁴. The population difference saturates due to dephasing associated with the thermal spread of the G values.

We are interested in the $\langle \hat{\sigma}^Z(x) \rangle$ density defined as

$$\langle \hat{\sigma}^Z(x) \rangle = \sum_{n \in \mathbf{n}^i} \phi_n(x)^2 \langle \hat{\sigma}_n^Z \rangle = \frac{2\Delta\omega}{G} (\cos(Gt) - 1) \sum_{n \in \mathbf{n}^i} (n - N_{\mathbf{n}^i}^{\text{ave}}) \phi_n(x)^2. \quad (5.20)$$

In Fig. 5.7 this formula is compared to a numerical DMRG simulation at zero temperature, with parameters taken from [Du2008]. Up to long times ($t = 100/\omega \approx \pi/G$) Eq. 5.20 differs from the numerics by at most 10%.

⁴ The asymptotic value of the spin density imbalance is chosen to be 0.4, which matches the experimental values from 500-1000ms. Relaxation due to other decoherence mechanisms occurs at ~ 2 s.

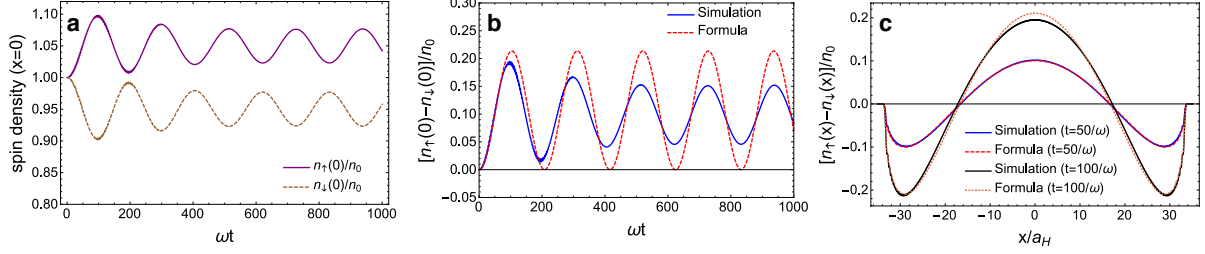


Figure 5.7: Spin segregation dynamics at zero temperature with parameters taken from [Du 2008]. (a) DMRG simulation of the time evolution of the spin densities $n_\alpha(x)$, $\alpha = \uparrow, \downarrow$, at the center of the trap ($x = 0$) normalized by $n_0 = (n_\uparrow(0) + n_\downarrow(0))/2$. (b) Simulated time evolution of $(n_\uparrow(0) - n_\downarrow(0))/n_0$ compared with the analytic formula in Eq. 5.20. The formula accurately predicts the timescale of the oscillation over many periods, and accurately captures the amplitude for about one oscillation period, whose timescale is set by the gap G . The damping seen in the numerics comes from leakage of population outside of the Dicke/spin-wave manifolds. (c) Difference in cloud profiles $(n_\uparrow(x) - n_\downarrow(x))/n_0$ at $t = 50/\omega$ and $t = 100/\omega$: Eq. 5.20 predicts the cloud shape to within about 10%.

5.7.1 Zero temperature spin density profile

At zero temperature the fermions occupy modes $0, \dots, N-1$ and the density profile is given by

$$P_N(x) \equiv \sum_{n=0}^{N-1} \phi_n(x)^2 = \frac{e^{-x^2}}{\sqrt{\pi}} \frac{1}{N!2^N} [(N+1) H_n^2(x) - N H_{N-1}(x) H_{N+1}(x)]. \quad (5.21)$$

In the limit of a large number of particles, this profile is approximately equal to the Thomas-Fermi distribution $F_N(x)$:

$$P_N(x) \approx F_N(x) = \frac{R_N^{TF}}{\pi} \sqrt{1 - \left(\frac{x}{R_N^{TF}}\right)^2}, \quad N \gg 1, \quad (5.22)$$

where $R_N^{TF} = \sqrt{2N}$ is the Thomas-Fermi radius. Defining $f(t) = \frac{2\Delta\omega}{G} (\cos(Gt) - 1)$ and applying Eq. 5.20 yields

$$\begin{aligned} \langle \hat{\sigma}^Z(x) \rangle^{T=0} &= f(t) \sum_{n=0}^{N-1} \left(n - \frac{N-1}{2}\right) \phi_n(x)^2 = f(t) \left[\sum_{n=0}^{N-1} n \phi_n(x)^2 - \left(\frac{N-1}{2}\right) \sum_{n=0}^{N-1} \phi_n(x)^2 \right] \\ &= f(t) \left[Q_N(x) - \left(\frac{N-1}{2}\right) P_N(x) \right], \end{aligned} \quad (5.23)$$

where $Q_N(x)$ is defined as

$$\begin{aligned}
Q_N(x) &\equiv \sum_{n=0}^{N-1} n \phi_n(x)^2 = \sum_{n=1}^{N-1} \phi_n(x)^2 + \sum_{n=2}^{N-1} \phi_n(x)^2 + \sum_{n=3}^{N-1} \phi_n(x)^2 + \dots \\
&= \left(N \sum_{n=0}^{N-1} \phi_n(x)^2 \right) - \phi_0(x)^2 - \sum_{n=0}^1 \phi_n(x)^2 - \sum_{n=0}^2 \phi_n(x)^2 - \sum_{n=0}^3 \phi_n(x)^2 - \dots \\
&= NP_N(x) - \sum_{k=1}^{N-1} P_k(x),
\end{aligned} \tag{5.24}$$

so

$$\begin{aligned}
\langle \hat{\sigma}^Z(x) \rangle^{T=0} &= f(t) \left[NP_N(x) - \sum_{k=1}^{N-1} P_k(x) - \left(\frac{N-1}{2} \right) P_N(x) \right] \\
&= \frac{2\Delta\omega}{G} (\cos(Gt) - 1) \left[\left(\frac{N+1}{2} \right) P_N(x) - \sum_{k=1}^{N-1} P_k(x) \right].
\end{aligned} \tag{5.25}$$

We can now approximately evaluate the sum $\sum_{k=1}^{N-1} P_k(x)$ using the Thomas-Fermi profiles:

$$\begin{aligned}
\sum_{k=1}^{N-1} P_k(x) &\approx \\
\sum_{k=1}^{N-1} \frac{R_k^{TF}}{\pi} \sqrt{1 - \left(\frac{x}{R_k^{TF}} \right)^2} &= \frac{1}{\pi} \sum_{k=1}^{N-1} \sqrt{2k - x^2} = \frac{\sqrt{2}}{\pi} \text{Re} \left[\zeta \left(-\frac{1}{2}, 1 - x^2 \right) - \zeta \left(-\frac{1}{2}, N - x^2 \right) \right]
\end{aligned} \tag{5.26}$$

where $\zeta(s, a) \equiv \sum_{k=0}^{\infty} (k+a)^{-s}$ is a generalization of the Riemann zeta function known as the Hurwitz zeta function. Thus we obtain the following approximate analytic solution for the zero-temperature density:

$$\begin{aligned}
\langle \hat{\sigma}^Z(x) \rangle^{T=0} &\approx \\
\frac{2\sqrt{2}\Delta\omega}{\pi G} (\cos(Gt) - 1) &\left\{ \left(\frac{\sqrt{N}(N+1)}{2} \right) \sqrt{1 - \frac{x^2}{2N}} - \text{Re} \left[\zeta \left(-\frac{1}{2}, 1 - x^2 \right) - \zeta \left(-\frac{1}{2}, N - x^2 \right) \right] \right\}.
\end{aligned} \tag{5.27}$$

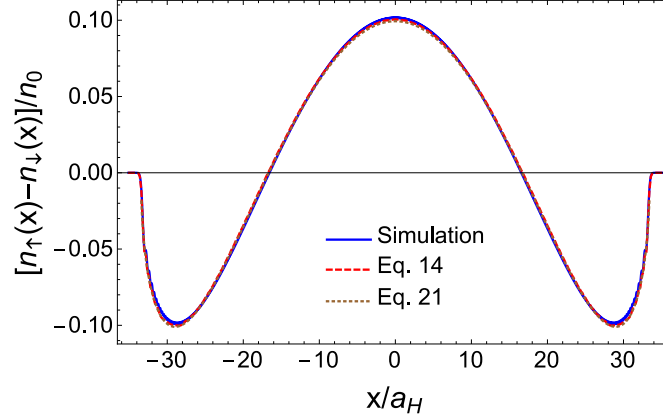


Figure 5.8: Comparison of the cloud profiles $(n_{\uparrow}(x) - n_{\downarrow}(x))/n_0$ at $t = 50/\omega$ between the DMRG simulation, Eq. 5.20 which sums over every oscillator mode, and the approximate analytic expression in Eq. 5.27 which is valid for $N \gg 1$. The three cloud shapes have almost perfect agreement at this time.

5.7.2 High temperature spin density profile

At high temperatures such as those in [Du2009] where $T \approx 4T_F$ we can approximate the cloud shape using Maxwell-Boltzmann statistics. The overall density of the cloud is

$$n(x) = N \sum_{n=0}^{\infty} e^{-\beta\omega(n+1/2)} \phi_n(x)^2 / \mathcal{Z},$$

$$\mathcal{Z} = \sum_{n=0}^{\infty} e^{-\beta\omega(n+1/2)} = \frac{1}{2 \sinh\left(\frac{\beta\omega}{2}\right)} \quad (5.28)$$

This sum is a special case of the Mehler Kernel

$$\sum_{n=0}^{\infty} \frac{H_n(x) H_n(y) w^n}{n!} = \frac{1}{\sqrt{1-4w^2}} \exp\left[\frac{2w(2w(x^2+y^2) - 2xy)}{4w^2 - 1}\right], \quad |w| < \frac{1}{2},$$

$$\rightarrow \sum_n \psi_n^2(x) z^n \equiv \mathcal{M}(x, z) = \frac{1}{\sqrt{\pi(1-z^2)}} \exp\left(\frac{z-1}{z+1} x^2\right) \quad (5.29)$$

This results in the density profile:

$$n(x) = N e^{-\beta\omega/2} \mathcal{M}\left(x, e^{-\beta\omega}\right) / \mathcal{Z} = \frac{2N e^{-\frac{\beta\omega}{2}} \sinh\left(\frac{\beta\omega}{2}\right) e^{-\tanh\left(\frac{\beta\omega}{2}\right) x^2}}{\sqrt{\pi(1 - e^{-2\beta\omega})}}. \quad (5.30)$$

Thermal averaging will damp the Rabi oscillations seen at zero temperature. Inspired by Eq. 5.19, we assume that each $\langle \hat{\sigma}_n^Z \rangle$ evolves as

$$\langle \hat{\sigma}_n^Z \rangle = \frac{2\Delta\omega}{G} (\langle n \rangle - n) \mathcal{F}(t), \quad (5.31)$$

where $\mathcal{F}(t)$ accounts for dephasing and is no longer a pure oscillation. Assuming that $\mathcal{F}(t)$ is independent of n , we can calculate the $\langle \hat{\sigma}^Z(x) \rangle$ density profile:

$$\begin{aligned}
\langle \hat{\sigma}^Z(x) \rangle &= N \sum_{n=0}^{\infty} e^{-\beta\omega(n+1/2)} \phi_n(x)^2 \langle \hat{\sigma}_n^Z \rangle / \mathcal{Z}, \\
&= \frac{2N\Delta\omega\mathcal{F}(t)}{G} \sum_{n=0}^{\infty} e^{-\beta\omega(n+1/2)} \phi_n(x)^2 (\langle n \rangle - n) / \mathcal{Z}, \\
&= \frac{2N\Delta\omega\mathcal{F}(t)}{G} \sum_{n=0}^{\infty} e^{-\beta\omega(n+1/2)} \phi_n(x)^2 \left[(e^{\beta\omega} - 1)^{-1} - n \right] / \mathcal{Z}, \\
&= \frac{2N\Delta\omega\mathcal{F}(t)}{G} \left[(e^{\beta\omega} - 1)^{-1} \sum_{n=0}^{\infty} e^{-\beta\omega(n+1/2)} \phi_n(x)^2 / \mathcal{Z} - \sum_{n=0}^{\infty} e^{-\beta\omega(n+1/2)} n \phi_n(x)^2 / \mathcal{Z} \right], \\
&= \frac{2N\Delta\omega\mathcal{F}(t)}{G} \left[\frac{(e^{\beta\omega} - 1)^{-1} n(x)}{N} - \sum_{n=0}^{\infty} e^{-\beta\omega(n+1/2)} n \phi_n(x)^2 / \mathcal{Z} \right], \\
&= \frac{2N\Delta\omega\mathcal{F}(t)}{G} \left[\frac{(e^{\beta\omega} - 1)^{-1} n(x)}{N} - e^{-\frac{\beta\omega}{2}} z \frac{\partial}{\partial z} \mathcal{M}(x, z) / \mathcal{Z} \Big|_{z=e^{-\beta\omega}} \right], \\
&= \frac{\Delta\omega\mathcal{F}(t) \left(\coth\left(\frac{\beta\omega}{2}\right) - 2x^2 \right) n(x)}{G (\cosh(\beta\omega) + 1)}. \tag{5.32}
\end{aligned}$$

In the zero temperature case, $\mathcal{F}(t) = 1 - \cos(Gt)$, so we expect the long time behavior of the thermal $\mathcal{F}(t) \rightarrow 1$. Thus we can predict the steady state cloud shape to be

$$\begin{aligned}
\left[\frac{n^\uparrow(x) - n^\downarrow(x)}{(n^\uparrow(0) + n^\downarrow(0))/2} \right]_{t \rightarrow \infty} &= \frac{2\langle \hat{\sigma}^Z(x) \rangle}{n(0)} \Big|_{\mathcal{F}(t) \rightarrow 1} = \frac{2\Delta\omega \left(\coth\left(\frac{\beta\omega}{2}\right) - 2x^2 \right) n(x)}{G (\cosh(\beta\omega) + 1) n(0)}, \\
&= \frac{2\Delta\omega \left(\coth\left(\frac{\beta\omega}{2}\right) - 2x^2 \right) e^{-\tanh(\frac{\beta\omega}{2})x^2}}{G (\cosh(\beta\omega) + 1)}. \tag{5.33}
\end{aligned}$$

This high temperature is only valid when $\Delta\omega/G$. For a thermal cloud the Dicke gap will be significantly smaller than at quantum degeneracy since the density is lower. However, since the system starts in the Dicke manifold, the results are still valid at short times when $|\langle \hat{\sigma}_n^Z \rangle| \ll 1$. A comparison with the thermal cloud taken from [15] is shown in Fig. 5.9. Unfortunately this cloud image was taken at the “long time” of 200ms, but the thermal result still qualitatively predicts the cloud shape at this time.

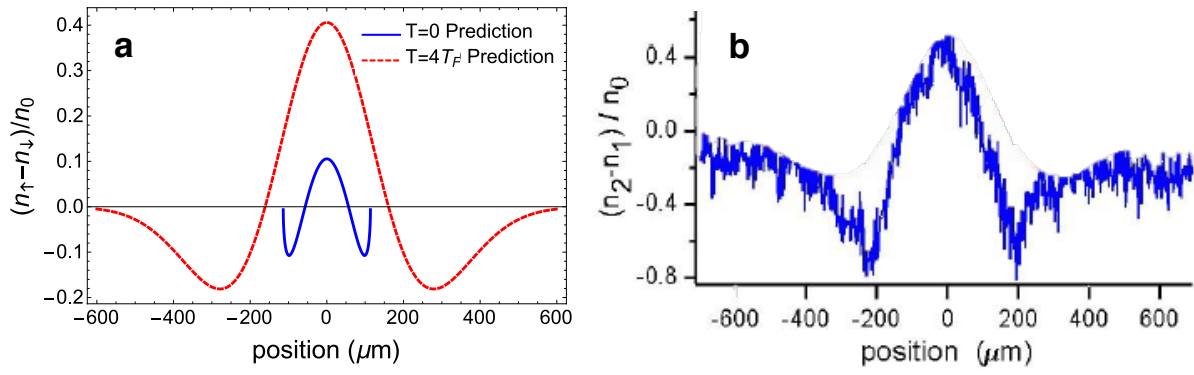


Figure 5.9: (a) Analytic results for the spin segregated cloud shape at both zero temperature and $T = 4T_F$ taken at 200ms. The thermal cloud is shown at a late time, past its time of validity, but nevertheless qualitatively reproduces many of the features seen in the cloud image from [14] shown in (b).

5.7.3 Comparison with experiment in Ref. [14]

To make a comparison with experiment we first benchmarked the system with a one dimensional DMRG simulation of the dynamics to determine the role of single particle motion in the experiment. In this regime DMRG is fully reliable. The experiment in Ref. [14] was conducted with 2×10^5 atoms in a cigar-shaped geometry with trapping frequencies $\{\omega_x, \omega_y, \omega_z\} = \{145 \times 2\pi \text{ Hz}, 4360 \times 2\pi \text{ Hz}, 4360 \times 2\pi \text{ Hz}\}$. A zero temperature version of this gas would fill up the harmonic oscillator modes in the lowest energy configuration, resulting in about 560 particles in the x -direction (occupying modes $n_x = 0$ through $n_x = 559$) and 19-particles in each of the transverse directions. Our simulation used $N = 560$, with $n_x = n_y = 0$ for all the particles, and the results are shown in Fig. 3(b,c) of the main text. From this simulation we concluded that coherences between mode sectors are unimportant since single particle motion is negligible. The lack of single particle motion is due to the very small inhomogeneity along the x -direction: $\Delta\omega = (\omega^\uparrow - \omega^\downarrow) / 2\omega_x = 8.62 \times 10^{-6}$.

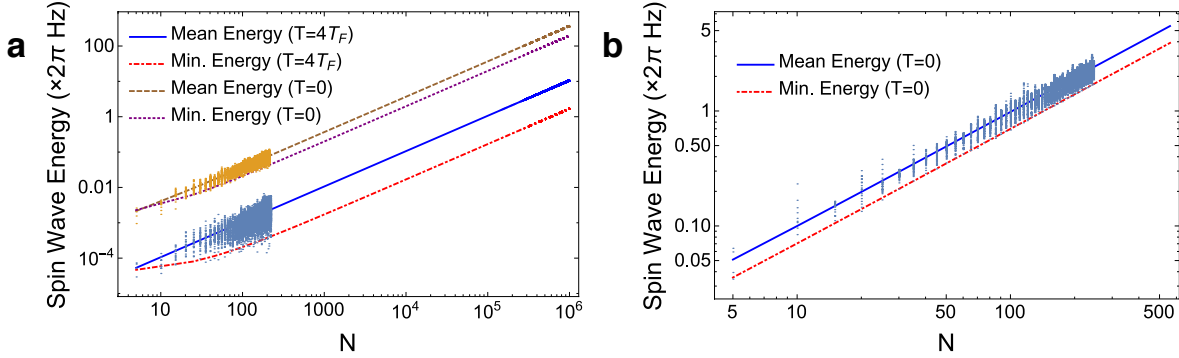


Figure 5.10: (a) Spin wave energies vs. particle number for a 3D system with parameters taken from [14], based on Monte Carlo sampling of harmonic oscillator mode configurations. Extrapolated to $N = 2 \times 10^5$ particles, at $T = 4T_F$ the average energy is $\approx 2.12 \times 2\pi \text{ Hz}$ and the Dicke gap (minimum energy) is $\approx 0.34 \times 2\pi \text{ Hz}$, both much smaller than the single particle inhomogeneity of $4.85 \times 2\pi \text{ Hz}$. For $N = 2 \times 10^5$ particles at $T = 0$ the Dicke gap is $\approx 39.53 \times 2\pi \text{ Hz}$. (b) Spin wave energies vs. particle number for a 1D system at $T = 0$ with parameters taken from [14]. At $N = 560$ the Dicke gap is $3.92 \times 2\pi \text{ Hz}$, much larger than the inhomogeneity of $0.70 \times 2\pi \text{ Hz}$.

The experiment was conducted at a high temperature of $27\mu\text{K} \approx 4T_F$, where T_F is the Fermi temperature. The average harmonic oscillator mode occupations were: $\bar{N}_i \approx \hbar\omega_i/k_B T$:

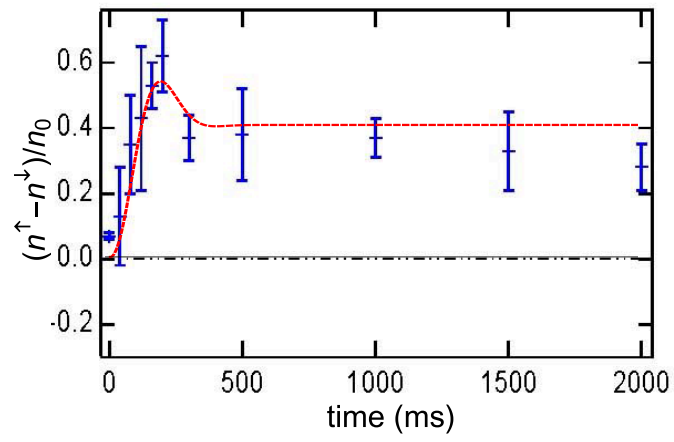


Figure 5.11: Dynamics of the cloud center taken from [14]. The dynamics can be reproduced using a high temperature average.

$\{\bar{N}_x, \bar{N}_y, \bar{N}_z\} = \{3878, 129, 129\}$. We performed a Monte Carlo sampling of the energy separation of the spin-wave and Dicke states, where mode configurations were sampled from a thermal distribution and the spin wave energies were computed and plotted in Fig. 5.10(a). The mean, standard deviation, and minimum (Dicke gap) of the spin wave energies increases linearly with particle number, allowing us to extrapolate to higher particle number. For 2×10^5 particles at $T = 4T_F$ the Dicke gap is $\approx 0.34 \times 2\pi$ Hz, the average energy of the spin wave states is $\approx 2.12 \times 2\pi$ Hz, and the standard deviation of the energies is $\approx 1.13 \times 2\pi$ Hz. A typical magnitude of the coupling via the inhomogeneity is $\bar{N}_x \Delta\omega = 4.85 \times 2\pi$ Hz, much larger than all of these energies. The typical thermal energy per particle is also much higher than all of these energies.

In such a high temperature system the protection from the Dicke gap is significantly suppressed and the long time dynamics are potentially difficult to analyze. However in Ref. [14] the spin density at the cloud center, $(n^\uparrow(x=0) - n^\downarrow(x=0))/n_0$, exhibited a damped oscillation that quickly reached an asymptotic value of $(n^\uparrow(x=0) - n^\downarrow(x=0))/n_0|_{t \rightarrow \infty} \equiv \bar{\Delta n}$. Since initially all the atoms were prepared in the Dicke manifold, the initial transfer of population from the Dicke manifold to the spin wave manifold that happens at short times should be captured by our analytic expressions. To match the short time to the long time dynamics we use the asymptotic value of the population, $\bar{\Delta n}$ as a fitting parameter. We compute the thermal average by sampling our analytic expression over a Gaussian distribution of Dicke gaps. The mean, G_0 , and the standard deviation, ΔG , were extracted by a Monte-Carlo sampling of the gaps evaluated from matrices constructed accordingly to Eq. 8.1. In the limit of a sum of many such oscillations, the dynamics can be approximated as an integral:

$$(n^\uparrow(0) - n^\downarrow(0))/n_0 \approx \bar{\Delta n} \int dG (1 - \cos(Gt)) \frac{e^{-\frac{(G-G_0)^2}{2\Delta G^2}}}{\sqrt{2\pi}\Delta G} = \bar{\Delta n} (1 - \cos(G_0 t)) e^{-\frac{(\Delta G t)^2}{2}}. \quad (5.34)$$

The thermal average of the population imbalance extracted from Eq. 5.34 agrees well with the data from [14] and is shown in Fig. 5.11.

5.8 Scaling of dynamical quantities

The short time dynamics of a generic XXZ Hamiltonian for a state initially polarized along the X direction is [135]

$$\langle \hat{S}^X \rangle = \frac{N}{2} - \frac{(u_{\uparrow\downarrow} t)^2}{16} \sum_{n \neq m} \Delta_{nm}^2 + O(t^3) \approx \langle \hat{S}^X \rangle_{t=0} (1 - (t/\tau_M)^2), \quad \tau_M = \frac{1}{u_{\uparrow\downarrow}} \sqrt{\frac{2N}{\sum_{n \neq m} \Delta_{nm}^2}}, \quad (5.35)$$

where $\Delta_{nm} \equiv J_{nm}^Z - J_{nm}^\perp$ and τ_M is defined as the demagnetization time. For a linear gradient we expand the parameters in x_0/a_H , set $a_H = 1$, and find $\Delta_{nm} = J_{nm}^Z - J_{nm}^\perp \approx 2x_0^2 \Lambda_{nm}$, where

$$\begin{aligned} \Delta_{nm} \approx & nJ_{n-1,m}^0 - 2\sqrt{nm}J_{n-1,n,m-1,m}^0 - 2\sqrt{n(n+1)}J_{n-1,n+1,m,m}^0 + \\ & -2\sqrt{m(m+1)}J_{n,n,m-1,m+1}^0 + (1+m)J_{n,m+1}^0 + mJ_{n,m-1}^0 - 2\sqrt{(m+1)(n+1)}J_{n,n+1,m,m+1}^0 + \\ & + (1+n)J_{n+1,m}^0 + 2\sqrt{n(m+1)}J_{n-1,n,m,m+1}^0 + 2\sqrt{m(n+1)}J_{n,n+1,m-1,m}^0, \end{aligned} \quad (5.36)$$

$J_{nmpq}^0 = \int_{-\infty}^{\infty} dx \phi_n(x) \phi_m(x) \phi_p(x) \phi_q(x)$, and $J_{nm}^0 \equiv J_{nnmm}^0$. The formula $\overline{\Lambda_{nm}} \approx \overline{nJ_{nm}^0} \sim \sqrt{N}$ works well, where $\overline{X_{nm}} \equiv \sum_{n,m \in \mathbf{n}^i} X_{nm} / (N(N-1))$ is the arithmetic average and we have used $\overline{J_{nm}^0} \sim 1/\sqrt{N}$. We find that for $x_0 \ll a_H$, $\overline{\Delta_{nm}} \sim x_0^2 \sqrt{N}$. Further assuming $\overline{\Delta_{nm}^2} \approx (\overline{\Delta_{nm}})^2$, this implies $\tau_M \sim (Nu_{\uparrow\downarrow} x_0^2)^{-1}$. Fig. 5.12(a) shows the scaling of τ_N vs. N . Fitting the dynamics to a Gaussian decay function $A \exp(-t^2/\tau_M^2)$ we find that $\tau_M \sim N^{-.823}$, close to the prediction of N^{-1} . In Fig. 5.12(b) we show the scaling of τ_M vs. x_0 , which agrees well with the x_0^{-2} prediction.

In Fig. 5.12(c,d) we show how $\langle \hat{S}^X \rangle$ depends on N and ω_B , respectively. We use a cosine fitting function $A \cos(\omega_{rot} t)$ to extract the collective Bloch vector precession frequency ω_{rot} and compare with the prediction $N\Delta\omega$. In Fig. 5.12(c) we use $\omega_B = 0.1\omega$ and a relatively large interaction strength $u_{\uparrow\downarrow} = 0.35\omega \gg \Delta\omega$. This is the self-rephasing regime so the prediction works well. In Fig. 5.12(d) we fix $N = 10$ and $u_{\uparrow\downarrow} = 0.35\omega$, and vary ω_B . We see deviations from the prediction for large ω_B , because interactions are not strong enough to protect against population leakage outside of the Dicke manifold.

We can quantify spin segregation by the second moment of the spin density

$$\mu_{2z} = 2 \int_{-\infty}^{\infty} dx x^2 \langle \hat{S}^Z(x) \rangle. \quad (5.37)$$

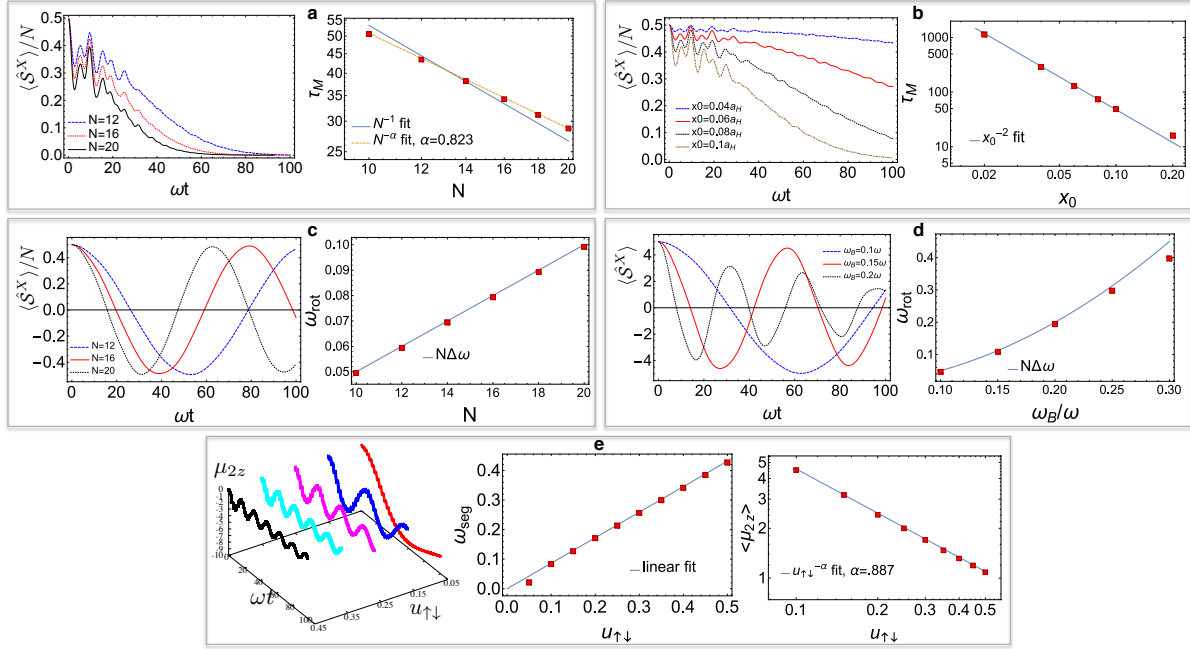


Figure 5.12: Scaling. (a) Dynamics vs. N for a constant gradient $x_0 = 0.1a_H$, from which τ_M is extracted and found to scale like $\tau_M \sim N^{-.823}$, close to the N^{-1} prediction. (b) Dynamics and scaling of τ_M vs. x_0 which agrees well with the prediction x_0^{-2} , for $N = 10$. (c) $\langle \hat{S}^X \rangle / N$ vs. N , when $\omega_B = 0.1\omega$, from which ω_{rot} is extracted and agrees well with the prediction $\omega_{rot} = N\Delta\omega$. (d) $\langle \hat{S}^X \rangle$ vs. ω_B for $N = 10$. Predictions fail when $\omega_B \sim u_{\uparrow\downarrow}$. (All cases are $u_{\uparrow\downarrow} = 0.35\omega$.) (e) μ_{2z} , vs. $u_{\uparrow\downarrow}$; oscillations become more pronounced for stronger interactions. ω_{seg} scales linearly with $u_{\uparrow\downarrow}$. $\langle \mu_{2z} \rangle \sim u_{\uparrow\downarrow}^{-.887}$, close to the prediction of $u_{\uparrow\downarrow}^{-1}$.

For a homogeneous spin distribution, $\mu_{2z} = 0$. When the \uparrow (\downarrow) spins are concentrated more towards the edges of the trap, the sign of μ_{2z} is positive (negative). In Fig. 5.12(e) we plot μ_{2z} dynamics for various interaction strengths, fixing $N = 10$ and $\omega_B = 0.1\omega$. For larger interactions the oscillations become smaller, faster, and less damped, confirming the “Rabi oscillation” behavior of spin segregation. We fit μ_{2z} to an offset cosine function $A + B \cos(\omega_{seg}t + \phi)$ to extract the scaling of the segregation frequency ω_{seg} , and the average value of the segregation, $\langle \mu_{2z} \rangle = A$. A linear fit of ω_{seg} vs. $u_{\uparrow\downarrow}$ with slope of 0.86 confirms linear scaling with interaction energy. We find $\langle \mu_{2z} \rangle \sim u_{\uparrow\downarrow}^{-0.887}$, close to the prediction of $u_{\uparrow\downarrow}^{-1}$.

5.9 Spin collisions in a one dimensional harmonic trap

We now use the spin model approximation to investigate the collision of two ultracold fermionic atomic clouds that are initially prepared in different well-defined spin states. The fermions interact via s -wave interactions through the \uparrow, \downarrow channel (but not the \uparrow, \uparrow or \downarrow, \downarrow channels). We are interested in the dynamics of the spin clouds in space and the propagation of correlations. We focus on the weakly-interacting regime in one dimension where fully-quantum treatments of the interactions are tractable. This work is meant to model the experiments in Refs. [122, 123] in the weakly-interacting, quantum degenerate regime.

Similar to the problems considered earlier in this chapter, we consider s -wave interactions of the form

$$\hat{H}^{Full} = u_{\uparrow\downarrow} a_H \int dx \hat{\rho}_{\uparrow}(x) \hat{\rho}_{\downarrow}(x) \quad (5.38)$$

where the interaction strength $u_{\uparrow\downarrow}$ has units of energy and is proportional to the s -wave scattering length a_s ⁵, $\hat{\rho}_{\alpha}(x) = \hat{\psi}_{\alpha}^{\dagger}(x) \hat{\psi}_{\alpha}(x)$, and $\hat{\psi}_{\alpha}(x)$ is the fermionic field operator for spin α at point x . We can expand the field operators in the basis of single particle eigenstates: $\hat{\psi}_{\alpha}(x) = \sum_n \hat{c}_{n\alpha} \phi_n(x)$.

⁵ $u_{\uparrow\downarrow}$ is calculated by integrating the s -wave pseudopotential $\frac{4\pi\hbar^2 a_s}{m} \delta(r) \frac{\partial}{\partial r} r$ over two tightly-confined directions of a three dimensional harmonic trap.

The interaction Hamiltonian becomes

$$\hat{H}^{Full} = u_{\uparrow\downarrow} \sum_{nmpq} A_{nmpq} \hat{c}_{n\uparrow}^\dagger \hat{c}_{m\uparrow} \hat{c}_{p\downarrow}^\dagger \hat{c}_{q\downarrow} \quad (5.39)$$

where $A_{nmpq} = a_H \int dx \phi_n(x) \phi_m(x) \phi_p(x) \phi_q(x)$. We can invoke the spin model approximation by requiring that the single-particle modes before and after an interaction event either remain the same or are swapped between the two particles. This leaves only parameters $J_{nm} \equiv A_{nnmm} = \int dx \phi_n^\uparrow(x)^2 \phi_m^\downarrow(x)^2$. We define spin operators $\vec{\sigma}_n \equiv \sum_{\alpha,\beta} \hat{c}_{n\alpha}^\dagger \vec{\sigma}_{\alpha\beta} \hat{c}_{n\beta}$, where $\alpha, \beta = \uparrow, \downarrow$, and $\vec{\sigma}$ is the usual Pauli vector $\{\hat{\sigma}^X, \hat{\sigma}^Y, \hat{\sigma}^Z\}$. The resulting spin Hamiltonian is a fully-connected Heisenberg model,

$$\hat{H}^{sm} = -\frac{u_{\uparrow\downarrow}}{4} \sum_{n \neq m} J_{nm} \vec{\sigma}_n \cdot \vec{\sigma}_m. \quad (5.40)$$

Note that since there is no magnetic field gradient in this problem there is no difference between direct and exchange terms in the Hamiltonian.

For our system, the initial state contains many coherences due to its preparation via a quench. The state of the system is a superposition of many configurations of spins, each evolving under a realization of the spin model, and observables measure the coherences between these realizations. We test the spin model approximation with numerical simulations of four particles, shown in Fig. 5.14. Plotted is the center of mass position of the spin- \uparrow cloud as a function of time. In all cases the spin model does not correctly predict the amplitude of center of mass oscillations but it captures the timescales of the growth and decay of those oscillations.

5.9.1 Protocol 1: coherent spin domain wall

In Ref. [123] a spin domain wall was imprinted on a gas of fermions by a spatially-varying Rabi pulse. The gas was prepared entirely in the \downarrow spin state, and then partially illuminated by a “masked laser” π -pulse, which flipped the spins on the right side of the trap to the \uparrow spin state. The intensity was completely dark on the left side, and partially illuminated in the center. The net result was a smoothly-varying spin twist over the extent of the (coherent) domain wall.

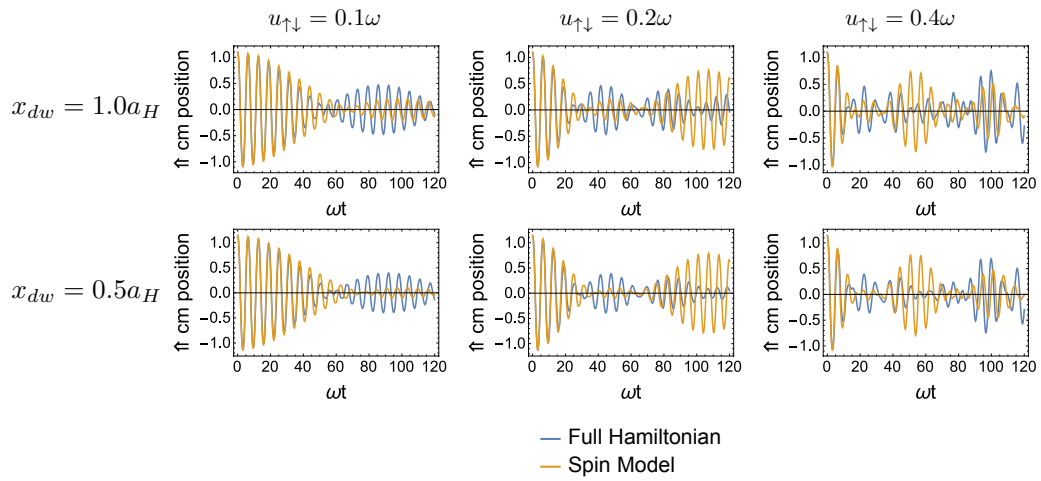


Figure 5.13: Testing the spin model approximation with simulations of four particles for an initial state with a domain wall. Plotted are the center of mass position of the spin- \uparrow cloud as a function of time for two different domain wall sizes ($x_0 = \{1.0a_H, 0.5a_H\}$) and three different interaction strengths ($u_{\uparrow,\downarrow} = \{0.1\omega, 0.2\omega, 0.4\omega\}$). We see that the spin model captures the timescales of the decay and growth of those oscillations, but does not accurately capture the amplitude after the initial collapse.

The initial state is prepared as follows: 1) N fermions are prepared in their \downarrow spin state and loaded into a harmonic trap at zero temperature. They occupy the lowest N modes of the trap $V(x) = \frac{1}{2}m_a\omega x^2$, where m_a is the atomic mass and ω is the trapping frequency. 2) A Rabi pulse with spatial dependence $\Omega(x) = \frac{\Omega_0}{2}(1 + \tanh(x/x_{dw}))$ is applied, where x_{dw} is the extent of the domain wall, for time T such that $\Omega_0 T = \pi$. This function is chosen to imprint the correct spin twist on the sample – spins on the left remain down, spins on the right are flipped up, spins in the middle twist smoothly from down to up.

5.9.2 Protocol 2: coherent displaced initial state

Another way to prepare the system is as follows: 1) N fermions are prepared in their \downarrow spin state and loaded into a harmonic trap at zero temperature. The total spin is then rotated to point along the X -direction, so every atom is in a superposition of both spin states. The trapping potential is then adiabatically changed in a spin-dependent fashion to $V^{\uparrow\downarrow}(x) = \frac{1}{2}m_a\omega(x \mp x_0)^2$, so that the up and down spin densities are shifted by x_0 to the right and left, respectively. This can be accomplished by slowly ramping on a magnetic field gradient. At this point the centers of the clouds are each a distance x_0 from the origin and $2x_0$ from each other. The trap is then quenched back to its initial form $V(x)$ where \uparrow and \downarrow see the same potential.

The quench induces oscillations of the two spin clouds in opposite directions. The single particle dynamics can be computed analytically. A harmonic oscillator eigenstate displaced by distance x_0 has dynamics

$$\psi_n(x_0, x, t) = e^{-i(n+\frac{1}{2})\omega t + i\frac{x_0^2}{a_H^2}(\frac{1}{2}\cos(\omega t)\sin(\omega t) - \sin(\omega t)) + ix_0\sin(\omega t)x/a_H^2} \phi_n\left(\frac{x - x_0\cos(\omega t)}{a_H}\right), \quad (5.41)$$

where a_H is the harmonic oscillator length. It is clear that the center of mass of each cloud moves as $x_{cm}(t) = x_{cm}(0)\cos(\omega t)$. The magnitude and direction of the transverse magnetization is captured by the observable $\hat{S}^+ = \hat{S}^X + i\hat{S}^Y$. For a single particle

$$\langle \hat{S}^+ \rangle_n = \frac{i}{2} \int dx \psi_n^\uparrow(x, t)^* \psi_n^\downarrow(x, t) = \frac{i}{2} \int dx \psi_n(x_0, x, t)^* \psi_n(-x_0, x, t). \quad (5.42)$$

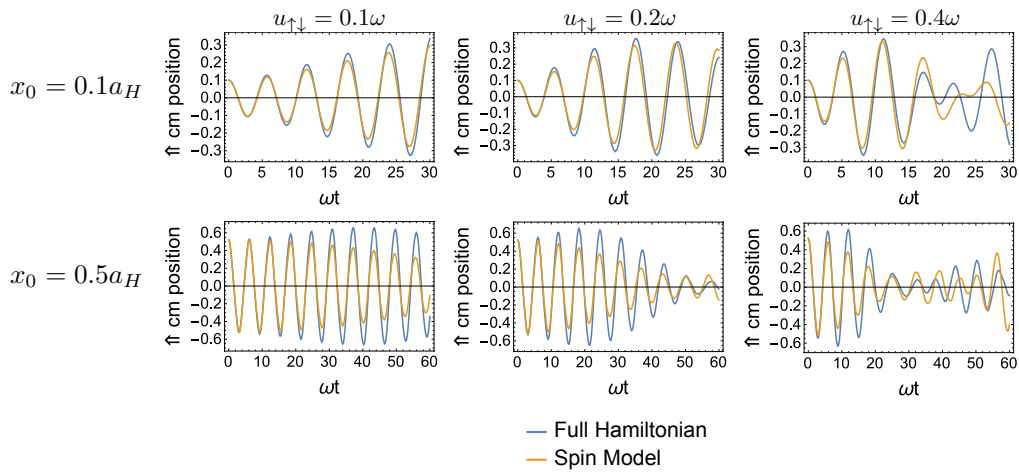


Figure 5.14: Testing the spin model approximation with simulations of four particles for a coherent displaced initial state. Plotted are the center of mass position of the spin- \uparrow cloud as a function of time for two different initial displacements ($x_0 = \{0.1a_H, 0.5a_H\}$) and three different interaction strengths ($u_{\uparrow,\downarrow} = \{0.1\omega, 0.2\omega, 0.4\omega\}$). We see that the spin model captures the timescales of the growth and decay of those oscillations, but does not accurately capture the amplitude of those oscillations.

5.10 Outlook

We have discussed an approach to model the interplay of motional and spin degrees of freedom in weakly interacting fermionic systems in spin-dependent potentials. Simulations reproduce several collective dynamical phenomena that were recently observed in cold gas experiments, and we can understand the physics behind these effects with simple considerations. For larger systems and in higher dimensions, methods such as the discrete truncated Wigner approximation could be utilized [125–127, 149]. Our formulation may also be useful for modeling other spin transport experiments [122, 123].

Fig. 5.4(a) shows the counterintuitive result that in a weakly interacting Fermi gas, the correlations spread globally rather than linearly. Not much is understood about the crossover between the weakly interacting regime and the strongly interacting regime, where a linear spreading is expected. The behavior of the spreading of correlations in a gas is somewhat of a research frontier. Some studies have already appeared in the literature [25, 150, 151], but not from the perspective that there may be a qualitative change as the interaction strength is increased from weak to strong. One of the challenges is that there are not very many techniques that are trustworthy for studying this problem. Some promising strategies are to use short-time perturbation theory, exact diagonalization for small systems, and density matrix renormalization group methods. There are then a number of additional questions that can be explored: What if the interactions are long-ranged? Do the correlations spread in a similar fashion for both Bose and Fermi gases? Does the spin degree of freedom play a role, and if so, would gases with larger spin ($> 1/2$) behave differently? What about gases with anisotropic interactions, such as dipolar gases? An understanding of these phenomena could be potentially useful for future quantum technologies that utilize quantum gases.

Chapter 6

Beyond the Spin Model Approximation

6.1 Introduction

In this chapter we examine in detail effects that occur beyond the spin model approximation which was used throughout this thesis to study interactions in atomic clocks and Fermi gases. We begin with a careful study of the validity of the spin model for two fermionic atoms in an atomic clock. The atoms experience an inhomogeneous rotation due to misalignment of the clock laser and are probed with Ramsey spectroscopy. The inhomogeneous rotation leads to s-wave interactions. We compare the predictions of the spin model to analytic expressions for the dynamics and find that the spin model can fail at times much longer than the trap period. This failure is related to the redistribution of modes in the harmonic trap due to the evenly spaced energy levels. We then discuss how for $N > 2$ resonant mode changes can occur even in a Fermi-degenerate population since interactions can induce spin flips, after which resonant mode changes are no longer blocked by the Pauli exclusion principle. Finally, we re-examine the problem of a Fermi gas with spin-dependent traps and discuss corrections to the spin model approximation.

6.2 The spin model approximation for two atoms in an atomic clock

Ramsey spectroscopy, a technique initially designed to interrogate microwave atomic clocks, has become an important modern tool for probing dynamics of interacting many-body systems with internal (pseudospin) degrees of freedom. Ramsey spectroscopy applies (see Fig. 6.1 (a)) two strong resonant pulses to a system initially prepared in a well-defined pseudospin state, separated

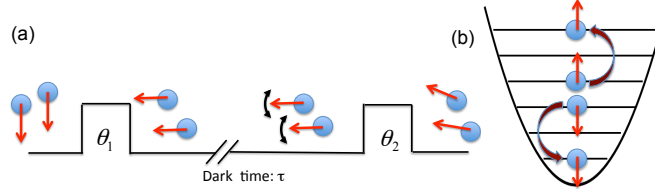


Figure 6.1: (a) Ramsey spectroscopy of two interacting spin-1/2 particles. (b) In a harmonic trap the spectrum degeneracy allows near-resonant mode-changing collisions coupled to the spin dynamics.

by a dark time of free evolution. The first pulse initializes the pseudospin dynamics by preparing the system in a nontrivial superposition of eigenstates, i.e. it introduces a quantum quench [152]. The second pulse reads the coherence or correlations developed during the dark time. Recently, Ramsey spectroscopy has been proposed for extracting real-space and time correlations [153–157], characterizing topological order [70, 158], measuring spin diffusion dynamics in bosonic [12, 13, 118, 120, 159, 160] and fermionic systems [9, 14, 98, 101], and as a means to probe many-body interactions in atomic, molecular, and trapped ion systems [3, 4, 115, 116, 119, 121, 161–163].

Generally speaking, Ramsey spectroscopy measures the collective pseudospin and traces out other external degrees of freedom involved during the free evolution. In most atomic setups the latter are associated with motional degrees of freedom in the harmonic trapping potential and/or lattice potential confining the atoms. The external degrees of freedom can affect the spin dynamics in a non-trivial way, however. A great simplification could be gained if it were possible to decouple the motional and spin degrees of freedom, and reduce the many-body dynamics down to those extracted from a pure interacting spin model. Evidence that this scenario is possible, even far from quantum degeneracy, has been reported in recent experiments [12, 116–121], where the observed spin dynamics corresponded to those of a pure spin Hamiltonian. These observations are opening a path for the investigation of quantum magnetism in atomic systems without the need for ultra-low temperatures. It is thus important to determine the parameter regime in which a pure interacting-spins picture is valid.

In this section we provide insight on the validity of a pure spin model description of Ramsey

spectroscopy by performing exact calculations for fermions with s -wave interactions and an internal pseudospin-1/2 degree of freedom, confined in quasi-1D and quasi-2D harmonic traps. We show that the large degeneracy of the harmonic oscillator spectrum can limit the validity of the spin model to time scales less than the inverse interaction strength, due to resonant collisionally-induced excitation of spatial modes (see Fig. 6.1 (b)). Cold atom experiments are protected from this problem if the temperature is high enough that atoms probe the actual Gaussian shape of the potential which breaks the harmonic spectrum degeneracy. This was shown to be the case for example in Refs. [116, 119, 120] where a pure spin model well described the experimental observations. At very low temperatures, Pauli blocking can also prevent mode changing collisions, as recently observed in Ref. [148]. However, the degeneracy is a concern for intermediate temperatures at which the set of populated levels are effectively harmonic. Here we show that surprisingly, in two dimensions and to first order in the interaction strength, the full two-particle dynamics can be described in terms of an effective spin model with appropriate parameters. Our two-body calculations are not only a first step towards understanding the interplay between spin and particle motion in generic many-body ensembles, but are also directly applicable to optical clocks that interrogate an array of 1D tube-shaped traps, each with fewer than three atoms [49, 117, 164].

6.2.1 Setup

Consider two fermions with internal degrees of freedom $\{\uparrow, \downarrow\}$ corresponding, for instance, to the 1S_0 - 3P_0 electronic levels in alkaline-earth-based optical lattice clocks, and assume their interactions are primarily described by an s -wave pseudo-potential. The atoms are also illuminated by a laser beam detuned by $\delta = \omega_L - \omega_0$ from the atomic transition ω_0 , with wavevector \vec{k} and bare Rabi frequency Ω . The two-particle Hamiltonian is then given by $\hat{H}(\vec{x}_1, \vec{x}_2) = \sum_{i=1,2} \hat{H}_L(\vec{x}_i) + \hat{H}_D(\vec{x}_1, \vec{x}_2)$:

$$\begin{aligned} \hat{H}_L(\vec{x}_i) &= -\frac{\hbar\Omega}{2} e^{-i(\omega_L t - \vec{k} \cdot \vec{x}_i)} \hat{\sigma}_i^+ + \text{H.c.} \\ \hat{H}_D(\vec{x}_1, \vec{x}_2) &= H_{sp}(\vec{x}_1) + H_{sp}(\vec{x}_2) + g\hat{P}_s \delta(\vec{r}) \frac{\partial}{\partial r} r. \end{aligned} \quad (6.1)$$

Here $\hat{H}_L(\vec{x}_i)$ describes the atom-laser interaction: $\hat{\sigma}_i^+$ is the spin raising operator acting on atom i , and H.c. is the Hermitian conjugate. $H_{sp}(\vec{x}_i) = -\hbar^2/(2M)\nabla_i^2 + V(\vec{x}_i) + (\hbar\omega_0/2)\hat{\sigma}_i^z$ is the single particle Hamiltonian with an external potential, V , assumed for simplicity to be independent of the internal state and separable. $H_{sp}(\vec{x}_i)$ has eigenfunctions $\phi_{\mathbf{n}}(\vec{x}_i)$ and eigenenergies $E_{\mathbf{n}}$ with $\mathbf{n} = \{n_x, n_y, n_z\}$. M is the particle's mass and $\hat{\sigma}^z$ the Pauli matrix. $\vec{r} = \vec{x}_1 - \vec{x}_2$ is the relative coordinate, $g = 4\pi\hbar^2 a_s^{\uparrow\downarrow}/M$ and $a_s^{\uparrow\downarrow}$ the 3D s -wave scattering length. $\hat{P}_s = |s\rangle\langle s|$ is the projector into the singlet state, $|s\rangle = \frac{1}{\sqrt{2}}(|\uparrow\downarrow\rangle - |\downarrow\uparrow\rangle)$. Only fermions in the singlet state can interact, while spin triplet states, $|t_{\downarrow\downarrow}\rangle = |\downarrow\downarrow\rangle$, $|t_{\downarrow\uparrow}\rangle = \frac{1}{\sqrt{2}}(|\uparrow\downarrow\rangle + |\downarrow\uparrow\rangle)$, and $|t_{\uparrow\uparrow}\rangle = |\uparrow\uparrow\rangle$ cannot experience s -wave interactions.

6.2.2 The spin model.

The assumptions of the spin model are: if there are no degeneracies in the two-atom non-interacting spectrum, i.e. $(E_{\mathbf{m}} + E_{\mathbf{n}}) = (E_{\mathbf{m}'} + E_{\mathbf{n}'})$ occurs only for $(\mathbf{m}, \mathbf{n}) = (\mathbf{m}', \mathbf{n}')$ or $(\mathbf{m}, \mathbf{n}) = (\mathbf{n}', \mathbf{m}')$, and interactions are treated as a perturbation, scattering processes that change the single-particle modes become off-resonant and atoms remain frozen during the dynamics. In this case interactions are diagonal in the single-particle basis and for particles in modes (\mathbf{m}, \mathbf{n}) they are fully characterized by the interaction energy

$$\hbar U_{\uparrow\downarrow}^{\mathbf{n}\mathbf{m}} = g \int d^3\vec{x} |\phi_{\mathbf{n}}(\vec{x})|^2 |\phi_{\mathbf{m}}(\vec{x})|^2. \quad (6.2)$$

6.2.3 Fermions with s -wave interactions in one dimension

We begin with the case of two atoms tightly confined transversally in their ground state and with dynamics only along the z -direction, where they experience a 1D harmonic trapping potential with angular trapping frequency ω_z . The two atoms are initially prepared in the state $\frac{1}{\sqrt{2}}(|n_1, n_2\rangle - |n_2, n_1\rangle)|t_{\downarrow\downarrow}\rangle$.

The atoms are assumed to be in the Lamb-Dicke regime, with Lamb-Dicke parameter $\eta = k_z a_{ho}/\sqrt{2} \ll 1$. $a_{ho} = \sqrt{\hbar/M\omega_z}$ is the harmonic oscillator length, and k_z the projection of the probe laser wavevector along z . Mode changes during the laser interrogation can be suppressed if the laser

detuning from the atomic transition, δ , and the bare Rabi frequency, Ω , satisfy $\delta, \eta\Omega \ll \omega_z$. In this regime the mode-dependence of the Rabi frequencies is $\Omega_n = \Omega e^{-\frac{\eta^2}{2}} L_n^0(\eta^2)$ [165]. The Hamiltonian in the rotating frame of the laser [3, 4, 115, 116] under the spin model approximation can be written as $\hat{H}_{sm}^{n_1, n_2} = \hat{H}_L^{n_1, n_2} + \hat{H}_D^{n_1, n_2}$, where

$$\begin{aligned}\hat{H}_L^{n_1, n_2} &= \hbar \Delta \Omega^{n_1, n_2} \frac{(\hat{\sigma}_1^x - \hat{\sigma}_2^x)}{2} - \hbar \bar{\Omega}^{n_1, n_2} \hat{s}_x, \\ \hat{H}_D^{n_1, n_2} &= 2\hbar u_{\uparrow\downarrow}^{n_1, n_2} \hat{P}_s - \hbar \delta \hat{s}_z.\end{aligned}\tag{6.3}$$

$\hat{H}_L^{n_1, n_2}$ acts only during the two laser pulses, and $\hat{H}_D^{n_1, n_2}$ acts only during the dark time. Here $\hat{s}_{x,y,z} = (\hat{\sigma}_1^{x,y,z} + \hat{\sigma}_2^{x,y,z})/2$ are collective spin operators and $\bar{\Omega}^{n_1, n_2} = (\Omega_{n_1} + \Omega_{n_2})/2$ is the mean Rabi frequency. $\Delta\Omega^{n_1, n_2} = (\Omega_{n_1} - \Omega_{n_2})/2$ arises from the excitation inhomogeneity and can transfer some of the initial triplet population to the singlet, allowing interactions. The interaction energy $\hbar u_{\uparrow\downarrow}^{n_1, n_2} = \hbar U_{\uparrow\downarrow}^{\mathbf{n}\mathbf{m}}$ in Eq. (6.2) with $\mathbf{n} = \{0, 0, n_1\}$ and $\mathbf{m} = \{0, 0, n_2\}$. We can ignore the detuning and interactions during the laser pulses if the pulses are short compared to the timescales set by those energies. We also ignore single-particle energies which are constants and do not contribute to the dynamics.

The spin model assumptions break down in a harmonic trap due to the degeneracy of the non-interacting two-atom spectrum: even weak interactions can transfer atoms initially in modes $\{n_1, n_2\}$ to the various degenerate configurations $\{n_1+k, n_2-k\}$ (for integer k) during the dynamics. To account for these mode changes, we take advantage of the exact eigenfunctions and eigenvalues of $\hat{H}_D(\vec{x}_1, \vec{x}_2)$ in Eq. (6.1) for two atoms with s -wave interactions in a harmonic trap [166]. These solutions exploit the separability of the Hamiltonian in the center-of-mass coordinate R and relative coordinate r . There is no degeneracy in the relative coordinate degree of freedom.

6.2.4 Ramsey dynamics in the spin model approximation

Denoting τ the Ramsey dark time, the population difference between the two spin states measured after the second pulse takes the generic form

$$\langle \hat{s}_z \rangle(\tau) = A(\tau) \cos(\delta\tau) + B(\tau) \sin(\delta\tau) + C(\tau).\tag{6.4}$$

$A(\tau)$, $B(\tau)$, and $C(\tau)$ have the form $A(\tau) = I_1(\tau)f_1 + f_2$, $B(\tau) = I_2(\tau)f_3$, $C(\tau) = I_3(\tau)f_4 + f_5$, where $I_i(\tau)$ depend on the dark time physics, and f_i are independent of the dark time physics and depend only on the laser pulse quantities $\{\Delta\theta_{j=1,2}^{n_1,n_2}, \bar{\theta}_{j=1,2}^{n_1,n_2}\}$:

$$\begin{aligned}
f_1 &= \sin(\Delta\theta_1^{n_1,n_2}) \sin(\Delta\theta_2^{n_1,n_2}) \cos(\bar{\theta}_1^{n_1,n_2}) \cos(\bar{\theta}_2^{n_1,n_2}) \\
f_2 &= \cos(\Delta\theta_1^{n_1,n_2}) \cos(\Delta\theta_2^{n_1,n_2}) \sin(\bar{\theta}_1^{n_1,n_2}) \sin(\bar{\theta}_2^{n_1,n_2}) \\
f_3 &= \cos(\Delta\theta_1^{n_1,n_2}) \cos(\bar{\theta}_2^{n_1,n_2}) \sin(\Delta\theta_1^{n_1,n_2}) \sin(\Delta\theta_2^{n_1,n_2}) \\
f_4 &= -\sin(\Delta\theta_1^{n_1,n_2}) \sin(\Delta\theta_2^{n_1,n_2}) \sin(\bar{\theta}_1^{n_1,n_2}) \sin(\bar{\theta}_2^{n_1,n_2}) \\
f_5 &= -\cos(\Delta\theta_1^{n_1,n_2}) \cos(\Delta\theta_2^{n_1,n_2}) \cos(\bar{\theta}_1^{n_1,n_2}) \cos(\bar{\theta}_2^{n_1,n_2}), \tag{6.5}
\end{aligned}$$

$\Delta\theta_j^{n_1,n_2} = \Delta\Omega^{n_1,n_2}t_j$ and $\bar{\theta}_j^{n_1,n_2} = \bar{\Omega}^{n_1,n_2}t_j$, with $t_{1,2}$ the pulse durations. In the spin model approximation, the dark time functions depend simply on interactions: $I_1^{\text{sm}} = I_3^{\text{sm}} = \cos(u_{\uparrow\downarrow}^{n_1,n_2}\tau)$, $I_2^{\text{sm}} = \sin(u_{\uparrow\downarrow}^{n_1,n_2}\tau)$.

6.2.5 Ramsey dynamics in the weakly interacting regime ($u_{\uparrow\downarrow}^{1,0} \ll \omega_z$)

For weakly interacting atoms ($u_{\uparrow\downarrow}^{1,0} \ll \omega_z$), we are able to write the dynamics (beyond the spin model approximation) in a closed analytic form. These expressions for the dynamics are exact for times $\tau \ll \omega_z/(u_{\uparrow\downarrow}^{1,0})^2$:

$$\begin{aligned}
I_1^{\text{exact}} &= I_3^{\text{exact}} = 2 \sum_{n_r=0, \text{even}}^{n_1+n_2} |d_{n_r}^{n_1,n_2}|^2 \cos \left[\frac{\Delta E_s(n_r)}{\hbar} \tau \right], \\
I_2^{\text{exact}} &= 2 \sum_{n_r=0, \text{even}}^{n_1+n_2} |d_{n_r}^{n_1,n_2}|^2 \sin \left[\frac{\Delta E_s(n_r)}{\hbar} \tau \right]. \tag{6.6}
\end{aligned}$$

Here $d_{n_r}^{n_1,n_2}$ are the change of basis coefficients defined later in this section. Comparing Eq. (6.6) to the spin model solution, we see the single frequency $u_{\uparrow\downarrow}^{n_1,n_2}$ in the spin-model dynamics gets replaced by a sum over many frequencies $\Delta E_s(n_r)/\hbar$ in the exact dynamics. These frequencies are associated with the first order correction of the eigenenergies due to interactions [166]: $\Delta E_s(n_r) = \hbar u_{\uparrow\downarrow}^{1,0} \frac{\Gamma(n_r/2+1/2)}{\sqrt{\pi}\Gamma(n_r/2+1)} \left(1 + \mathcal{O}(u_{\uparrow\downarrow}^{1,0}/\omega_z)\right)$. The many frequencies that appear come from the resonant mode-changing processes. States with odd n_r do not experience s -wave interactions and do not contribute.

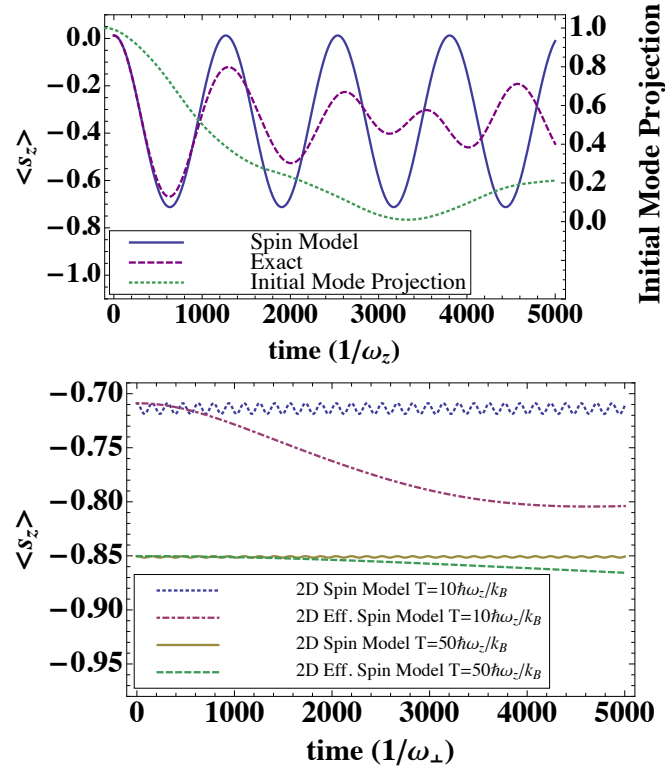


Figure 6.2: Ramsey dynamics [see Eq. (6.4)] with $\delta = 0$: (a) 1D spin model, exact solution, and projection of population onto initial mode (here $n_1 = 10$ and $n_2 = 0$), with $u_{\uparrow\downarrow}^{1,0} \approx 0.2\omega_z$. Dephasing of the exact dynamics results from mode changes. (b) Thermal averages in 2D: spin model vs. effective spin model, at different temperatures, with $u_{\uparrow\downarrow}^{1,0} \approx 0.04\omega_\perp$. For both figures: $\theta_1 = \theta_2 = \pi/3$, with thermally-averaged inhomogeneity $\langle \Delta\Omega \rangle / \langle \Omega \rangle = 0.3$. $\theta_i = \Omega t_i$ are bare pulse areas.

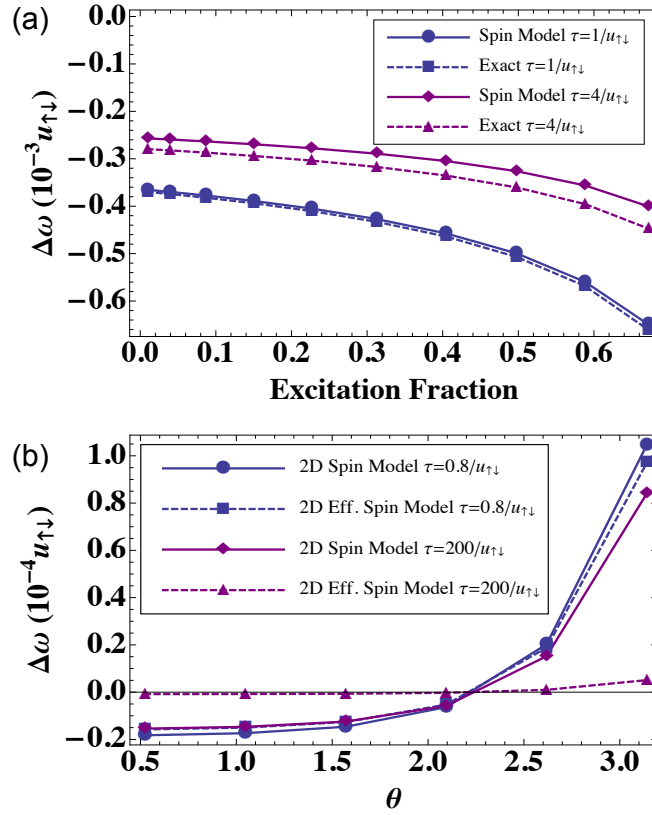


Figure 6.3: Thermally averaged frequency shifts: (a) 1D spin model and exact solution vs. population excitation fraction (number of atoms in \uparrow divided by the total number of atoms) after the first pulse, at intermediate and long times. Here $u_{\uparrow\downarrow} \equiv u_{\uparrow\downarrow}^{1,0} \approx 0.2\omega_z$. (b) Frequency shifts for 2D spin model vs. effective spin model, with $u_{\uparrow\downarrow} \equiv u_{\uparrow\downarrow}^{1,0} \approx 0.04\omega_{\perp}$. For both figures: $T = 208\hbar\omega_{\perp}/k_B$, $\theta = \theta_1 = \theta_2$, $\omega_z = \omega_{\perp} = 700 \times 2\pi\text{Hz}$, and thermally-averaged inhomogeneity $\langle\Delta\Omega\rangle/\langle\Omega\rangle = 0.3$. $\theta_i = \Omega t_i$ are bare pulse areas.

The formula in Eq. 6.6 is derived as follows: we begin with two particles in the state $\frac{1}{\sqrt{2}}(|n_1, n_2\rangle - |n_2, n_1\rangle)|t_{\downarrow\downarrow}\rangle$, where n_1 and n_2 are quantum numbers for two different (non-interacting) harmonic oscillator modes. A laser pulse is applied, whose action is characterized by \hat{H}_L in Eq. (6.3). The first pulse has effective pulse area $\bar{\theta}_1^{n_1, n_2}$ and inhomogeneity $\Delta\theta_1^{n_1, n_2}$. After the first pulse, the state $\frac{1}{\sqrt{2}}(|n_1, n_2\rangle + |n_2, n_1\rangle)|s\rangle$ becomes populated. We expand its spatial wave-function into center-of-mass and relative coordinates. To capture the Ramsey dynamics to first order in interaction strength g , it is sufficient to leave the wavefunctions unchanged during the dark time. (When we calculate dynamics for strong interactions, we modify these wavefunctions according to Ref. [166].) During the Ramsey dark time, the even relative coordinate modes acquire energies given by $\Delta E_s(n_r) = \hbar u_{\uparrow\downarrow}^{1,0} \frac{\Gamma(n_r/2+1/2)}{\sqrt{\pi}\Gamma(n_r/2+1)} \left(1 + \mathcal{O}(u_{\uparrow\downarrow}^{1,0}/\omega_z)\right)$.

After the dark time, we expand the singlet back into individual-particle coordinates which is the convenient basis to calculate the action of a second laser pulse, with effective pulse area $\bar{\theta}_2^{n_1, n_2}$ and inhomogeneity $\Delta\theta_2^{n_1, n_2}$. The observable $\langle\hat{s}_z\rangle$ is calculated as the population difference between the $|t_{\uparrow\uparrow}\rangle$ and $|t_{\downarrow\downarrow}\rangle$ spin states, summed over each spatial mode. However, only the triplet contributes to the $\langle\hat{s}_z\rangle$ dynamics, and the triplet only contains the original spatial modes $|n_1, n_2\rangle$ and $|n_2, n_1\rangle$, so a major simplification can be made by only summing over these two modes. This simplification is what allows us to calculate the analytic form of Eq. (6.6).

The exact solutions rely on a change of basis between the individual-particle coordinate basis with wavefunctions $\psi_{n_1}(z_1)\psi_{n_2}(z_2)$ and the center of mass-relative coordinate basis with wavefunctions $\Psi_{n_R}(R)\Psi_{n_r}(r)$. To convert between these bases we introduce raising operators acting on the vacuum state $|0, 0\rangle$, which is the same in both bases: $|n_1 = 0, n_2 = 0\rangle = |n_R = 0, n_r = 0\rangle$. We use the usual form of a raising operator $\hat{a}^\dagger = (\hat{x} - i\hat{p})/\sqrt{2}$ to define

$$\hat{a}_R^\dagger = \frac{1}{\sqrt{2}}(\hat{a}_{z_1}^\dagger + \hat{a}_{z_2}^\dagger), \quad \hat{a}_r^\dagger = \frac{1}{\sqrt{2}}(\hat{a}_{z_1}^\dagger - \hat{a}_{z_2}^\dagger) \quad (6.7)$$

We can create a particular state out of the vacuum to convert between the two bases:

$$|n_R, n_r\rangle = \frac{(\hat{a}_R^\dagger)^{n_R}(\hat{a}_r^\dagger)^{n_r}}{\sqrt{n_R!n_r!}}|0, 0\rangle, \quad |n_1, n_2\rangle = \frac{(\hat{a}_{z_1}^\dagger)^{n_1}(\hat{a}_{z_2}^\dagger)^{n_2}}{\sqrt{n_1!n_2!}}|0, 0\rangle \quad (6.8)$$

These binomials need to be expanded and re-grouped in the form

$$\langle R, r | n_R, n_r \rangle = \sum_{i=0}^{n_R+n_r} c_i^{n_R, n_r} \psi_i(x) \psi_{n_R+n_r-i}(y), \quad \langle x, y | n_1, n_2 \rangle = \sum_{i=0}^{n_1+n_2} d_i^{n_1, n_2} \Psi_i(R) \Psi_{n_1+n_2-i}(r) \quad (6.9)$$

Grouping the terms, we find

$$c_i^{n_R, n_r} = \sqrt{\frac{i!(n_R + n_r - i)!}{2^{n_R} 2^{n_r} n_R! n_r!}} \sum_{j=\max[0, n_r-i]}^{\min[n_r, n_R+n_r-i]} (-1)^j \binom{n_R}{n_R + n_r - i - j} \binom{n_r}{j} \\ d_i^{n_1, n_2} = \sqrt{\frac{i!(n_x + n_y - i)!}{2^{n_x} 2^{n_y} n_x! n_y!}} \sum_{j=\max[0, n_y-i]}^{\min[n_y, n_x+n_y-i]} (-1)^j \binom{n_x}{n_x + n_y - i - j} \binom{n_y}{j} \quad (6.10)$$

When we compare the exact dynamics to those predicted by the spin model we find that they agree for short times, $\tau u_{\uparrow\downarrow}^{1,0} \ll 1$. The spin model fails at longer times, however, when leakage of population to other modes in the individual-particle coordinate basis becomes significant (See Fig. 6.2 (a)). This is reflected in the behavior of the angular frequency shift $\Delta\omega(\tau)$ – an important quantity for atomic clock experiments – defined as $\Delta\omega(\tau)\tau = -\arctan[B(\tau)/A(\tau)]$, which is the observed change in the atomic transition due to interactions [see Fig. 6.3 (a)]. The failure of the spin model at times longer than the inverse interaction strength limits its applicability to model the new generation of atomic clocks that use ultra coherent lasers [167, 168], allowing interrogation times exceeding a few seconds. A spin model treatment will be insufficient when conditions are such that the atoms see an almost purely harmonic potential.

6.2.6 Ramsey dynamics in the strongly-interacting regime ($u_{\uparrow\downarrow}^{1,0} \gtrsim \omega_z$)

The spin model fails when $u_{\uparrow\downarrow}^{1,0} \gtrsim \omega_z$. To maintain the separation between interaction-induced effects and laser-induced effects, we imagine interactions set to be weak during the laser pulses and suddenly increased after the first pulse using for example a Feshbach resonance [116, 169, 170]

¹. For this situation, we can solve for the dynamics, given an initial pair of modes, although

¹ During the pulses we require $u_{\uparrow\downarrow}^{1,0} \ll \Omega$ to ignore interactions, $\eta\Omega \ll \omega_z$ to ignore laser induced mode changes, and $\eta^2\Omega \gg u_{\uparrow\downarrow}^{1,0}$ to populate all of the interacting modes in the singlet. These three conditions cannot simultaneously be satisfied unless $u_{\uparrow\downarrow}^{1,0} \ll \omega_z$.

there is no closed form solution (the dark time functions $I_i(\tau)$ are more complicated, but the laser dependence through f_j remains the same as in the previous cases). We find that, in the limit of strong interactions ($u_{\uparrow\downarrow}^{1,0} \gg \omega_z$), the population imbalance exhibits periodic oscillations at the axial trapping frequency ω_z , in contrast with the spin model prediction of much faster oscillations at the interaction frequency. The frequency shift (proportional to this oscillation frequency), saturates to a value on the order of ω_z , instead of increasing without bound. These results reflect the fact that for strong interactions (unitarity), the fermions maximally-repel each other, and the trap energy becomes the only relevant energy scale in the system. This behavior, expected to be a universal result, should apply even in the many-body case as seen in Refs. [161, 162]. Fig. 6.4 confirms numerically that for three particles in the strongly interacting regime, the dynamics oscillates at the trap frequency rather than the interaction frequency.

Fig. (6.4) shows the Ramsey dynamics predicted by both the spin model and exact calculation for the case of strong interactions. For two fermions with strong interactions, the relative coordinate wavefunction of the $\uparrow\downarrow$ channel develops a node and the interaction energy is no longer a relevant energy scale. The only remaining energy scale in the problem is the trap frequency, and the Ramsey dynamics oscillate at the trap frequency. The spin model predicts oscillations at the interaction frequency, which are much faster than the true dynamics which oscillate at the trapping frequency.

Refs. [4, 116] showed that s -wave frequency shifts can be cancelled by setting the second pulse area to $\bar{\theta}_2^{n_1, n_2} = \pi/2$. This result, obtained using the spin model, survives the inclusion of resonant mode-changes even for strong interactions during the dark time, since the dependence of the dynamics on the functions f_i , and thus $\bar{\theta}_2^{n_1, n_2}$, remains the same even when interactions are strong. Interactions induce mode changes and introduce new frequencies only to the singlet. The triplet is what determines the dynamics, however, where only the original modes $|n_1, n_2\rangle$ and $|n_2, n_1\rangle$ are present. The second pulse area affects these modes in exactly the same manner as in the spin model treatment of Refs. [3, 4, 115, 116].

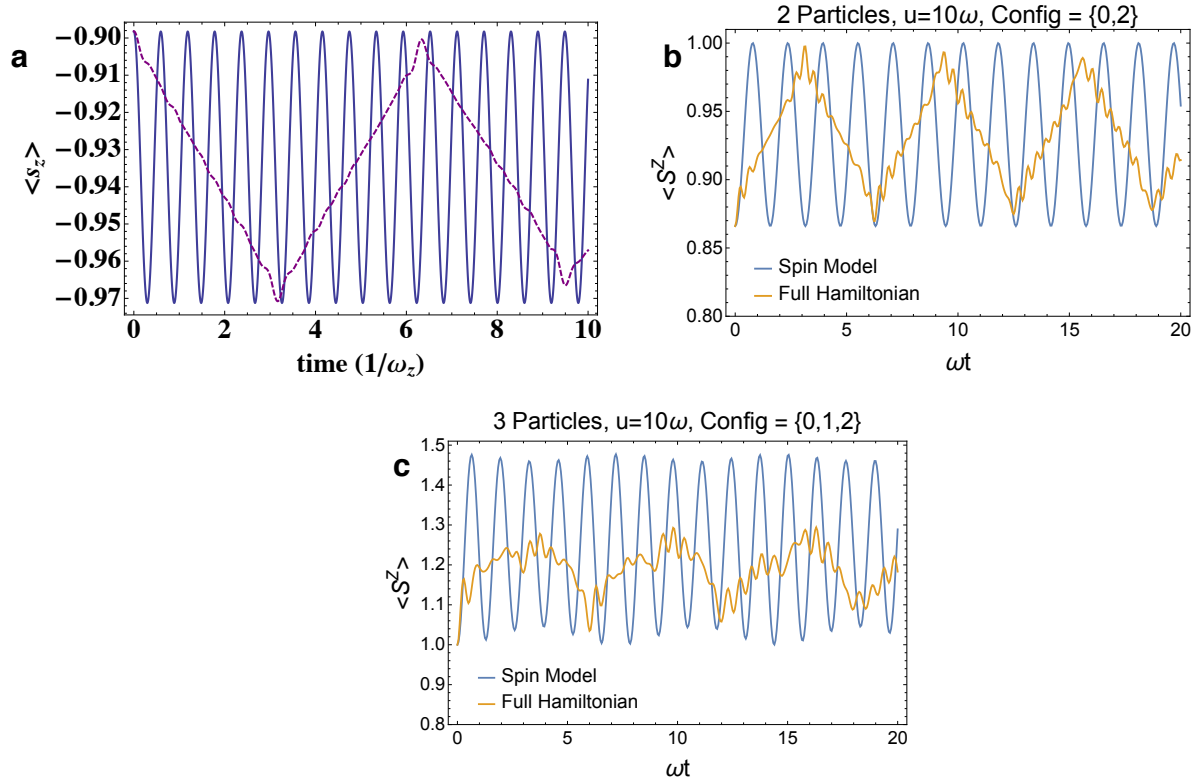


Figure 6.4: (a) Ramsey dynamics [see Eq. (6.4)] with $\delta = 0$ predicted by the 1D spin model (solid) and the exact solution (dashed) for an initial $(n_1 = 6, n_2 = 3)$ mode configuration. Strong interactions ($u_{\uparrow\downarrow}^{1,0} = 100\omega_z$) are assumed during the dark time. In the limit of strong interactions the two particles develop a node in their relative coordinate and the period of the Ramsey dynamics becomes the trap period since it is the only energy scale left in the problem. (b) Numerical results for the $(n_1 = 0, n_2 = 1)$ mode configuration with initial conditions and parameters described in Section 6.3 and $u = 10\omega$, confirming the result that Ramsey dynamics takes place at the trap period for strong interactions. (c) Numerical results for the $(n_1 = 2, n_2 = 1, n_3 = 0)$ mode configuration with initial conditions and parameters described in Section 6.3 and $u = 10\omega$, again showing oscillations at the trap frequency rather than the interaction frequency.

6.2.7 Fermions with s-wave interactions in two dimensions

For an anisotropic 2D harmonic potential with no accidental degeneracies, the treatment will be similar to the 1D case. An isotropic 2D harmonic potential, however, is more difficult to treat, due to the large degeneracy. In 2D the spin model remains the same as Eq. (6.3), with populated modes now $\mathbf{n}_i = \{n_{xi}, n_{yi}, 0\}$, and interaction energy $\hbar u_{\uparrow\downarrow}^{\vec{n}_1, \vec{n}_2} = \hbar U_{\uparrow\downarrow}^{\mathbf{n}_1 \mathbf{n}_2}$ in Eq. (6.2). To go beyond the spin model we use polar relative coordinates to eliminate much of the degeneracy. For non-interacting particles, the eigenfunctions can be parameterized by quantum numbers n and m , with energy $E = \hbar\omega_{\perp}(2n + |m| + 1)$ and angular momentum component $L_z = \hbar m$, where ω_{\perp} is the 2D oscillator frequency. S -wave interactions only affect states with $m = 0$, and this subset of states contains no degeneracy (other than the center-of-mass degeneracy). To first order in perturbation theory the interaction energy shift is independent of the radial quantum number n : $\Delta E = \frac{g}{2\sqrt{2}\pi^{3/2}a_z a_{\perp}^2} \left(1 + \mathcal{O}(u_{\uparrow\downarrow}^{1,0}/\omega_{\perp})\right)$, where a_z and a_{\perp} are the oscillator lengths along the tightly-confined z -direction and the weakly-confined x and y -directions, respectively, and in 2D $u_{\uparrow\downarrow}^{1,0} \equiv u_{\uparrow\downarrow}^{\vec{n}_1, \vec{n}_2}$ with $\vec{n}_1 = (1, 0, 0)$, $\vec{n}_2 = (0, 0, 0)$. This result is striking: despite the large degeneracy in 2D, each interacting state with $m = 0$ receives the same energy shift to first order in perturbation theory, and accumulates the same phase during the dark time. An effective spin model, with diagonal matrix element $2\hbar u_{\uparrow\downarrow}^{\vec{n}_1, \vec{n}_2}$ replaced by ΔE , will be *exact* for the $m = 0$ states, to first order in the interaction strength. We can replace $\hat{H}_D^{n_1, n_2}$ in Eq. (6.3) with:

$$\hat{H}_{D, \text{esm}}^{\vec{n}_1, \vec{n}_2} = \Delta E \hat{P}_{m=0} - \hbar \delta \hat{s}_z, \quad (6.11)$$

where $\hat{P}_{m=0}$ projects onto interacting states with $m = 0$. For a properly symmetrized initial state $\Psi_{\mathbf{n}_1, \mathbf{n}_2}(\vec{x}_1, \vec{x}_2)$ in modes $(\mathbf{n}_1, \mathbf{n}_2)$, we denote the fraction of the population with $m = 0$ in the relative coordinate by $\mathcal{P}_{\mathbf{n}_1, \mathbf{n}_2}^{m=0}$, which can be calculated as $\mathcal{P}_{\mathbf{n}_1, \mathbf{n}_2}^{m=0} = \int d^3\vec{x}_1 d^3\vec{x}_2 |\Psi_{\mathbf{n}_1, \mathbf{n}_2}(\vec{x}_1, \vec{x}_2)|^2 \delta(\vec{x}_1 - \vec{x}_2) = \frac{4\sqrt{2}\pi^{3/2}}{g} \hbar u_{\uparrow\downarrow}^{\vec{n}_1, \vec{n}_2}$, where $u_{\uparrow\downarrow}^{\vec{n}_1, \vec{n}_2}$ is the 2D interaction energy calculated from Eq. (6.2). The dark time dynamics of this effective spin model are simple: $I_1^{\text{esm}} = I_3^{\text{esm}} = (1 - \mathcal{P}_{\mathbf{n}_1, \mathbf{n}_2}^{m=0}) + \mathcal{P}_{\mathbf{n}_1, \mathbf{n}_2}^{m=0} \cos(\Delta E \tau / \hbar)$, $I_2^{\text{esm}} = \mathcal{P}_{\mathbf{n}_1, \mathbf{n}_2}^{m=0} \sin(\Delta E \tau / \hbar)$.

In the original spin model, $\hbar u_{\uparrow\downarrow}^{\vec{n}_1, \vec{n}_2}$ is used as the interaction energy. We see that this param-

eter appears in the effective spin model to quantify the population of interacting modes ($\mathcal{P}_{\mathbf{n}_1, \mathbf{n}_2}^{m=0}$), instead of their energy. This dramatic result is seen in Fig. 6.2 (b), comparing thermal averages of the previously-implemented spin model with the new effective spin model. Oscillations during the dynamics remain at the same frequency ΔE at higher temperatures, but the amplitude of the oscillations, proportional to $\mathcal{P}_{\mathbf{n}_1, \mathbf{n}_2}^{m=0}$, decreases. The previously-implemented spin model, on the other hand, predicts smaller interaction energies (slower oscillations) at higher temperatures. The frequency shift predicted by the original spin model is only valid at short times (see Fig. 6.3 (b)).

6.3 Validity of the spin model for $N > 2$

In this section we investigate the validity of the spin model approximation beyond the two particle case. We will first investigate the problem of Ramsey spectroscopy of N spins where the inhomogeneity in the Rabi frequencies is “exaggerated” and large enough such that a Rabi pulse imprints a spin-spiral initial state on the spins, with equally spaced spin rotations between neighboring spins. We will choose this angle between adjacent spins to be $\pi/6$. The Ramsey sequence we are investigating starts with all spins in the down spin state followed by:

$$\text{Rabi pulse (spiral)} \rightarrow \text{dark time } t \text{ (interactions)} \rightarrow \text{Rabi pulse (spiral)} \rightarrow \text{measure } \hat{S}^Z.$$

This sequence mimics the case of inhomogeneous Rabi frequencies which arise in atomic clocks and were investigated earlier in this chapter. Figure 6.5 shows the results of such a sequence for $N = 2$ and $N = 3$ at both $u = 0.1\omega$ and $u = 0.3\omega$ interaction strengths². We choose the initial mode configuration to be the Fermi degenerate configuration. Two particles in this initial state cannot experience resonant mode changes, so the failure of the spin model is due to either changes in the wavefunctions which modify the interactions, or from non-resonant mode changes. In Fig. 6.5 (a, b) the deviations from the spin model predictions manifest as a small interaction strength-dependent phase shift. For three particles, on the other hand, resonant mode changes are possible after interactions flip two of the spins. We can see in Fig. 6.5 (c, d) that the spin model

² Here the interaction strength u is the bare interaction strength, not including the numerical factors that arise from integrating the harmonic oscillator wavefunctions.

breaks down at long times due to these mode changes, similar to the results for two particles with a non-Fermi-degenerate initial state.

6.3.1 Many Body Spin Echo

A many body spin echo sequence is a Ramsey sequence where a π pulse is applied halfway through the dark time evolution (a normal spin echo), and the interaction Hamiltonian is reversed for the second half of the dark time. The many body echo seeks to “undo” the spin-spin interactions in the system. The question is, for a system where spin and motion are coupled, what is the effect of the many body spin echo?

Fig. 6.6 shows the Ramsey dynamics for two particles with inhomogeneous Rabi frequencies, with and without a normal spin echo sequence, and with a many body spin echo sequence. A spin echo sequence does not change the Ramsey dynamics under the spin model approximation but does modify the dynamics under the full Hamiltonian, due to the coupling of spin and motion via mode changes. Similarly, the many body spin echo completely removes the dynamics under the spin model approximation but does not remove all the effects of the full Hamiltonian. Thus the many body spin echo sequence might be used as a way of detecting processes beyond the spin model approximation in real systems.

6.4 Validation of the spin model for spin-dependent traps and importance of corrections

In this section we continue the discussion from Ch. 5 of the validity of the spin model for the problem of a two component Fermi gas in a spin-dependent trapping potential and discuss the effect of corrections to the spin model Hamiltonian. This section is adapted from an unfinished manuscript by Michael L. Wall.

The spin model is, at face value, a rather severe approximation. In particular, taking the expectation of the spin model Hamiltonian for a non-interacting state is equivalent to first-order perturbation theory in the interaction Hamiltonian. However, since our approximation is made

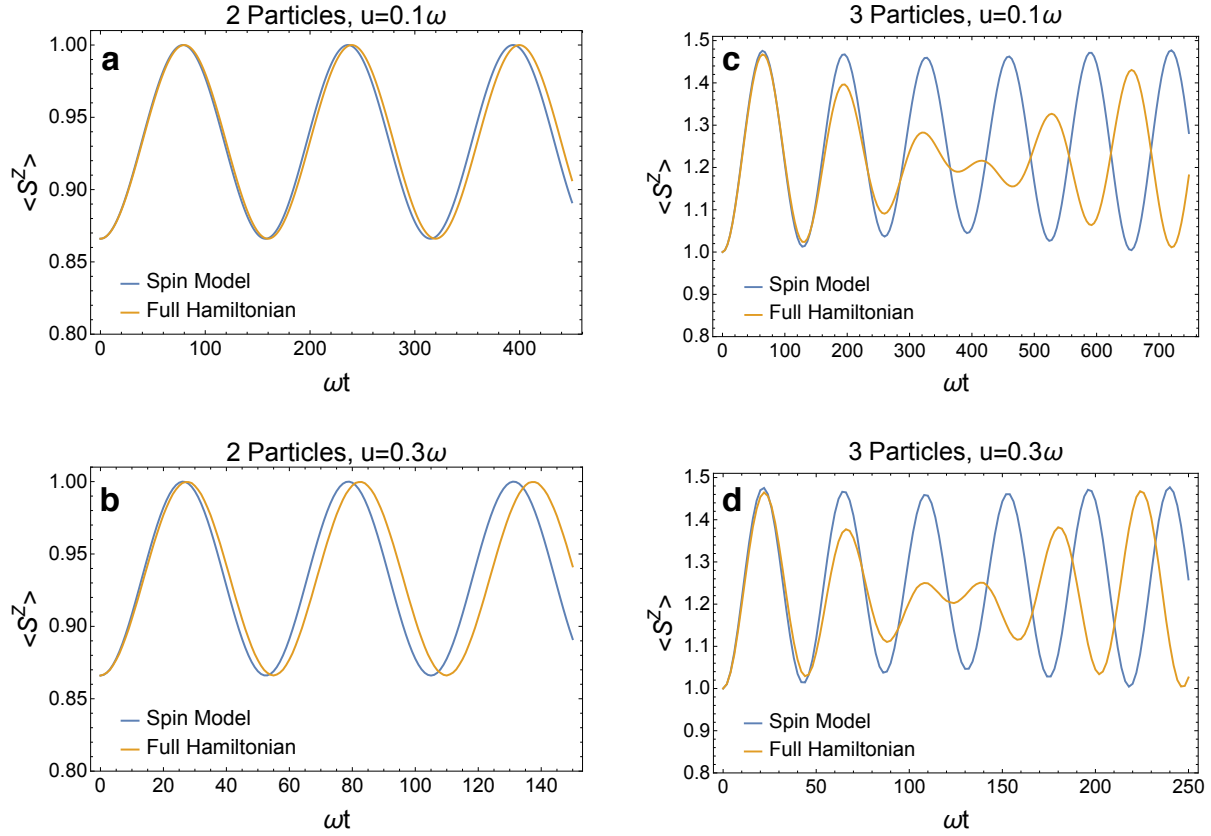


Figure 6.5: Dynamics of a Ramsey sequence in a one dimensional harmonic trap with inhomogeneous Rabi frequencies. For two particles in a Fermi-degenerate initial condition (a, b), the predictions of the spin model closely match those of the full Hamiltonian up to a phase shift that depends on the interaction strength u . For two particles in this initial configuration, no resonant mode changes are possible, so this phase shift results from either changes in the wavefunctions or from non-resonant mode changes. For three particles in a Fermi degenerate initial condition (c, d), the spin model does not work as well at long times since after two of the spins are flipped, Pauli blocking no longer prevents resonant mode changes.

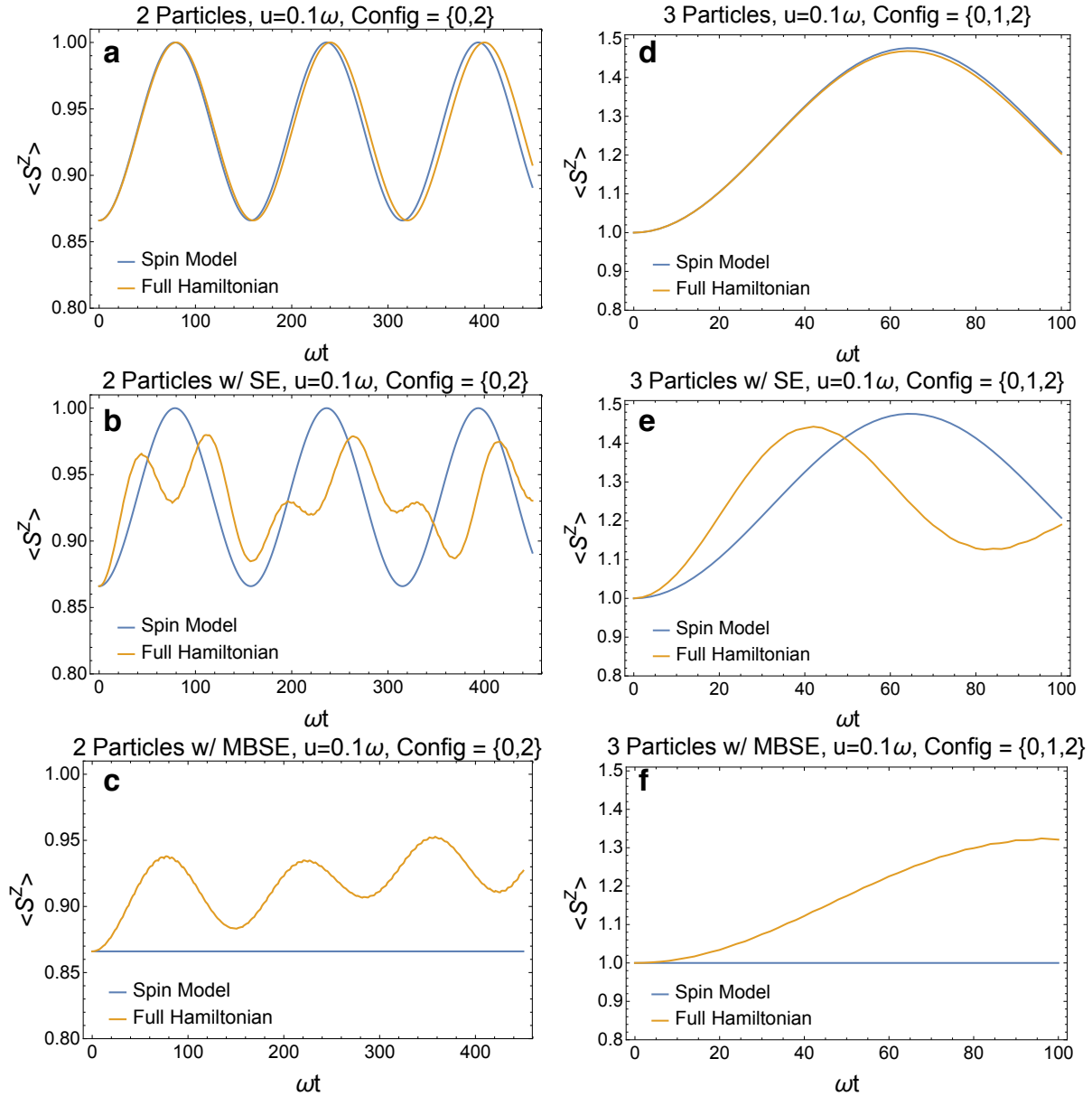


Figure 6.6: Effect of a spin echo and many body spin echo sequence. (a) Ramsey dynamics with inhomogeneous Rabi frequencies, comparing the spin model and Full Hamiltonian. (b) A spin echo sequence does not change the Ramsey dynamics under the spin model approximation but does modify the dynamics under the full Hamiltonian, due to the coupling of spin and motion via mode changes. (c) Similarly, the many body spin echo completely removes the dynamics under the spin model approximation but does not remove all the effects of the full Hamiltonian. Parts (d - f) show similar results for three particles.

at the operator level rather than the expectation value level, dynamics obtained with the spin model Hamiltonian includes contributions to all orders in perturbation theory for certain terms in the interaction Hamiltonian, while completely neglecting the effects of other terms. That is to say, the spin model is not equivalent to perturbation theory in the interaction Hamiltonian for dynamics. In spite of its seeming severity, the spin model performs extraordinarily well in predicting some quantities, such as the decay of the contrast in Ramsey spectroscopy following a sudden spin-dependent quench of the trapping parameters [?]. The purpose of this section is to numerically benchmark the spin model against solutions of the full Hamiltonian for small systems where computing the full dynamics is possible. In addition, we consider what the dominant corrections to the spin model are for weak to moderate interactions compared to the trapping frequency, and how the importance of these corrections is modified by adding realistic anharmonicity to the trap.

In what follows, we will consider a system with $N = 5$ spin-1/2 fermions experiencing only s -wave interactions. Our initial state is the motional ground state in a spin-independent harmonic trap with all spins pointing along the x direction. As all of the particles are prepared identically, they do not experience the s -wave interactions. We then suddenly quench on a spin-dependent potential in the form of a spin-dependent displacement of the traps. This change in the trapping potential results in spin-dependent motion in the trap, which in turn leads to s -wave collisions. This is the same problem that was studied in Ch. 5.

One of the most striking consequences of s -wave collisions is coherent demagnetization of the system, evinced by decay of $\langle \mathcal{S}^x \rangle$ to zero. Examples of this demagnetization behavior for an interaction strength $U = \omega/\sqrt{8}$ and trap displacements of $x_0 = 0.1a_H$ and $x_0 = 0.3a_H$ are shown in Fig. 6.7, with the solutions of the full model corresponding to solid red lines and the spin model prediction as dashed blue lines. On a coarse scale, we see that the spin model does an excellent job of capturing the overall envelope and timescale of the collapse of magnetization. However, a closer analysis (insets) shows that there are small oscillations on top of this envelope which correspond to spin-dependent motion in the trap which arises from both single-particle and interaction effects.

The spin model only captures the single-particle component of this motion, and ignores interaction effects, and so only reproduces the exact result at short times.

The full model, which fully incorporates the effects of interactions on motion in the trap, contains in principle $\mathcal{O}(N_{\text{modes}}^4)$ parameters for a fixed set of N_{modes} single-particle modes. In contrast, the spin model contains only $\mathcal{O}(N_{\text{modes}}^2)$ parameters. Clearly, not all of the neglected parameters contribute equally, and so a natural question is which of these parameters are most important for capturing interaction effects on motion. Motivated by perturbation theory, we expect that the parameters $I_{n'_1, n'_2; n_2, n_1}$ which preserve single-particle energy, i.e. $n'_1 + n'_2 = n_1 + n_2$, will be the most relevant, followed by those parameters which change the single-particle energy by ± 1 quantum, ± 2 quanta, etc. Further, within the set of parameters which do not change the single-particle energy, those which involve modes n'_1 and n'_2 which are closest to n_1 and n_2 (up to exchange) will have a larger matrix element. Hence, we can classify Hamiltonians including corrections beyond the spin model with two numbers (n, d) , where $n = \max(n'_1 + n'_2 - (n_1 + n_2))$ is the difference in the single-particle energy of the initial and final configurations and d is the maximum “mode distance”

$$\mathcal{M}(n'_1, n'_2; n_1, n_2) = \min(|n'_1 - n_1| + |n'_2 - n_2|, |n'_1 - n_2| + |n'_2 - n_1|) \quad (6.12)$$

which accounts for exchange. In terms of this notation, the spin model is the Hamiltonian $(0, 0)$, involving no difference in single-particle energy and also no “mode separation” between the initial and final configurations.

As a strict measure of how well the spin model and corrections to it perform, we will consider the fidelity of the state evolved under such an approximate Hamiltonian with evolution under the full Hamiltonian, $F = |\langle \psi_{\text{exact}} | \psi_{\text{approx.}} \rangle|$. An example for $x_0 = 0.1a_H$ is shown in Fig. 6.8, which compares the infidelities $(1 - F)$ of the spin model $(0, 0)$ as well as the spin models with corrections $(0, \infty)$, $(1, \infty)$, $(2, \infty)$ at $U = 0.1\omega$ for two different spin-dependent trap displacements. Allowing all resonant mode changes $(0, \infty)$ enhances the fidelity approximately 100-fold. The inclusion

of non-resonant terms, $(1, \infty)$, for instance, enhances the fidelity but by a smaller margin. This demonstrates the expected result that the most important corrections to the spin model come from resonant terms that conserve single particle energy. Convergence with range for resonant processes is shown in Fig. 6.9. Most of the convergence of the fidelity of the state is accomplished by the inclusion of the first non-resonant term $(0, 1)$.

As shown in the above analysis, dominant corrections come from resonant terms. In a harmonic potential, there are a large number of such resonances due to the linear spacing of energy levels. In an anharmonic potential these resonances are no longer exact, and the only exactly resonant collisions are the direct and exchange kept by the spin model. To better understand the effects of anharmonicity on the fidelity of the spin model approach, we consider a Gaussian potential $-V \exp(-2x^2/\ell^2)$. The best harmonic approximation to this potential, given by matching the local curvature near $x = 0$, yields the harmonic frequency $\hbar\omega = \sqrt{8E_\ell V}$ with $E_\ell = \hbar^2/(2m\ell^2)$ and the harmonic length $a_H = \ell/(2V/E_\ell)^{1/4}$. Converting the Schrödinger equation to harmonic units as $\tilde{x} = x/a_H$, $\tilde{E} = E/(\hbar\omega)$, we find

$$\left[-\frac{1}{2} \frac{d^2}{d\tilde{x}^2} + \sqrt{\frac{\bar{V}}{8}} \exp\left(-\sqrt{\frac{2}{\bar{V}}} x^2\right) \right] \psi = \tilde{E} \psi, \quad (6.13)$$

where $\bar{V} = V/E_\ell$. Treating the quartic-order term in first-order perturbation theory, we find the energies

$$E_n \approx -\sqrt{\frac{\bar{V}}{8}} + \hbar\omega \left(n + \frac{1}{2}\right) + \frac{3}{2} \frac{\hbar\omega}{\sqrt{8\bar{V}}} \left(n^2 + n + \frac{1}{2}\right). \quad (6.14)$$

Hence, if we consider an interaction of modes n and m scattering into $(n + d)$ and $(m - d)$, that would be energy conserving in a harmonic trap, this process is off-resonant by an amount

$$\Delta E_{n,m,d} \approx \frac{3\hbar\omega}{\sqrt{8\bar{V}}} d [d - (m - n)], \quad (6.15)$$

$$= 3E_\ell d [d - (m - n)]. \quad (6.16)$$

As expected, this energy difference vanishes for $d = 0$ or $d = (m - n)$, corresponding to no change in the modes or a mode swap. The terms which are resonant in a harmonic trap are now off-resonant

by an anharmonic energy shift which is perturbatively equal to $-E_\ell[3 + 6n(n + 1)]/4$ for the n^{th} harmonic oscillator state. Fig. 6.10 confirms that the spin model approximation performs better in a gaussian potential than in a perfectly harmonic potential.

6.5 Summary and Outlook.

In this chapter we test the validity of a spin model treatment for Ramsey spectroscopy with exact calculations for two pseudospin-1/2 fermions in a harmonic trap. In 1D the spin model treatment breaks down for dark times on the order of the inverse interaction strength, and for strong interactions. In 2D we find an effective spin model which is exact to first order in perturbation theory, and whose dynamics can be quite different from those predicted by a spin model treatment. We then discussed the validity of the spin model for $N > 2$ and the importance of corrections to the spin model for the problem of spin-dependent traps. Future theoretical treatments of interacting systems probed by Ramsey spectroscopy must take these effects into account to correctly describe dynamics outside of the short-time and weakly-interacting regimes.

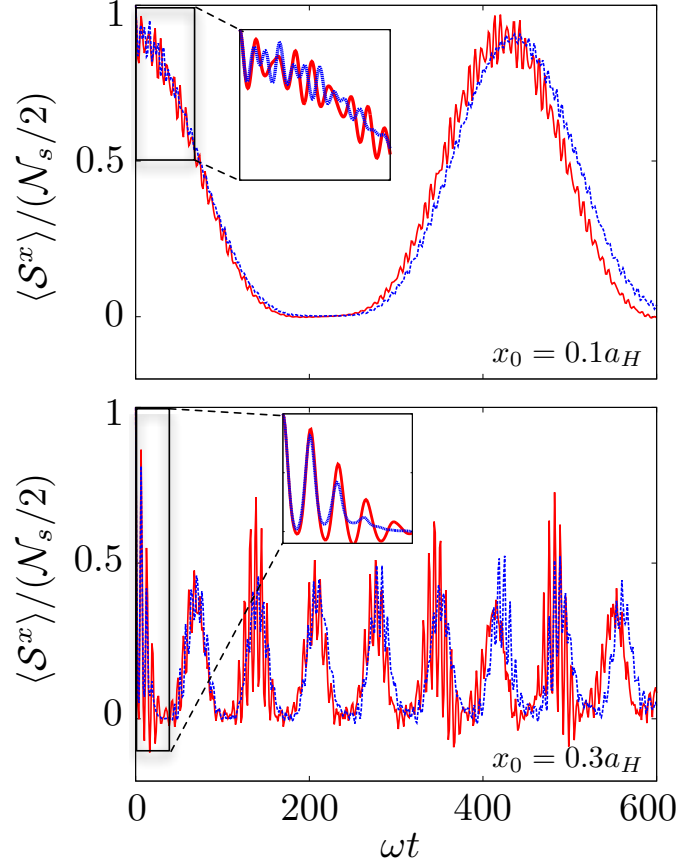


Figure 6.7: Demagnetization following a spin-dependent displacement. The exact (red solid) and spin-model (blue dashed) dynamics of the collective spin for an initially polarized state subject to a spin-dependent displacement of harmonic traps by $x_0 = 0.1a_H$ (top panel) or $x_0 = 0.3a_H$ (bottom panel). The overall demagnetization and revival timescales are well-captured by the spin model approach, while smaller-scale features due to interaction-modified motion in trap are not captured. Note that non-interacting motion in the trap is exactly captured within the spin model framework.

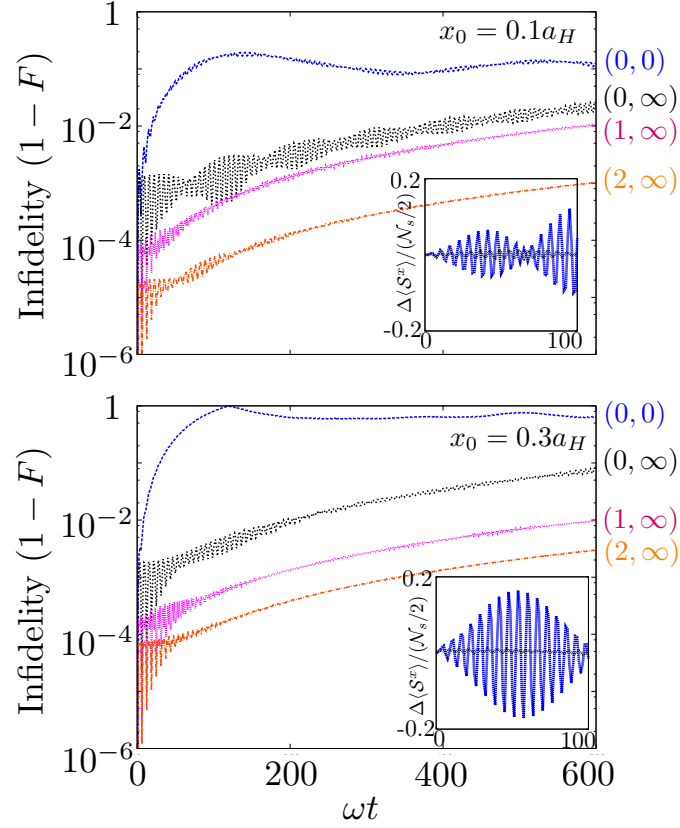


Figure 6.8: Infidelity of spin model in a harmonic trap with and without corrections. Allowing all resonant mode changes $(0, \infty)$ enhances the fidelity approximately 100-fold. Non-resonant terms, $(1, \infty)$, for instance, enhance the fidelity but by a smaller margin. Thus resonant terms are the most important corrections to the spin model.

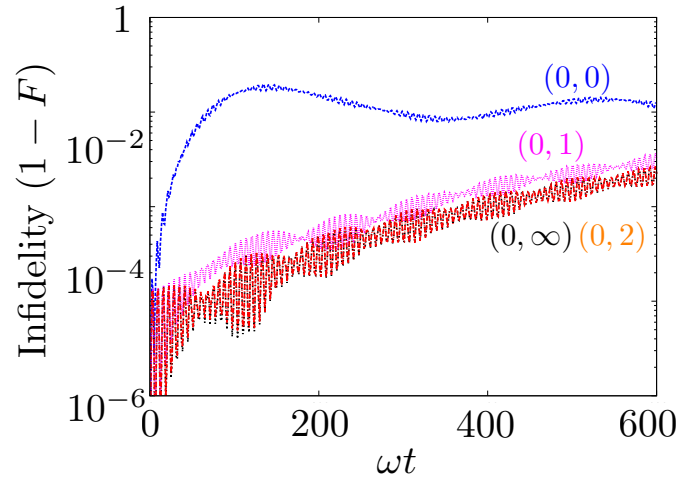


Figure 6.9: Convergence of spin model $(0, d)$ with range d . Most of the convergence of the fidelity of the state is accomplished by the inclusion of the first non-resonant term $(0, 1)$.

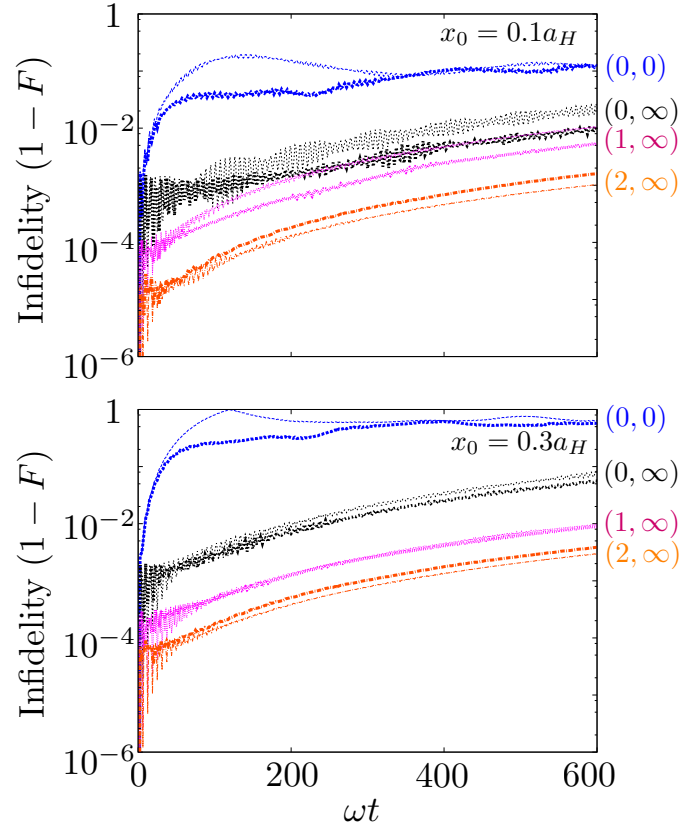


Figure 6.10: Infidelity of spin model in a gaussian trap (dark), compared to a harmonic trap (light), with and without corrections to the spin model, for $U = 0.1\hbar\omega$. The anharmonicity of the gaussian trap enhances suppresses mode changes and enhances the fidelity of the state.

Chapter 7

Appendix A: High-temperature thermal average of density shift

Here, we derive the high-temperature (compared to the tunneling bandwidth) thermal average from Ch. 3 of the first-order many-body dynamics. First, we expand the result of Eq. 3.19 to third order in time, finding

$$\begin{aligned}
\langle \hat{S}^z(\tau) \rangle = & \frac{1}{2} \sum_{i=1}^N (\cos(\delta\tau) \sin \theta_1 \sin \theta_2 - \cos \theta_1 \cos \theta_2) \\
& + \sum_{\{p_1, p_2\}} \frac{\sin \theta_1 \sin \theta_2}{L} \tau \left(C_{\{\mathbf{n}_{p_1}, \mathbf{n}_{p_2}\}} - \chi_{\{\mathbf{n}_{p_1}, \mathbf{n}_{p_2}\}} \cos \theta_1 \right) \sin \delta\tau \\
& + \frac{1}{2} \sum_{i=1}^N \Delta E_{\mathbf{n}_i}(q_i, \phi) \sin(\delta\tau) \sin \theta_1 \sin \theta_2 \tau \\
& - \sum_{\{p_1, p_2\}} \frac{\sin \theta_1 \sin \theta_2}{L} \frac{\tau^2}{2} \left(C_{\{\mathbf{n}_{p_1}, \mathbf{n}_{p_2}\}} - \chi_{\{\mathbf{n}_{p_1}, \mathbf{n}_{p_2}\}} \cos \theta_1 \right) (\Delta E_{\mathbf{n}_{p_1}} + \Delta E_{\mathbf{n}_{p_2}}) \cos \delta\tau \\
& - \frac{1}{4} \sum_{i=1}^N \Delta E_{\mathbf{n}_i}(q_i, \phi)^2 \cos(\delta\tau) \sin \theta_1 \sin \theta_2 \tau^2 \\
& - \sum_{\{p_1, p_2\}} \frac{\sin \theta_1 \sin \theta_2}{L} \frac{\tau^3}{24} \left[6 \left(C_{\{\mathbf{n}_{p_1}, \mathbf{n}_{p_2}\}} - \chi_{\{\mathbf{n}_{p_1}, \mathbf{n}_{p_2}\}} \cos \theta_1 \right) (\Delta E_{\mathbf{n}_{p_1}}^2 + \Delta E_{\mathbf{n}_{p_2}}^2) \right. \\
& \left. - (2 - \delta_{\mathbf{n}_{p_1} \mathbf{n}_{p_2}}) \zeta_{\{\mathbf{n}_{p_1}, \mathbf{n}_{p_2}\}} (\Delta E_{\mathbf{n}_{p_1}} - \Delta E_{\mathbf{n}_{p_2}})^2 \cos \theta_1 \sin \delta\tau \right] \\
& - \frac{1}{12} \sum_{i=1}^N \Delta E_{\mathbf{n}_i}(q_i, \phi)^3 \sin(\delta\tau) \sin \theta_1 \sin \theta_2 \tau^3 \Big\}. \tag{7.1}
\end{aligned}$$

To perform thermal averages, we now enact the tight-binding approximation, in which $E_{\mathbf{n}}(q) = \bar{E}_{\mathbf{n}} - 2J_{\mathbf{n}} \cos(q)$, and compute the partition function as

$$\begin{aligned} Z &= \sum_{nq} e^{-\beta E_{\mathbf{n}}(q)} \approx \sum_{\mathbf{n}} e^{-\beta \bar{E}_{\mathbf{n}}} \int_{-1}^1 dq e^{2\beta J_{\mathbf{n}} \cos(\pi q)} \\ &= 2 \sum_{\mathbf{n}} e^{-\beta \bar{E}_{\mathbf{n}}} I_0(2\beta J_{\mathbf{n}}) = 2 \sum_{\mathbf{n}} e^{-\beta \bar{E}_{\mathbf{n}}} [1 + \mathcal{O}(\beta^2 J_{\mathbf{n}}^2)] , \end{aligned} \quad (7.2)$$

where $I_{\nu}(x)$ is the modified Bessel function of order ν and β the inverse radial temperature. Hence, for temperatures sufficiently high compared to the bandwidth $J_{\mathbf{n}}$, the partition function is just a constant times the partition function of the transverse modes. Now,

$$\begin{aligned} \langle \Delta E_{\mathbf{n}}(q, \phi) \rangle_{T_R} &= \frac{1}{Z} \sum_{\mathbf{n}} e^{-\beta \bar{E}_{\mathbf{n}}} 4J_{\mathbf{n}} (1 - \cos \phi) I_1(2\beta J_{\mathbf{n}}) \\ &= \frac{1}{Z_{\mathbf{n}}} \sum_{\mathbf{n}} e^{-\beta \bar{E}_{\mathbf{n}}} 2\beta J_{\mathbf{n}} (1 - \cos \phi) + \mathcal{O}(\beta^2 J_{\mathbf{n}}^2) , \end{aligned} \quad (7.3)$$

where $Z_{\mathbf{n}} = \sum_{\mathbf{n}} e^{-\beta \bar{E}_{\mathbf{n}}}$ is the partition function of the transverse modes. This result gives that terms which are linear in $\Delta E_{\mathbf{n}}(q, \phi)$ for a specific q , including terms like $dE11dE22$, vanish at least as fast as $\mathcal{O}(\beta)$ at high temperatures. In contrast, we find

$$\begin{aligned} \langle \Delta E_{\mathbf{n}}^2(q, \phi) \rangle_{T_R} &= \frac{1}{Z} \sum_{\mathbf{n}} e^{-\beta \bar{E}_{\mathbf{n}}} 16J_{\mathbf{n}}^2 \left[\frac{1}{\beta J_{\mathbf{n}}} I_1(2\beta J_{\mathbf{n}}) + I_2(2\beta J_{\mathbf{n}}) (1 - \cos \phi) \right] \sin^2 \frac{\phi}{2} \\ &= \frac{1}{Z_{\mathbf{n}}} \sum_{\mathbf{n}} e^{-\beta \bar{E}_{\mathbf{n}}} 4J_{\mathbf{n}}^2 (1 - \cos \phi) + \mathcal{O}(\beta^2 J_{\mathbf{n}}^2) , \end{aligned} \quad (7.4)$$

and so the thermal average of $\Delta E_{\mathbf{n}}^2(q, \phi)$ is a constant to lowest order in a high-temperature expansion.

Using these results, we find that the leading order approximation in a high-temperature series expansion is

$$\begin{aligned} \langle \langle \hat{S}_{\theta_2}^z \rangle \rangle_{T_R} &= \\ &= \frac{N}{2} (\sin \theta_1 \sin \theta_2 \cos(\delta\tau) - \cos \theta_1 \cos \theta_2) + \frac{\tau N(N-1)}{2L} \sin \theta_1 \sin \theta_2 \sin(\delta\tau) (\langle C \rangle_{T_R} - \langle \chi \rangle_{T_R} \cos \theta_1) \\ &\quad - 2N \langle J^2 \rangle_{T_R} \sin \theta_1 \sin \theta_2 \cos(\delta\tau) \sin^2 \frac{\phi}{2} \tau^2 \\ &\quad - \frac{\langle J^2 \rangle_{T_R} \tau^3 N(N-1)}{6} \sin^2 \frac{\phi}{2} [6(\langle C \rangle_{T_R} - \langle \chi \rangle_{T_R} \cos \theta_1) - 2\langle \zeta \rangle_{T_R} \cos \theta_1] , \end{aligned} \quad (7.5)$$

where we have neglected interactions between pairs of particles with the same transverse mode for simplicity, $\langle \bullet \rangle_{T_R}$ denotes a thermal average with respect to the transverse modes, and we have assumed that, e.g. $\langle J^2 C \rangle_{T_R} \approx \langle J^2 \rangle_{T_R} \langle C \rangle_{T_R}$, which is valid when the tunneling is only weakly temperature dependent. From this, we find the density shift

$$\Delta\nu = \Delta\nu_0 \left[1 + \frac{4}{3} \langle J^2 \rangle_{T_R} \tau^2 \sin^2 \frac{\phi}{2} \frac{\langle \zeta \rangle_{T_R} \cos \theta_1}{\langle C \rangle_{T_R} - \langle \chi \rangle_{T_R} \cos \theta_1} \right], \quad (7.6)$$

where $\Delta\nu_0$ is the density shift in the absence of tunneling.

Chapter 8

Appendix B: Behavior of the Dicke Gap G

Here we will now discuss the behavior of the gap between the spin- $N/2$ (“Dicke states”) and spin- $(N/2 - 1)$ (“spin wave states”), referred to as the Dicke gap G , for a general Heisenberg model of the form $\hat{H} = -\frac{1}{4} \sum_{q \neq q'} J_{qq'} \hat{\sigma}_q \cdot \hat{\sigma}_{q'}$. The only condition we impose is that the coupling matrix \mathbb{J} is real, for compactness of the resulting formulas, and because all couplings considered in this work are real. Noting that the diagonal terms of \mathbb{J} only contribute an overall constant to the energy and hence do not affect the Dicke gap, they can be ignored. By direct calculation, the energy of the (degenerate) Dicke states, defined as $|N/2, m_z\rangle = \sqrt{\binom{N}{\frac{N}{2}+m_z}^{-1}} \left(\sum_{i=1}^N \hat{S}_i^+ \right)^{\frac{N}{2}+m_z} |\downarrow \dots \downarrow\rangle$, with m_z the magnetization, is $E_{\text{Dicke}} = \langle N/2, m_z | -\frac{1}{4} \sum_{q \neq q'} J_{qq'} \hat{\sigma}_q \cdot \hat{\sigma}_{q'} | N/2, m_z \rangle = -\sum_{q \neq q'} J_{q,q'}/4$. Because of the $\text{SU}(2)$ spin-rotation symmetry of \hat{H} , the Dicke states are guaranteed to be eigenstates. The spin-wave states, which span the total spin- $(N/2 - 1)$ manifold, can be defined in terms of the Dicke states as $|N/2 - 1, m_z, k\rangle = \sqrt{\frac{(N-1)}{(\frac{N}{2}-m_z+1)(\frac{N}{2}-m_z)}} \sum_{n=1}^N e^{2\pi i k n/N} \hat{S}_n^+ |N/2, m_z - 1\rangle$, where $k = 1, \dots, N - 1$. In the case of a translationally invariant Heisenberg coupling $J_{q,q'} = J_{|q-q'|}$ with $|q - q'|$ the chordal distance, the spin wave states as stated are eigenstates of \hat{H} , but when the interactions are not translationally invariant (as is the case for the spin models discussed in this work), the spin wave states only form a basis for the spin- $(N/2 - 1)$ subspace. Straightforward calculations lead to the matrix elements of the Hamiltonian in this subspace:

$$\begin{aligned} \langle \frac{N}{2} - 1, m_z, k | -\frac{1}{4} \sum_{q \neq q'} J_{q,q'} \hat{\sigma}_q \cdot \hat{\sigma}_{q'} | \frac{N}{2} - 1, m_z, k' \rangle = \\ \delta_{k,k'} E_{\text{Dicke}} + \frac{1}{N} \sum_{q \neq q'} J_{q,q'} \left[e^{\frac{2\pi i}{N}(k'-k)q} - e^{\frac{2\pi i}{N}(k'q'-kq)} \right]. \end{aligned} \quad (8.1)$$

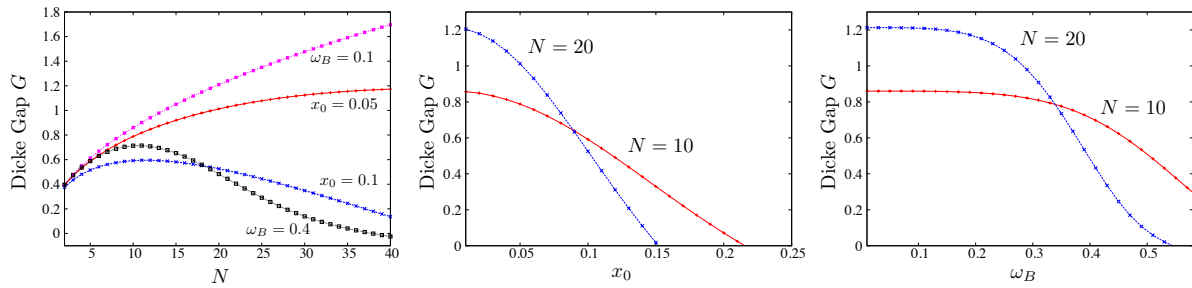


Figure 8.1: Scaling of the Dicke gap G with magnetic field gradient and particle number. (Left panel) Scaling of the Dicke gap with particle number for constant gradients of strength $x_0 = 0.05$ and 0.1 and linear gradients of strength $\omega_B = 0.1$ and 0.4 (all quantities are measured in oscillator units). All gaps increase with N to a certain gradient-dependent critical value and then decrease, with larger gaps for smaller gradients. (Right panels) Scaling of the Dicke gap at fixed particle number $N = 10$ and 20 with the constant (center panel) or linear (right panel) gradient strength. The gap closes for weaker gradient as the particle number increases, demonstrating that larger particle numbers require smaller gradients to be in the near-Heisenberg regime. For even smaller gradients, the gap increases with particle number, more effectively enforcing collective behavior.

The Dicke gap is then defined as the difference between the smallest eigenvalue of this matrix and the energy of the Dicke states. As two concrete examples, in the all-to-all case, $J_{q,q'} = J(1 - \delta_{q,q'})$, the Dicke gap is $G = JN$, and in the nearest-neighbor case $J_{q,q'} = \delta_{|q-q'|,1}J$, $G = 2(1 - \cos(2\pi/N)) \sim \frac{4\pi^2}{N^2} + \mathcal{O}(1/N^3)$. These examples illustrate the general observation that long-range, near-collective interactions cause the Dicke gap to grow with particle number, while the Dicke gap decreases with N for sufficiently short-range interactions.

In Fig. 8.1 we show the Dicke gap G for a Heisenberg model with $J_{q,q'} = J_{q,q'}^\perp$, where \mathbb{J}^\perp corresponds to different realizations of the energy-lattice spin model. The leftmost panel shows the scaling of the gaps at fixed gradient strength with particle number. The gaps are always larger for smaller gradient strength, showing that smaller gradients always lead to a more collective, near-Heisenberg behavior. The rightmost panels show the behavior of the gaps at fixed particle number as a function of gradient strength. For any fixed number of particles, there is a finite critical gradient strength where the Dicke gap closes. This critical gradient decreases with increasing particle number. However, at small enough gradient strengths, the Dicke gap is larger for increasing particle number. This demonstrates that increasing the particle number can either increase or decrease the Dicke gap.

Chapter 9

Appendix C: Matrix product state simulations

The variational matrix product state (MPS) studies of the main text were performed using extensions of the open source MPS library [132, 133]. We use an MPS ansatz which explicitly conserves total particle number, but does not conserve the total magnetization. While the dynamics preserve the total magnetization, the initial collective rotation of spins along the x direction involves a sum over many different magnetization sectors, and so leaving the magnetization unconstrained is convenient. Following this collective rotation, the next step is to enact the sudden quench of trapping parameters, which amounts to applying a spin-dependent displacement ($\psi(x) \rightarrow \psi(x + \lambda)$, constant gradient) or spin-dependent dilation ($\psi(x) \rightarrow \sqrt{\lambda}\psi(\lambda x)$, linear gradient) to the single-particle states. Since we assume harmonic traps, the displacement and dilation operators are known analytically as

$$\begin{aligned}\hat{U}_{\text{displacement}} &= e^{(\hat{a} - \hat{a}^\dagger)\lambda/(\sqrt{2}a_H)}, \\ \hat{U}_{\text{dilation}} &= e^{\ln \lambda (\hat{a}^2 - (\hat{a}^\dagger)^2)/2},\end{aligned}\tag{9.1}$$

where \hat{a} and \hat{a}^\dagger are the ladder operators of the original (no gradient) harmonic oscillator. Writing these ladder operators in second quantized form on the energy lattice, the basis transformations above take the form of time evolution under a hopping model with spin-dependent and inhomogeneous hopping amplitudes. Here, time evolution refers to the fact that the operation consists of applying the exponential of an anti-Hermitian many-body operator. In the constant gradient case, the hopping model contains only nearest-neighbor hopping, while the linear gradient case

is a model with only next-nearest neighbor hopping. We enact this effective time evolution by decomposing it into a product of few-site unitaries using a Trotter decomposition with the error controlled by a small “step size” $\Delta\lambda$, and then applying these few-site unitaries to the MPS via standard techniques [124].

Next, we wish to perform time evolution under the long-range spin model

$$\begin{aligned}\hat{H} = & \frac{u_{\uparrow\downarrow}}{4} \sum_{n \neq m} \left[J_{nm}^Z \left(\hat{N}_n \hat{N}_m - \hat{\sigma}_n^Z \hat{\sigma}_m^Z \right) - J_{nm}^\perp \left(\hat{\sigma}_n^X \hat{\sigma}_m^X + \hat{\sigma}_n^Y \hat{\sigma}_m^Y \right) + \frac{1}{2} (J_{nm}^Z - J_{mn}^Z) \left(\sigma_n^Z \hat{N}_m - \sigma_m^Z \hat{N}_n \right) \right] \\ & + u_{\uparrow\downarrow} \sum_n J_{nn} \hat{N}_n^\uparrow \hat{N}_n^\downarrow + \sum_n \left[\bar{\omega} (n + 1/2) \hat{N}_n + \Delta\omega (n + 1/2) \hat{\sigma}_n^Z \right],\end{aligned}\quad (9.2)$$

where $J_{nn} \equiv A_{nnnn}$. We perform time evolution using the second-order method of Zaletel **et al.** [171]. In this method, an explicit matrix product operator (MPO) approximation to the propagator \hat{U} is formed from the MPO form of the Hamiltonian, which is then applied to the state at time t , $|\psi(t)\rangle$ by variational minimization of the functional $\left| |\phi\rangle - \hat{U}|\psi(t)\rangle \right|^2$ over all MPSs $|\phi\rangle$ with fixed resources. For the variational minimization, we perform four sweeps per timestep and impose an upper limit on the discarded weight per bond of 10^{-9} . The maximum bond dimension used in the simulations of this work is roughly 2000.

In order to apply the method of Zaletel **et al.**, we must construct an MPO representation of the Hamiltonian Eq. (9.2). For long-range interactions which are translationally invariant, $\hat{H} = \sum_{i < j} f(j - i) \hat{A}_i \hat{B}_j$, a well-established procedure exists for converting this interaction into an MPO [172, 173]. In this procedure, the function $f(r)$ is fitted to a sum of n_{exp} exponentials via the ansatz $\tilde{f}(r) = \sum_{n=1}^{n_{\text{exp}}} J_n \lambda_n^r$, and then a known MPO construction of exponentially decaying interactions is used. Interactions on the single-particle mode space lattice are not translationally invariant, and so this procedure does not apply. However, we have devised a related procedure, in which an inhomogeneous interaction $\hat{H} = \sum_{i < j} f(i, j) \hat{A}_i \hat{B}_j$ is modeled by a sum of exponentials with site-dependent weights and exponential decay parameters via the ansatz $\tilde{f}(i, j) = \sum_{n=1}^{n_{\text{exp}}} J_{i,n} \prod_{k=i}^{j-1} \lambda_{k,n}$. These parameters are variationally optimized using an alternating least squares algorithm. Imposing the condition that the residual $\sum_{i < j} \left| f(i, j) - \tilde{f}(i, j) \right|^2 < 10^{-7}$ leads to approximations with

$n_{\text{exp}} \sim 7$ exponentials.

Bibliography

- [1] A. P. Koller, M. Beverland, A. V. Gorshkov, and A. M. Rey. Beyond the spin model approximation for ramsey spectroscopy. Phys. Rev. Lett., 112:123001, Mar 2014.
- [2] Michael E Beverland, Gorjan Alagic, Michael J Martin, Andrew P Koller, Ana M Rey, and Alexey V Gorshkov. Realizing exactly solvable su (n) magnets with thermal atoms. Physical Review A, 93(5):051601, 2016.
- [3] A. M. Rey and A. V. Gorshkov and C. Rubbo. Many-body treatment of the collisional frequency shift in fermionic atoms. Phys. Rev. Lett., 103:260402, 2009.
- [4] Kurt Gibble. Decoherence and collisional frequency shifts of trapped bosons and fermions. Physical Review Letters, 103:113202, 2009.
- [5] A.M. Rey, A.V. Gorshkov, C.V. Kraus, M.J. Martin, M. Bishof, M.D. Swallows, X. Zhang, C. Benko, J. Ye, N.D. Lemke, and A.D. Ludlow. Probing many-body interactions in an optical lattice clock. Annals of Physics, 340(1):311 – 351, 2014.
- [6] Michael L. Wall, Andrew P. Koller, Shuming Li, Xibo Zhang, Nigel R. Cooper, Jun Ye, and Ana Maria Rey. Synthetic spin-orbit coupling in an optical lattice clock. Phys. Rev. Lett., 116:035301, Jan 2016.
- [7] S Kolkowitz, SL Bromley, T Bothwell, M L. Wall, GE Marti, AP. Koller, X Zhang, AM Rey, and J Ye. Spin orbit coupled fermions in an optical lattice clock. arXiv1608.0303854 (Accepted to Nature), Aug 2016.
- [8] Andrew P. Koller, Michael L. Wall, Josh Mundinger, and Ana Maria Rey. Dynamics of interacting fermions in spin-dependent potentials. Phys. Rev. Lett., 117:195302, Nov 2016.
- [9] Marco Koschorreck, Daniel Pertot, Enrico Vogt, and Michael Kohl. Universal spin dynamics of two-dimensional fermi gases. Nature Physics, 9:405, 2013.
- [10] A. B. Bardon, S. Beattie, C. Luciuk, W. Cairncross, D. Fine, N. S. Cheng, G. J. A. Edge, E. Taylor, S. Zhang, S. Trotzky, and J. H. Thywissen. Transverse demagnetization dynamics of a unitary fermi gas. Science, 344(6185):722–724, 2014.
- [11] S. Trotzky, S. Beattie, C. Luciuk, S. Smale, A. B. Bardon, T. Enss, E. Taylor, S. Zhang, and J. H. Thywissen. Observation of the leggett-rice effect in a unitary fermi gas. Phys. Rev. Lett., 114:015301, Jan 2015.

- [12] C. Deutsch, F. Ramirez-Martinez, C. Lacroûte, F. Reinhard, T. Schneider, J. N. Fuchs, F. Piéchon, F. Laloë, J. Reichel, and P. Rosenbusch. Spin self-rephasing and very long coherence times in a trapped atomic ensemble. Phys. Rev. Lett., 105:020401, Jul 2010.
- [13] H. J. Lewandowski, D. M. Harber, D. L. Whitaker, and E. A. Cornell. Observation of anomalous spin-state segregation in a trapped ultracold vapor. Phys. Rev. Lett., 88:070403, Jan 2002.
- [14] X. Du, L. Luo, B. Clancy, and J. E. Thomas. Observation of anomalous spin segregation in a trapped fermi gas. Phys. Rev. Lett., 101:150401, 2008.
- [15] X. Du, Y. Zhang, J. Petricka, and J. E. Thomas. Controlling spin current in a trapped fermi gas. Phys. Rev. Lett., 103:010401, Jul 2009.
- [16] Andrew P. Koller, Joshua Mundinger, Michael L. Wall, and Ana Maria Rey. Demagnetization dynamics of noninteracting trapped fermions. Phys. Rev. A, 92:033608, Sep 2015.
- [17] Junjun Xu, Qiang Gu, and Erich J. Mueller. Collisionless spin dynamics in a magnetic field gradient. Phys. Rev. A, 91:043613, Apr 2015.
- [18] A. G. Sykes, J. P. Corson, J. P. D’Incao, A. P. Koller, C. H. Greene, A. M. Rey, K. R. A. Hazzard, and J. L. Bohn. Quenching to unitarity: Quantum dynamics in a three-dimensional bose gas. Phys. Rev. A, 89:021601, Feb 2014.
- [19] Michael E. Beverland, Gorjan Alagic, Michael J. Martin, Andrew P. Koller, Ana M. Rey, and Alexey V. Gorshkov. Realizing exactly solvable $su(n)$ magnets with thermal atoms. arXiv:1409.3234, 20014.
- [20] Philip Makotyn, Catherine E Klauss, David L Goldberger, EA Cornell, and Deborah S Jin. Universal dynamics of a degenerate unitary bose gas. Nature Physics, 10(2):116–119, 2014.
- [21] Xiao Yin and Leo Radzihovsky. Quench dynamics of a strongly interacting resonant bose gas. Physical Review A, 88(6):063611, 2013.
- [22] JJRM van Heugten and HTC Stoof. Theory of unitary bose gases. arXiv preprint arXiv:1302.1792, 2013.
- [23] A Rançon and K Levin. Equilibrating dynamics in quenched bose gases: characterizing multiple time regimes. Physical Review A, 90(2):021602, 2014.
- [24] John P Corson and John L Bohn. Bound-state signatures in quenched bose-einstein condensates. Physical Review A, 91(1):013616, 2015.
- [25] M Kira. Coherent quantum depletion of an interacting atom condensate. Nature communications, 6, 2015.
- [26] Tatsumi Aoyama, Masashi Hayakawa, Toichiro Kinoshita, and Makiko Nio. Tenth-order electron anomalous magnetic moment: Contribution of diagrams without closed lepton loops. Phys. Rev. D, 91:033006, Feb 2015.
- [27] BJ Bloom, TL Nicholson, JR Williams, SL Campbell, M Bishof, X Zhang, W Zhang, SL Bromley, and J Ye. An optical lattice clock with accuracy and stability at the 10-18 level. Nature, 506(7486):71–75, 2014.

- [28] T. L. Nicholson, S. L. Campbell, R. B. Hutson, G. E. Marti, B. J. Bloom, R. L. McNally, W. Zhang, M. D. Barrett, M. S. Safronova, G. F. Strouse, et al. Systematic evaluation of an atomic clock at 2×10^{-18} total uncertainty. Nature Communications, 6, 2015.
- [29] Immanuel Bloch, Jean Dalibard, and Wilhelm Zwerger. Many-body physics with ultracold gases. Reviews of Modern Physics, 80(3):885, 2008.
- [30] Claude Cohen-Tannoudji. Advances in Atomic Physics: An Overview. World Scientific Publishing Company, Singapore, 1st edition, 2011.
- [31] Stefano Giorgini, Lev P Pitaevskii, and Sandro Stringari. Theory of ultracold atomic fermi gases. Reviews of Modern Physics, 80(4):1215, 2008.
- [32] Victor Galitski and Ian B Spielman. Spin-orbit coupling in quantum gases. Nature, 494(7435):49–54, 2013.
- [33] Zhengkun Fu, Lianghai Huang, Zengming Meng, Pengjun Wang, Long Zhang, Shizhong Zhang, Hui Zhai, Peng Zhang, and Jing Zhang. Production of Feshbach molecules induced by spin-orbit coupling in Fermi gases. Nature Physics, 10(2):110–115, 2014.
- [34] BK Stuhl, H-I Lu, LM Aycok, D Genkina, and IB Spielman. Visualizing edge states with an atomic Bose gas in the quantum Hall regime. Science, 349(6255):1514–1518, 2015.
- [35] Jean Dalibard, Fabrice Gerbier, Gediminas Juzeliūnas, and Patrik Öhberg. Colloquium: Artificial gauge potentials for neutral atoms. Reviews of Modern Physics, 83(4):1523, 2011.
- [36] M Mancini, G Pagano, G Cappellini, L Livi, M Rider, J Catani, C Sias, P Zoller, M Inguscio, M Dalmonte, et al. Observation of chiral edge states with neutral fermions in synthetic Hall ribbons. Science, 349(6255):1510–1513, 2015.
- [37] Hui Zhai. Degenerate quantum gases with spin-orbit coupling: a review. Reports on Progress in Physics, 78(2):026001, 2015.
- [38] Janne Ruostekoski, Gerald V Dunne, and Juha Javanainen. Particle number fractionalization of an atomic fermi-dirac gas in an optical lattice. Physical review letters, 88(18):180401, 2002.
- [39] J Ruostekoski, J Javanainen, and Gerald Vincent Dunne. Manipulating atoms in an optical lattice: Fractional fermion number and its optical quantum measurement. Physical Review A, 77(1):013603, 2008.
- [40] Andrew J Daley, Martin M Boyd, Jun Ye, and Peter Zoller. Quantum computing with alkaline-earth-metal atoms. Physical review letters, 101(17):170504, 2008.
- [41] Alexey V Gorshkov, Ana Maria Rey, Andrew J Daley, Martin M Boyd, Jun Ye, Peter Zoller, and Mikhail D Lukin. Alkaline-earth-metal atoms as few-qubit quantum registers. Physical Review Letters, 102(11):110503, 2009.
- [42] Andrew D Ludlow, Martin M Boyd, Jun Ye, Ekkehard Peik, and Piet O Schmidt. Optical atomic clocks. Reviews of Modern Physics, 87(2):637, 2015.
- [43] Thomas H. Loftus, Tetsuya Ido, Martin M. Boyd, Andrew D. Ludlow, and Jun Ye. Narrow line cooling and momentum-space crystals. Physical Review A, 70:063413, Dec 2004.

- [44] B. J. Bloom, T. L. Nicholson, J. R. Williams, S. L. Campbell, M. Bishof, X. Zhang, W. Zhang, S. L. Bromley, and J. Ye. An optical lattice clock with accuracy and stability at the 10^{-18} level. Nature, 506(7486):71–75, 02 2014.
- [45] TL Nicholson, MJ Martin, JR Williams, BJ Bloom, M Bishof, MD Swallows, SL Campbell, and J Ye. Comparison of two independent Sr optical clocks with 1×10^{-17} stability at 10^3 s. Physical Review Letters, 109(23):230801, 2012.
- [46] N. Hinkley, J. A. Sherman, N. B. Phillips, M. Schioppo, N. D. Lemke, K. Beloy, M. Pizzocaro, C. W. Oates, and A. D. Ludlow. An atomic clock with 10^{-18} instability. Science, 341(6151):1215–1218, 2013.
- [47] Ichiro Ushijima, Masao Takamoto, Manoj Das, Takuya Ohkubo, and Hidetoshi Katori. Cryogenic optical lattice clocks. Nature Photonics, 9(3):185–189, 2015.
- [48] M. J. Martin, M. Bishof, M. D. Swallows, X. Zhang, C. Benko, J. von Stecher, A. V. Gorshkov, A. M. Rey, and J. Ye. A quantum many-body spin system in an optical lattice clock. Science, 341(6146):632–636, 2013.
- [49] N. D. Lemke, J. Von Stecher, J. A. Sherman, A. M. Rey, C. W. Oates, and A. D. Ludlow. p-wave cold collisions in an optical lattice clock. Physical Review Letters, 107:103902, 2011.
- [50] X. Zhang, M. Bishof, S. L. Bromley, C. V. Kraus, M. S. Safronova, P. Zoller, A. M. Rey, and J. Ye. Spectroscopic observation of SU(N)-symmetric interactions in Sr orbital magnetism. Science, 345(6203):1467–1473, 2014.
- [51] A. M. Rey, A. V. Gorshkov, C. V. Kraus, M. J. Martin, M. Bishof, M. D. Swallows, X. Zhang, C. Benko, J. Ye, N. D. Lemke, et al. Probing many-body interactions in an optical lattice clock. Annals of Physics, 340(1):311–351, 2014.
- [52] Michael Bishof, Michael J Martin, Matthew D Swallows, Craig Benko, Yige Lin, Goulven Quémener, Ana Maria Rey, and Jun Ye. Inelastic collisions and density-dependent excitation suppression in a 87 sr optical lattice clock. Physical Review A, 84(5):052716, 2011.
- [53] A. D. Ludlow, N. D. Lemke, J. A. Sherman, C. W. Oates, G. Quemener, J. von Stecher, and A. M. Rey. Cold-collision-shift cancellation and inelastic scattering in a yb optical lattice clock. Phys. Rev. A, 84:052724, 2011.
- [54] Ross A Williams, Lindsay J LeBlanc, Karina Jimenez-Garcia, Matthew C Beeler, Abigail R Perry, William D Phillips, and Ian B Spielman. Synthetic partial waves in ultracold atomic collisions. Science, 335(6066):314–317, 2012.
- [55] DJ Thouless. Quantization of particle transport. Physical Review B, 27(10):6083, 1983.
- [56] Lei Wang, Matthias Troyer, and Xi Dai. Topological charge pumping in a one-dimensional optical lattice. Physical review letters, 111(2):026802, 2013.
- [57] Feng Mei, Jia-Bin You, Dan-Wei Zhang, XC Yang, Rosario Fazio, Shi-Liang Zhu, and Leong Chuan Kwek. Topological insulator and particle pumping in a one-dimensional shaken optical lattice. Physical Review A, 90(6):063638, 2014.

- [58] Ran Wei and Erich J Mueller. Anomalous charge pumping in a one-dimensional optical superlattice. Physical Review A, 92(1):013609, 2015.
- [59] N. R. Cooper and A. M. Rey. Adiabatic control of atomic dressed states for transport and sensing. Physical Review A, 92(2):021401, 2015.
- [60] Michael Lohse, Christian Schweizer, Oded Zilberberg, Monika Aidelsburger, and Immanuel Bloch. A thouless quantum pump with ultracold bosonic atoms in an optical superlattice. Nature Physics, 2015.
- [61] Shuta Nakajima, Takafumi Tomita, Shintaro Taie, Tomohiro Ichinose, Hideki Ozawa, Lei Wang, Matthias Troyer, and Yoshiro Takahashi. Topological thouless pumping of ultracold fermions. Nature Physics, 2016.
- [62] H-I Lu, Max Schemmer, Lauren M Aycock, Dina Genkina, Seiji Sugawa, and Ian B Spielman. Geometrical pumping with a bose-einstein condensate. Physical review letters, 116(20):200402, 2016.
- [63] Francesco Scazza, Christian Hofrichter, Moritz Höfer, PC De Groot, Immanuel Bloch, and Simon Fölling. Observation of two-orbital spin-exchange interactions with ultracold su (n)-symmetric fermions. Nature Physics, 10(10):779–784, 2014.
- [64] Giacomo Cappellini, Marco Mancini, Guido Pagano, Pietro Lombardi, Lorenzo Livi, M Siciliani de Cumis, Pablo Cancio, Marco Pizzocaro, Davide Calonico, Filippo Levi, et al. Direct observation of coherent interorbital spin-exchange dynamics. Physical review letters, 113(12):120402, 2014.
- [65] M. L. Wall, K. R. A. Hazzard, and A. M. Rey. Effective many-body parameters for atoms in nonseperable Gaussian optical potentials. Physical Review A, 92:013610, 2015.
- [66] A Celi, P Massignan, J Ruseckas, N Goldman, IB Spielman, G Juzeliūnas, and M Lewenstein. Synthetic gauge fields in synthetic dimensions. Physical Review Letters, 112(4):043001, 2014.
- [67] Dario Hügél and Belén Paredes. Chiral ladders and the edges of quantum Hall insulators. Physical Review A, 89(2):023619, 2014.
- [68] Y Hatsugai. Topological aspects of the quantum hall effect. Journal of Physics: Condensed Matter, 9(12):2507, 1997.
- [69] L. Tarruell, D. Greif, T. Uehlinger, G. Jotzu, and T. Esslinger. Moving and merging dirac points with a fermi gas in a tunable honeycomb lattice. arXiv, 1111.5020, 2011.
- [70] M. Atala, M. Aidelsburger, J. T. Barreiro, D. Abanin, T. Kitagawa, E. Demler, and I. Bloch. Direct measurement of the zak phase in topological bloch bands. arXiv:1212.0572, 2012.
- [71] Lucia Duca, Tracy Li, Martin Reitter, Immanuel Bloch, Monika Schleier-Smith, and Ulrich Schneider. An Aharonov-Bohm interferometer for determining Bloch band topology. Science, 347(6219):288–292, 2015.
- [72] Chuanwei Zhang, Sumanta Tewari, Roman M Lutchyn, and S Das Sarma. $p_x + ip_y$ superfluid from s-wave interactions of fermionic cold atoms. Physical Review Letters, 101(16):160401, 2008.

- [73] B Juliá-Díaz, T Graß, O Dutta, DE Chang, and M Lewenstein. Engineering p-wave interactions in ultracold atoms using nanoplasmonic traps. Nature communications, 4, 2013.
- [74] Michael L Wall, Andrew P Koller, Shuming Li, Xibo Zhang, Nigel R Cooper, Jun Ye, and Ana Maria Rey. Synthetic spin-orbit coupling in an optical lattice clock. Physical Review Letters, 116(3):035301, 2016.
- [75] J. Dalibard, F. Gerbier, G. Juzelinas, and P. Ahberg. Colloquium: Artificial gauge potentials for neutral atoms. Rev. Mod. Phys., 83:1523, 2010.
- [76] Marcos Atala, Monika Aidelsburger, Michael Lohse, Julio T Barreiro, Belén Paredes, and Immanuel Bloch. Observation of chiral currents with ultracold atoms in bosonic ladders. Nature Physics, 10(8):588–593, 2014.
- [77] Monika Aidelsburger, Marcos Atala, Michael Lohse, Julio T Barreiro, B Paredes, and Immanuel Bloch. Realization of the Hofstadter Hamiltonian with ultracold atoms in optical lattices. Physical review letters, 111(18):185301, 2013.
- [78] Hirokazu Miyake, Georgios A Siviloglou, Colin J Kennedy, William Cody Burton, and Wolfgang Ketterle. Realizing the Harper Hamiltonian with laser-assisted tunneling in optical lattices. Physical Review Letters, 111(18):185302, 2013.
- [79] Junru Li, Wujie Huang, Boris Shteynas, Sean Burchesky, Furkan Cagri Top, Edward Su, Jeongwon Lee, Alan O Jamison, and Wolfgang Ketterle. Spin-orbit coupling and spin textures in optical superlattices. arXiv preprint arXiv:1606.03514, 2016.
- [80] Simone Barbarino, Luca Taddia, Davide Rossini, Leonardo Mazza, and Rosario Fazio. Magnetic crystals and helical liquids in alkaline-earth fermionic gases. Nature Communications, 6:8134, 2015.
- [81] Nathaniel Q Burdick, Yijun Tang, and Benjamin L Lev. A long-lived spin-orbit-coupled degenerate dipolar Fermi gas. arXiv preprint arXiv:1605.03211, 2016.
- [82] Bo Song, Chengdong He, Shanchao Zhang, Yueyang Zou, Elnur Hacıyev, Wei Huang, Xiong-Jun Liu, and Gyu-Boong Jo. Spin-orbit coupled two-electron Fermi gases of ytterbium atoms. arXiv preprint arXiv:1608.00478, 2016.
- [83] S Blatt, Jan Westenker Thomsen, GK Campbell, AD Ludlow, MD Swallows, MJ Martin, MM Boyd, and Jun Ye. Rabi spectroscopy and excitation inhomogeneity in a one-dimensional optical lattice clock. Physical Review A, 80(5):052703, 2009.
- [84] Pierre Lemonde and Peter Wolf. Optical lattice clock with atoms confined in a shallow trap. Physical Review A, 72(3):033409, 2005.
- [85] Léon Van Hove. The occurrence of singularities in the elastic frequency distribution of a crystal. Physical Review, 89(6):1189, 1953.
- [86] Philip Kim, Teri W Odom, Jin-Lin Huang, and Charles M Lieber. Electronic density of states of atomically resolved single-walled carbon nanotubes: Van Hove singularities and end states. Physical Review Letters, 82(6):1225, 1999.

- [87] Maxime Ben Dahan, Ekkehard Peik, Jakob Reichel, Yvan Castin, and Christophe Salomon. Bloch oscillations of atoms in an optical potential. Physical Review Letters, 76(24):4508, 1996.
- [88] Philipp M Preiss, Ruichao Ma, M Eric Tai, Alexander Lukin, Matthew Rispoli, Philip Zupancic, Yoav Lahini, Rajibul Islam, and Markus Greiner. Strongly correlated quantum walks in optical lattices. Science, 347(6227):1229–1233, 2015.
- [89] Colin V Parker, Li-Chung Ha, and Cheng Chin. Direct observation of effective ferromagnetic domains of cold atoms in a shaken optical lattice. Nature Physics, 9(12):769–774, 2013.
- [90] Gregor Jotzu, Michael Messer, Rémi Desbuquois, Martin Lebrat, Thomas Uehlinger, Daniel Greif, and Tilman Esslinger. Experimental realization of the topological Haldane model with ultracold fermions. Nature, 515(7526):237–240, 2014.
- [91] N Fläschner, BS Rem, M Tarnowski, D Vogel, D-S Lühmann, K Sengstock, and C Weitenberg. Experimental reconstruction of the Berry curvature in a Floquet Bloch band. Science, 352(6289):1091–1094, 2016.
- [92] Torben Müller, Simon Fölling, Artur Widera, and Immanuel Bloch. State preparation and dynamics of ultracold atoms in higher lattice orbitals. Physical Review Letters, 99(20):200405, 2007.
- [93] I. B. Spielman, P. R. Johnson, J. H. Huckans, C. D. Fertig, S. L. Rolston, W. D. Phillips, and JV Porto. Collisional deexcitation in a quasi-two-dimensional degenerate bosonic gas. Physical Review A, 73(2):020702, 2006.
- [94] Michael J Martin. Quantum metrology and many-body physics: pushing the frontier of the optical lattice clock. PhD thesis, Citeseer, 2013.
- [95] Miguel A Cazalilla and Ana Maria Rey. Ultracold fermi gases with emergent $su(n)$ symmetry. Reports on Progress in Physics, 77(12):124401, 2014.
- [96] S. L. Campbell et al. A Fermi-degenerate 3D optical lattice clock. in preparation, Sept 2016.
- [97] M. Gulacsi. The kondo lattice model. Philosophical Magazine, 86:1907, 2006.
- [98] Stefan S. Natu and Erich J. Mueller. Anomalous spin segregation in a weakly interacting two-component fermi gas. Phys. Rev. A, 79:051601, May 2009.
- [99] Ulrich Ebling, André Eckardt, and Maciej Lewenstein. Spin segregation via dynamically induced long-range interactions in a system of ultracold fermions. Phys. Rev. A, 84:063607, Dec 2011.
- [100] G M Bruun. Spin diffusion in fermi gases. New Journal of Physics, 13(3):035005, 2011.
- [101] F. Piéchon, J. N. Fuchs, and F. Laloë. Cumulative identical spin rotation effects in collisionless trapped atomic gases. Phys. Rev. Lett., 102:215301, May 2009.
- [102] O. Goulko, F. Chevy, and C. Lobo. Spin drag of a fermi gas in a harmonic trap. Phys. Rev. Lett., 111:190402, Nov 2013.

- [103] M. O. Oktel, T. C. Killian, D. Kleppner, and L. S. Levitov. Sum rule for the optical spectrum of a trapped gas. Phys. Rev. A, 65:033617, 2002.
- [104] J. N. Fuchs, D. M. Gangardt, and F. Laloë. Internal state conversion in ultracold gases. Phys. Rev. Lett., 88:230404, May 2002.
- [105] J. E. Williams, T. Nikuni, and C. W. Clark. Longitudinal spin waves in a dilute bose gas. Phys. Rev. Lett., 88:230405, 2002.
- [106] A S Bradley and C W Gardiner. Theory of ramsey spectroscopy and anomalous segregation in ultracold rubidium. Journal of Physics B: Atomic, Molecular and Optical Physics, 35(20):4299, 2002.
- [107] Tudor D. Stanescu, Chuanwei Zhang, and Victor Galitski. Nonequilibrium spin dynamics in a trapped fermi gas with effective spin-orbit interactions. Phys. Rev. Lett., 99:110403, Sep 2007.
- [108] Stefan S. Natu and S. Das Sarma. Spin dynamics in a spin-orbit-coupled fermi gas. Phys. Rev. A, 88:033613, Sep 2013.
- [109] J. J. Sakurai. Modern Quantum Mechanics. Addison Wesley, revised edition, 1993.
- [110] H. Y. Carr and E. M. Purcell. Effects of diffusion on free precession in nuclear magnetic resonance experiments. Phys. Rev., 94:630–638, May 1954.
- [111] E. Pinney. The nonlinear differential equation $y + p(x)y + cy^{-3} = 0$. Proc. Amer. Math. Soc., 1:681, 1950.
- [112] K. Gottfried and T.-M. Yan. Quantum Mechanics. Springer, New York, 2nd edition, 2004.
- [113] A P Ramirez. Colossal magnetoresistance. Journal of Physics: Condensed Matter, 9(39):8171, 1997.
- [114] Tilman Enss. Nonlinear spin diffusion and spin rotation in a trapped fermi gas. Phys. Rev. A, 91:023614, Feb 2015.
- [115] Z. H. Yu and C. J. Pethick. Clock shifts of optical transitions in ultracold atomic gases. Phys. Rev. Lett., 104:010801, 2010.
- [116] E.L. Hazlett, Y. Zhang, R.W. Stites, K. Gibble, and K. M. O’Hara. s-wave collisional frequency shift of a fermion clock. Phys. Rev. Lett., 110:160801, 2013.
- [117] Matthew D Swallows, Michael Bishof, Yige Lin, Sebastian Blatt, Michael J Martin, Ana Maria Rey, and Jun Ye. Suppression of collisional shifts in a strongly interacting lattice clock. science, 331(6020):1043–1046, 2011.
- [118] Wilfried Maineult, Christian Deutsch, Kurt Gibble, Jakob Reichel, and Peter Rosenbusch. Spin waves and collisional frequency shifts of a trapped-atom clock. Phys. Rev. Lett., 109:020407, Jul 2012.
- [119] M. J. Martin, M. Bishof, M. D. Swallows, X. Zhang, C. Benko, J. von Stecher, A. V. Gorshkov, A. M. Rey, and Jun Ye. A quantum many-body spin system in an optical lattice clock. Science, 341:632, 2013.

- [120] H.K. Pechkis, J.P. Wrubel, A. Schwettmann, P.F. Griffin, R. Barnett, E. Tiesinga, and P.D. Lett. Spinor dynamics in an antiferromagnetic spin-1 thermal bose gas. Phys. Rev. Lett., 111:025301, 2013.
- [121] B. Yan, S. A. Moses, B. Gadway, J. P. Covey, K. R. A. Hazzard, A. M. Rey, D. S. Jin, and J. Ye. Observation of dipolar spin-exchange interactions with lattice-confined polar molecules. Nature, 501:521–525, 2013.
- [122] Ariel Sommer, Mark Ku, Giacomo Roati, and Martin W Zwierlein. Universal spin transport in a strongly interacting fermi gas. Nature, 472(7342):201–204, 2011.
- [123] D. Niroomand, S. D. Graham, and J. M. McGuirk. Longitudinal spin diffusion in a nondegenerate trapped ^{87}Rb gas. Phys. Rev. Lett., 115:075302, Aug 2015.
- [124] Ulrich Schollwöck. The density-matrix renormalization group in the age of matrix product states. Annals of Physics, 326(1):96 – 192, 2011. January 2011 Special Issue.
- [125] A. Polkovnikov. Phase space representation of quantum dynamics. Annals of Physics, 325:1790, 2010.
- [126] J. Schachenmayer, A. Pikovski, and A. M. Rey. Many-body quantum spin dynamics with monte carlo trajectories on a discrete phase space. Phys. Rev. X, 5:011022, Feb 2015.
- [127] Lorenzo Pucci, Analabha Roy, and Michael Kastner. Simulation of quantum spin dynamics by phase space sampling of bbgky trajectories. arXiv:1510.03768, 20015.
- [128] Gerard G. Emch. Non-markovian model for the approach to equilibrium. Journal of Mathematical Physics, 7(7), 1966.
- [129] Charles Radin. Approach to equilibrium in a simple model. Journal of Mathematical Physics, 11(10), 1970.
- [130] M. Kastner. Diverging equilibration times in long-range quantum spin models. Phys. Rev. Lett., 106:130601, 2011.
- [131] M. Foss-Feig. Personal communication, 2013.
- [132] Open source mps, <http://sourceforge.net/projects/openmps/>.
- [133] M L Wall and Lincoln D Carr. Out-of-equilibrium dynamics with matrix product states. New Journal of Physics, 14(12):125015, 2012.
- [134] A. M. Rey, L. Jiang, M. Fleischhauer, E. Demler, and M. D. Lukin. Many-body protected entanglement generation in interacting spin systems. Phys. Rev. A, 77:052305, 2008.
- [135] Kaden R. A. Hazzard, Mauritz van den Worm, Michael Foss-Feig, Salvatore R. Manmana, Emanuele G. Dalla Torre, Tilman Pfau, Michael Kastner, and Ana Maria Rey. Quantum correlations and entanglement in far-from-equilibrium spin systems. Phys. Rev. A, 90:063622, Dec 2014.
- [136] Vlatko Vedral. Entanglement in the second quantization formalism. Open Physics, 1(2):289–306, 2003.

- [137] SR Clark, C Moura Alves, and D Jaksch. Efficient generation of graph states for quantum computation. New Journal of Physics, 7(1):124, 2005.
- [138] Philipp Hauke and Luca Tagliacozzo. Spread of correlations in long-range interacting quantum systems. Physical review letters, 111(20):207202, 2013.
- [139] J Schachenmayer, BP Lanyon, CF Roos, and AJ Daley. Entanglement growth in quench dynamics with variable range interactions. Physical Review X, 3(3):031015, 2013.
- [140] Jens Eisert, Mauritz van den Worm, Salvatore R Manmana, and Michael Kastner. Breakdown of quasilocality in long-range quantum lattice models. Physical review letters, 111(26):260401, 2013.
- [141] Zhe-Xuan Gong, Michael Foss-Feig, Spyridon Michalakis, and Alexey V Gorshkov. Persistence of locality in systems with power-law interactions. Physical review letters, 113(3):030602, 2014.
- [142] Philip Richerme, Zhe-Xuan Gong, Aaron Lee, Crystal Senko, Jacob Smith, Michael Foss-Feig, Spyridon Michalakis, Alexey V Gorshkov, and Christopher Monroe. Non-local propagation of correlations in quantum systems with long-range interactions. Nature, 511(7508):198–201, 2014.
- [143] Masahiro Kitagawa and Masahito Ueda. Squeezed spin states. Physical Review A, 47(6):5138, 1993.
- [144] Tomáš Opatrný and Klaus Mølmer. Spin squeezing and schrödinger-cat-state generation in atomic samples with rydberg blockade. Physical Review A, 86(2):023845, 2012.
- [145] E. Lieb and Robinson D. The finite group velocity of quantum spin systems. Commun. Math. Phys., 28:251–257, 1972.
- [146] Bruno Nachtergaele, Yoshiko Ogata, and Robert Sims. Propagation of correlations in quantum lattice systems. Journal of statistical physics, 124(1):1–13, 2006.
- [147] Marc Cheneau, Peter Barmettler, Dario Poletti, Manuel Endres, Peter Schauß, Takeshi Fukuhara, Christian Gross, Immanuel Bloch, Corinna Kollath, and Stefan Kuhr. Light-cone-like spreading of correlations in a quantum many-body system. Nature, 481(7382):484–487, 2012.
- [148] J.S. Krauser, U. Ebling, N. Flaschner, J. Heinze, K. Sengstock, M. Lewenstein, A. Eckardt, and C. Becker. Giant spin oscillations in an ultra cold fermi sea. arxiv1307.8392, 2013.
- [149] J Schachenmayer, A Pikovski, and A M Rey. Dynamics of correlations in two-dimensional quantum spin models with long-range interactions: a phase-space monte-carlo study. New Journal of Physics, 17(6):065009, 2015.
- [150] Jan C. Zill, Tod M. Wright, Karén V. Kheruntsyan, Thomas Gasenzer, and Matthew J. Davis. Relaxation dynamics of the lieb-liniger gas following an interaction quench: A coordinate bethe-ansatz analysis. Phys. Rev. A, 91:023611, Feb 2015.
- [151] Jan C Zill, Tod M Wright, Karén V Kheruntsyan, Thomas Gasenzer, and Matthew J Davis. A coordinate bethe ansatz approach to the calculation of equilibrium and nonequilibrium correlations of the one-dimensional bose gas. New Journal of Physics, 18(4):045010, 2016.

- [152] Anatoli Polkovnikov, Krishnendu Sengupta, Alessandro Silva, and Mukund Vengalattore. *Colloquium* : Nonequilibrium dynamics of closed interacting quantum systems. Rev. Mod. Phys., 83:863–883, Aug 2011.
- [153] M. Knap, A. Kantian, T. Giamarchi, I. Bloch, M. D. Lukin, and E. Demler. Probing real-space and time-resolved correlation functions with many-body ramsey interferometry. Phys. Rev. Lett., 111:147205, 2013.
- [154] T. Kitagawa, S. Pielawa, A. Imambekov, J. Schmiedmayer, V. Gritsev, and E. Demler. Ramsey interference in one-dimensional systems: the full distribution function of fringe contrast as a probe of many-body dynamics. Phys. Rev. Lett., 104:255302, 2010.
- [155] Michael Knap, Aditya Shashi, Yusuke Nishida, Adilet Imambekov, Dmitry A. Abanin, and Eugene Demler. Time-dependent impurity in ultracold fermions: Orthogonality catastrophe and beyond. Phys. Rev. X, 2:041020, Dec 2012.
- [156] A. Widera, O. Mandel, M. Greiner, S. Kreim, T. W. Hansch, and I. Bloch. Entanglement interferometry for precision measurement of atomic scattering properties. Phys. Rev. Lett., 92:160406, 2004.
- [157] Anatoly Kuklov, Nikolay Prokof'ev, and Boris Svistunov. Detecting supercounterfluidity by ramsey spectroscopy. Phys. Rev. A, 69:025601, Feb 2004.
- [158] Dmitry A. Abanin, Takuya Kitagawa, Immanuel Bloch, and Eugene Demler. Interferometric approach to measuring band topology in 2d optical lattices. Phys. Rev. Lett., 110:165304, Apr 2013.
- [159] J. M. McGuirk, H. J. Lewandowski, D. M. Harber, T. Nikuni, J. E. Williams, and E. A. Cornell. Spatial resolution of spin waves in an ultracold gas. Phys. Rev. Lett., 89:090402, Aug 2002.
- [160] D. M. Harber, H. J. Lewandowski, J. M. McGuirk, and E. A. Cornell. Effect of cold collisions on spin coherence and resonance shifts in a magnetically trapped ultracold gas. Phys. Rev. A, 66:053616, Nov 2002.
- [161] M. W. Zwierlein, Z. Hadzibabic, S. Gupta, and W. Ketterle. Spectroscopic insensitivity to cold collisions in a two-state mixture of fermions. Phys. Rev. Lett., 91:250404, 2003.
- [162] S. Gupta, Z. Hadzibabic, M. W. Zwierlein, C. A. Stan, K. Dieckmann, C. H. Schunck, E. G. M. van Kempen, B. J. Verhaar, and W. Ketterle. Radio-frequency spectroscopy of ultracold fermions. Science, 300:1723, 2003.
- [163] J. W. Britton, B. C. Sawyer, A. C. Keith, C. C. J. Wang, J. K. Freericks, H. Uys, M. J. Biercuk, and J. J. Bollinger. Engineered two-dimensional ising interactions in a trapped-ion quantum simulator with hundreds of spins. Nature, 484:489, 2012.
- [164] N. Hinkley, J. A. Sherman, N. B. Phillips, M. Schioppo, N. D. Lemke, K. Beloy, M. Pizzocaro, C. W. Oates, and A. D. Ludlow. An atomic clock with 10^{-18} instability. arXiv:1305.5869, 2013.

- [165] G. K. Campbell, M. M. Boyd, J. W. Thomsen, M. J. Martin, S. Blatt, M. D. Swallows, T. L. Nicholson, T. Fortier, C. W. Oates, S. A. Diddams, N. D. Lemke, P. Naidon, P. Julienne, J. Ye, and A. D. Ludlow. Probing interactions between ultracold fermions. Science, 324:360, 2009.
- [166] T. Busch, B. G. Englert, K. Rzazewski, and M. Wilkens. Two cold atoms in a harmonic trap. Found. Phys., 28:549, 1998.
- [167] T. L. Nicholson, M. J. Martin, J. R. Williams, B. J. Bloom, M. Bishof, M. D. Swallows, S. L. Campbell, and J. Ye. Comparison of two independent sr optical clocks with 1×10^{-17} stability at 10^3 s. Phys. Rev. Lett., 109:230801, Dec 2012.
- [168] BJ Bloom, TL Nicholson, JR Williams, SL Campbell, M Bishof, X Zhang, W Zhang, SL Bromley, and J Ye. An optical lattice clock with accuracy and stability at the 10-18 level. Nature, 506(7486):71–75, 2014.
- [169] Philip Makotyn, Catherine E. Klauss, David L. Goldberger, Eric. A. Cornell, and Deborah S. Jin. Universal dynamics of a degenerate unitary bose gas. arXiv:1308.3696, 2013.
- [170] K. O’Hara. Personal communication, 2013.
- [171] Michael P. Zaletel, Roger S. K. Mong, Christoph Karrasch, Joel E. Moore, and Frank Pollmann. Time-evolving a matrix product state with long-ranged interactions. Phys. Rev. B, 91:165112, Apr 2015.
- [172] Gregory M. Crosswhite, A. C. Doherty, and Guifré Vidal. Applying matrix product operators to model systems with long-range interactions. Phys. Rev. B, 78:035116, Jul 2008.
- [173] B Pirvu, V Murg, J I Cirac, and F Verstraete. Matrix product operator representations. New Journal of Physics, 12(2):025012, 2010.